

University of Southampton Research Repository

Copyright © and Moral Rights for this thesis and, where applicable, any accompanying data are retained by the author and/or other copyright owners. A copy can be downloaded for personal non-commercial research or study, without prior permission or charge. This thesis and the accompanying data cannot be reproduced or quoted extensively from without first obtaining permission in writing from the copyright holder/s. The content of the thesis and accompanying research data (where applicable) must not be changed in any way or sold commercially in any format or medium without the formal permission of the copyright holder/s.

When referring to this thesis and any accompanying data, full bibliographic details must be given, e.g.

Thesis: Author (Year of Submission) "Full thesis title", University of Southampton, name of the University Faculty or School or Department, PhD Thesis, pagination.

Data: Author (Year) Title. URI [dataset]

University of Southampton

Faculty of Engineering and Physical Sciences

School of Engineering

Developing Magnesium Alloys with a Combination of Strength and Ductility

Based on Friction Stir-Based Technologies

by

Xingjian Zhao

Thesis for the degree of Doctor of Philosophy

09/2025

ORCiD:0000-0001-5909-3043

University of Southampton

Abstract

Faculty of Engineering and Physical Sciences
School of Engineering
Doctor of Philosophy

Developing Magnesium Alloys with a Combination of Strength and Ductility Based on Friction Stir-Based Technologies

by Xingjian Zhao

Magnesium (Mg) and its alloys are the lightest structural metallic materials. The density of Mg and its alloys is approximately two-thirds of the density of aluminium (AI) alloys and nearly four to five times lighter than steel. Due to the low density and high strength-to-weight ratio, Mg alloys have been used in transportation applications where mass reduction is essential, such as automobiles, aeronautics, and astronautics. The reduction of structural weight can improve the efficiency of fuel usage and produce less emission. However, the high energy cost of Mg production weakens the benefit of less emission by using light-weight Mg alloy structures. Moreover, because of the hexagonal close packed (HCP) crystal structure, Mg alloys often face severe strength-ductility trade-off. As a result, producing Mg alloys with a combination of strength and ductility with lower energy consumption is essential for the development of Mg industry.

Friction stir-based technologies are considered promising for the production of Mg alloys with a combination of strength and ductility. As variants developed from friction stir welding (FSW), friction stir based technologies share similar features of the microstructure evolution such as grain refinement, large second phase particle fragmentation, pore closure, etc. The work involved three variants, including stationary shoulder friction stir channelling (SS-FSC, Coreflow®), friction stir processing (FSP), and additive friction stir deposition (AFSD). SS-FSC and FSP were used in combination with spark plasma sintering (SPS) to recycle waste Mg-4Y-3RE (WE43C) scraps, turning them into wires and disks, respectively. AFSD was used to achieve the additive manufacturing (AM) of WE43C.

The mechanical stirring and generated friction heat during the processing, and thus dynamic recrystallisation (DRX), especially the continuous dynamic recrystallisation (CDRX) actively participated in the grain evolution. DRX occurred during the fabrication produced

refined grains with an average grain size \sim 1-10 µm in the final products. Besides, the presence of fine thermal stable oxide particles either originated from the oxide film grown during the SPS or in-situ formed during the processing can further assist in controlling the grain size. Due to the mechanical stirring and elevated temperature during the processing, pre-existing second phase particles can be fragmented and partly re-dissolve into the matrix. Pre-existing oxide films, if there were some in the material, can also be fragmented but not re-dissolved. These particles were further redistributed throughout the material. Oxide nanoparticles were also in-situ formed during AFSD and provided extraordinary thermal stability at elevated temperature by pinning the grain boundary migration. Basal texture developed during the deformation. The orientation of the $\{0001\}$ planes was strongly dependent on the material flow behaviour, which is mainly parallel to the material flow plane. Pores were detected in the material. Pore shape is closely related to the material flow behaviour as they all exhibited flake-like shapes and the thickness were parallel to the normal direction of the material flow plane.

Refined grain size provided strengthening effects by the volume increment in grain boundaries, contributing to the strength improvement of the material. For WE43C Mg alloys, when subjected to further ageing treatment at 200 °C, plate-like β_1 phase precipitated on $\{10\bar{1}0\}$ planes of α -Mg matrix. These precipitates acted as obstacles to the movement of dislocations and thus increased the strength of the fabricated material. In addition, a quicker ageing response around 30-40 h in these materials was observed, at the cost of a reduction in hardness enhancement. Apart from these factors, pores also played an essential role in the mechanical properties, especially the elongation of the material. FSPed material, where the pore size and fraction were higher than the other two samples, exhibited much lower elongation and even partly failure of the material during tensile tests. Refined grains, weakened gradient basal texture produced by friction stir-based technologies provided the combination of strength and ductility, yet if pores were not well controlled, a significant drop in the ductility could occur.

This work explored producing Mg alloy with a good combination of strength and ductility with lower environmental impact using friction stir based technologies. It specifically reveals the effects of processing on the final texture gradient in SS-FSC and the role of oxide formation on the subsequent heat treatment, including the ageing peak shift and strengthening effect, which were not previously investigated in detail.

Key words: Mg alloys, friction stir based technologies, microstructure, texture, mechanical properties.

Table	of C	ontent	s	IV
Table	of T	ables .		IX
Table	of F	igures		X
Rese	arch	Thesis	: Declaration of Authorship	XVII
Ackn	owle	dgeme	nts	XIX
Defin	itions	s and A	Abbreviations	xx
Chap	ter 1	Intro	duction	1
1.1	Back	ground	information	1
Chap	ter 2	Litera	iture review	4
2.1	Gene	eral info	ormation and brief history of magnesium	4
2.2	Basi	c prope	erties of magnesium	5
2.3	Strer	ngtheni	ng mechanism in Mg and its alloys	7
2	.3.1 (Grain bo	oundary strengthening (Hall-Petch strengthening)	7
2	.3.2 \	Work ha	rdening	8
2	.3.3	Solid so	lution strengthening	8
2	3.4 F	Precipit	ation strengthening	9
2.4	Alloy	ing ele	ements and studies of Mg-Al-Zn and Mg-Y-RE alloys	99
2	2.4.1	Major al	lloying elements	10
	2	2.4.1.1	Aluminium	10
	2	2.4.1.2	Zinc	11
	2	2.4.1.3	Manganese	12
	2	2.4.1.4	Yttrium	13
	2	2.4.1.5	Rare earths	14
	2	2.4.1.6	Zirconium	14
2	2.4.2	Mg-Al-Z	n (AZ series) and Mg-Y-RE (WE series)	15

		2.4.2.1	AZ series and AZ31B	. 15
	2.4.3	Mg-Y-RE	(WE series) and Elektron 43 (WE43C)	. 16
2.5	Bri	ef situatio	on of Mg and its alloys production	. 16
2.6	Frie	ction stir-	based technology	. 17
	2.6.1	Friction	stir welding (FSW) and the grain refinement mechanism	. 17
	2.6.2	Friction	stir processing (FSP)	. 21
	2.6.3		stir channelling (FSC) and stationary shoulder friction stir ing (SS-FSC, CoreFlow [®])	. 23
	2.6.4	Additive	friction stir deposition (AFSD)	. 24
2.7	Cui	rrent cha	lenges of Mg alloys	. 26
	2.7.1	High ene	ergy input and environmental effects of production	. 27
	2.7.2	Insufficie	ent strength-ductility combination	. 27
2.8	Cui	rrent app	roaches under investigation	. 28
	2.8.1	Current	research aiming at the green production of magnesium	. 28
		2.8.1.1	Recycling of magnesium	. 28
		2.8.1.2	Additive manufacturing (AM) of magnesium	. 31
	2.8.2		research aiming at the simultaneous achievement of strength a	
		2.8.2.1	Texture weakening by specific alloying element addition	. 35
		2.8.2.2	Grain refinement by severe plastic deformation (SPD)	. 36
2.9	Res	search foo	eus of the present study	. 40
Cha	pter	3 Materi	als and methodology	. 43
3.1	Ma	terials		. 43
3.2	. Ma	terials pr	ocessing	. 44
	3.2.1	Spark pla	asma sintering (SPS)	. 44
	3.2.2	Stationa	ry shoulder friction stir channelling (SS-FSC)	. 46
	3.2.3	Friction	stir processing (FSP)	. 48

	3.2.4	Additive friction stir deposition (AFSD)	. 49
3.3	Pos	st heat treatment	. 50
3.4	Mic	crostructure characterisation	. 51
	3.4.1	SEM, SEM-EDS, EBSD and the sample preparation	. 51
	3.4.2	X-ray diffraction (XRD) characterisation	. 51
	3.4.3	X-ray computed tomography (XCT) characterisation	. 52
	3.4.4	Transmission electron microscopy (TEM) and the sample preparation	. 53
3.5	Med	chanical property characterisation	. 53
	3.5.1	Microhardness tests	. 53
	3.5.2	Tensile tests	. 53
Cha	pter 4	4 Investigation of microstructure and mechanical properties of	of
		AZ31B wire produced by SS-FSC	56
4.1	Intr	roduction	. 56
4.2	? Res	sults	. 57
	4.2.1	Microstructure and texture evolution	. 57
	4.2.2	Mechanical properties and fractography	. 62
4.3	B Dis	cussion	C 4
1 1			. 64
4.4	Cor	nclusions	
			. 68
		nclusions	. 68 PS
	apter (nclusions5 Recycled WE43C Mg alloy wire production incorporating SF	. 68 PS . 70
Cha	apter (nclusions 5 Recycled WE43C Mg alloy wire production incorporating SF and SS-FSC	. 68 PS . 70 . 70
Cha 5.1	apter s	nclusions 5 Recycled WE43C Mg alloy wire production incorporating SF and SS-FSC	. 68 . 70 . 70 . 71
Cha 5.1	apter s	nclusions	. 68 . 70 . 70 . 71
Cha 5.1	apter s	nclusions	. 68 . 70 . 71 . 71

5.2.2 Mechanical properti	es83
5.2.2.1 Microhardr	ness tests83
5.2.2.2 Tensile tes	ts and fractography85
5.3 Discussion	87
5.3.1 Evolution of microst	ructure and texture87
5.3.1.1 WE43C sc	rap and SPSed disk87
5.3.1.2 SS-FSC ex	ktruded WE43C wire90
5.3.2 Effects of post heat	treatment and mechanical properties93
5.4 Conclusions	95
Chapter 6 Recycled WE43	C disk preparation incorporating SPS and FSP
	97
6.1 Introduction	97
6.2 Results	98
6.2.1 Microstructure and	texture evolution from scraps to FSPed disk 98
6.2.1.1 WE43C sc	rap and SPSed disk98
6.2.1.2 FSPed WE	l3C disk 98
6.2.2 Ageing treatment an	d the resulting hardness and precipitation evolution 105
6.2.3 Tensile tests and fra	ctography 108
6.3 Discussion	110
6.3.1 Evolution of grain siz	e, second phases, texture and porosity 110
6.3.2 Effects of post heat	treatment and mechanical properties113
6.4 Conclusions	116
Chapter 7 Solid-state addi	tive manufacturing of WE43C by additive
friction stir dep	osition (AFSD)118
7.1 Introduction	118
7.2 Results	119

7.2.1	Microstr	ucture of the feedstock	119
7.2.2	Microstr	ucture of the as-printed WE43C	120
	7.2.2.1	Grain structure and texture	120
	7.2.2.2	Second phases and oxides	123
	7.2.2.3	Pore structure	128
7.2.3	Hardnes	s tests of the as-printed WE43C	129
7.2.4	Solid sol	ution treatment (SST) and thermal stability	130
7.2.5	Ageing tr	eatment and mechanical properties	136
7.3 Dis	cussion		.140
7.3.1	Microstr	ucture and texture evolution during AFSD	140
7.3.2	SST and	Thermal stability	145
	7.3.2.1	Grain growth behaviour	145
	7.3.2.2	Driving force and retarding force of the grain growth	146
	7.3.2.3	Effects of nanoparticles	149
7.3.3	Mechani	ical property evolution during the ageing heat treatment	150
7.4 Cor	nclusions	· · · · · · · · · · · · · · · · · · ·	.153
Chapter 8	8 Concl	usive discussion and summary	155
Chapter 9	9 Futur	e work	158
9.1 Fut	ure explo	ration of SS-FSC for WE43C recycling	.158
9.2 Opt	timisation	n of processing parameters for WE43C recycling by FSP	.159
9.3 Hig	h temper	ature mechanical tests of AFSDed WE43C	.159
Appendi	хΔ	[List of publications and attended conferences]	160
			161

Table of Tables

Table 3.1 Chemical composition of AZ31B Mg alloy43
Table 3.2 Chemical composition of WE43C Mg alloy43
Table 3.3 Parameters of SS-FSC for AZ31B and WE43C47
Table 3.4 Sample size and set up for XCT52
Table 4.1 Lengths fraction of GBs and area fraction of GOS value of as-received and SS-FSC extruded samples
Table 4.2 YS, UTS, and El of as-received and SS-FSC extruded AZ31B63
Table 5.1 EDS Chemical composition (weight %) for major second phase particle in the SPSed WE43C72
Table 5.2 YS, UTS, and El of SS-FSC and SS-FSC + T5 treated WE43C86
Table 6.1 Tensile tests results of FSPed and FSP+aged specimen108
Table 7.1 Summary of grain size for three different sites taken from the centre layer 122
Table 7.2 EDS scan results of the nanoparticles in the AFSDed WE43C127
Table 7.3 EDS Chemical composition (atomic %) for regions detailed in Figure 7.14 134

Table of Figures

Figure 2.1 (a) A unit cell of Mg, (b) basal and prismatic slip systems, (c) first and second
pyramidal slip systems, (d) extension and contraction twinning systems6
Figure 2.2 Critical resolved shear stress values for different slip and twinning modes and their variation with temperature in pure Mg [9]7
Figure 2.3 Mg-Al binary phase diagram[6]11
Figure 2.4 Mg-Zn binary phase diagram[6]12
Figure 2.5 Part of the Mg-Mn binary phase diagram[6]13
Figure 2.6 Part of the Mg-Y binary phase diagram [6]14
Figure 2.7 Part of the Mg-Zr binary phase diagram[6]15
Figure 2.8 Schematic illustration of the FSW process [82]18
Figure 2.9 Progress of CDRX [85]20
Figure 2.10 Progress of DDRX [85]21
Figure 2.11 Schematic illustration of the FSP process [89]22
Figure 2.12 Schematic illustration of the SS-FSC/CoreFlow® process [100]24
Figure 2.13 Schematic illustration of the AFSD process [101]25
Figure 2.14 Schematic illustration of the LPBF process [133]
Figure 2.15 Schematic illustration of the conventional LDED process [137]33
Figure 2.16 Schematic illustration of the wire-based LDED process [133]34
Figure 2.17 Schematic illustration of WAAM [138]34
Figure 2.18 Schematic illustration of the ECAP process
Figure 2.19 Schematic illustration of the thin disc-HPT process [149]39
Figure 2.20 Schematic illustration of principles of the accumulative roll bonding (ARB) process [159]

Table of Figures

Figure 3.1 WE43C scraps produced from the machining44
Figure 3.2 WE43C feedstock for AFSD44
Figure 3.3 Designated temperature and applied force with time for the SPS45
Figure 3.4 A schematic of coordinates for SPSed disk45
Figure 3.5 A photo of the SS-FSC tool and set up46
Figure 3.6 A schematic of coordinates for SS-FSC extruded (CoreFlowed) wire48
Figure 3.7 A schematic of coordinates for FSPed disk49
Figure 3.8 Schematic of the AFSD set up [160]50
Figure 3.9 (a) Deben CT500 tensile stage for tensile tests, (b) tensile test sample set up in the
Deben CT500 tensile stage, (c) sketch of the cylindrical tensile test sample of SS-FSC
extruded wire54
Figure 3.10 Sketch of (a) position of the tensile specimens of FSPed material, (b) size of the
tensile test specimens of FSPed material55
Figure 3.11 Sketch of tensile tests samples of AFSDed material (a) locations of specimens,
(b) sizes of specimens [160]55
Figure 4.1 (a) A photo of the consolidated AZ31B wire, (b) A photo of other wires which were
not fully consolidated58
Figure 4.2 (a-1) EBSD IPF map of as-received AZ31B along TD (IPF-Z//TD), (a-2) position of
EBSD zone on as-received sample; (b-1) EBSD IPF map of SS-FSC extruded AZ31B along TD
(IPF-Z//ED), (b-2) position of EBSD zone on SS-FSC extruded zone58
Figure 4.3 (a-1)-(a-7) PFs and (b-1)-(b-7) IPFs of as-received and SS-FSC extruded AZ31B60
Figure 4.4 GOS maps of (a) as-received AZ31B along TD, (b) SS-FSC extruded AZ31B along TD
60
Figure 4.5 (a) A typical region of uncompleted CDRX occurrence in SS-FSC extruded AZ31B,
(b) The cumulative disorientation from point A to B61

Figure 4.6 BSE images of (a) as-received AZ31B along TD, (b) SS-FSC extruded AZ31B TD1-
TD2 plane, (c) SS-FSC extruded AZ31B TD1-ED plane, (d) A 3D view of second-phase particles
in a cylindrical volume extracted from SS-FSC extruded AZ31B XCT result62
Figure 4.7 (a) Engineering and true stress-strain curves of SS-FSC extruded and as-received
AZ31B, (b) SE image of fractured surface of as-received AZ31B, (c) SE image of fractured
surface of SS-FSC extruded AZ31B64
Figure 5.1 Schematic of the solid-state recycling method combining SPS and SS-FSC71
Figure 5.2 (a) BSE image of the scrap, (b-f) ESD maps of the scrap corresponding to the BSE
image, (g) EDS line scan data from the site in the BSE image indicated by the arrow, (h) EDS
point scan data of the cuboidal particle73
Figure 5.3 (a) EBSD IPF of the scrap, (b) The accumulative disorientation plot within in a grain,
corresponding to the white arrow in the IPF map. (c). Band contrast map with an over layer
of special grain boundaries, (d) relative frequency of grain boundary disorientation map. 74
Figure 5.4 (a) SEM-BSE image of the SPSed disk, (b-f) ESD maps of the SPSed disk
corresponding to the BSE image75
Figure 5.5 (a) STEM-HAADF image of the SPSed disk, (b) TEM-BF image of the thin-layered
structure, (c) EDS line scan of the thin layered structure, at the site of the orange line in (a)
76
Figure 5.6 3D view of second phases and pores in the SPSed disk (a) 5mm-diameter
cylindrical volume (C1), (b) 1.2mm-diameter cylindrical volume (C2)77
Figure 5.7 (a) IPF map of the SPSed disk, (b) Pole figure, (c) GOS map of the SPSed disk, (d)
the BSE image of the EBSD region78
Figure 5.8 SEM-BSE images of (a) SS-FSC extruded wire from the edge to the centre, stitched,
(b) wire edge, (c) wire centre79
Figure 5.9 (a) A representative XCT 2d slice of the TD1-TD2 plane, (b) 3D view of the pore in
the SS-FSC extruded wire
Figure 5.10 The comparison regarding pores in the SPSed and SS-FSC extruded material .81
Figure 5.11 (a) EBSD IPF map, IPF//ED (b) pole figure (c) GOS map of the SS-FSC extruded
WE43C wire82

Figure 5.12 (a1-a5) EBSD-IPF maps of R1-R5, IPF//ED, (b1-b5) GOS maps of R1-R5, (c1-c5) Pole figures of R1-R583
Figure 5.13 Vickers microhardness values of the SS-FSC extruded wire at 3 different sites
Figure 5.14 Vickers microhardness evolution during the T5 heat treatment at 200 °C85
Figure 5.15 Hardness values of SPSed, SS-FSCed, and SS-FSC+T5 treated sample85
Figure 5.16 Stress strain curves of SS-FSC recycled WE43C sample and SS-FSC +T5 sample
Figure 5.17 (a1-a3) SEM-SE image of the entire fractured surface, magnified fractured surface, and BSE image in the SS-FSCed sample, (b1-b3) SEM-SE image of the entire fractured surface, magnified fractured surface, and BSE image in the SS-FSC+T5 treatment sample.
Figure 5.18 Scattered point plot of mechanical properties of WE43C alloys prepared by various methods and the SS-FSC recycled material (a) yield strength-elongation plot and (b) ultimate tensile strength-elongation plot. [39, 43, 45, 86, 129, 135, 178, 198-203]
Figure 6.1 Schematic of the solid-state recycling method combining SPS and FSP98
Figure 6.2 (a1-a2) regions with homogeneous microstructure, (b1-b2) regions with heterogeneous microstructure, 'fuzzy' regions with finer grains and denser second phases, together with a pore.
Figure 6.3 (a) SEM-BSE image of oxide particles in the FSPed disk, (b) EDS line scan data .99
Figure 6.4 3D view of second phases and pores in the FSPed disk (a) 5mm-diameter cylindrical volume (C3), (b) 1.2mm-diameter cylindrical volume (C4)
Figure 6.5 The comparison regarding pores in the SPSed and FSPed material 101
Figure 6.6 EBSD IPF maps of the FSPed material at different sites in the processed zone.
Figure 6.7 The corresponding region of the observed zone in Figure 6.6
Figure 6.8 GOS maps of the FSPed material at different sites in the processed zone 103

Figure 6.9 (a) EBSD IPF map of R2-4, (b) higher magnification map of the unindexed region104
Figure 6.10 (0002) pole figures of the FSPed material at different sites in the processed zone.
Figure 6.11 (a) Hardness evolution during the T5 treatment at 200 °C, (b) comparison of the
hardness of SPSed, FSPed, and FSP+aged WE43C 106
Figure 6.12 XRD spectrum of FSPed and FSP+aged WE43C107
Figure 6.13 (a) SEM-BSE image of the FSP+aged sample, (b) STEM-HAADF image and SAED
pattern of the precipitates. (c) HRTEM image of the β_1 precipitate
Figure 6.14 (a1) Photo of the FSPed specimens after fracture, (a2) engineering stress-strain
curves of the FSPed specimens, (b) Photo of the FSP+aged specimens after fracture, (b2)
engineering stress-strain curves of the FSP+aged specimens109
Figure 6.15 (a1-a2) SEM image of the fractured surface of the FSPed specimens, (b1-b2) SEM
image of the fractured surface of the FSP+aged specimens
Figure 6.16 precipitation sequence in the Mg-Y-Nd alloy system [23]113
Figure 6.17 Scattered point plot of mechanical properties of Mg-4Y-3RE alloys prepared by
various methods and the SPS-FSP recycled material (a) yield strength-elongation plot and
(b) ultimate tensile strength-elongation plot. [39, 43, 45, 86, 129, 135, 178, 198-203] 116
Figure 7.1 (a) EBSD IPF map of the feedstock, IPF//ED, (b) (0002) pole figure, (c) inverse pole
figure along the ED, (d) SEM-BSE image of the feedstock
Figure 7.2 (a) position of samples taken from the printed WE43C component, (b) a large-area
EBSD IPF maps of the base material-printed material interface, (c1-3) EBSD IPF maps of the
centre part, middle part, edge part in the centre layer of the printed wall 122
Figure 7.3 (a1-a3) GOS map of the centre part, including overall map, carse grain regions and
fine grain regions, (b1-b3) GOS map of the middle part, including overall map, carse grain
regions and fine grain regions, (c1-c3) GOS map of the edge part, including overall map,
carse grain regions and fine grain regions123
Figure 7.4 Pole figures of (0002) basal planes in the regions at centre, middle, and edge part

Figure 7.5 (a1-a3) SEM images of the centre, middle and edge part, 100 times magnification,
(b1-b3) SEM images of the centre, middle and edge part, 1000 times magnification 124
Figure 7.6 SEM-BSE image containing coarse grain regions and fine grain regions, and the
corresponding EDS maps125
Figure 7.7 TEM-HAADF image showing the second phase difference between coarse grained
and fine grained regions126
Figure 7.8 TEM images and EDS maps of (a) coarse second phases around 1 μm (b)
nanoparticles in the AFSDed WE43C127
Figure 7.9 TEM images of nanoparticles (a) different structures and sizes, (b) orientation
relationship between the single particle and the matrix
Figure 7.10 3D view of XCT results of of the (a) centre part, (b) middle part, (c) edge part. 129
Figure 7.11 (a) Vickers microhardness test results along the TD, (b) Vickers microhardness
test results along the BD. Both corresponding to the locations shown in Figure 7.2a 130
Figure 7.12 EBSD IPF maps of AFSDed samples after SST for (a) 0h, (b) 4h, (c) 24h, (d) 72h,
under $\times 500$ magnification. BD is the building direction, TD is the transverse direction, LDis
the processing direction (longitudinal direction); and extruded feeds tock samples after SST $$
for (e) 0h, (f) 0.5h, (g) 1h, (h) 2h, under ×400, ×150, ×150, and ×100 magnification
Figure 7.13 AFSDed sample (a) SEM-BSE image, (b) HAADF image, (c) BF image; AFSDed-4h-
SST sample (d) SEM-BSE image, (e) HAADF image, (f) BF image; SEM-BSE images of
feedstock sample (g) 0h-SST, (h) 2h-SST
Figure 7.14 XRD spectrum of as-AFSDed material and 4h-SST
Figure 7.15 BF images, HAADF images, and EDS maps of nanoparticles in the 4h-SST sample
134
Figure 7.16 S/TEM images of a region in AFSDed-4h-SST (a) HAADF image, (b) BF image, (c)
BF image with a sketch of grain boundaries. (d)-(f) BF images of other regions with grain
boundary bowing, indicated by red arrows
Figure 7.17 Microhardness value evolution during the T6 post heat treatment
Figure 7.18 Vickers hardness test results of WE43C in different conditions

Table of Figures

Figure 7.19 IEM-BF images and EDS scans of (a) precipitates at grain boundaries (b) plate-
like precipitates in the grain interior
Figure 7.20 (a) STEM-BF images of precipitates (b) HRTEM images of the plate-like precipitate
Figure 7.21 stress strain curves of as-AFSDed WE43C, tension along the LD
Figure 7.22 A schematic of the grain evolution history during the AFSD143
Figure 7.23 (a) Grain size change with time, (b) Plot of $D2.5 - D02.5$ against time 146
Figure 7.24 GOS maps of (a) AFSDed sample; (b) feedstock material
Figure 7.25 Pole figures of (a) AFSDed sample, (b) feedstock material
Figure 7.26 Scattered point plot of mechanical properties of Mg-4Y-3RE alloys prepared by
various methods and the SPS-FSP recycled material (a) yield strength-elongation plot and
(b) ultimate tensile strength-elongation plot. [39, 43, 45, 86, 129, 135, 178, 198-203] 153
Figure 9.1 EBSD IPF maps of SS-FSC recycled wire (a) as-received state (b) 30min SST (c) 4h
SST158

Research Thesis: Declaration of Authorship

Print name: Xingjian Zhao

Title of thesis: Developing Magnesium Alloys with a Combination of Strength and Ductility Based on Friction Stir-Based Technologies

I declare that this thesis and the work presented in it are my own and has been generated by me as the result of my own original research.

I confirm that:

- 1. This work was done wholly or mainly while in candidature for a research degree at this University;
- 2. Where any part of this thesis has previously been submitted for a degree or any other qualification at this University or any other institution, this has been clearly stated;
- 3. Where I have consulted the published work of others, this is always clearly attributed;
- 4. Where I have quoted from the work of others, the source is always given. With the exception of such quotations, this thesis is entirely my own work;
- 5. I have acknowledged all main sources of help;
- 6. Where the thesis is based on work done by myself jointly with others, I have made clear exactly what was done by others and what I have contributed myself;
- 7. Parts of this work have been published as:
- [1] **X. Zhao**, X. Zeng, L. Yuan, J. Gandra, Q. Hayat, M. Bai, W.M. Rainforth, D. Guan, A novel approach for producing Mg-3Al-1Zn-0.2 Mn alloy wire with a promising combination of strength and ductility using CoreFlowTM, Scripta Materialia 227 (2023) 115301.
- [2] **X. Zhao**, Y. Xie, J. Gandra, M. Murphy, W.M. Rainforth, D. Guan, A Succinct Method to Recycle WE43 Mg Alloys—From Wasted Chips to Consolidated Billets, TMS Annual Meeting & Exhibition, Springer, (2024), 151-153.
- [3] **X. Zhao**, D. Olden, B. Williams, A. Pariyar, D. Zhang, M. Murphy, P. Reed, P. Allison, B. Jordon, J. Qi, W. M. Rainforth, D. Guan, Grain growth stagnation at 525° C by nanoparticles in a solid-state additively manufactured Mg-4Y-3RE alloy, Journal of Magnesium and Alloys (2024), 4976-4987.
- [4] **X. Zhao**, J. Gandra, M. Murphy, R. Mitchell, F. A. Borges, S. Holdsworth, L. Ma, B. Guan, W. M. Rainforth, D. Guan, A solid-state recycling method for Mg-4Y-3RE alloy scraps incorporating spark plasma sintering and friction stir processing, in preparation

Research Thesis: Declaration of Authorship

The author contributed to all the experimental work, data analysis, visualisation, and manuscript writing and editing, except the XCT and TEM data acquisition.

Signature: Date: 16/09/2025

Acknowledgements

When I'm writing this part, I realise I am approaching the end of the 4-year PhD life, and also the end of my 20-year life as a student. It is hard to believe that I have spent 10 years studying materials science and engineering, and I'm soon going to use this knowledge to support my career in a few months. Before the end of my PhD life, please let me express my gratitude to those who helped me during the past 4 years.

First, I would like to express my deepest gratitude to my first supervisor Dr. Dikai Guan. In the past four years, from Sheffield to Southampton. He has guided me on how to do experiments from the very beginning step by step, and has always been generous in sharing his own experience, skills, and knowledge in each academic aspect. I would like to thank my secondary/external supervisor Prof. Mark Rainforth for his help with academic writing and microstructure characterisation over the past four years. I would also like to thank my secondary supervisor Prof. Philippa Reed, for her suggestions about research.

Second, I would like to thank my colleagues, all the academic staff and technicians who offered help, and my friends during my research and daily life. Dr. Xun Zeng, Dr Le Ma, Haoran Yi, Zhiyu Quan, Yanheng Xie, Dr Joao Gandra, and others. It is a really long list, and forgive me for not listing them all. PhD project is a learning process, and I learned a lot from these people. Without their help, either in work or daily life, I am not able to complete it on time. I would also like to thank my girlfriend Qianqian Liu for her support in the final year, accompanying me in the hardest part of the PhD life.

Finally, I would like to thank my dear father and mother, and all other family members.

I would have never achieved what I have today without my parents' love and support. No words could ever fully convey the depth of my gratitude towards them.

Definitions and Abbreviations

2D Two dimensional

3D...... Three dimensional

AFSD Additive friction stir deposition

AGG...... Abnormal grain growth

AM Additive manufacturing

ARB Accumulative roll bonding

AS..... advancing side

BCC Body-centred cubic

BF..... Bright field

BM Base material

BSE Backscattered electron

CDRX Continuous dynamic recrystallisation

DDRX Discontinuous dynamic recrystallisation

DF..... Dark field

DRV Dynamic recovery

DRX...... Dynamic recrystallisation

EBSD..... Electron backscattered diffraction

ECAP Equal channel angular pressing

EDS Energy dispersive spectroscopy

FCC Face-centred cubic

FEM Finite element modelling

FSC Friction stir channelling

FSE..... Friction stir extrusion

FSP..... Friction stir processing

FSW..... Friction stir welding

GND...... Geometrically necessary dislocation

Definitions and Abbreviations

GOS...... Grain orientation spread HAADF High angle annular dark field HAGB High angle grain boundary HAZ Heat affected zone HCP Hexagonal close-packed HPT High pressure torsion IPF...... Inverse pole figure LAGB Low angle grain boundary MUD Multiples of uniform density ODS...... Oxide dispersion strengthened PF..... Pole figure PFZ...... Precipitation free zone ROI Region of interest RE...... Rare earth RS...... Retreating side SEM..... Scanning electron microscope SF..... Schmid factor SFE...... Stacking fault energy SPH Smoothed particle hydrodynamic SPS Spark plasma sintering SRV Static recovery SRX Static recrystallisation SS-FSE...... Stationary shoulder friction stir extrusion SSSS Super saturated solid solution STEM...... Scanning transmission electron microscope SZ..... Stir zone TEM Transmission electron microscope TMAZ..... Thermal mechanical affected zone

Definitions and Abbreviations

XCT	X-ray computed tomography
XRD	X-ray diffraction

Chapter 1 Introduction

1.1 Background information

Magnesium (Mg) and its alloys offer a range of distinct advantages that make them highly attractive for modern engineering applications. Mg and its alloys are the lightest structural metallic materials. The density of Mg and its alloys is around 1.74g/cm³, approximately two-thirds of the density of aluminium (AI) alloys and nearly four to five times lighter than steel. Although the strengths of Mg and its alloys are lower than those of Al alloys and steels, the low density compensates for these limitations, providing strength-to-weight ratio. This promotes the use of Mg and its alloys in some weight-critical applications, such as automobiles, aeronautics, and astronautics. The weight reduction by using Mg alloys contributes to the reduction of energy cost and carbon emission, and thus generates more environmental and economic benefits. Another advantage of Mg and its alloys is good cast ability. It benefits from the low melting point, which requires less energy during processing and extends the life of moulds and tools. Magnesium alloys also have high fluidity, allowing them to fill intricate and thin-walled moulds efficiently. This is especially beneficial for manufacturing lightweight, complex parts with detailed geometries. They also exhibit good biocompatibility. Mg naturally degrades in the body, releasing non-toxic by-products that are safely absorbed or excreted. Its mechanical properties are similar to human bone, reducing stress shielding and promoting natural healing. Additionally, magnesium ions support bone regeneration and metabolic functions.

However, there are still some unsolved problems inhibiting further widespread use of components made of Mg alloys. The first one is the flammability. The ignition temperature of Mg alloys is relatively low, especially in powdered or molten conditions. This makes Mg alloys needed to be handled with extreme caution during production. Once ignited, common water-based and CO₂ extinguishers cannot be used as they would react with Mg. The low corrosion

resistance is another important issue. As an alkaline earth metal, Mg has a low electrode potential, making it highly anodic compared to other common structural metals. The corrosion product usually cannot provide highly effective protection as Al alloys. This leads to a high corrosion rate in several circumstances such as moist and marine environments.

In addition, there is a severe strength-ductility trade-off. Although achieving a good combination of strength and ductility is a universal challenge for nearly all metallic materials, it is especially a serious challenge to Mg alloys. Due to the inherent hexagonal close-packed (HCP) crystal structure, independent slip systems in Mg alloys are fewer than in commonly used structural metals such as some steels of body-centred cubic (BCC) structure and Al alloys of face-centred cubic (FCC) structure. The lower symmetry of HCP structure in Mg alloys makes the basal <a> slip much easier to activate at room temperature compared to other slip systems. In addition to slipping, twinning is another essential deformation mode in Mg alloys, though their contribution to the overall plastic deformation before failure can be less significant when a high ductility needs to be achieved. The limited plastic deformation modes in Mg alloys make it challenging to achieve high ductility and strength simultaneously. The second problem inhibiting the application of Mg is the environmental impact of Mg production. The environmental impact of material production has become one of the major concerns, because it has been widely accepted that the energy consumption and emissions, such as carbon dioxide (CO₂) must be reduced wherever possible to achieve sustainable development. There is no doubt that when replacing components made of traditional high-density alloys with Mg alloys in transportation applications, the mass reduction can reduce the energy consumed and carbon emitted. However, the energy input to produce Mg is the second highest among common metallic materials, being second only to Titanium (Ti) and higher than the commonly used ferrous metals and Al products. What is more, the machining of Mg alloy products inevitably produce large amounts of waste such as chips/swarf during the machining process. It was estimated that the mass of the produced waste can sometimes be equivalent to 60-70% of the final casting product [1].

The friction stir-based technology is believed to be a potential technology to address these issues. This technology originated from the friction stir welding (FSW) developed by The Welding Institute (TWI), and many emerging variants have been developed during the past decades for diverse purposes. It is proved to be applicable to the processing of various materials such as copper (Cu) alloys and stainless steels and also low-melting-point materials such as Al and Mg alloys. There are several advantages of producing Mg alloys by using friction stir-based techniques. Firstly, the grain refinement by DRX can be achieved by friction stir-based methods. Refined grains can potentially improve the strength of the material without compromise in ductility. Secondly, the texture can be modified by the material flow generated by friction stir-based technologies. Thirdly, the second phases can be redistributed by friction stir-based technologies, and post heat treatment can be further applied for modification. In addition, friction stir-based technologies can process larger samples compared with other conventional SPD methods. Currently, the maximum scale of the workpiece can be up to metres long. Last but not least, machines for friction stir welding have already been commercialised and even an ordinary milling machine can be adapted to carry out friction stir processing. These make technologies based on FSW promising for industrial scale production of Mg alloys with better mechanical properties. Nevertheless, there are also some limitations of friction stir based technology, such as relatively low production capacity and high labour cost, compared to traditional processing represented by melting-based methods [2].

Chapter 2 Literature review

2.1 General information and brief history of magnesium

Magnesium (Mg) is a common alkaline earth element. It is the sixth abundant element in the crust of earth, constituting nearly 2% of the crust mass [3]. Magnesium is known to exist in over 60 minerals, including carnallite (KMgCl₃•6H₂O), magnesite (MgCO₃), dolomite (CaCO₃• MgCO₃), brucite (Mg(OH)₂), olivine (Mg₂Fe₂SiO₄), bischofite (MgCl₂•6H₂O), etc [4]. And it is also the third plentiful element in seawater [5]. Despite the huge reserves, elemental magnesium was not successfully isolated until 1808. A British chemist Sir Humphrey Davy was the first researcher to produce elemental magnesium via electrolysis [6]. Although several approaches had been developed to isolate magnesium after its first discovery, the application of magnesium remained on the periphery of attention. The first explosive growth of magnesium production occurred during the First World War, stimulated by the rapidly increasing demand for military applications, such as tracer bullets, flares and aeroplane components [6]. After the Great War, some defence-related technologies of magnesium were converted for civil use. Magnesium alloy parts have been used in vehicles since this period. The outbreak of the Second World War triggered another explosive growth of magnesium production. Due to the prosperity of aeronautics, the consumption of magnesium alloy reached a peak during the war. After the war ended, a rapid shrinkage of magnesium production took place due to the decreasing military demand and restrictions applied to vanquished countries. However, the recovery of magnesium production soon happened with the rebuild and development. The magnesium industry then aimed to develop applications for Mg beyond the military sector, including food packaging, vehicles, civil aviation, and astronautics, benefiting from the low density of Mg [6]. Over the past few decades, Mg alloys have gained increasing attention, especially since the beginning of the 21st century, as environmental protection, energy issues, and resource problems have become significant concerns [7]. This is primarily due to the high specific strength of Mg alloys, which can potentially reduce the weight of structural materials.

2.2 Basic properties of magnesium

Pure magnesium (Mg) is considered the lightest structural metal, with a density of merely 1.738 g/cm³, which is approximately two-thirds of the density of aluminium (Al) at 2.702 g/cm³ and nearly four to five times lighter than steel, which has a density around 7.85 g/cm³ [8]. Such a low density makes Mg and its alloys have high specific strengths. As an alkaline earth element, Mg exhibits a reducibility and can easily react with oxidants. Mg can react with oxygen in the atmosphere and the oxidized layer usually cannot provide full protection against further reaction[8]. As an important macro element in the human body, Mg also shows good biocompatibility, indicating it introduces no measurable harm to the host.

Magnesium has a hexagonal closed packed (HCP) configuration, where a four-axis coordinate and the corresponding four-figure miller indices (a_1 - a_2 - a_3 -c) are used to describe the crystallographic parameters as depicted in Figure 2.1a. At room temperature, the lattice parameters of the Mg unit cell are determined to be: a=0.32092 nm and c=0.52105 nm. The c/a ratio, standing at 1.624 at room temperature, is very close to the calculated value for the ideal HCP structure, which is 1.633. This ratio governs the activity of the slip systems. And this makes { $10\overline{1}0$ } planes the most close-packed planes in Mg system at room temperature. Higher planar packing density indicates larger interplanar spacing, which significantly affects the resistance of dislocation movement within the plane. Thus, as shown in Figure 2.2, the critical resolved shear stress (CRSS) of {0001} < $11\overline{2}0$ > (i.e. basal <a>) slip system is much lower than that of other slip systems. Other common slip systems shown in Figure 1(b) and (c), including { $10\overline{1}0$ } < $11\overline{2}0$ > slip (i.e. first prismatic <a>), { $10\overline{1}1$ } < $\overline{1}\overline{1}23$ > slip (i.e. first pyramidal <c + a>), and { $11\overline{2}2$ } < $11\overline{2}3$ > slip (I.e. second pyramidal <c+a>), usually are activated only at high temperatures, or under high stresses at room temperature [8, 9] (shown in Figure 2). In addition to slipping, deformation twinning also plays an essential role in plastic

deformation. The most active twinning system $\{10\overline{1}2\} < \overline{1}011 > (i.e. tension/extension twinning),$ whose CRSS is almost equivalent to that of basal <a> slip, is activated much easier than the other twinning systems and can accommodate extension deformation along the c-axis[9]. By contrast, $\{10\overline{1}1\}$ $<\overline{1}012>$ and $\{10\overline{1}3\}$ $<\overline{3}032>$ twinning system (I.e. compression/contraction twinning) can accommodate contraction deformation along the c-axis. Besides, double twinning $\{10\overline{1}1\} - \{10\overline{1}2\}$ and $\{10\overline{1}3\} - \{10\overline{1}2\}$ can also be activated in plastic deformation. According to von Mises theory of deformation, to achieve uniform plastic deformation without failure at grain boundary regions, at least 5 independent systems are required. However, only basal <a> slip and extension twinning can be activated in the beginning of plastic deformation due to their lower CRSS values. The basal <a>a> slip cannot accommodate deformation along the c-axis, whilst the extension twinning system, though can accommodate extension along the c-axis, the overall contribution is relatively limited. Other systems only begin to participate at higher stresses or temperatures [10-13]. Intergranular mechanisms like grain rotation and grain boundary sliding have also been observed to occur, but their contribution matters only when the grain size is small enough [9, 14] (usually around or under 1 µm). As a result, for most of the commercial Mg alloys, the formability is relatively limited under cold work conditions.

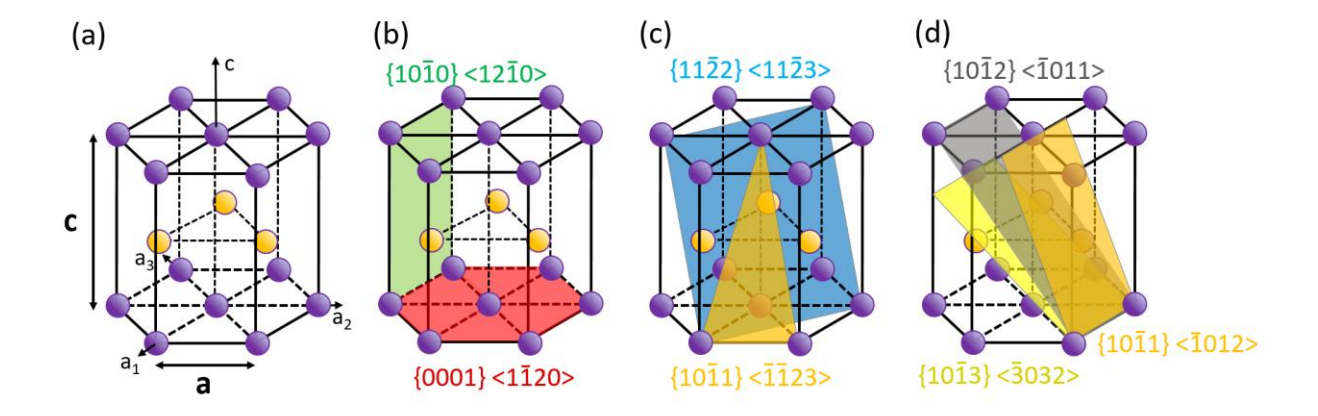


Figure 2.1 (a) A unit cell of Mg, (b) basal and prismatic slip systems, (c) first and second pyramidal slip systems, (d) extension and contraction twinning systems.

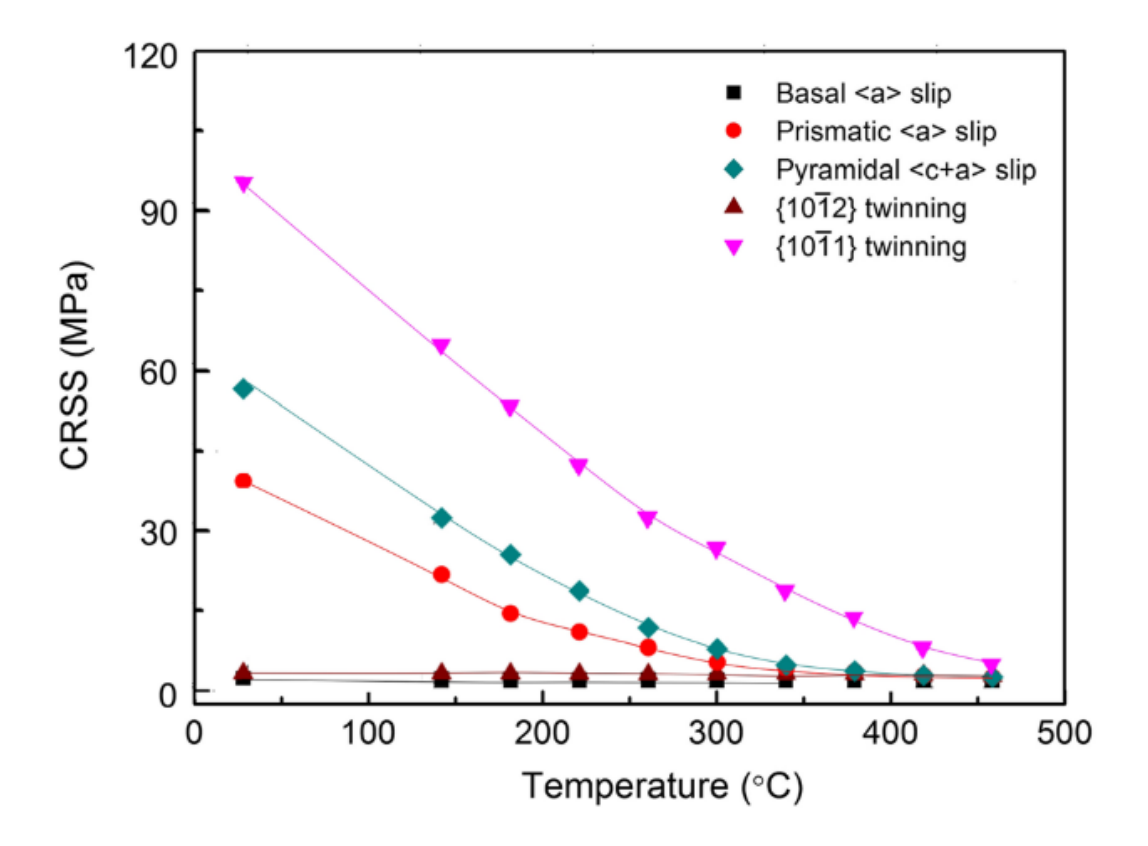


Figure 2.2 Critical resolved shear stress values for different slip and twinning modes and their variation with temperature in pure Mg [9]

2.3 Strengthening mechanism in Mg and its alloys

2.3.1 Grain boundary strengthening (Hall-Petch strengthening)

Grain boundary strengthening, also known as Hall–Petch strengthening, is one of the most fundamental and effective mechanisms to enhance the mechanical properties of metallic materials, including Mg and its alloys. Grain boundaries can act as obstacles to dislocation gliding at room temperature, and thus, the increase in the density of grain boundaries results in an increase in material strength. In other words, grain refinement can increase the strength of metallic materials. The relationship between the grain size and yield strength (YS) is empirically described by the Hall-Petch equation [10]:

$$\sigma_{v} = \sigma_{0} + kd^{-\frac{1}{2}}$$
 (2.1)

where σ_y is the yield stress, σ_0 is a material constant for the starting stress for dislocation movement, k is the strengthening coefficient, and d is the average grain size. For Mg alloys, refining the grain size is particularly beneficial because the HCP structure limits ductility at room temperature. Fine-grained Mg alloys often exhibit not only enhanced strength but also improved ductility. In addition, the strengthening coefficient k varies, depending on the orientation due to the low asymmetry of HCP crystal structure [10, 15].

2.3.2 Work hardening

Work hardening, also known as strain hardening or cold working, is the process by which a metal becomes stronger and harder as it undergoes plastic deformation. The achievement of work hardening is mainly via the dislocation interaction during the plastic deformation. With the ongoing of plastic deformation, new dislocations are generated and interact in various ways, forming kinks, jogs or dislocation forests [16-19]. These structures can increase the energy for further dislocation movement and increase the strength of the material. The work hardening process is usually divided into three stages based on the relationship between stress and strain [16]. In stage I, which is also referred to as 'easy glide', dislocations move easily on primary slip systems with minimal interaction, resulting in a relatively small increase in stress. In stage II, the dislocation glide occurs in several non-parallel slip planes. Dislocation interactions become significant, and the work hardening rate is increased due to the increased energy barrier caused by kinks and jogs. In stage III, with further increase in stress, cross-slip or climb of the dislocation begins to be activated, and the work hardening rate starts to decrease. However, work hardening leads to a drop in ductility [20].

2.3.3 Solid solution strengthening

When an alloying element (solute) is added to a base metal (solvent), the solute atoms can occupy substitutional sites or interstitial sites, forming a solid solution. In Mg and its alloys,

only substitutional sites can be occupied, as the interstitial sites are too small to fit other alloying elements. Solute atoms can cause lattice distortion attributed to several factors, including the atom size misfit, modulus misfit, and chemical misfit [21, 22]. This means different kinds of solute atoms can generate different levels of lattice distortion. The lattice distortion increases the energy barrier for the dislocation movement and thus increases the strength of the material.

2.3.4 Precipitation strengthening

Precipitation strengthening relies on the controlled formation of a second-phase precipitate from a supersaturated solid solution, which obstructs dislocation motion and thereby increases the strength of the material. The precipitates can be categorised into deformable particles and non-deformable particles [9, 23]. For deformable particles, which are coherent or semi-coherent, the bypass of the dislocation would create new interfaces between the particle and the matrix, and thus the energy for dislocation movement is higher. The elastic stress around the particles also increases the resistance of dislocation cutting through. For rigid non-deformable particles, which are usually non-coherent, dislocation lines get curved when passing by and finally leave loops around them. The formation of these loops requires extra energy, and the dislocation loops would further act as obstacles. This mechanism is also referred to as Orowan looping [23].

2.4 Alloying elements and studies of Mg-Al-Zn and Mg-Y-RE alloys

The strength of pure magnesium is unsatisfactory and can hardly be used for engineering purposes. To fulfil the requirement of becoming a kind of structural material, alloying elements are essential, just like most of the metallic materials. The addition of certain alloying elements can generate solid solution hardening [8], precipitation hardeningt [24, 25], and grain boundary hardening (grain refinement) [26-28]. Furthermore, some alloying

elements can also help reduce the density, improve the castability, corrosion resistance, damping properties, creep resistance, etc [4]. Combined use of more than one alloying elements can generate synergetic effects, achieving comprehensive improvements in several aspects. Based on these, many matured alloy systems have been developed for different purposes.

2.4.1 Major alloying elements

2.4.1.1 Aluminium

Aluminium (Al) is one of the most common and fundamental alloying elements in Mg alloys. Figure 2.3 shows the Mg-Al binary phase diagram. Al can form a eutectic system with Mg. At the eutectic temperature of 436 °C, the solubility of Al reaches the maximum value of about 12.7 wt.%. Whilst the solubility limit of Al drops to around 2 wt% at room temperature[4]. The Al exceeding the solubility limit can form Mg₁₇Al₁₂ with Mg from the matrix. The hard intermetallic phase Mg₁₇Al₁₂ can improve tensile strength, but those large particles form at grain boundaries and lead to lower ductility, especially when the concentration of Al is over 8 wt.%[8]. The Mg₁₇Al₁₂ at grain boundaries can redissolve into the matrix by solid solution treatment and precipitate again during the subsequent ageing treatment following the procedure below

Super saturated solid solution (SSSS) ----
$$\beta$$
 (Mg₁₇Al₁₂) (2.2)

The precipitated β phases are usually in the shape of plates or laths on (0001) planes of matrix Mg. Although the melting point of Mg₁₇Al₁₂ is about 460 °C, the softening begins when the temperature goes beyond 120 °C and thus the strengthening effects become weak [4].

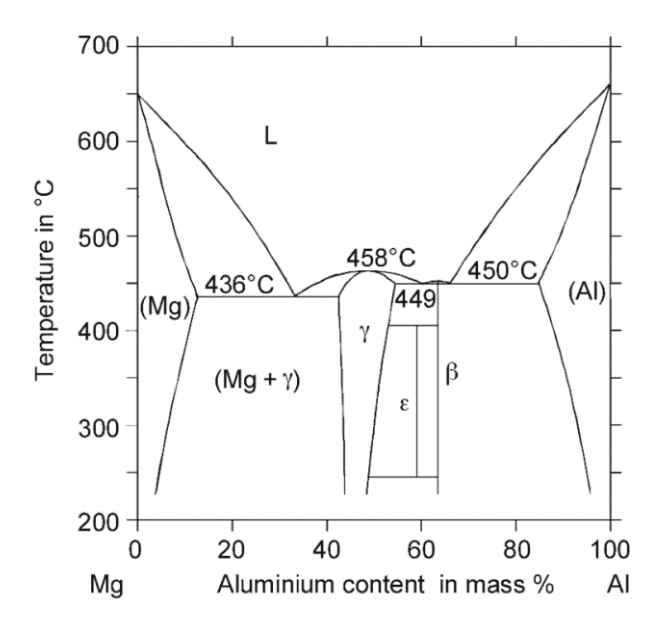


Figure 2.3 Mg-Al binary phase diagram[6]

2.4.1.2 Zinc

Zinc (Zn) is one of the major alloying elements in Mg alloys. Figure 2.4 shows the Mg-Zn binary phase diagram. Zn can form a eutectic system with Mg. At the eutectic temperature of about 340 °C, the solubility of Zn reaches the maximum value of about 6.2 wt.%, which is much lower than that of Al [8]. Nevertheless, with the same atomic solid solution dose, the solid solution hardening response of Zn is higher than that of Al. In other words, Zn is more effective than Al regarding solid solution hardening. Age hardening can also be achieved in Mg-Zn binary system. The precipitation procedure follows

SSSS ---- G.P. zones ----
$$\beta'_1$$
 (Mg₄Zn₇) ---- β'_2 (MgZn₂) ---- β (MgZn) (2.3)

The peak ageing usually can be achieved when coherent β'_2 plates forming on (0001) planes of Mg matrix [8]. In addition to solid solution hardening and precipitation hardening, Zn also improve the castability of Mg alloy, by decreasing the liquid metal's surface tension and viscosity, allowing the melt to fill complex mould geometries more easily [8]. However, it increases the tendency of micro-porosity occurrence [8].

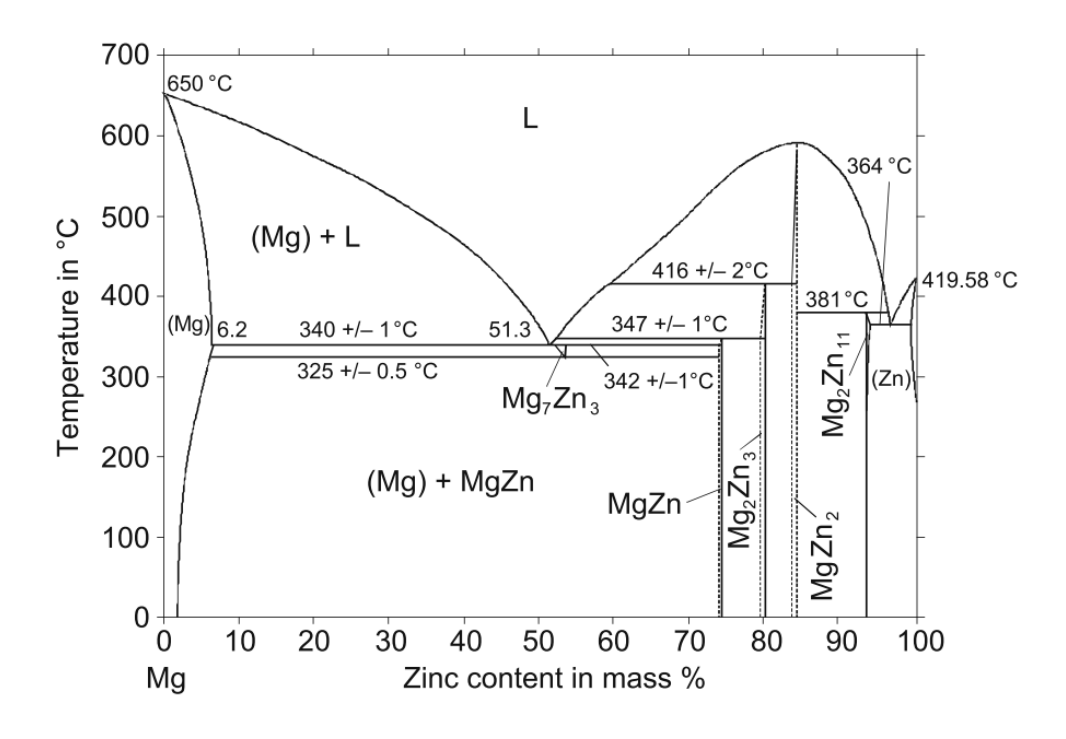


Figure 2.4 Mg-Zn binary phase diagram[6]

2.4.1.3 Manganese

Manganese is commonly used in Mg alloys. Figure 2.5 shows part of the Mg-Mn binary phase diagram. Unlike AI and Zn mentioned above, Mn cannot form a eutectic system with Mg. Instead, Mg-Mn can form a peritectic system. The solubility of Mn in Mg reaches the maximum value of 2.2 wt.% at the peritectic temperature of 653 °C [4]. The addition of Mg can improve the yield strength and the tensile strength when the content exceeds 1.5 wt% [4]. It can also improve the corrosion resistance of Mg by reducing the solubility of iron (Fe) which is a detrimental impurity [4].

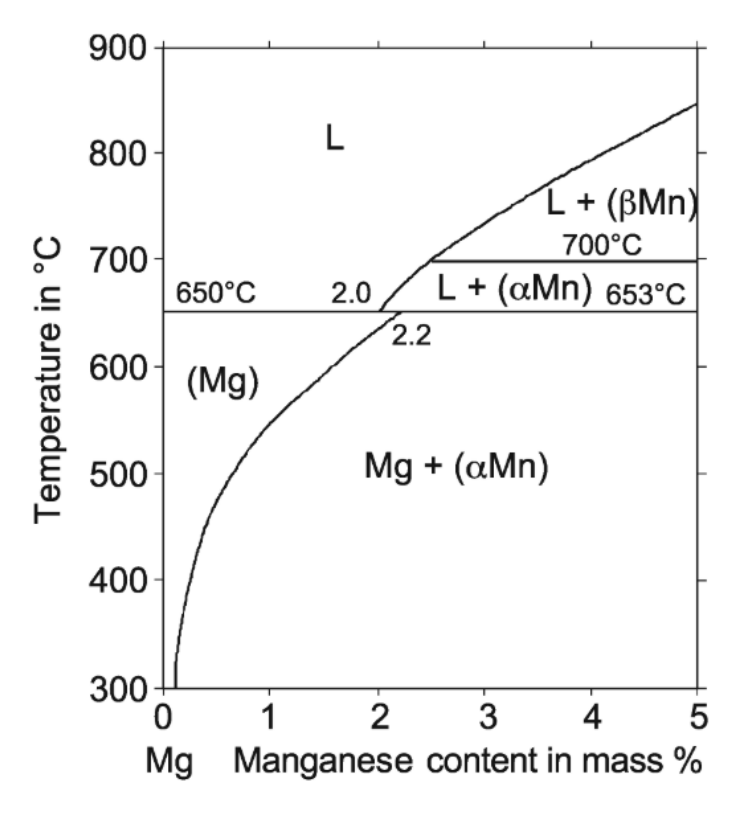


Figure 2.5 Part of the Mg-Mn binary phase diagram[6]

2.4.1.4 Yttrium

Yttrium (Y) is an element often used with rare earth elements. Figure 2.6 shows part of the binary phase diagram of Mg-Y. Y and Mg can form a eutectic system. The solubility limit is up to about 12.5 wt.% [8]. In addition, Y can generate significant lattice distortion. So, Y is considered an effective solid solution hardening alloying element. Y has strong affinity to oxygen and can form Y_2O_3 at elevated temperatures [4].

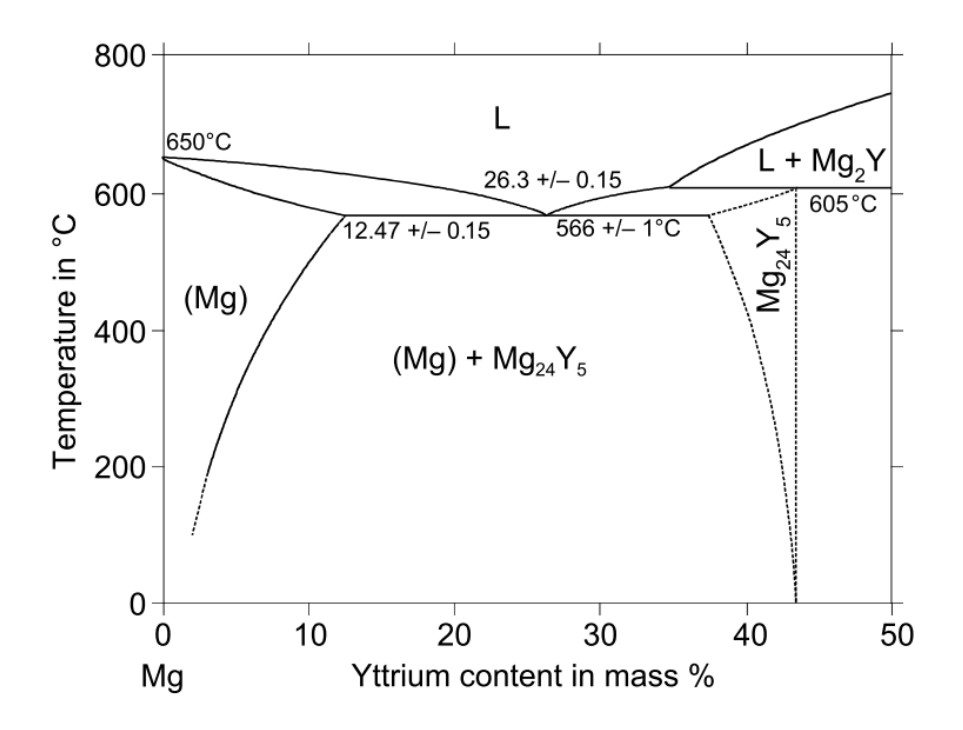


Figure 2.6 Part of the Mg-Y binary phase diagram [6]

2.4.1.5 Rare earths

Rare earth (RE) elements are a series of elements which has similar chemical properties. Including gadolinium (Gd), neodymium (Nd), cerium (Ce), thorium (Th), lanthanum (La), praseodymium (Pr), etc. Although the effects of different RE elements are not the same, there are some features in common. RE elements can form second phases which remain hard at high temperatures, improving high temperature strength and creep resistance[4]. They can affect the texture evolution during processing, producing "RE textures" [3, 29-36], which can potentially affect the formability. Despite the advantages of RE elements, the much higher price of RE elements compared with other alloying elements such as Al and Zn inhibits the widespread application.

2.4.1.6 Zirconium

Zirconium (Zr) is considered an effective grain refiner for Mg alloys, yet the mechanism behind it remains debated. Some researchers propose that the grain refinement effect is due to the resemblance of Mg-Zr lattice parameters, the peritectic system, and the high saturation

of Zr at the Mg- Zr peritectic temperature [4] (shown in Figure 2.7). Whilst others believe that it is attributed to the high affinity to O. Oxides form during casting and act as effective nuclei during solidification [8]. Zr are usually not used with Al, Mn and Si because these elements impede the grain refinement effects.

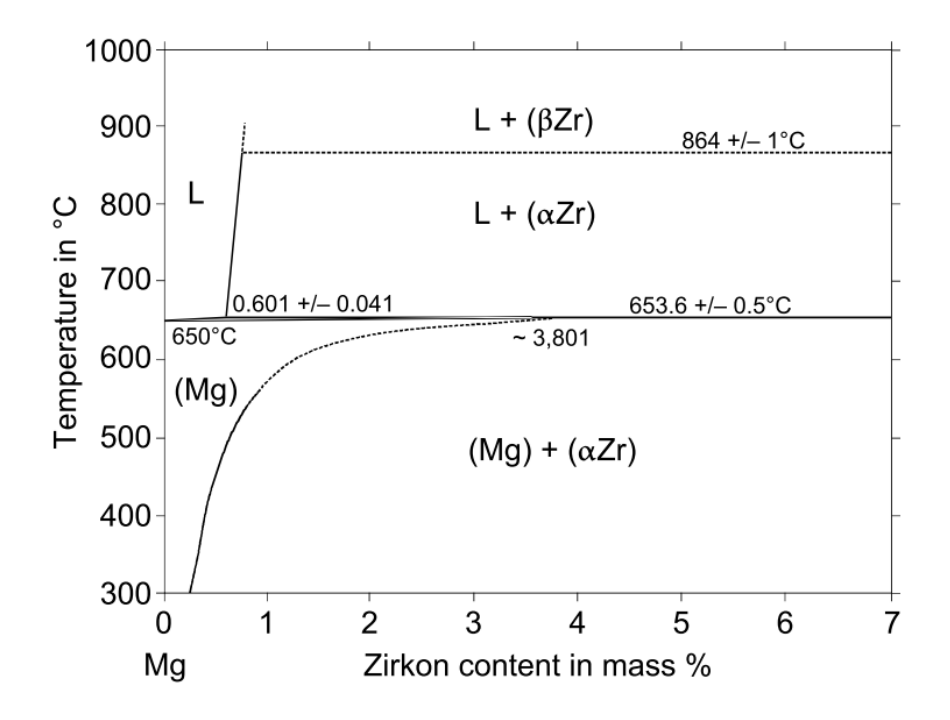


Figure 2.7 Part of the Mg-Zr binary phase diagram[6]

2.4.2 Mg-Al-Zn (AZ series) and Mg-Y-RE (WE series)

2.4.2.1 AZ series and AZ31B

AZ series magnesium alloys are a group of magnesium-based materials that primarily contain AI (A) and Zn (Z) as their main alloying elements. The designation "AZ" is followed by two numbers, which correspond to the weight percentages of aluminium and zinc, respectively. For example, AZ31 has about 3% of AI and 1% of Zn in weight percent. AZ31B is one of the most widely used wrought magnesium alloys in the AZ series. In addition to AI and Zn, small amounts of Mn is also added to improve corrosion resistance [37, 38]. Unlike many other magnesium alloys that are primarily cast, AZ31B is available in wrought forms such as sheets,

plates, bars, rods, and extrusions, and is especially known for its good formability at elevated temperatures, making it suitable for processes like rolling, extrusion, and stamping.

2.4.3 Mg-Y-RE (WE series) and Elektron 43 (WE43C)

The WE series magnesium alloys are a group of magnesium-based materials that primarily contain Y (W) and mixed RE elements (E). The designation "WE" is followed by two numbers, which roughly correspond to the weight percentages of Y and RE elements, respectively. For example, WE43 has about 4% of Y and 3% of mixed rare earths in weight percent. Elektron 43 (WE43C) is optimised as a specific wrought group. The addition of Y and RE not only increase the room temperature strengths due to the solid solution strengthening and precipitation strengthening, but also increase high temperature performances like high temperature strength, creep resistance, and oxidation resistance [39-49]. This makes WE43C can be used at temperatures up to 250–300°C.

2.5 Brief situation of Mg and its alloys production

There are two major methods for the primary production of Mg. One is the thermal process, relying on the reduction process of minerals such as dolomite (CaCO₃• MgCO₃), magnesite (MgCO₃) and carnallite (KMgCl₃•6H₂O) at elevated temperatures [50]. The above mines are subjected to crushing, calcination, briquetting, reduction, melting, and refining stages to obtain Mg ingots. The other way is the electrolytic process [50]. The mined magnesite (MgCO₃) is subjected to leaching with HCl, and then the purification, dehydration, and electrolysis are applied to obtain the Mg ingots. The source for electrolysis production of Mg can also come from brine and sea water. The production of prime Mg has been increasing rapidly in the past decade. About 0.5 million tonnes of prime Mg were produced in 2010, and the number doubled by the end of 2022, reaching 1.1 million tonnes [50].

The majority of Mg alloy component production are via casting [51-53], including sand casting, die casting, squeeze casting, thixocasting, rheocasting, etc. Among these casting

methods, die casting is the dominant production method, with a significantly higher fraction compared to other casting methods. It even contributes to over 1/3 of the total industrial application of Mg and its alloys. Several alloy systems with excellent castability and low cost have been successfully developed for the cast production, including Mg-Al-Zn (AZ series), Mg-Al-Mn (AM series), Mg-Al-RE (AE series), Mg-Zn-Ca (ZX series), etc. Some of the alloys such as Mg-Y-RE (WE series) and Mg-Gd-Y (GW series) can be heat treated (e.g. T6) to produce fine precipitates for higher strengths [9, 23].

Wrought Mg and its alloys also play a fundamental role in the industrial production [14, 34, 35, 51, 54-60]. Although the formability of Mg alloys is generally unsatisfactory at room temperature, common forming approaches like rolling, extrusion, forging, etc., are still applicable at elevated temperatures. Common extrusion alloy systems include Mg-Al-Zn (AZ series), Mg-Zn-Zr (ZK series), Mg-Al-Mn (AM series). Recent years, new alloy systems with improved mechanical properties or extrudability have been developed, such as Mg-Zn-RE (ZE series), Mg-Sn-Ca (TX series), Mg-Al-Ca-Mn (AXM series) [3, 21, 61-64]. For rolled sheets and plates, common alloys such as Mg-Al-Zn (AZ series), Mg-Zn-Zr (ZK series), Mg-Mn-RE (ME series) and others have been widely used for production [57, 65-68].

Other technologies like powder metallurgy are also in use [46, 69-73]. These Mg alloys are mainly used in products where mass reduction is important, such as sports equipment, electronic equipment, automobiles, and aircraft [4, 74]. They also play an essential role in medical treatment as Mg alloys can be used for biodegradable orthopaedic implants and tissue engineering [58, 75-77].

2.6 Friction stir-based technology

2.6.1 Friction stir welding (FSW) and the grain refinement mechanism

Friction stir-based technology is a series of technologies originated from friction stir welding (FSW), a solid state welding technique developed by The Welding Institute (TWI) in

the UK in 1991 [78]. The setup of a typical FSW process is shown in Figure 2.8. The key part of a FSW machine is the tool. It is generally composed of two parts, a shoulder and a probe. When the welding process begins, the tool begins to rotate, reaching the set rotational speed and then inserting at the gap between the two workpieces. The probe is usually fully plunged into the material, and the lower surface of the shoulder would be in contact or slightly cut into the workpiece surface, applying a certain downward force (i.e. force control) or keeping a designated plunge depth (i.e. depth control). When a certain load of depth is reached, the tool travels along the workpiece gap. The deformation heat and friction heat would soften the material and make it flow with the tool. The material get mixed and achieve metallurgical bonding when the tool passes by [79-84].

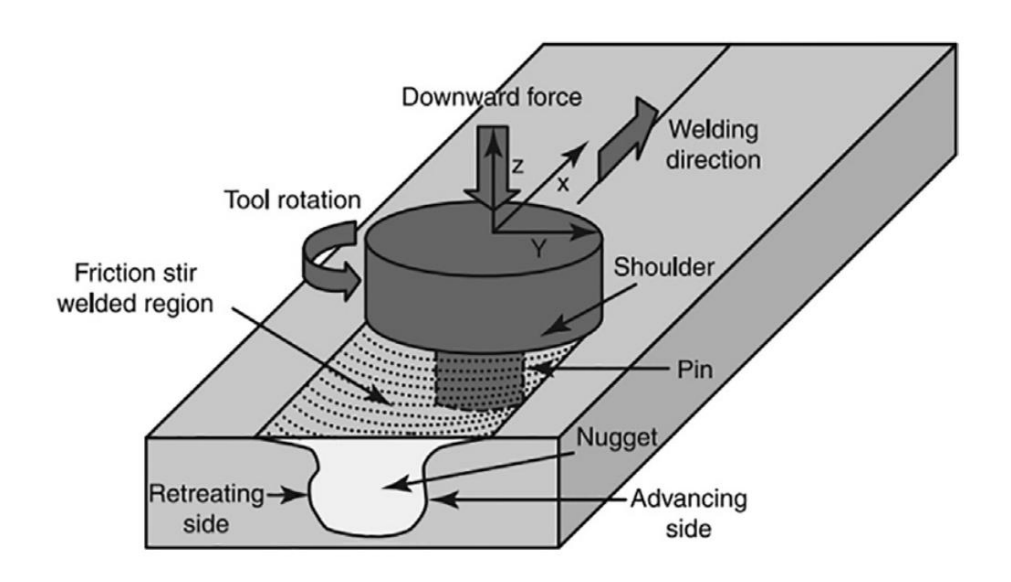


Figure 2.8 Schematic illustration of the FSW process [82]

During the welding process, the deformation and heat generated by the rotational tool can induce dynamic recovery (DRV) or dynamic recrystallisation (DRX) [85]. These two modes usually compete with each other. In materials with higher stacking fault energy (SFE), DRV is more favourable as dislocations have higher mobility by climbing and cross slipping, which suppresses the occurrence of DRX. DRX plays a key role in grain refinement in FSW. There are two major modes of DRX, continuous dynamic recrystallisation (CDRX) and discontinuous dynamic recrystallisation (DDRX) [85]. The word 'continuous' implies the key feature of CDRX.

CDRX does not have distinctive nucleation and grain growth stage. Instead, it relies on the continuous movement of dislocations. The process of CDRX is sketched in Figure 2.9. During CDRX, dislocations first rearrange to form subgrains. With the proceeding of plastic deformation, dislocations are introduced into the material, and due to the high temperature, these dislocations keep moving to subgrain boundary sites, leading to a continuous increase of misorientation of subgrains. With the misorientation increase, the original deformed grains transform into several smaller recrystallised grains. CDRX can happen in almost all the metallic materials. Unlike CDRX, DDRX has two distinctive stages of nucleation and grain growth. The process of DDRX is sketched in Figure 2.10. Firstly, subgrains developed in the vicinity of serrated grain boundaries, forming bulged DRX nuclei. Regions next to the bulged nuclei become sites for plastic deformation concentration. Then there is a dislocation density difference at two sides of the serrated boundaries. Such difference provides the driving force for nuclei to grow. The grain boundary would migrate from the side with lower dislocation toward the side with higher dislocation. Grain growth will be suppressed when the recrystallized grains begin to impinge with each other or when the dislocation density in the recrystallized grains gets equivalent to the original deformed grains during the following deformation. DDRX usually happens at high temperatures over 0.5 Tm (melting temperature) and low strains which assist the nuclei formation and dislocation density difference [85]. Besides, there is another type of DRX in addition to DDRX and CDRX, which is closely related to the twinning during the deformation and named as twin-assisted dynamic recrystallisation (TDRX). TDRX is more often observed in the material with HCP structures (e.g. Mg) than those with FCC or BCC structure. In Mg alloys, as illustrated previously, lack of slip systems makes twinning an essential deformation mode to accommodate plastic deformation. And the activity of twinning in Mg alloys is dependent on several factors, such as grain size, temperature, total strain and strain rate. Generally speaking, larger grain sizes, lower temperatures, low strains and high strain rates are favourable for TDRX to occur. In addition to the DRX mechanisms, particle stimulated nucleation (PSN) can also contributed to the

recrystallisation and grain refinement during the FSW. Particles with sizes beyond a threshold can act as sites for heterogeneous nucleation sites of recrystallised nuclei to form, increasing the number of recrystallised nuclei and refine the grain structure.

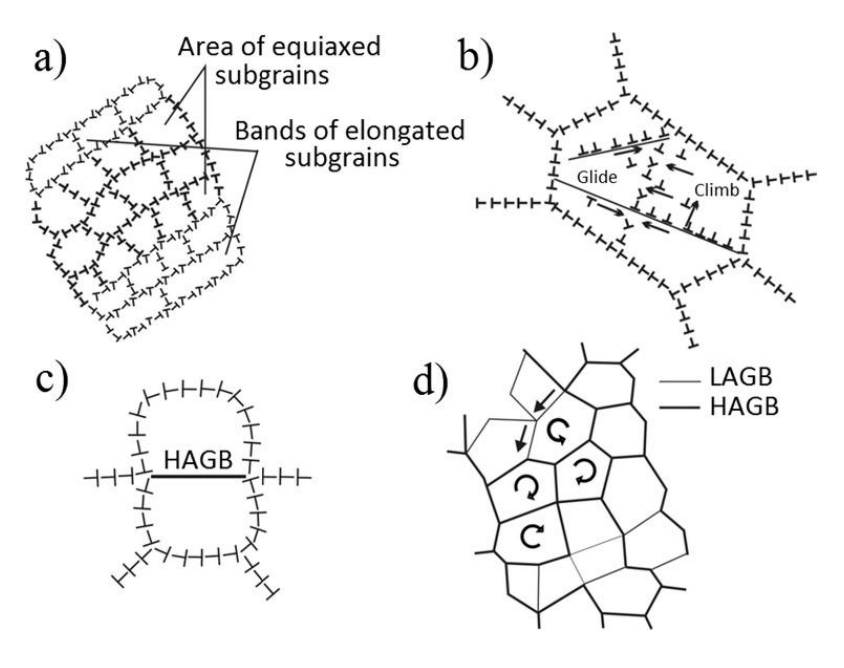


Figure 2.9 Progress of CDRX [85]

Based on the combined effect of deformation and heat input, the final microstructure, in the FSWed material can be divided into 4 different zones, including nugget zone/stir zone (NZ/SZ), thermal mechanical affected zone (TMAZ), heat affected zone (HAZ), and base material (BM). SZ is the region right at or very close to the probe. The material in this region is strongly affected by the rotational probe. Extremely large strain and high temperature are the characteristics of SZ. The peak temperature of SZ can be up to 0.75-0.9 T_m [85]. SZ featuring fine equiaxed grains, as friction heat and plastic deformation allow DRX to thoroughly occur in this region. TMAZ is slightly away from the probe, next to the SZ. The strain is smaller and the temperature is lower in TMAZ, and thus the heat input is not enough for grains to fully recrystallise. Thus, in the TMAZ, a bimodal microstructure with 'necklace structure' produced by DDRX or large grains containing several subgrains produced by not fully completed CDRX, or a combination of both, can be observed in the materials with HCP structures such as Mg and Ti [85]. HAZ is the outer layer of TMAZ. It is not affected by the mechanical stirring but

the friction heat is conducted to this region. Grain growth is observed in this region. BM is the rest region that is far away from the probe, so that both the mechanical stirring and heat cannot affect the microstructure in this region. The geometry of these zones is usually not symmetric against the central line. This is because the tool is rotational, and thus the relative velocity between the tool and the material is different on two sides. On one side, the rotational direction and the traverse direction of the probe are the same. This side is usually referred to as advancing side (AS). But on the other side, the directions are different. This side is usually called the retreating side (RS). This generates the strain and temperature difference, and material flow difference, generating the asymmetry in the geometry of the track.

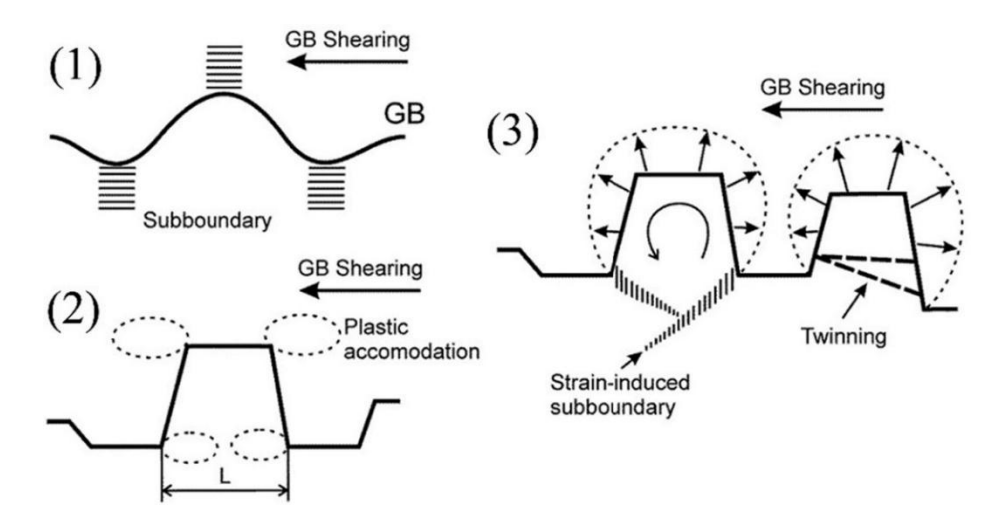


Figure 2.10 Progress of DDRX [85]

2.6.2 Friction stir processing (FSP)

FSP is one of the major techniques that originated from FSW. The setup of FSP is shown in Figure 2.11. It is very similar to that of FSW. The only difference is that FSP does not aim at joining two parts together. Instead, it aims at using the severe plastic deformation generated by the tool to modify the microstructure of the workpiece, without substantial change of the shape and geometry. Although FSP is usually regarded as a SPD technique, it does not require extra heat input like ECAP and HPT as heat can be generated by friction [86, 87]. The

strain and temperature adjacent to or away from the rotational probe are different, and thus the microstructure is not homogeneous [88].

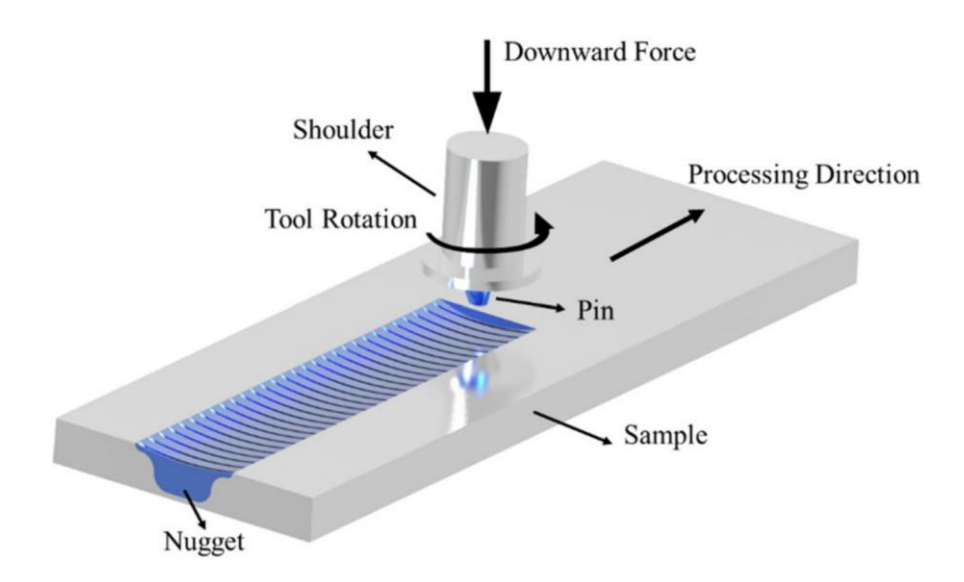


Figure 2.11 Schematic illustration of the FSP process [89]

It is apparent that a single track of FSP can only produce a narrow line of processed material but not covering the whole workpiece. So, the multi-track FSP [90-94] is indispensable when a fully processed workpiece is needed. Several parameters in addition to the basic ones can be adjusted to tailor the final microstructure, such as the overlapping rate, the overlap of AS or RS, etc. Emerging methods and apparatus have also been applied in recent years. To achieve a higher cooling rate for refined grains, extra cooling methods such as water cooling, liquid nitrogen cooling embedded in the tool, copper back plates and submerged FSP (i.e. the workpiece immersed in the cooling media during processing). To obtain better surface quality and heat input, a stationary shoulder has been developed.

Darras and Kishta [95] did FSP on AZ31B with air cooling, the average grain size was refined from over 100 μ m to less than 20 μ m, and thus the elongation was increased from approximately 2% to 16%. Chai et al. used submerged FSP to process a hot-rolled AZ31B sheet. The grains were successfully refined from 100 μ m to 2.8 μ m. And the elongation was increased by nearly 80%, reaching 45%. Nia et al. [90] used a two-pass FSP with water cooling back plate. The grains in the FSPed AZ31B alloy were refined from 18 μ m to a gradient

structure ranging from 3.4-5.3 µm. The UTS was increased from 251.8 MPa to 333.9 MPa. Liu et al. [96] used copper back plate with channels for water cooling as an extra cooling method for FSP. The grains of the semi-continuous casted AZ31B were refined from 75 µm to 5 µm. The strength and ductility were thus improved simultaneously. The ultimate tensile strength (UTS) was increased from 160 MPa to 255 MPa, and the elongation (EI) was improved from 9% to 20%. With appropriate processing parameters, the strength can be improved with hardly any compromise in the ductility, and vice versa. The strength and ductility can potentially be improved simultaneously.

2.6.3 Friction stir channelling (FSC) and stationary shoulder friction stir channelling (SS-FSC, CoreFlow®)

Friction stir channelling (FSC) is a subsurface processing technology adapted from FSW. This technology intends to enlarge a type of defect called 'wormhole', which are cavities formed in the SZ. By enlarging the cavity on purpose, a subsurface channel with certain crosssection size and geometry, and designated path can be manufactured in plates. These plates with subsurface channels can be used for heat exchangers, heat sink for semi-conductors, water cooled engine blocks, wall chambers with cooling channels, etc. [97-100]. There are several variants developed during the past decades. The very first type of FSC was achieved with a shoulder-workpiece clearance, invented by Mishra [100]. In other words, there is a gap between the shoulder and the workpiece. The excess material from the wormhole region is re-deposited in the gap between the tool and the workpiece. The next generation of FSC is operated without the shoulder-workpiece clearance developed by Vidal and Vilaca [100]. The threaded probe and the scrolled shoulder design can produce larger subsurface channels with better cross-section control and surface quality. After that, a stationary shoulder friction stir channelling (SS-FSC) was developed, which was patented using the name CoreFlow[®]. Different from previous variants, a stationary shoulder instead of a rotary shoulder is used in SS-FSC, as shown in Figure 2.12. The extracted subsurface material partially redeposited on the surface and partially transported upward along the threads during the probe rotation. These extracted material are then extruded out via the embedded hole in the stationary shoulder. It was found that the extracted material can consolidate and form a wire. Research has been carried out on Al alloys, Cu alloys and Ti alloys. Current studies mainly focus on the channel formation. However, the potential application of SS-FSC in wire extrusion has not been studied yet.

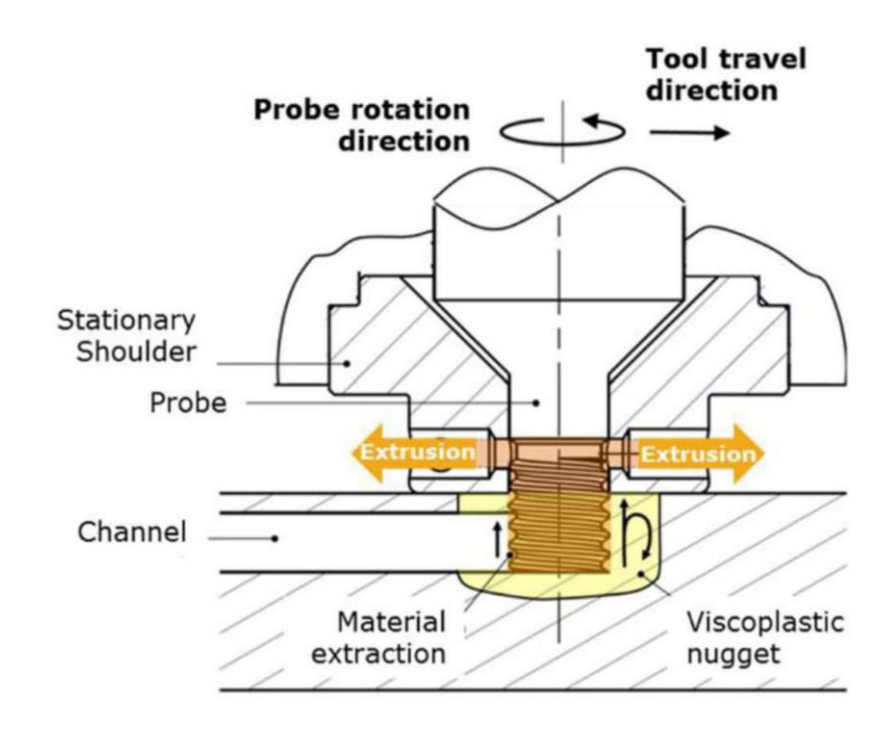


Figure 2.12 Schematic illustration of the SS-FSC/CoreFlow® process [100]

2.6.4 Additive friction stir deposition (AFSD)

Additive friction stir deposition (AFSD) is an emerging additive manufacturing (AM) technology developed from the FSW. Different from common traditional AM technologies of metals such as laser powder bed fusion (LPBF) wire arc additive manufacturing (WAAM), and direct energy deposition (DED), the deposition of material by AFSD does not involve the melting of the material. This can significantly reduce or avoid the problems of melting and solidification, including porosity induced by solidification, residual stresses or even hot cracks induced by large thermal gradients, and coarse or columnar grains in the final component.

Compared to traditional melting-based AM techniques, AFSD also exhibit advantages like high deposition rates and low energy consumption.

The typical set-up of AFSD is shown in Figure 2.13. During the deposition, the tool keeps a distance away from the substrate surface and rotates. The feedstock is fed by the actuator and contact with the substrate surface, the friction between the feedstock and the substrate soften the material. Since there is a down force of the feedstock by the actuator, the soften material is forced to fill the gap between the tool and the substrate. Meanwhile, the tool or the substrate travels along the designated path to achieved continuous deposition of the material. Once the deposition of one layer of the material is completed. The gap between the tool and the substrate material is adjusted again to allow the deposition of the next layer. By repeating this process, the designated component can be produced.

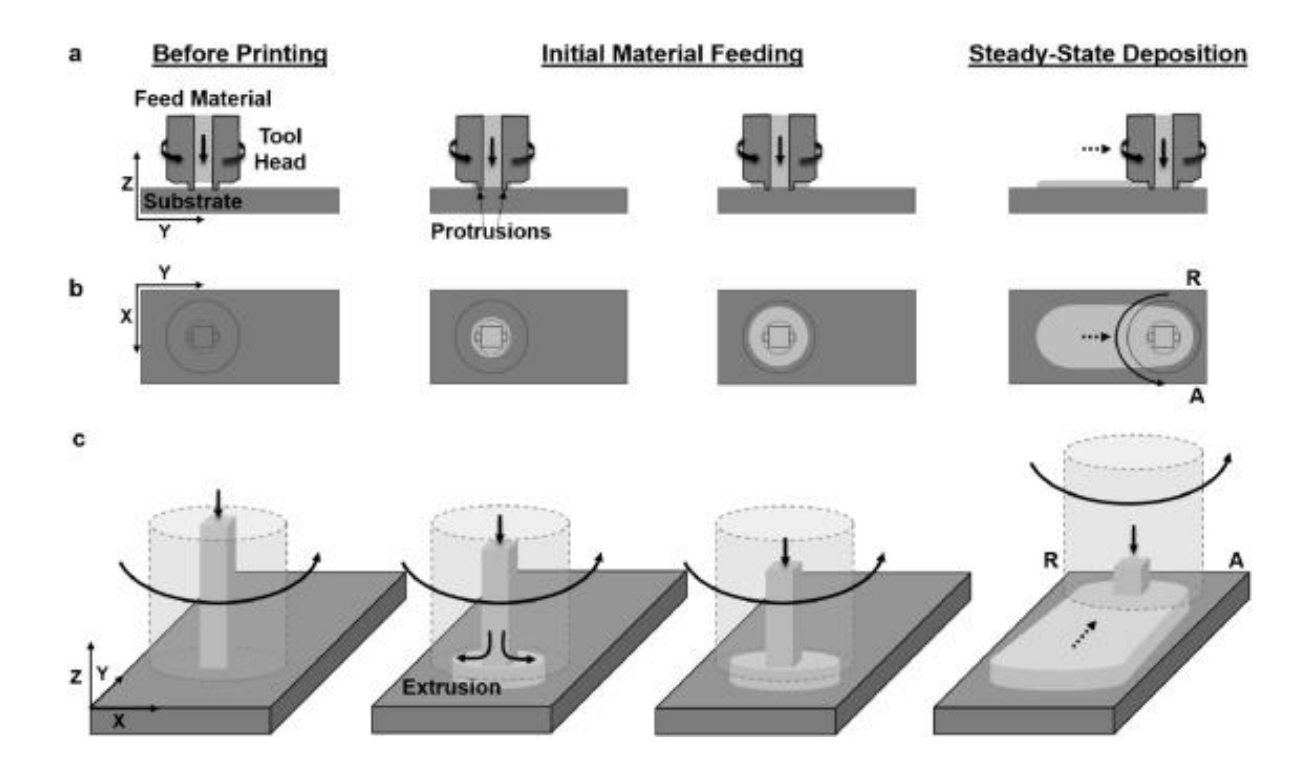


Figure 2.13 Schematic illustration of the AFSD process [101]

AFSD has been used to print various types of materials, including Al alloys, Ti alloys, Ni alloys, steels, Mg alloys, etc. Joshi et al. [65] deposited AZ31B magnesium alloy using the AFSD method. The average grain size was successfully refined from 13.5 μ m to 5-6 μ m. And

the Vickers hardness values were higher than the base material, reached 56-58 HV. Luo et al. [102] printed an 18-layer structure of Mg-8Gd-3Y-0.5Zr using a tool with protrusions. A gradient structure was obtained from one side to the other. Regions with coarse grains in the advancing side (AS) exhibited a yield strength of 269.9 MPa and regions with finer grains in the retreating side (RS) exhibited a higher strength of 295.4 MPa.

2.7 Current challenges of Mg alloys

Despite the rapid development of Mg alloys over the past decades, the overall application of Mg alloys is still very limited, compared with aluminium alloys and ferrous alloys. It was reported that in the year of 2021, the total weight of the global metallic material production reached 2.8 billion tonnes [103]. Among these produced metals, the total weight of iron reached around 2.6 billion tonnes, accounting for the majority of the metal production. The weight of aluminium production ranked the first place in non-ferrous metals, reaching about 68 million tonnes. However, the weight of produced magnesium was only about 1 million tonnes, which is far less than that of ferrous alloys and aluminium. The low production of magnesium indicates that there are still some factors inhibiting the widespread use of Mg alloys. There are still some problems inhibiting the widespread use of Mg and its alloys. The first one is the flammability. The ignition temperature of Mg alloys is relatively low, especially in powdered or molten conditions. This makes Mg alloys needed to be handled with extreme caution during production. Once ignited, common water-based and CO₂ extinguishers cannot be used as they would react with Mg. The low corrosion resistance is another important issue. As an alkaline earth metal, Mg has a low electrode potential, making it highly anodic compared to other common structural metals. The corrosion product usually cannot provide highly effective protection as Al alloys. This leads to a high corrosion rate in several circumstances such as moist and marine environments. However, this research will not focus on the afore mentioned problems. This work focus on the high energy input and environmental effects of Mg production, and the insufficient strength-ductility combination.

2.7.1 High energy input and environmental effects of production

Several studies have investigated the energy inputs and environmental effects of magnesium production. It was pointed out that if the production of material is evaluated by the embodied energy, which indicates the energy of the fossil fuel consumption to produce 1 kg of the material, the embodied energy of magnesium is second only to titanium among the common structural metallic materials [104]. When the energy input of magnesium production is evaluated by the consumption of coal, the production of 1 kg of magnesium needs about 4 kg of coal to provide the required energy [38, 105, 106]. These years, with the increasing concern of the possible environmental impact originating from the industry, the goal of carbon neutralisation has been accepted. And the emission reduction of CO₂ has become an important factor to consider during the production, especially for the energy intensive industries such as the magnesium production. To promote the application of magnesium alloys, further investigation of the new production strategies must be carried out.

2.7.2 Insufficient strength-ductility combination

Although the trade-off between good ductility and high strength remains challenging for almost all kinds of metallic alloys, it is more significant in Mg alloys. The formability of Mg alloys is usually lower than Al alloys and steels. This is inherently attributed to the crystal structure of Mg alloys. The HCP structure can provide fewer possible slip systems compared to FCC and BCC structural materials due to the lower symmetry. In section 2.2, the characteristics of the plastic deformation mode, including slip and twinning, was systematically elaborated. The prominent occurrence of basal <a> slip and less intervention of other slip systems in the deformation can affect the mechanical properties of the products. The dominant basal <a> slip can lead to a strong basal texture in the wrought Mg alloy products, because during the deformation process, the basal planes have a tendency to align in a certain way. For example, in the rolled plates of Mg alloys, the normal direction of the basal planes tend to align with the normal plane of the plates [25, 26, 34, 51, 107, 108]. Such deformation texture

cannot be effectively altered with further heat treatment such as annealing. Strong textures further weakens the combination of strength and ductility, as the similar orientation of grains makes the basal slip activated in similar planes. The wrought products can have a lower strength and a higher ductility along one direction, if the load is applied along the direction where basal <a> slip is easy to be activated. Whilst for another direction, there will be a higher strength and a lower ductility, since the loading is applied along the hard direction for basal slip to activate [9]. To summarise, the lack of multiple easily activated slip systems leads to an inherent low ductility. The achievement of a balanced combination of strength and ductility is more intractable for Mg alloys compared to other commonly used structural metallic materials such as Al and ferrous alloys.

2.8 Current approaches under investigation

2.8.1 Current research aiming at the green production of magnesium

2.8.1.1 Recycling of magnesium

The recycling of magnesium has been investigated as an essential strategy to reduce the environmental impact and waste production [24, 104, 109-111]. It was estimated that the mass of circulating scraps can be equivalent to 60-70% of the final casting product [1]. However, the current fraction of the waste used for further recycling can be very low [112]. The recycling of the Mg alloy waste during production can be categorised into two types. The first one is functional recycling, which means the Mg waste is reused for the production of Mg alloys. The second one is non-functional recycling, which means the Mg waste is collected and used for the production of other purposes such as the production of Al alloys. It was proposed that the non-functional recycling of Mg accounts for about 87% in the production [50]. As a result, it is of vital importance to seek an effective way to recycle the waste and turn it into bespoke secondary products.

At the current stage, several methods have been developed for the recycling of Mg and its alloys. Current recycling methods can be categorised into two different strategies based on the state of the material. The first method is liquid-state recycling, which mainly involves re-melting the waste and casting it to produce secondary products [52, 105]. Piotr Dudek et al. [1] investigated the casting of mixture of ingots and circulating scraps of AZ91 Mg alloy. The non-recycled cast material exhibited a yield strength (YS) of 79 MPa, an ultimate tensile strength (UTS) of 128 MPa, and an elongation (EI) of 1.5%. The sample containing 75% of circulating scraps exhibited a YS of 106 MPa, a UTS of 153 MPa, and an El of 1.3%. Liu et al. [113] used rheo-diecasting (RDC) to recycle AZ91D scraps. The as-cast state AZ91D produced from the primary material and circulating scraps did not show any statistically meaningful difference in YS, UTS, and EI, although after further T5 and T6 heat treatment, the El of the samples produced from circulating scraps was slightly lower than the primary products. Spyridon Tzamtzis et al. [52] applied high pressure die cast (HPDC) to recycle mixture AM50 and AM60 scraps. The recycled material reached a UTS of 230.9 MPa and an El of 12.4%, which was equivalent to those of AM50 and AM60 produced by HPDC. Generally speaking, re-melting is a versatile method. It is possible to remove impurities during the melting process by forming slugs containing salts, oxides, and intermetallics with proper control using the re-casting methods for recycling [24], but new undesired inclusions can also possibly form during the melting process [91]. The residual oxide can be detrimental in the recycled products produced by casting, as agglomeration of oxide particles after solidification can be detrimental to the mechanical properties of the recycled products, especially the elongation. Besides, the energy input and CO₂ emission of the liquid state recycling are high since elevated temperatures are required to achieve the liquid state of alloys. This remarkably restricts the advantage of recycling, as the purpose of recycling is to minimise the environmental impact. Material loss is another challenge that liquid-state recycling must face, especially for Mg alloys which have a relatively low vaporisation point [71, 114].

The second method is solid-state recycling. Compared to the liquid-state recycling methods, solid-state recycling usually involves lower energy input and thus lower CO2 emission. For example, it was estimated that the CO₂ emission of the solid state friction stir extrusion (FSE) recycling method is only about 1/7 of the CO₂ emission by traditional gas furnace for melting [111]. Solid-state recycling methods mainly rely on powder metallurgy and plastic deformation [104]. The powder metallurgical approach, represented by spark plasma sintering (SPS), can quickly produce consolidated disks or billets [70, 71]. Li et al. [70] used spark plasma sintering (SPS) to recycle Mg-Gd-Y-Zn-Zr chips. The compression yield strength (CYS), ultimate compression strength (UCS), and compression failure strain (CFS) of recycled billets via SPS at 500 °C for 10min reached 217 MPa, 467 MPa, and 20.4%, respectively. This is higher than the cast billets which exhibited a CYS of 181 MPa, a UCS of 405 MPa, and a CFS of 19.5%. Paraskevas et al. [71] used SPS to recycle pure Mg and AZ31 Mg alloy machining chips. The SPS-recycled pure Mg billet exhibited an increase of 19 MPa in UCS compared to that of the cast material, and the SPS-recycled AZ31 Mg alloy billets exhibited an increase of 35 MPa in UCS compared to that of the cast material. Generally speaking, the SPS technology can provide a quicker recycling approach compared to casting, as the sintering process at the maximum temperature usually takes around 10 min to complete. The lower temperature compared to casting methods can also produce finer equiaxed grains, which is beneficial to the increase in strengths. However, coarse second phase particles can be maintained from the scraps machined from cast products. Oxide films on the scrap or chip surface can also maintain and even grow thicker during the SPS [69]. Large oxide films can affect the continuity of the matrix and act as sites for cracks to nucleate, undermining the ductility of the recycled material. Porosity is another problem for the SPS-recycled products, because the circulating chips usually have large size and irregular shapes compared to powders designated for sintering, the relative density of the SPS-recycled billets is slightly lower than that of products produced from powder. Although the reported density of SPSrecycled billets is comparable to the cast counterparts, mechanical tests were mainly operated under the compression condition [69, 70, 72, 115]. All these factors can lead to compromise of mechanical properties of the recycled product.

The plastic deformation approach is another series of solid-state recycling method. It include several methods, such as extrusion [116-118], equal channel angular pressing (ECAP) [119-121], friction stir extrusion (FSE) [122-124], etc. By applying plastic deformation, scraps or chips achieve metallurgical bonding and form the final products. However, these techniques often requires an extra step of cold compaction, hot compaction, or a combination of both plastic deformation [116-118], which aims at producing billets of certain shapes and sizes as feedstocks for the following deformation step. These pre-compaction products usually exhibited a relative density around 85-95% [116-118, 125]. In the following plastic deformation stage, the pre-compacted material will be further densified, reaching metallurgical bonding. Unlike the powder metallurgy method, large plastic deformation can assist the fragmentation of the oxide layer on the scraps and offer increased mechanical properties [116-118]. However, for recycled products by severe plastic deformation, there are often several repetitive steps and the size can be very limited. Extrusion method can potentially produce much larger products. However, it was reported that the large oxide particles can often leave holes behind them during the extrusion. The refinement and fragmentation of oxide particles may not be effective enough, unless the extrusion ratio is very high. These limit the further improvement of the application of recycling by plastic deformation.

2.8.1.2 Additive manufacturing (AM) of magnesium

Additive manufacturing (AM), also known as 3D printing, is a process of creating components by building them layer by layer from a digital model. Unlike traditional manufacturing methods which involves subtracting material such as machining, AM adds material only where needed. This feature can reduce the material waste, since only the material required is used the fabrication processes. It significantly increases the design flexibility, enabling complicated and customised geometries which are challenging with

traditional methods. The mechanical properties have also been improved in recent years with the progressing of the technology [39, 65, 126-130].

There are several matured AM techniques which have been applied to the production of Mg alloy parts. Based on the mechanism of the material deposition, the AM techniques can be categorised into different types. Powder bed fusion (PBF) is considered a promising method for building complex structures [131]. Laser source is the major energy source, which is referred to as LPBF or selective laser melting (SLM). During the LPBF process, a layer of metal powder is first coated on a platform and then a laser beam scans the powder along a certain path to melt and solidify the material. Layer by layer scanning can produce components with complex shapes, as shown in Figure 2.14. Since the laser beam can be focused into small spots down to 60 µm or even smaller, LPBF can achieve a high shape precision. LPBF has been successfully used for the fabrication of various alloys, including AI, Ti, steels, etc. However, the low evaporation temperature of Mg at 1091 °C can cause preferential evaporation than other common alloying elements and lead to a change in the composition in the final product. Porosity is another inevitable problem, yet with the proper control of printing parameters, the density of printed Mg alloys can go beyond 99.9% [132].

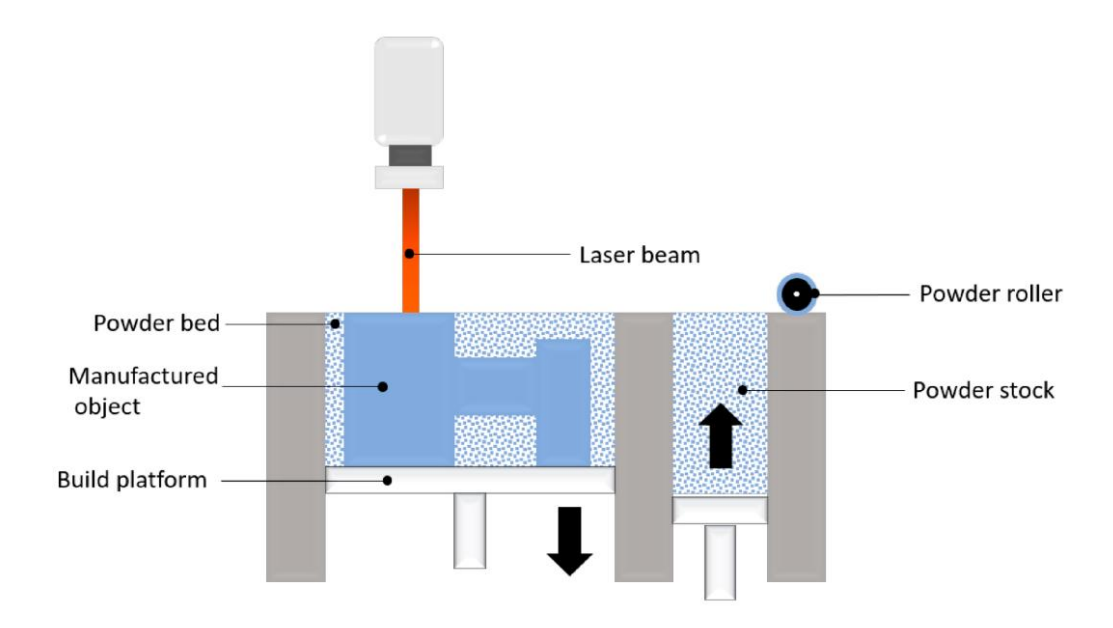


Figure 2.14 Schematic illustration of the LPBF process [133]

Direct energy deposition (DED) employs high levels of input laser energy and large amount of materials to achieve a high deposition of materials [134]. The most common energy source for DED is laser (LDED), and the feeding material can be either powder or wires, as shown in Figure 2.15 and Figure 2.16. Wire arc DED or sometimes which is also referred to as wire arc additive manufacturing (WAAM) [129, 135] is another important type of DED. WAAM uses arc as the heat source and uses metal wire as the feeding material, as shown in Figure 2.11. The deposition rate of DED is much higher than that of LPBF. The possible size of the final product is higher than that of LPBF, because the product size is not limited by the build chamber size. Despite of the advantages, the precision of printing of DED is lower than that of LPBF, as the spot size of DED is much larger [132]. The AM of Mg alloys can be achieved using DED is possible but challenging due to the high evaporation and high flammability of Mg powder [136].

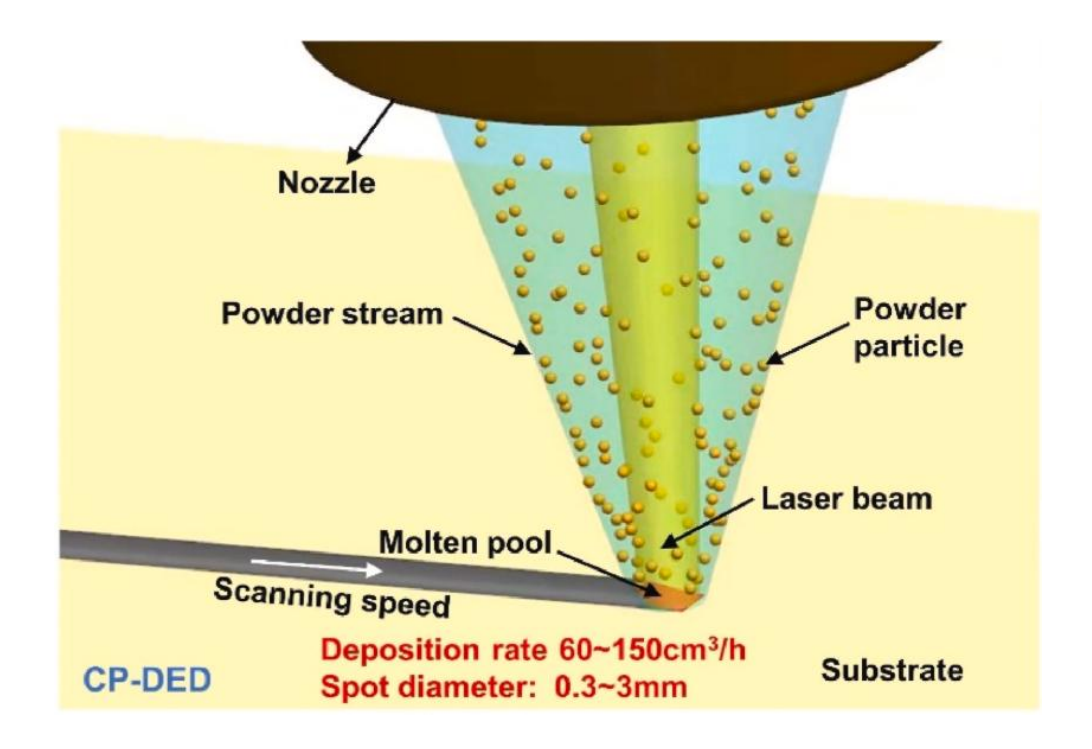


Figure 2.15 Schematic illustration of the conventional LDED process [137]

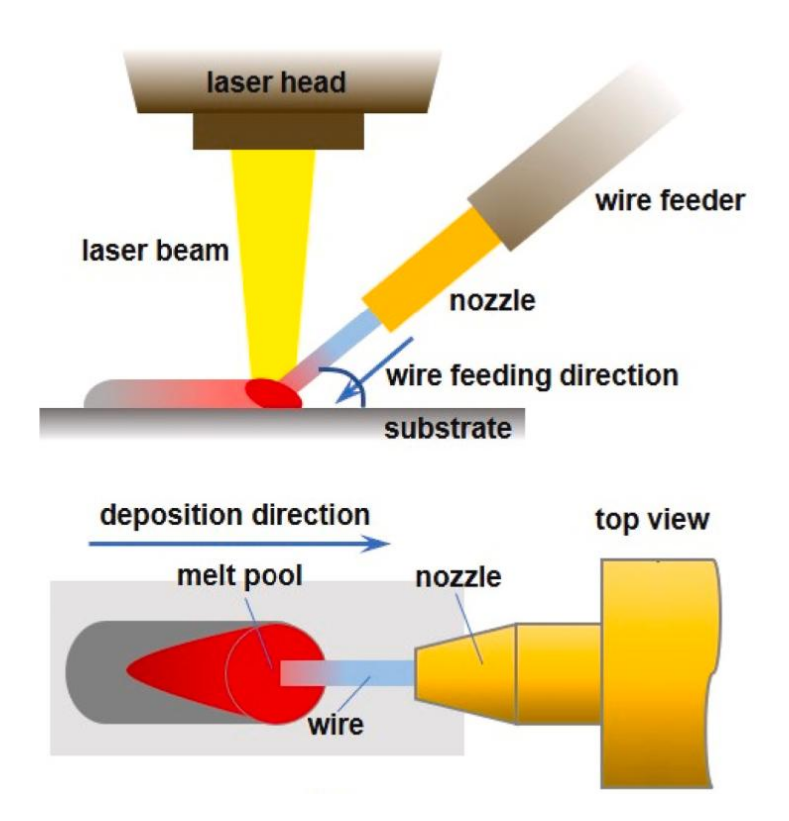


Figure 2.16 Schematic illustration of the wire-based LDED process [133]

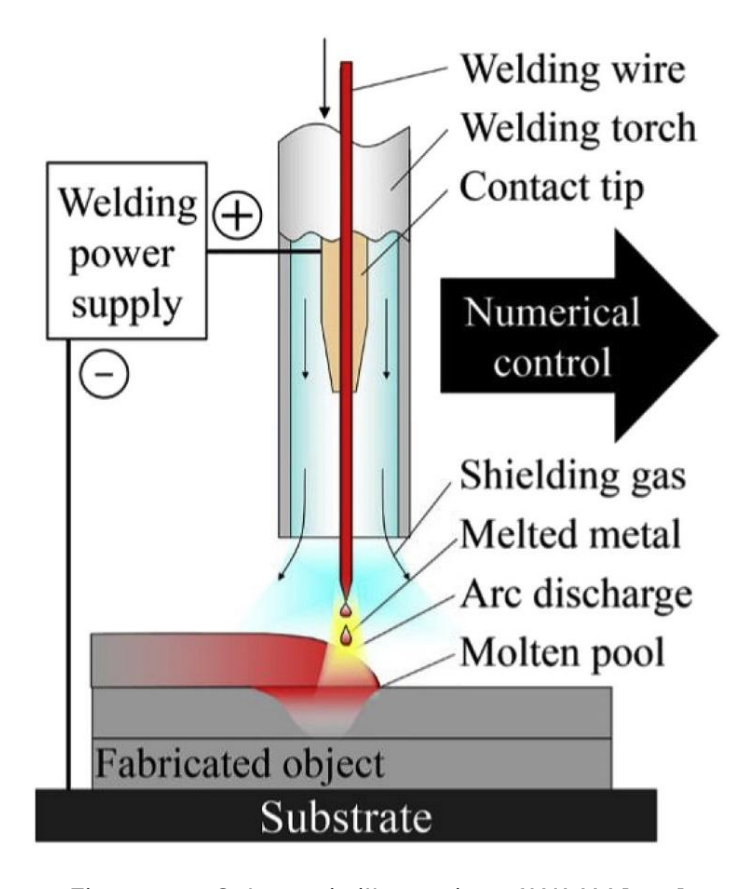


Figure 2.17 Schematic illustration of WAAM [138]

These technologies have been used to fabricate various Mg alloy systems including Mg-Al-Zn and Mg-Y-RE. Chen et al. [129] used WAAM to deposit WE43 Mg alloy, the YS, UTS and El of the material reached 147 MPa, 221 MPa, and 7.2% respectively. Hartmann et al. [39] used LDED to print WE43. After T6 heat treatment, the YS, UTS and El of the material reached 85.9 MPa, 192.7 MPa, and 3.8 %, respectively. Hyer et al. [139] used LPBF to prepare WE43, the YS, UTS and El of the material reached 214.4 MPa, 250.9 MPa, and 2.62 %, respectively In addition to the aforementioned AM technologies, there are also many other methods for metallic materials, including binding and bind-less jetting technologies [133], paste extrusion deposition [133, 138], cold spray additive manufacturing [133], friction stir additive manufacturing [128, 140], etc.

However, there are still some limitations and thus the AM has not seen massive application in the production of Mg alloys. Compared to traditional manufacturing methods, the production speed of AM is significantly lower than that of traditional methods including casting, extrusion, and rolling [65, 141-143]. The raw material for the AM is generally more expensive, as it usually, though not always, involves powder. The production, transportation and storage of powders are more demanding [65, 143]. Besides, due to the high reactivity of Mg alloys, the powder-based production can only be processed under vacuum conditions or gas protection [131].

2.8.2 Current research aiming at the simultaneous achievement of strength and ductility

2.8.2.1 Texture weakening by specific alloying element addition

The direct way to solve the strength-ductility trade-off is to weaken the texture in wrought Mg alloys. The weakening of the texture provides a scattered grain orientation distribution. There is a higher fraction of high Schmid Factor (SF) orientations for non-basal slip like prismatic slip and pyramidal slip to occur. The activation of non-basal slips, especially

pyramidal slips which can accommodate deformation along the c-axis, can help improve the ductility of Mg alloys under deformation.

To date, several elements have been reported to be effective in weakening the texture in wrought Mg alloys. The most common and effective group is rare earth (RE) elements [32, 33, 144-147]. The Mg alloys with RE element addition tend to exhibit similar textures after processing, for example, two split basal poles with lower intensity after rolling [34]. The mechanism behind the texture weakening effects is still in debate. Some researchers suggest that the large atomic radii of these RE elements can cause large lattice distortion [144]. This makes dislocation gliding easier in non-basal planes (i.e. pyramidal <c+a> slips). And thus the texture developed after recrystallisation shows a low intensity of basal orientation. Some researchers believe that these RE elements tend to segregate at grain boundaries and change the grain boundary energy [144]. Such energy change will influence the recrystallisation behaviour, inhibiting the preferred growth of grains with basal orientation. In addition to RE elements, Ca has also been reported to have similar effects on texture development [21, 148]. Although the mechanism is not fully understood, the addition of RE elements and Ca is regarded as an effective way of improving ductility by weakening the texture.

2.8.2.2 Grain refinement by severe plastic deformation (SPD)

Grain refinement is an approach which can possibly improve the strength and ductility at the same time. Finer grains mean there are more grains in the material and thus more grains with orientation favourable for non-basal slip systems to activate will assist ductility improvement. In addition, for Mg alloys, inter-grain deformation modes such as grain rotation can become significant when the grain size approaches ultrafine level. This can help accommodate plastic deformation besides the dislocation glide and twinning, contributing to higher formability. To obtain finer grains, SPD is regarded as an effective method. SPD is a series of technologies producing extremely large plastic deformation without substantial

change in the sample size and geometry [149-153]. Although commercialised SPD equipment capable of carrying out continuous production has not been developed, it is still considered one of the most potential technologies for producing ultrafine or even nano-scale metals with reasonable efficiency. Considering there are too many SPD technologies, and it is developing rapidly, only three major SPD methods are introduced in this section.

Equal channel angular pressing (ECAP) is one of the most widely used SPD methods. An ECAP equipment generally has a set-up as shown in Figure 2.18. It has a curved channel and a plunge fitting the channel. During the ECAP processing, a workpiece is pressed by the plunge, passing through the first section to the second section and deforming at the curved junction part. Intensive shear stress is generated when passing through the curved junction part and finer grains can be produced during this stage [152]. Repetitive pressing steps are often used to generate ultra-fine grains. The final microstructure can be tailored by rotating the workpiece between each pass as the strain path is changed. Krajnak et al. [154] used ECAP to process AX41 Mg alloys with an initial average grain size of around 200 μm. The grain size was successfully refined to 2.0-4.5 μm. And the elongation reached 100-175% due to the grain refinement. Minarik et al. [155] applied 8 passes of ECAP to WE43 Mg alloys and refined the grain from 110 μm to only about 340 nm. The compression yield strength was increased by about 340%.

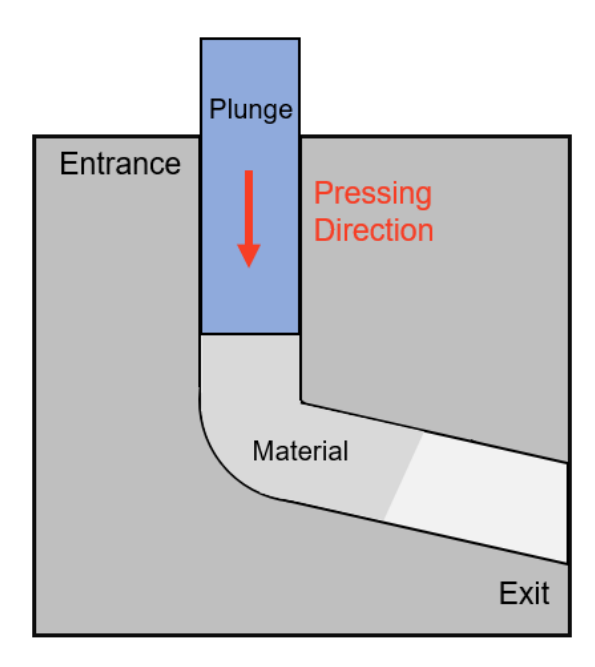


Figure 2.18 Schematic illustration of the ECAP process

High pressure torsion (HPT) is a popular SPD technology. A typical machine of HPT has two key parts, a fixed anvil and a rotational anvil, as shown in Figure 2.19. Samples for HPT usually have the shape of small and thin disk or plate, yet samples with other geometry are also possible. During the HPT processing, the sample is placed at the centre of the lower stationary anvil. The upper anvil applies high pressure and rotates to generate torsion. Liu et al.[86] used HPT to process extruded WE43 Mg alloy. The average grain size was successfully refined from 12 µm to 200-300 nm after 10 turns. And the hardness was increased from 95Hv to 129 Hv at the edge part. Seenuvasaperumal et al. [87] applied HPT to as—cast AZ31B Mg alloy. The average grain size was refined from around 276 µm in as-cast condition to about 276 nm after a 5-turn HPT. The hardness was thus increased from 50 Hv to 125 Hv.

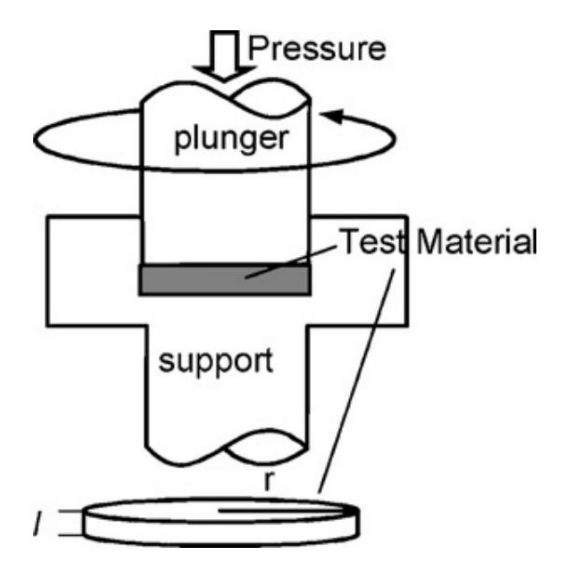


Figure 2.19 Schematic illustration of the thin disc-HPT process [149]

Accumulative roll bonding (ARB) is another major SPD technology. The typical workflow of ARB is shown in Figure 2.20. The surface of two plates is firstly treated to remove the oxide layer and grease, ensuring the bonding in the following steps. These two plates then get stacked and subjected to the two rotating mills. The bonded plate after rolling is cut and the aforementioned steps are repeated. The repeated steps ensure that metallurgical bonding can be achieved between plates and grains can be refined due to the severe plastic deformation. Zhan et al. [156] rapidly refined grains of AZ31 sheets to 1.317 μm after 3 cycles. Utsunomiya et al. [157] applied a 5-cycle ARB to AZ31B sheets. The average grain size was refined from 7.5 μm to 1.6 μm and thus the hardness was also increased. Li et al. [158] used ARB to process ME20 Mg alloy sheets. The average grain size was refined to 1-3 μm from 10 μm right after one cycle. And the following cycles assisted in achieving homogeneous microstructure. Further cycles improved the strength with a slight drop in elongation.

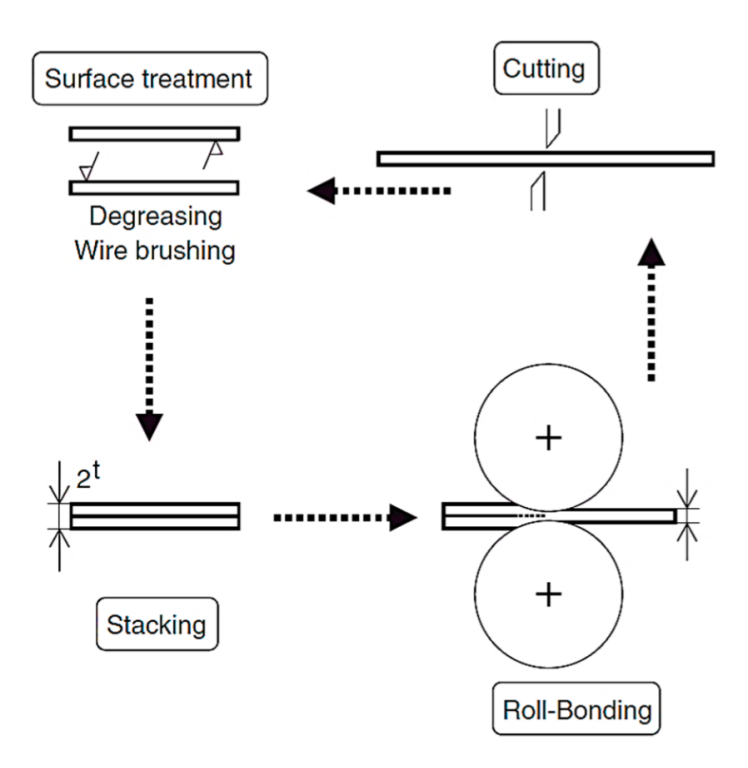


Figure 2.20 Schematic illustration of principles of the accumulative roll bonding (ARB) process [159]

2.9 Research focus of the present study

The objective of this project is to push the research of developing Mg alloys with a combination of strength and ductility one more step toward industrial application using technologies based on FSW, including stationary shoulder friction stir channelling (SS-FSC), friction stir processing (FSP), and additive friction stir processing (AFSD). WE43C, which has high strength and intermediate ductility and can serve at elevated temperatures, was selected as the major base material. The relatively widespread use of WE43C Mg alloys in transportation and the high cost of added rare earth (RE) elements make it an ideal starting point, because the increase of the material use ratio can potentially bring high economic benefits.

The work of the project can be divided into four parts.

 a. Investigation of microstructure and mechanical properties of Mg-3Al-1Zn (AZ31B) wire produced by SS-FSC

SS-FSC can be applied on the processing of Mg alloys and the effects of processing parameters on the final product remains unknown. The effects of SS-FSC on the microstructure and texture of the extruded wire are investigated using rolled AZ31B Mg plate as the base material. Compared to WE43C, AZ31B has lower cost and wide window of processing, and thus ideal for the methodological development before carrying out the experiments on WE43C. This part of work aims at understanding the microstructural evolution and its relationship to the processing parameters, as well as the mechanical properties.

b. Recycled Mg-4Y-3RE (WE43C) wire production incorporating SPS and SS-FSC

Once the SS-FSC work on the AZ31B Mg plate is completed, the investigation of SS-FSC on the SPSed WE43C disk is carried out. Based on the outcomes of the previous part of work, this part further investigate the second phase, oxide, and pore evolution, as well as their effects and post heat treatment on the mechanical properties of the recycled wire.

c. Recycled Mg-4Y-3RE (WE43C) disk preparation incorporating SPS and FSP

Apart from the recycling work by SS-FSC, FSP is also carried out to produce recycled WE43C disk products. This part of work investigate the microstructural and texture evolution throughout the entire recycling process, as well as their effects and post heat treatment on the mechanical properties of the recycled disk.

d. Solid-state additive manufacturing of Mg-4Y-3RE (WE43C) by additive friction stir deposition (AFSD)

This part of work investigate the microstructural and texture evolution, especially the gradient structure due to the temperature and strain difference at different positions during the manufacturing. The effects of oxidation during the manufacturing significantly affect the post

heat treatment response and thermal stability, as well as the mechanical properties, which are also of high value to be studied.

In summary, this work explored producing Mg alloy with a good combination of strength and ductility with lower environmental impact using friction stir based technologies. Systematic microstructural and texture characterisation, including grain size, grain boundary, normal second phase particles, oxide particles and porosity, was carried out to reveal the effects of processing parameters and their contribution to final mechanical properties. It specifically reveals the effects of processing on the final texture gradient in SS-FSC and the role of oxide formation on the subsequent heat treatment, including the ageing peak shift and strengthening effect, which were not previously investigated in detail.

Chapter 3 Materials and methodology

3.1 Materials

AZ31B Mg alloys were used for the SS-FSC process. The chemical composition of AZ31B Mg alloys is shown in Table 3.1. The commercial AZ31B plates were subjected to rolling and annealing. The thickness of the plate was 10 mm.

Table 3.1 Chemical composition of AZ31B Mg alloy

Element	Al	Zn	Mn	Si	Cu	Mg
Weight Percent (wt%)	2.5-3.5	0.7-1.3	0.2 Min	0.05 Max	0.05 Max	Balance

WE43C (Elektron 43) Mg alloys were used for SS-FSC, FSP, and AFSD. The chemical composition of WE43C is shown in Table 3.2, which was provided by the supplier Luxfer MEL Technologies. The raw WE43C for different processing routes are in different state. For the SS-FSC and FSC experiments, the WE43C scraps were machined from cast WE43C components, as shown in Figure 3.1. No lubricant was used during the machining process. For the AFSD experiments, the feedstock was an extruded bar, as shown in Figure 3.2. The extruded bar had a square cross section and the length of the edge was 9.5 mm.

Table 3.2 Chemical composition of WE43C Mg alloy

Element	Υ	Rare Earths	Zr	Mg
Weight percent (wt %)	3.7-4.3	2.3-3.5	Minimum 0.2	Balance



Figure 3.1 WE43C scraps produced from the machining



Figure 3.2 WE43C feedstock for AFSD

3.2 Materials processing

3.2.1 Spark plasma sintering (SPS)

SPS was used to first consolidate the WE43C scrap for the following step of either SS-FSC or FSP. Scraps of WE43C were produced during the machining of the cast material. No extra surface cleaning was applied before the SPS. The SPS was operated by an FCT HPD25

machine. About 90 g of scraps were loaded into a graphite mould which has an inner diameter of 80 mm. Between the graphite mould and the scraps, layers of graphite papers were prepositioned to separate them. This not only increased the electric conductivity between the material and the mould, but also made it easier of the detachment of the consolidated disk from the graphite mould. Before positioning the loaded mould into the SPS machine, a manual pre-compacting was applied. The parameters of SPS programme are shown in Figure 3.3. The SPS was operated under a vacuum condition. The SPSed sample was taken out from the chamber when the temperature decreased to around room temperature. To describe the microstructure of the SPSed disk in the following chapters, the loading direction is denoted as ND, the two radial directions orthogonal to each other are denoted as TD and LD.

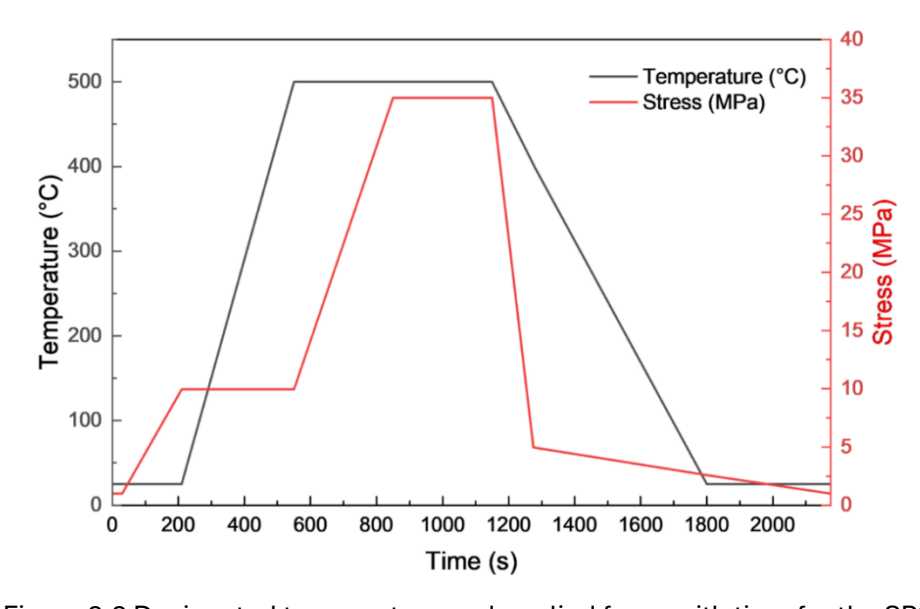


Figure 3.3 Designated temperature and applied force with time for the SPS

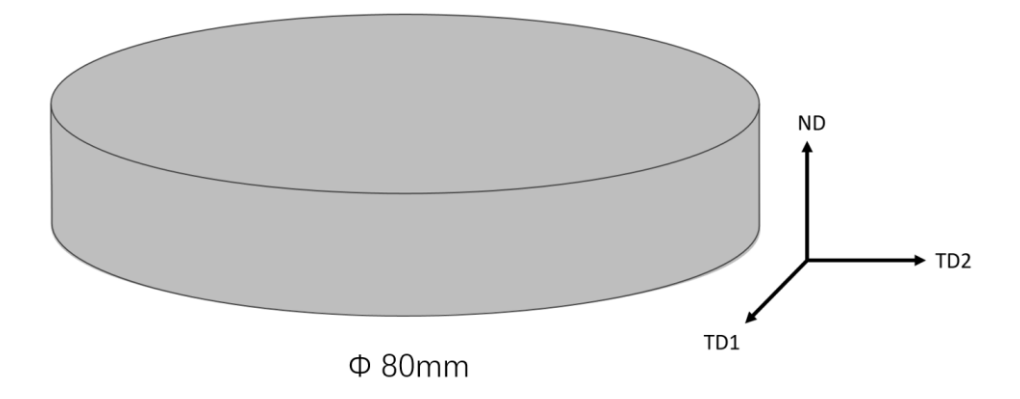


Figure 3.4 A schematic of coordinates for SPSed disk

3.2.2 Stationary shoulder friction stir channelling (SS-FSC)

The SS-FSC were operated on a non-commercial machine developed by TWI in Cambridge. The probe is made of MP159 nickel-cobalt alloy and has a diameter of 6 mm and a threaded length of 4 mm. The probe is decorated with 8 threads. A stationary shoulder with a single exit hole for material extrusion was used together with the probe. A position control mode was used, which means the shoulder of the tool was kept at a constant distance from the base material surface of 0.2 mm during the processing. A photo of a representative setup is shown in Figure 3.5. It needs to be noted that the probe in the image is not the one used for the SS-FSC work. The detailed schematic illustration of the tool design is not shown here due to confidentiality.

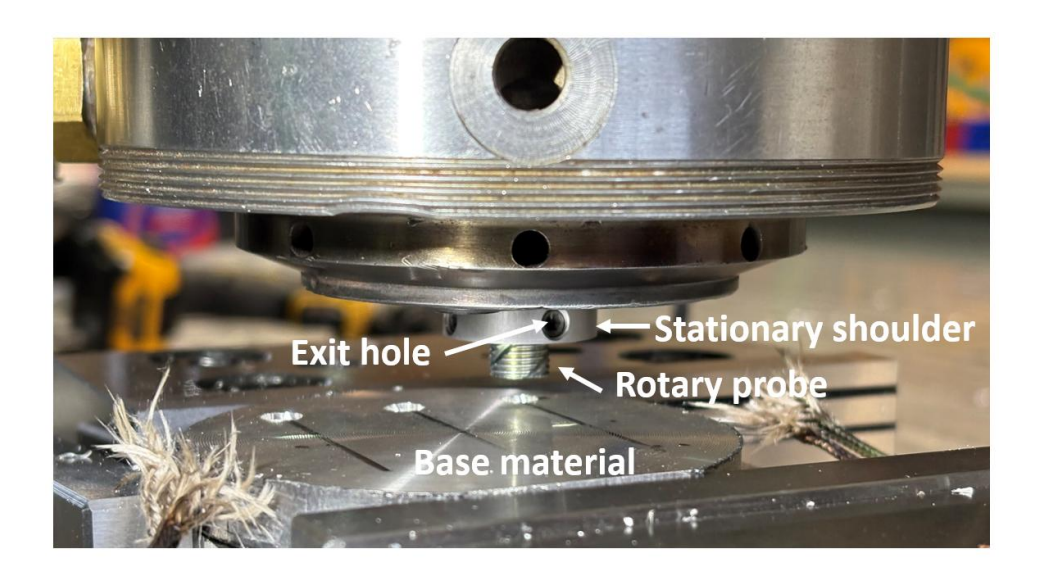


Figure 3.5 A photo of the SS-FSC tool and set up

During the SS-FSC process, the tool was first positioned to the starting point and accelerated to reach the designated rotational speed. When the torque of the tool stabilised, the tool moved down and plunged into the disk until the 0.2 mm gap was achieved. Then when the torque of the tool stabilised again, the tool traversed along a certain direction at the designated speed until the end of the track. During this process, the subsurface material was extracted out from the exit hole, forming the wire. In the end, the tool was raised and stopped.

To explore the processing window of SS-FSC on Mg alloys. The rolled AZ31B was first used for SS-FSC trials to explore the processing parameters. The traverse speed was selected to fix at 100 mm/min based on TWI's previous experience of FSP on Al and Mg alloys, and the tool rotational speed ranged from 400 to 1400 rpm, with an interval of 200 rpm. The processing parameters for the SPSed WE43C disk were adapted from the successful parameters of the AZ31B plate. The summary of the traverse speed and rotational speed used is shown in Table 3.3. The processing parameters for the AZ31B plate were determined to be 1200 rpm rotational speed and 100 mm/min traverse speed. The processing parameters for the SPSed WE43C disk were determined to be 1200 rpm rotational speed and 50 mm/min traverse speed. The selection of the processing parameters was based on whether wires can be continuously extruded without surface cracks or pores. Wires with continuity and non-obvious surface cracks or fractures are regarded to have acceptable quality.

Table 3.3 Parameters of SS-FSC for AZ31B and WE43C

Material	Traverse speed (mm/min)	Rotational speed (rpm)	Acceptable quality
AZ31B	100	600	No
	100	800	No
	100	1000	Yes
	100	1200	No
	100	1400	No
WE43C	100	1200	No
	50	1200	Yes

To describe the microstructure of the SS-FSC extruded wire, the wire extrusion direction (i.e. axial direction) is denoted as the ED, the two radial directions (i.e. transverse direction) are denoted as the TD1 and TD2, as shown in Figure 3.6.



Figure 3.6 A schematic of coordinates for SS-FSC extruded (CoreFlowed) wire

3.2.3 Friction stir processing (FSP)

The FSP was operated by a non-commercial machine developed by TWI in Cambridge. The tool has a typical integrated design, which means the shoulder and the probe are not separated. The shoulder has a concave shape with a diameter is 15 mm. The probe has a triflate design with a conical shape and the diameter ranges from 5 to 8 mm from the bottom to the top, with a dome-shaped tip. The FSP was carried out at a traverse speed of 200 mm/min and a rotational speed of 800 RPM. The depth-control mode was used where the plunged depth was determined to be 0.4 mm with a tilt angle of 1.5°. A multi-track strategy was used to cover a region of the disk instead of a single track. An offset of 5mm toward the retreating side (RS) was used. Compared to the previous track, the latter track has an extra 0.2 mm plunge depth to ensure reasonable contact between the tool and the billet. This generated more flashes but effectively avoided the adverse effects of the material loss at the processed surface such as poor surface quality, crack formation and voids, which were discovered in the previous trials without the incremental plunge depth. For the FSPed disk, the tool traverse direction is denoted as LD, which is also often referred to as the processing direction (PD) in other researches. The traverse direction of the track is denoted as TD the normal direction of the processed surface is denoted as ND, as shown in Figure 3.7.

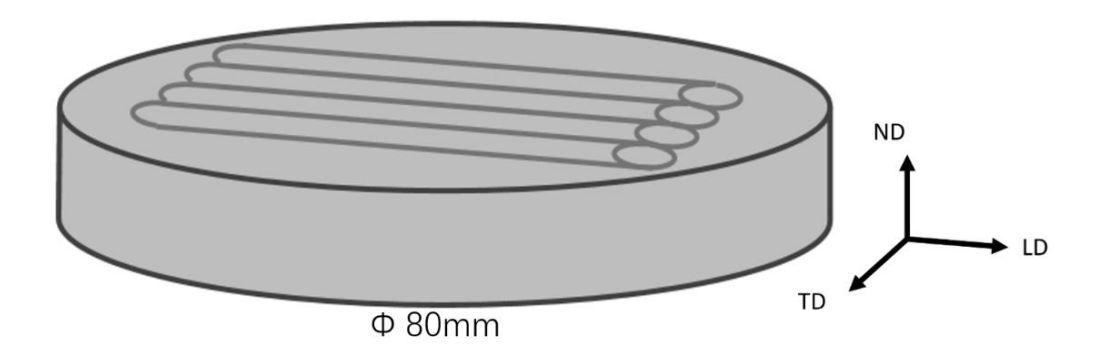


Figure 3.7 A schematic of coordinates for FSPed disk

3.2.4 Additive friction stir deposition (AFSD)

The AFSD process was performed on a commercially available MELD B8 machine. The tool for AFSD is made of H13 steel. It has a cylindrical shape with a square hollow channel embedded at the centre which is compatible with the feedstock. The bottom surface of the tool also has a 'teardrop' structure [160]. The rotational speed, feeding rate and traverse speed were 325 RPM, 63.5 mm/min, and 152.4 mm/min, respectively. A position control mode was used, which means the gap between the tool and the substrate was set constant, and the distance was kept 1mm. To describe the AFSDed component, the direction of the deposited layer thickness is denoted as the building direction (BD), the direction of the tool travelling is denoted as the longitudinal direction (LD), and the direction orthogonal to these two directions is denoted as the transverse direction (TD). The traverse direction of the tool of the odd number layer was along the positive direction of LD, whilst that of the even number layers was along the negative direction of LD, as shown in Figure 3.8.

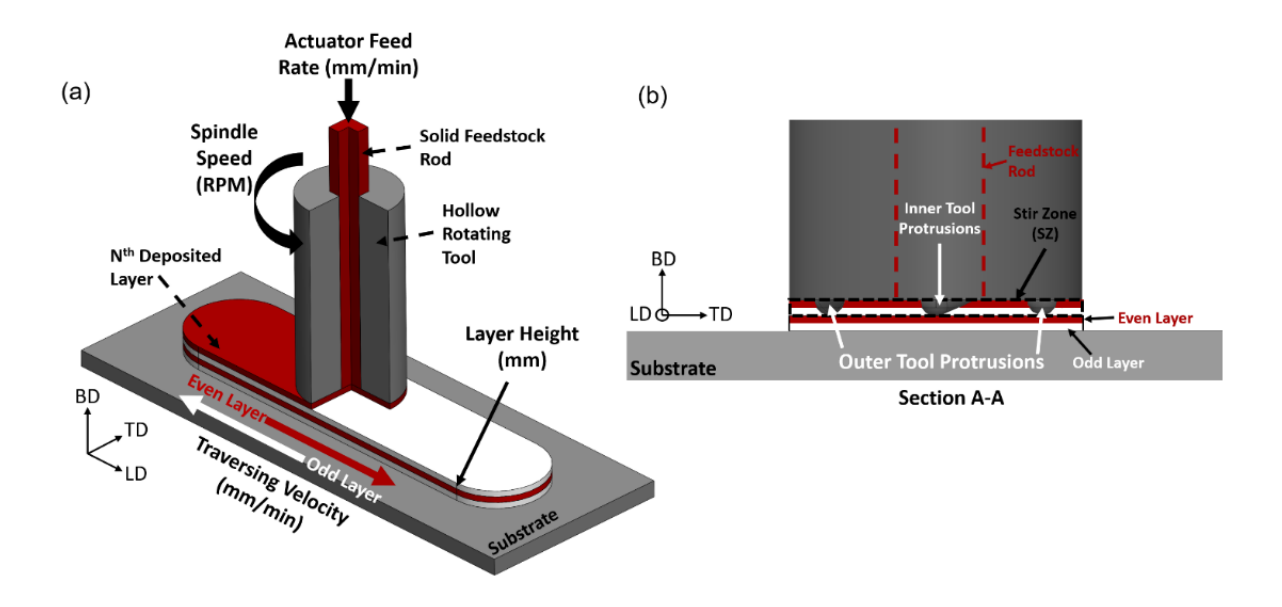


Figure 3.8 Schematic of the AFSD set up [160]

3.3 Post heat treatment

Precipitation hardening is an essential strengthening mechanism in WE43C Mg alloys. Since the friction stir-based technologies cannot directly produce precipitates which can effectively increase the strength of the material, further heat treatment was applied. Based on the microstructure in the material, either solid solution treatment (SST) + ageing (T6) or direct ageing (T5) was investigated. The SST was done at 525°C, which is a commonly used temperature both in industrial production and scientific research [161, 162]. The temperature is high enough to dissolve most of the second phases without causing partial melting. The SST time was chosen based on the condition of second phase dissolution and grain growth. Water quenching was used at the end of the SST. The ageing treatment was done at 200 °C, which is lower than the commonly used 250 °C in industry. Trials of ageing at 250 °C was conducted on the WE43C alloys fabricated by friction stir based technologies, and little hardness increase or even drop in hardness were observed. Lower ageing temperature at 200 °C could increase the strengthening response. Heat treatment was all completed in a box furnace. The thermal stability investigation of the AFSDed material was also carried out at 525°C.

3.4 Microstructure characterisation

Various techniques were used to investigate the microstructural information in the material at different conditions, including the grain size, texture, second phase particle, chemical composition, etc. The acquired information was used to assist the understanding of the processing and the resulting properties.

3.4.1 SEM, SEM-EDS, EBSD and the sample preparation

Samples for scanning electron microscope (SEM), SEM-energy dispersive spectroscopy (SEM-EDS) and electron backscattered diffraction (EBSD) were cold mounted in epoxy resin or directly cut into small cuboids. Samples for SEM were prepared by mechanical grinding and polishing using a Buehler Automet 250 Pro machine. The cuboidal samples were first ground using SiC grit papers, in the order of p1200, p2500, and p4000 grit papers. Then the samples were polished by 1 µm, 0.25 µm alcohol-based diamond suspension. The final mechanical polishing was done by 40 nm colloidal silica suspension. Part of the samples were further ion polished using a Gatan PECS II model 685 machine. SEM, SEM-EDS, and EBSD were operated on two SEM machines, including a JEOL JSM-7200F FEG-SEM equipped with a C-Nano EBSD detector, and a JEOL JSM-7900F FEG-SEM equipped with an Oxford Instruments AZtec Xmax-170 for EDS and an Oxford Instruments Aztec HKL Advanced Symmetry System for EBSD. The SEM images and EDS scans were taken at an accelerating voltage between 15-20 kV using Aztec. All the EBSD data were collected at an accelerating voltage of 20 kV using Aztec. The EDS and EBSD data were analysed using Aztec and AztecCrystal software, respectively.

3.4.2 X-ray diffraction (XRD) characterisation

Phase identification of the material was assisted by XRD. XRD scans were operated on a Rigaku SmartLab. The XRD was operated by a Cu-Kα radiation with a wavelength of

0.154059 nm. The accelerating voltage and beam current were set to 45 kV and 150 mA. A step degree of 0.02° was used for the scan. The collected data was processed using PDXL.

3.4.3 X-ray computed tomography (XCT) characterisation

XCT was employed to characterise the 3D distribution, shape and size of pores and second phase particles. For large samples with a size over 5 mm, including representative SPSed sample and a Diondo D5 machine was used for the scanning. XCT scans with a higher resolution were done on Zeiss Xradia Versa 510 and Zeiss Xradia Versa 620. The XCT data were processed and analysed using Avizo software. Details of scan parameters are shown in Table 3.4.

Table 3.4 Sample size and set up for XCT

Sample material and size	Machine	Accelerating	Power (W)	Voxel size
		voltage (kV)		(µm)
SS-FSC extruded AZ31B Φ2mm	Zeiss	50	4.5	2.18
	Xradia			
	Versa 620			
SPSed WE43C 5mm cubic	Diondo D5	300	12	3.49
SPSed WE43C 2mm cuboid	Zeiss	140	10	1.35
	Xradia			
	Versa 510			
SS-FSC extruded WE43C Φ2mm	Zeiss	140	10	1.35
	Xradia			
	Versa 510			
FSPed WE43C 5mm cubic	Diondo D5	300	12	3.49
FSPed WE43C 2mm cuboid	Zeiss	140	10	1.35
	Xradia			
	Versa 510			
AFSDed WE43C 4mm cuboid	Diondo D5	300	12	3.49

3.4.4 Transmission electron microscopy (TEM) and the sample preparation

TEM samples were first manually ground to have a thickness around 75 µm, and then punched out to be a 3mm diameter disk. Twin jet polishing was used to further reduce the thickness of the sample until they were suitable for TEM observation. TEM images and energy dispersive spectroscopy (EDS) scans were taken on an FEI Talos F200X microscope equipped with a Super-X G2 EDS detector, operated at an accelerating voltage of 200 kV. TEM images and EDS data were recorded and analysed by Digital Micrograph and Aztec, respectively.

3.5 Mechanical property characterisation

3.5.1 Microhardness tests

Microhardness tests were performed on a Zwick FM-300 hardness tester to investigate the mechanical property heterogeneity in the material and the ageing response. Vickers hardness mode was used. The load for all samples was set to 200 g, and the dwell time was 15 s. The distance between each indentation was 500 µm to avoid interference from the adjacent indentation.

3.5.2 Tensile tests

Tensile tests were performed to evaluate the strength and ductility of the material. Due to the significantly different size of the material, the dog-bone samples were also prepared in different shapes based on the sample size. For the SS-FSC extruded wires, the mechanical properties were characterised by running tensile tests on Deben CT500 rigs. The apparatus and sample size are shown in the Figure 3.9 below and the extension rate was set to 1.0 mm/min. The loading was applied along the ED of SS-FSC extruded samples. For the FSP work, dog-bone tensile test specimens were machined from the FSPed and FSP+aged samples using electron discharge machining (EDM). As shown in Figure 3.10, the width,

thickness, and length of the gauge part are 4mm, 1mm, and 18 mm, respectively. Tensile tests were performed on an Instron 5569 electromechanical testing system. The initial strain rate was set to 1×10⁻³ and the strain was monitored by an extensometer. A load cell of 2 kN was used. For the AFSDed work, the schematic of the dog-bone sample is shown in Figure 3.11. The length and the thickness of the gauge part were 5.5 mm and 4mm, respectively. Tensile tests were completed by Luxfer MEL Technologies. Tensile tests of the as-printed specimens were completed by C-column, along the LD. All the specimens were ground using P4000 grit paper to control the surface finishing of the specimens.

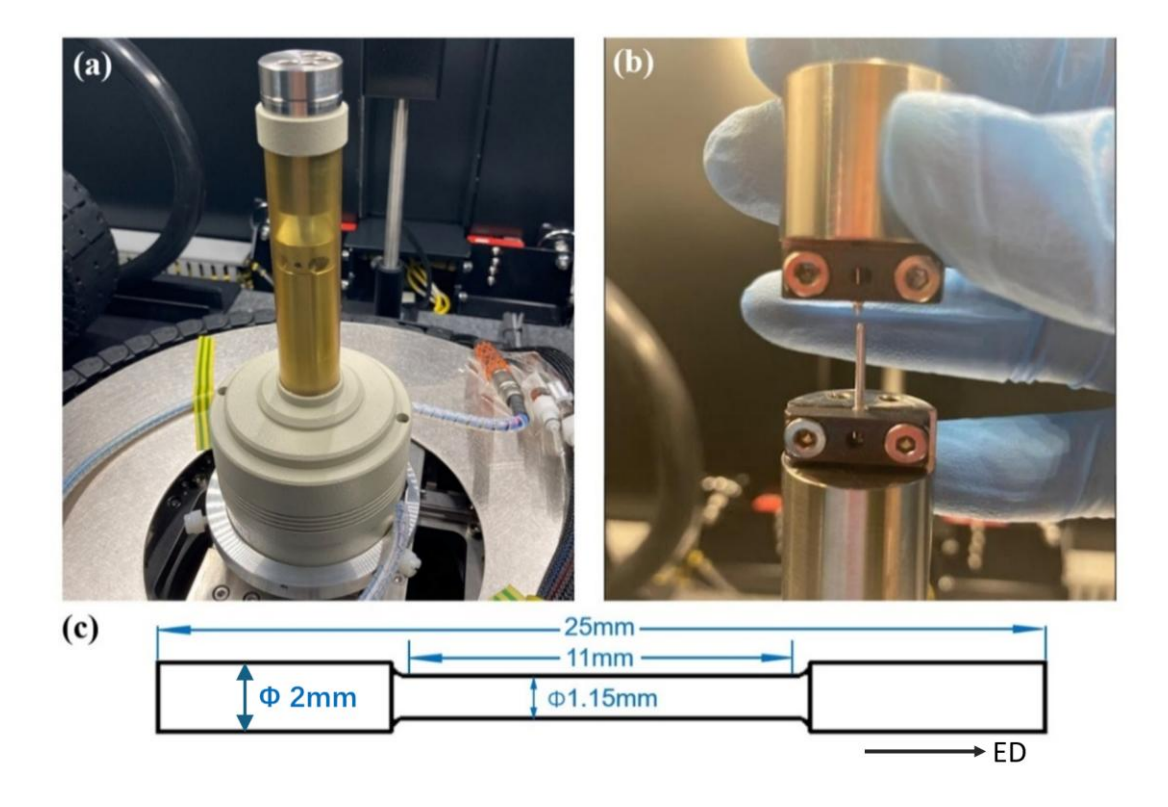


Figure 3.9 (a) Deben CT500 tensile stage for tensile tests, (b) tensile test sample set up in the Deben CT500 tensile stage, (c) sketch of the cylindrical tensile test sample of SS-FSC extruded wire.

Sketch of (a) position of the tensile specimens of FSPed material, (b) size of the tensile test specimens of FSPed material

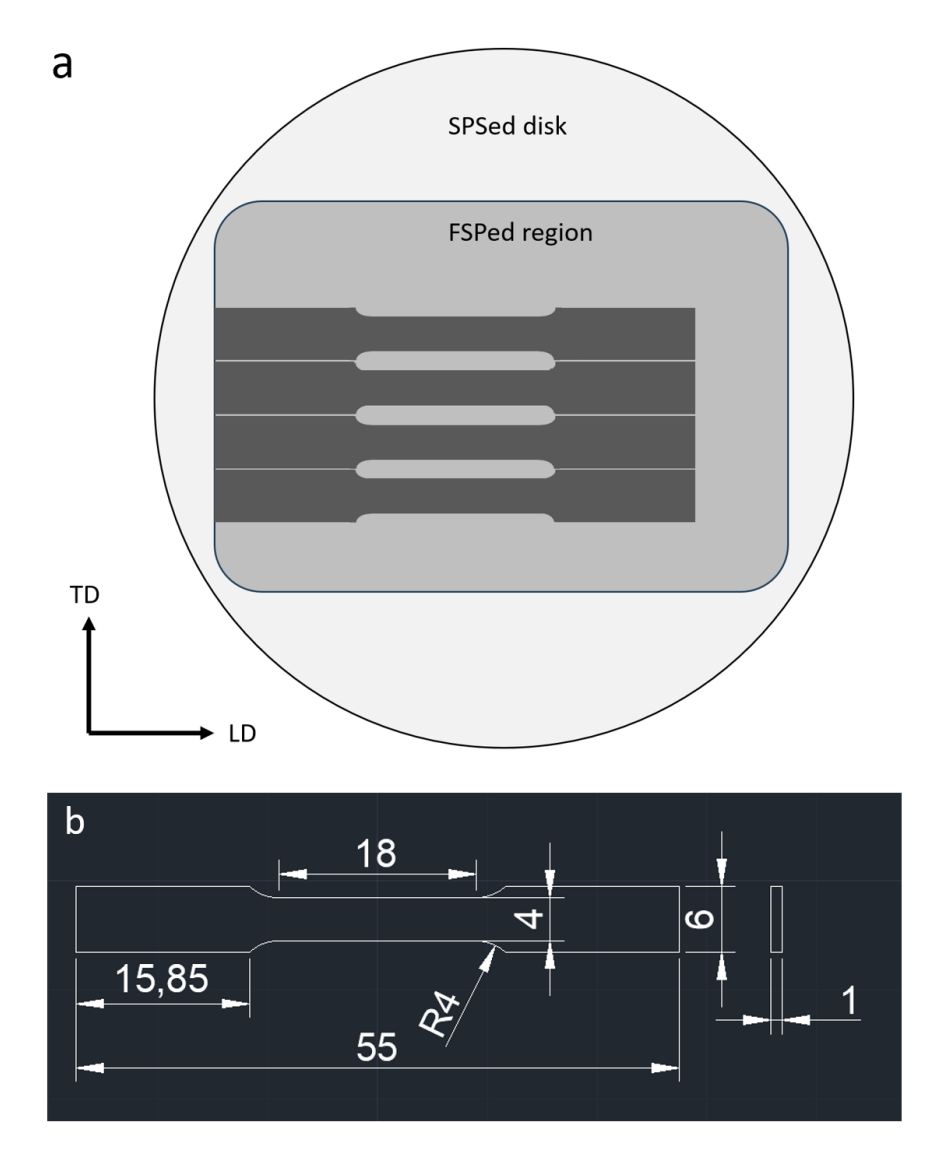


Figure 3.10 Sketch of (a) position of the tensile specimens of FSPed material, (b) size of the tensile test specimens of FSPed material

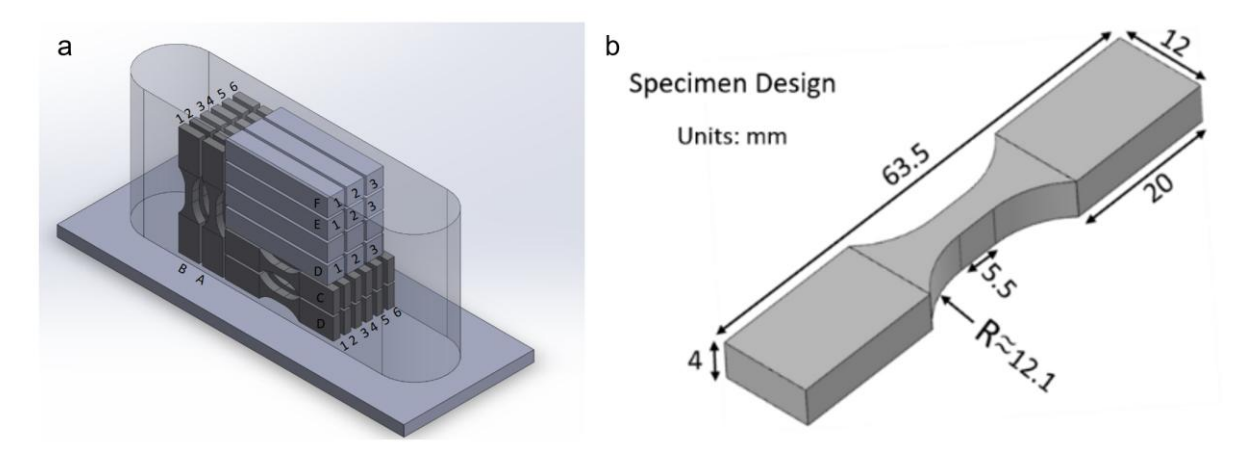


Figure 3.11 Sketch of tensile tests samples of AFSDed material (a) locations of specimens, (b) sizes of specimens [160]

Chapter 4 Investigation of microstructure and mechanical properties of AZ31B wire produced by SS-FSC

4.1 Introduction

Stationary shoulder friction stir channelling (SS-FSC), or the patented name 'Coreflow®', was developed by TWI to achieve subsurface channelling. Except for the capability of subsurface channel forming, the extracted subsurface material can be extruded in the form of wires. However, the potential for SS-FSC to extrude wires has not been investigated. In this chapter, trials of SS-FSC for AZ31B wire extrusion were carried out prior to the recycling work of WE43C as a pre-investigation. Since no work has been carried out regarding the SS-FSC process of Mg alloys previously, AZ31B alloy is an ideal base material for initial trials. AZ31B has much lower cost compared to WE43C, because the major added alloying elements of Al and Zn have significantly lower price compared to those in WE43C including Y, and RE elements. Besides, the process ability of AZ31B is better than WE43C due to the lower concentration of alloying elements.

This part of work explored the feasibility of SS-FSC on rolled AZ31B Mg alloy plate and explore the processing parameters. The texture and microstructure was investigated to understand the material deformation, recrystallisation and second phase evolution during the SS-FSC process. The mechanical properties of extruded wires were evaluated by tensile tests and the results were compared with the base material.

Part of this work has been published on:

X. Zhao, X. Zeng, L. Yuan, J. Gandra, Q. Hayat, M. Bai, W.M. Rainforth, D. Guan, A novel approach for producing Mg-3Al-1Zn-0.2Mn alloy wire with a promising combination of strength and ductility using CoreFlowTM, *Scripta Materialia* 227 (2023).

XCT scans and the tensile test were operated by staff of Sheffield Tomography Centre at The University of Sheffield.

4.2 Results

4.2.1 Microstructure and texture evolution

As illustrated in the previous chapter, only one fully consolidated AZ31B wire was produced when the traverse speed and rotational speed were 100 mm/min and 1200 rpm, respectively. A photo of it is shown in Figure 4.1a. The other trials produced wires continuously, yet the cross sections were near semicircles, and the wires were severely curly, as shown in Figure 4.1b. The inverse pole figure (IPF) maps of SS-FSC extruded (CoreFlowed) and asreceived AZ31B are shown in Figure 4.2. The Pole figures and inverse pole figures of the two samples are shown in Figure 4.3. The (0001) basal poles are aligned parallel to the normal direction (ND) with an intensity of 9.5 multiples of uniform density (MUD), implying a strong basal texture formation in the as-received material. The PFs of (0001) in SS-FSC extruded AZ31B indicate a gradient texture with a maximum intensity of 7.8 MUD evolved during the process. Based on the EBSD IPF map of SS-FSC extruded AZ31B, it can be identified that regions from the wire centre to the edge are dominated by grains with different crystal orientations. What is more, in the edge region, there are some needle-like regions dominated by grains with similar crystal orientations but distinctively different from the orientations of vicinal matrix grains.



Figure 4.1 (a) A photo of the consolidated AZ31B wire, (b) A photo of other wires which were not fully consolidated.

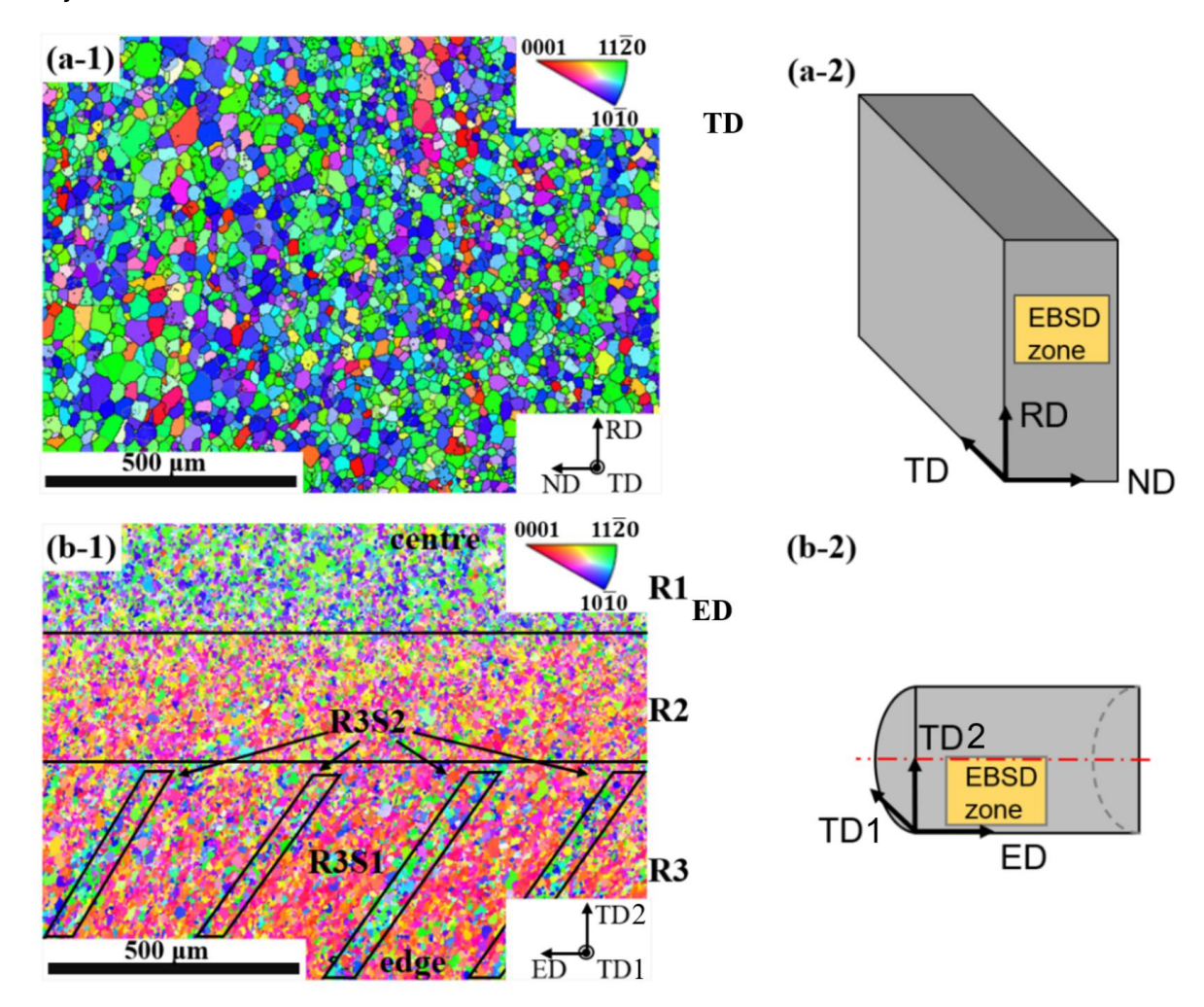


Figure 4.2 (a-1) EBSD IPF map of as-received AZ31B along TD (IPF-Z//TD), (a-2) position of EBSD zone on as-received sample; (b-1) EBSD IPF map of SS-FSC extruded AZ31B along TD (IPF-Z//ED), (b-2) position of EBSD zone on SS-FSC extruded zone.

Based on the texture difference in the EBSD IPF map in Figure 4.2, the SS-FSC extruded AZ31B was divided into three regions R1, R2, and R3 for analysis. Based on Figure 4.3, from R1 to R3 (i.e. wire centre to the edge), the (0001) pole gradually rotated toward the ED. In the PF of R3, two basal poles with intensity differences can be easily identified, and thus R3 was further categorised into region R3S1 and R3S2These two poles were attributed to R3S1 and R3S2. More specifically, there was a continuous shift of the basal pole along R1-R2-R3S1, yet a distinct change of basal pole alignment was observed in R3S2. The IPFs also verified the texture component change from R1 to R3. In R1, the $<11\bar{2}0>$ directions of grains primarily aligned along the ED. When it comes to R2 and R3, along the ED, grain orientations gradually shifted toward <0001>, becoming more off-basal. The difference between R3S1 and R3S2 was well illustrated by the IPFs in Figure 4.3. Compared with those in R3S1, grains in R3S2 aligned closer to <0001> along the ED, in other words, more off-basal.

The IPF maps indicate that the as-received sample has an equiaxed grain structure after annealing. The average grain size was measured to be 20.5±9.4 µm, 20.7±9.2 µm, and 20.0±9.1 µm along the rolling direction (RD), transverse direction (TD), and normal direction (ND), respectively. The average grain size in the SS-FSC extruded AZ31B was determined to be 6.5±4.2 µm along the transverse direction (TD) and 6.7±4.5 µm along the extrusion direction (ED). The fraction of low angle grain boundaries (LAGBs) with a disorientation between 2-10° and high angle grain boundaries (HAGBs) with a disorientation larger than 10° is summarised in Table 4.1. Apparently, the fraction of HAGBs in the as-received material was much higher than that in the SS-FSC extruded sample. The grain orientation spread (GOS) maps of the as-received and SS-FSC extruded samples indexed by the mean GOS value are shown in Figure 4.4. These maps directly reveal the level of the misorientation within grains in the sample which can be interpreted to the recovery and recrystallisation information. Grains with a mean GOS value smaller than 2° are usually regarded as recrystallised grains. The values of the two samples can also be found in Table 4.1.

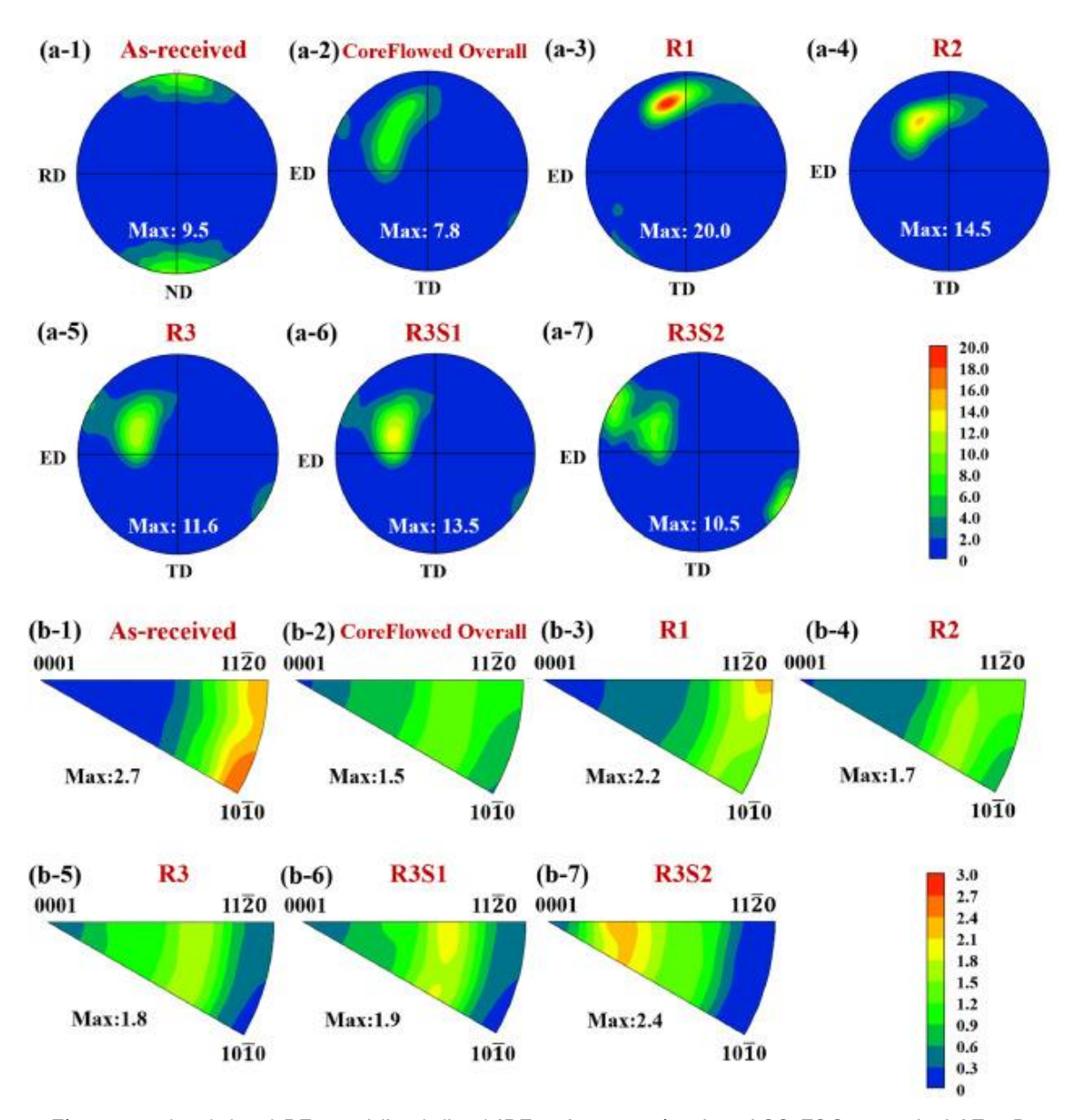


Figure 4.3 (a-1)-(a-7) PFs and (b-1)-(b-7) IPFs of as-received and SS-FSC extruded AZ31B.

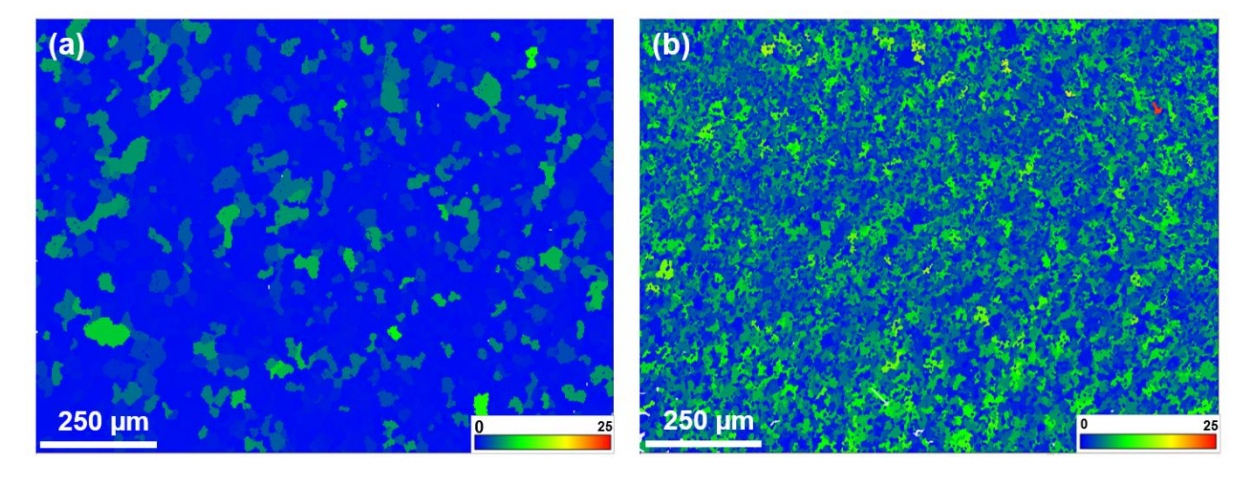


Figure 4.4 GOS maps of (a) as-received AZ31B along TD, (b) SS-FSC extruded AZ31B along TD

Table 4.1 Lengths fraction of GBs and area fraction of GOS value of as-received and SS-FSC extruded samples

Sample	HAGBs (%)	LAGBs (%)	GOS < 2°	GOS > 2° (%)
As-received TD	85.4	14.6	80.7	19.3
SS-FSC extruded TD	71.2	28.2	35.1	64.9

A representative magnified picture taken from the EBSD map of SS-FSC extruded AZ31B is shown in Figure 4.5a. It is evident that the selected grain is characterised by curved and serrated HAGBs and several well-defined internal LAGBs. The cumulative orientation change plots between selected points can also be found in Figure 4.5b.

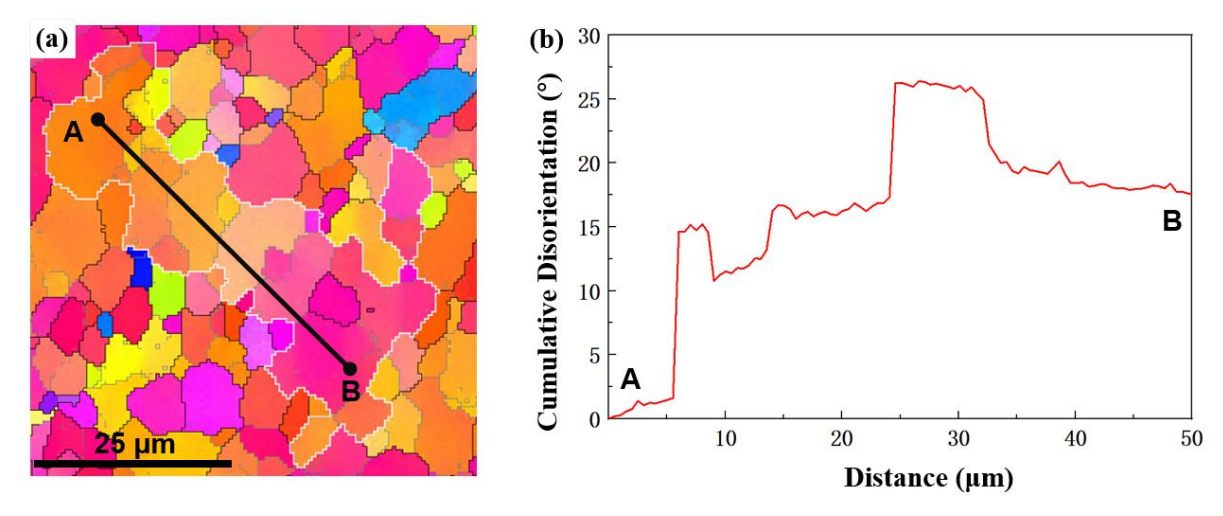


Figure 4.5 (a) A typical region of uncompleted CDRX occurrence in SS-FSC extruded AZ31B, (b) The cumulative disorientation from point A to B.

The SEM-BSE images illustrate the second phase differences in the as-received and SS-FSC extruded AZ31B, as shown in Figure 4.6. In the sample of the as-received AZ31B plate, second phase particles are mainly elongated and aligned linearly along the RD, yet a few round particles with slightly larger sizes were also observed. This is commonly observed in the rolled sample since previously formed large second phase particles get broken and aligned along the rolling direction during the deformation. Whilst in the SS-FSC extruded sample, second phase particles were found generally to be round and distributed

homogeneously, along both ED and TD. The 3D distribution of second phase particles generated from the XCT scanning, as shown in Figure 18, illustrates the spatial distribution. Second phase particles are homogeneously distributed throughout the wire. There was no obvious clustering or depleted zone, validating the homogeneous distribution of second phase particles from a 3D perspective.

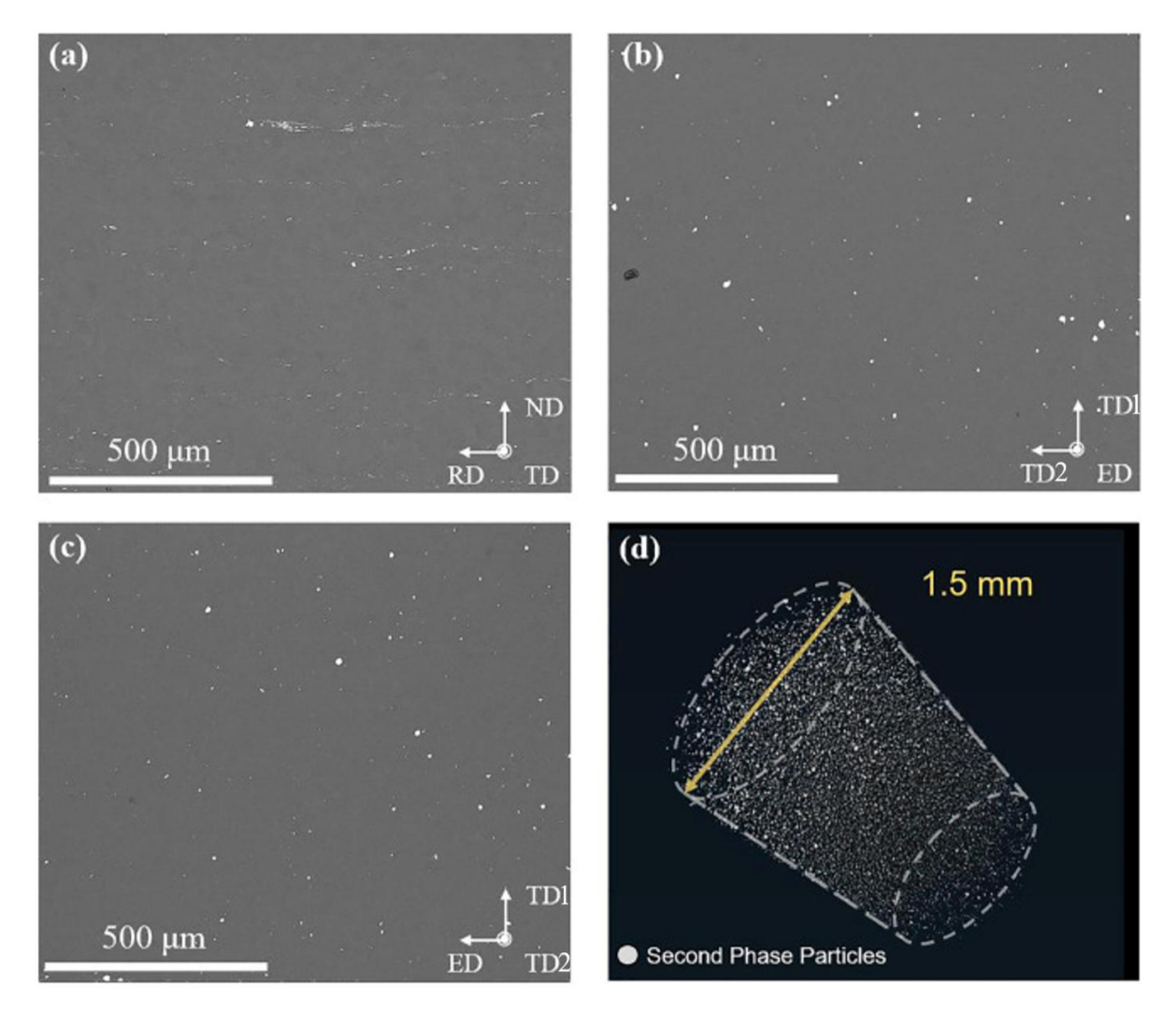


Figure 4.6 BSE images of (a) as-received AZ31B along TD, (b) SS-FSC extruded AZ31B TD1-TD2 plane, (c) SS-FSC extruded AZ31B TD1-ED plane, (d) A 3D view of second-phase particles in a cylindrical volume extracted from SS-FSC extruded AZ31B XCT result.

4.2.2 Mechanical properties and fractography

The tensile test were carried out along the ED and the results are shown in Table 4.2. Representative engineering and true stress-strain curves are shown in Figure 4.7. As no well-

defined yielding point was observed in the tensile testing, the 0.2% proof stress was used as the yielding strength. Both kinds of samples did not show an obvious necking stage during the tensile tests, though the elongation values were relatively reasonable. It is evident that the SSFSC extruded samples exhibited a significant increase in the elongation (EI). The elongation at failure reached 22.3±0.8%, which was 58% higher than that of the as-received ones (14.1±0.3%). Meanwhile, the yield strength (YS) and the ultimate tensile strength (UTS) of the SS-FSC extruded sample were equivalent to those of the as-received samples. The typical SEM images of fractured surfaces after tensile tests are shown in Figure 4.7b and c. The fractured surface of the as-received AZ31B plate sample exhibited well-defined step patterns and shallow dimples. Whilst in the SS-FSC extruded sample the fractured surface was dominated by much deeper dimples of different sizes, indicating increased ductility deformation modes.

Table 4.2 YS, UTS, and El of as-received and SS-FSC extruded AZ31B

Material	YS (MPa)	UTS (MPa)	EI (%)
As-received AZ31B	137 ± 9	260 ± 1	14.1 ± 0.3
SS-FSC extruded AZ31B	134 ± 6	258 ± 5	22.3 ± 0.8

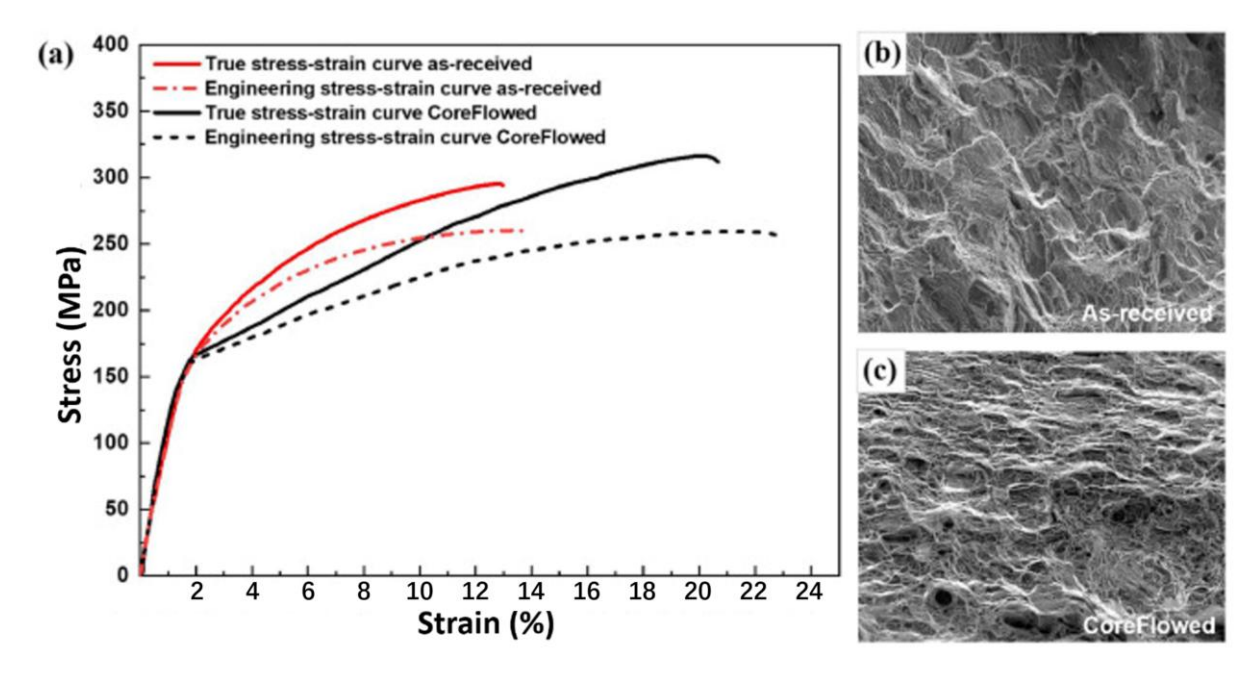


Figure 4.7 (a) Engineering and true stress-strain curves of SS-FSC extruded and as-received AZ31B, (b) SE image of fractured surface of as-received AZ31B, (c) SE image of fractured surface of SS-FSC extruded AZ31B.

4.3 Discussion

It is obvious that two samples subjected to rolling and SS-FSC showed significantly different textures and microstructures. The IPF of as-received AZ31B in Figure 4.3 showed a typical basal texture after rolling processing, with the (0001) basal poles aligned toward the ND. The second phase particles were elongated and broken into segmentations, linearly aligned with the RD. In the SS-FSC extruded wire, a gradient texture along the TD was observed, and second phase particles were re-distributed homogeneously. The texture and microstructure differences can be attributed to the result of complicated material flow during SS-FSC. Considering the resemblance between SS-FSC and FSE, a hypothesis of material flow can be developed based on previous research on FSE. The base material was firstly cut and extracted out by the rotating 8-thread probe. As the probe travelled forward, more material was cut from the plate and then forced into the channel embedded in the stationary shoulder. These materials are welded together and extruded out from the hole on the shoulder in a helical mode in the region where those threads end. And then the consolidated material was

extruded out through the channel embedded in the stationary shoulder and cooled by air. Several pieces of evidence from collected data support this material model. The gradient from the wire centre to the wire edge is consistent with such material flow. The helical material flow model suggests the material flow from the wire centre to the edge is not identical. The strain path of R1 should be very similar to that of conventional extrusion, represented by basal fibre textures. The IPF of R1 indicates that a basal fibre texture with $<11\bar{2}0>$ //ED developed, which is often observed in the recrystallised extruded AZ31B, consistent with the condition of SS-FSC extruded AZ31B. For R2 and further to R3, the peak in the IPFs shift to <0001>, suggesting that the texture components deviate from the "extrusion condition", becoming more affected by the rotation from R1 to R2 and R3. When it comes to R3, two separate basal poles were distinguished. The basal pole shift along R1-R2-R3S1 is continuous, whilst the basal pole of R3S2 is away from the path of such shift. The continuous basal pole shift along R1-R2-R3S1 is attributed to the increasing rotation effect from the wire centre to the wire edge. The separated basal pole of R3S2 is a result of seam welding. As mentioned before. The base material was cut into 8 parts and then formed a consolidated wire, which means these 8 different parts were welded together during the material flow processing. And the material in the vicinity of the 'welding line' was subjected to a different strain state. This makes the material of R3S2 (i.e. welding line) exhibit different texture components from the surrounding parts. This is also verified by the calculation of the needle-like R3S2 region periodicity. An equation can be established to describe the R3S2 region appearance if they are the result of the seam welding:

$$2D = ndtan\theta$$
 (4.1)

where D is the diameter of the wire, n is the number of threads on the probe, d is the distance between each R3S2 region, and θ is the angle between the long axis of R3S2 needle-like region and the ED axis. In this work, D was 2mm, the average value of d was measured to be 0.31mm from Figure 4.2, and the average value of $tan\theta$ was calculated to be 1.65. The

calculated value of n was 7.82, which is very close to the actual number of threads used for the wire extrusion. So, R3S2 regions at the wire edge are the trace of seam welding.

In addition to the texture modification, the microstructure was also modified by SS-FSC. The rotational probe generated not only severe plastic deformation, but also a large amount of heat by friction and deformation. These provide the condition for dynamic recrystallisation (DRX) in the AZ31B alloy. CDRX relies on the continuous movement of dislocation to LAGBs. The consumption of dislocation leads to a continuous increase in disorientation between neighbouring subgrains and thus LAGBs can transform to HAGBs. DDRX relies on bulging at deformed grain boundaries. The bulged parts form nuclei and grow by consuming the adjacent deformed grains. Both mechanisms can contribute to grain refinement. In this work, CDRX played an essential role in the microstructure evolution. As Figure 4.2 and Figure 4.5 indicate, misorientation across an entire grain was commonly observed and several well defined LAGBs were identified within the grain that was not fully recrystallised [107, 163-166], whilst features of DDRX including bulging brain boundaries and 'necklace structures' were not identified. The lower fractions of LAGBs and GOS < 2° in SS-FSC extruded AZ31B elucidates that the fraction of fully crystallised region, in other words, the progress of recrystallisation was lower in the SS-FSC extruded sample, compared with the as-received plate sample. This is because the heat source in SS-FSC only came from friction and deformation, instead of external heat input, and the small diameter (e.g. 2 mm) of the wire made the air cooling rate relatively high. The temperature dropped soon and the movement of dislocations was frozen, inhibiting further static recrystallisation (SRX) and maintaining subgrain structures formed in CDRX. There were also some large grains that had hardly deformed. These large, undeformed grains, incomplete recrystallised grains, and small fully recrystallised grains formed a heterogeneous structure. The mechanical stirring also changed the morphology and distribution of second phase particles. The approximately linear distribution of elongated second phase particles was transformed into a more homogenous distribution of rounder second phase particles throughout the whole wire.

It is unexpected that the yield strength was not improved. According to Hall-Petch relationship, the yield strength (YS) usually increases when the grain size decreases. However, no strengthening was detected in the SS-FSC extruded AZ31B wire with refined grains. This phenomenon, non-improved strength by refined grains, has also been reported by other researchers. A bimodal structural Mg-3Al-1Zn-0.4Mn alloy with an average grain size of 8.2 µm was developed by Zhang et al. [167], which has a slightly coarser grain structure than the 6.5 µm achieved here. The yield strength obtained from experiments was much lower than the calculated yield strength based on Hall-Petch relationship, as found here. Berbenni et al. [168] proposed that in materials with heterogeneous grain structures, Hall-Petch relationship based on the average grain size cannot provide an accurate prediction of yield strengths. Their analysis indicates that an increase in the dispersion of grain size results in a decrease in yield strength, which is believed to be associated with the internal stress and elastic stored energy between grains. Chen et al. [169] and Yuan et al. [170] suggests that the texture components also play an important role in the yield strength of Mg alloys. Textures with soft orientation for basal <a> slip to be activated usually results in a lower yield strength, which is the case in the SS-FSC extruded AZ31B wire, despite the refined grain structure compared with the as-asreceived material.

Nevertheless, the total elongation of SS-FSC extruded material was measured to be around 22%, significantly increased by about 58% compared with that of as-received plate. Such a good combination of strength and elongation (UTS 258±5 MPa and EI 22.3±0.8%) is not common for AZ31B Mg alloy. These properties are attributed to the fine grains with heterogeneous grain structure. An analysis of strain distribution in a Mg-3Al-1Zn-0.4Mn alloy with a similar grain size distribution was operated by Zhang et al. [171]. They observed a high work hardening in the alloy, which is believed to be associated with the grain size distribution. There was a significant micro-strain difference between large and small grains. Such a difference led to geometrically necessary dislocation (GND) pile-ups at the grain boundary, which played a key role in the high work hardening rate. In addition, Zhang et al. [172] also

observed a higher activity of non-basal slip systems with the increasing strain, contributing to ductility improvement. The weakened texture developed during the SS-FSC/CoreFlow® also contributes to the high elongation. The weakening of the texture provides a scattered grain orientation distribution, increasing the synergy of neighbouring grains with different orientation during the plastic deformation. In addition, the improved homogeneity of second phase particles, in terms of distribution, size, and shape, also aids the superior ductility. The refined and homogeneously distributed round particles can reduce the stress concentration and postpone the nucleation of cracks near the particle-matrix interface during tensile.

4.4 Conclusions

In summary, an AZ31B Mg alloy wire was successfully produced using SS-FSC (CoreFlow) in a single step at room temperature for the first time. The main findings are shown below:

- (1) SS-FSC extruded 2mm-wires from the rolled AZ31B plate with the combination of 100 mm/min and 1200 rpm. The extruded wire did not exhibit noticeable surface and internal defects.
- (2) SS-FSC produced finer grains in the extruded wires compared to the base material. The average grain size decreased from about 20-21 μm to around 6-7 μm. The grain refinement is attributed to the DRX during the process, and CDRX was found to be the major mode.
- (3) There was a weakened texture with gradient evolution from centre to edge and periodic needle-like regions with a distinctively different orientation from neighbouring regions around the edge area. These texture characteristics are assumed to be the result of different contributions from friction stir, extrusion, and seam welding along the TD during the process. Due to the contribution of each factor varied from the wire centre to the wire edge during the SS-FSC, the texture exhibited differences along the radius direction.
- (4) The UTS and El of the SS-FSC extruded sample reached 258 ± 5 MPa and 22.3 ± 0.8%, respectively. This means the SS-FSC increased the elongation of the AZ31B by nearly 60%

- without noticeable compromise of the strength, achieving a good combination of strength and ductility.
- (5) Such a good combination of strength and ductility for AZ31B Mg alloy is believed to be a result of several factors, including grain refinement with a heterogeneous grain size distribution, the weakened gradient texture, and homogeneously distributed second phase particles.

Chapter 5 Recycled WE43C Mg alloy wire production incorporating SPS and SS-FSC

5.1 Introduction

The production of Mg is energy intensive, ranking the second highest among the common metals. Besides, the traditional production methods inevitably produce large amount of waste during the machining. The significant environmental impact during the production can weaken the benefit of reduced weight and carbon emission of Mg alloy structures in use. As a result, the efficient use of material is an essential aspect of the current Mg industry.

In the previous chapter, the SS-FSC has been proved to be possible to continuously produce densified Mg-3Al-1Zn-0.2Mn (AZ31B) alloy wires. And the SS-FSC was further used together with spark plasma sintering (SPS) to achieve solid-state recycling of Mg-4Y-3RE (Elektron 43, WE43C) waste. The workflow of the major recycling procedure is shown in Figure. 5.1. Waste scraps produced from the machining process were first consolidated to an 80 mm diameter disk using SPS. Scraps were directly loaded into the SPS mould without any extra cleaning or pre-treatment. The applied electricity field during SPS generated heat and led to a quick rise in temperature. With the assistance of applied load, elevated temperature and vacuum condition, scraps were rapidly turned into a consolidated disk. This process produced much denser billets compared to the conventional cold or hot compaction. However, the SPSed disk still contained large pores and large second phase particles, which can be detrimental to mechanical properties, and thus further processing was applied to modify the microstructure of the SPSed disk.

After surface cleaning, the SPSed disk was further subjected to SS-FSC [88, 173-176]. A rotational tool was plunged into the SPSed disk and travelled along a certain direction. With the extraction of subsurface material, consolidated material got extruded from the exit hole and form wires. A T5 post heat treatment was also carried out for further investigation of the

effects of precipitation on the mechanical properties. The microstructure evolution and corresponding mechanical properties were thoroughly investigated to understand the effects of each recycling process. This work is expected to contribute to the circular economy of Mg industry and assist to achieve the NetZero goal [104, 109].

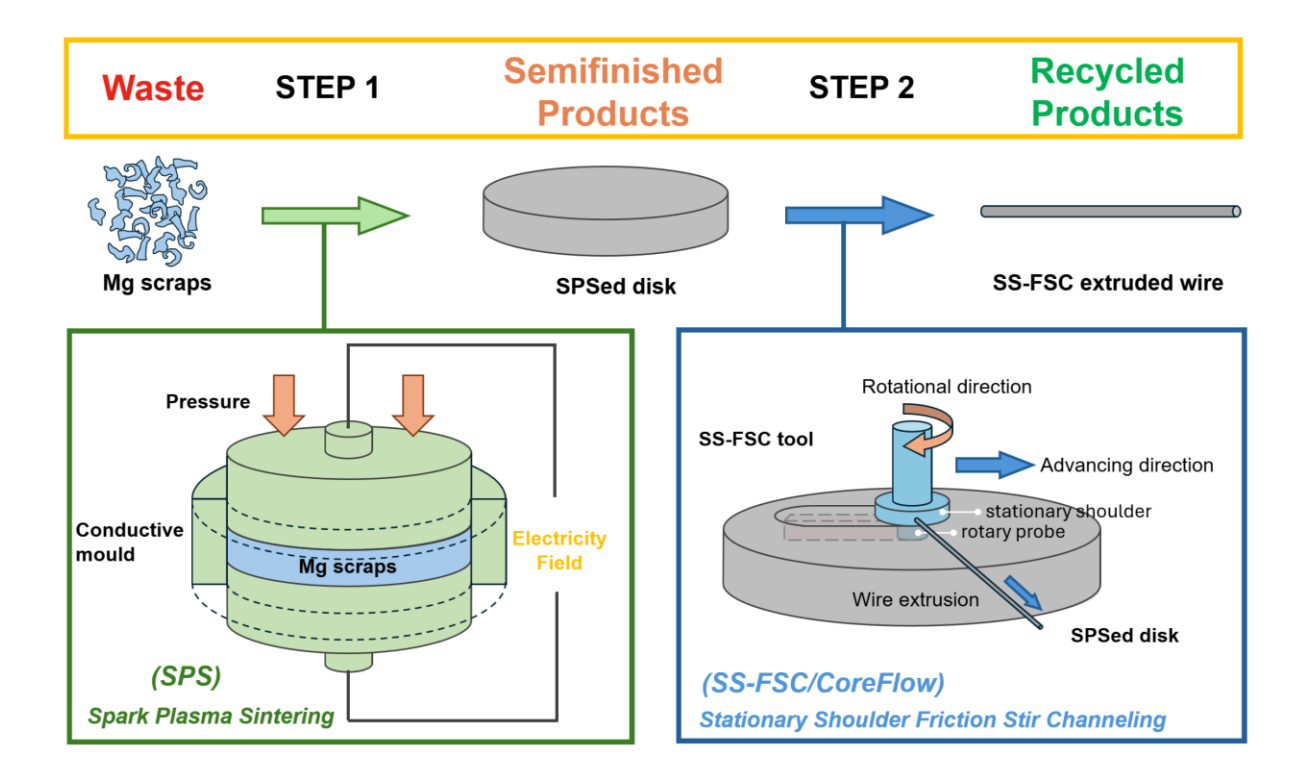


Figure 5.1 Schematic of the solid-state recycling method combining SPS and SS-FSC

5.2 Results

5.2.1 Microstructure and texture evolution

5.2.1.1 WE43C scrap

The SEM-BSE image, EDS maps, a line scan and a point scan of the scrap are shown in Figure 5.2. It is clear that there are evenly distributed coarse phases up with a size of tens of micrometres. These phases have well-defined lamellar structures and some eutectic phases are broken into several pieces. EDS maps indicate that these phases are mainly rich in rare earth (RE) elements of Nd and Gd, as well as some Y. Between the lamellas and around the outer layer of these eutectic phases, there are fine cuboidal phases which are

usually below 1 µm. EDS point scans suggest that these phases have a high concentration of Y, as listed in Table 5.1. Apart from bright second phase particles there are also brighter regions in the matrix. The EDS line scan indicate these regions have higher concentration of heavy elements including Y and Nd than the matrix exhibiting darker colour under BSE mode, as shown in Figure 5.2g. Further point scan of this phase is also summarised in Table 5.1. EBSD results are shown in Figure 5.3. IPF map and a representative line within a grain indicate that there are significant inner grain disorientation in the scrap. The band contrast map of the same site suggests that there are intense shear bands. In addition, the over layered special grain boundary map shows that there are several types of boundaries with specific orientations regarding $< 11\bar{2}0 >$ axis, including $< 11\bar{2}0 > 38^{\circ}, < 11\bar{2}0 > 56^{\circ},$ and $< 11\bar{2}0 > 86^{\circ},$ corresponding to the $\{10\overline{1}1\} - \{10\overline{1}2\}$ double twin boundary, $\{10\overline{1}1\}$ contraction twin boundary, and $\{10\overline{1}2\}$ extension twin boundary in Mg alloys [9]. Further neighbouring grain boundary disorientation distribution map also suggests that there is a high fraction of low angle grain boundaries (LAGBs) below 10°. A higher frequency of grain boundaries with disorientation angles around 38°, 56°, and 86° was also observed, matches the prominent occurrence of twin boundaries.

Table 5.1 EDS Chemical composition (weight %) for major second phase particle in the SPSed WE43C.

Element	Mg	Υ	Nd	Gd	Zr
Weight percent (wt%) in particle A	51.7	37.7	6.7	2.5	1.4
Weight percent (wt%) in particle B	57.8	11.3	29.1	1.7	0.1

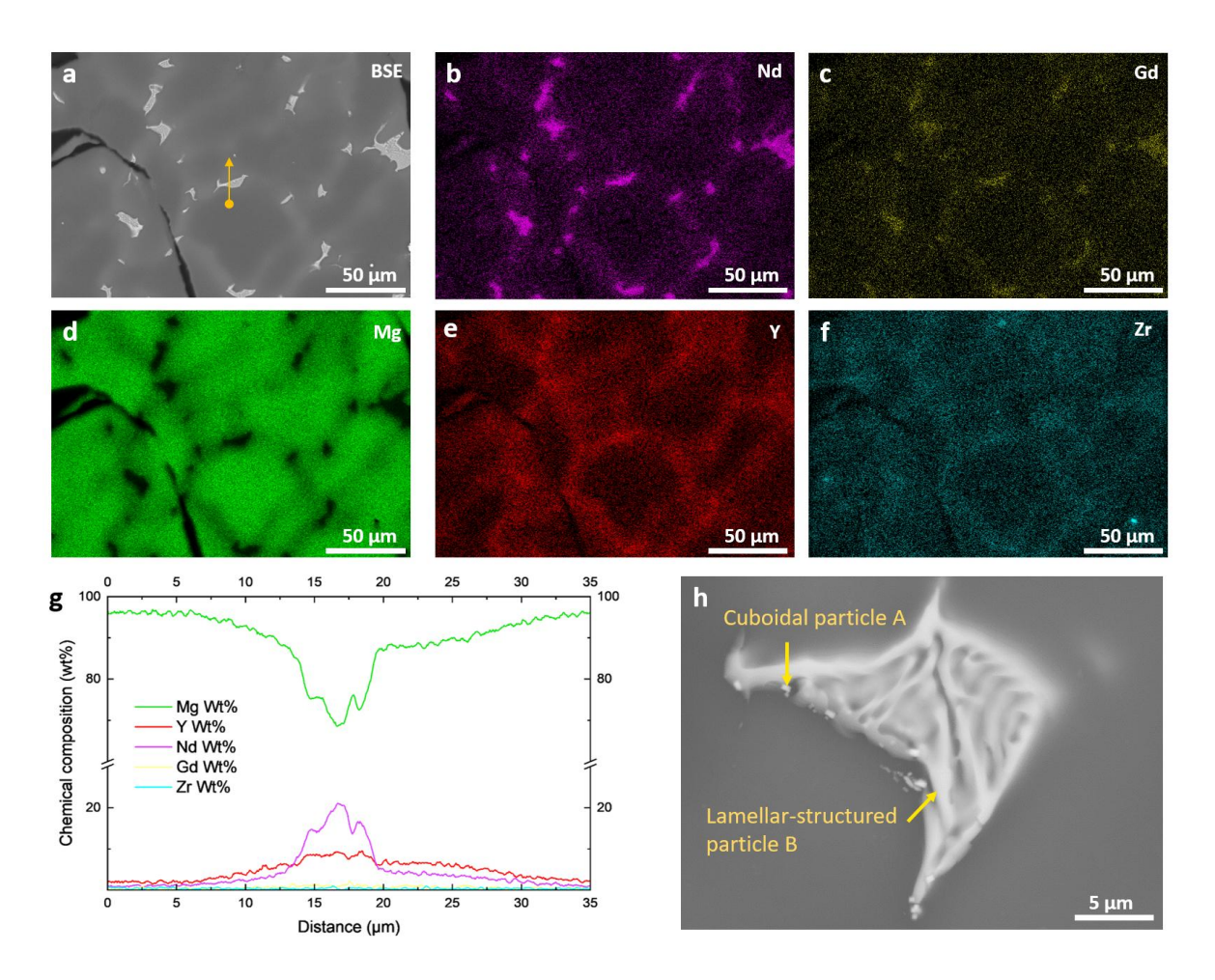


Figure 5.2 (a) BSE image of the scrap, (b-f) ESD maps of the scrap corresponding to the BSE image, (g) EDS line scan data from the site in the BSE image indicated by the arrow, (h) EDS point scan data of the cuboidal particle.

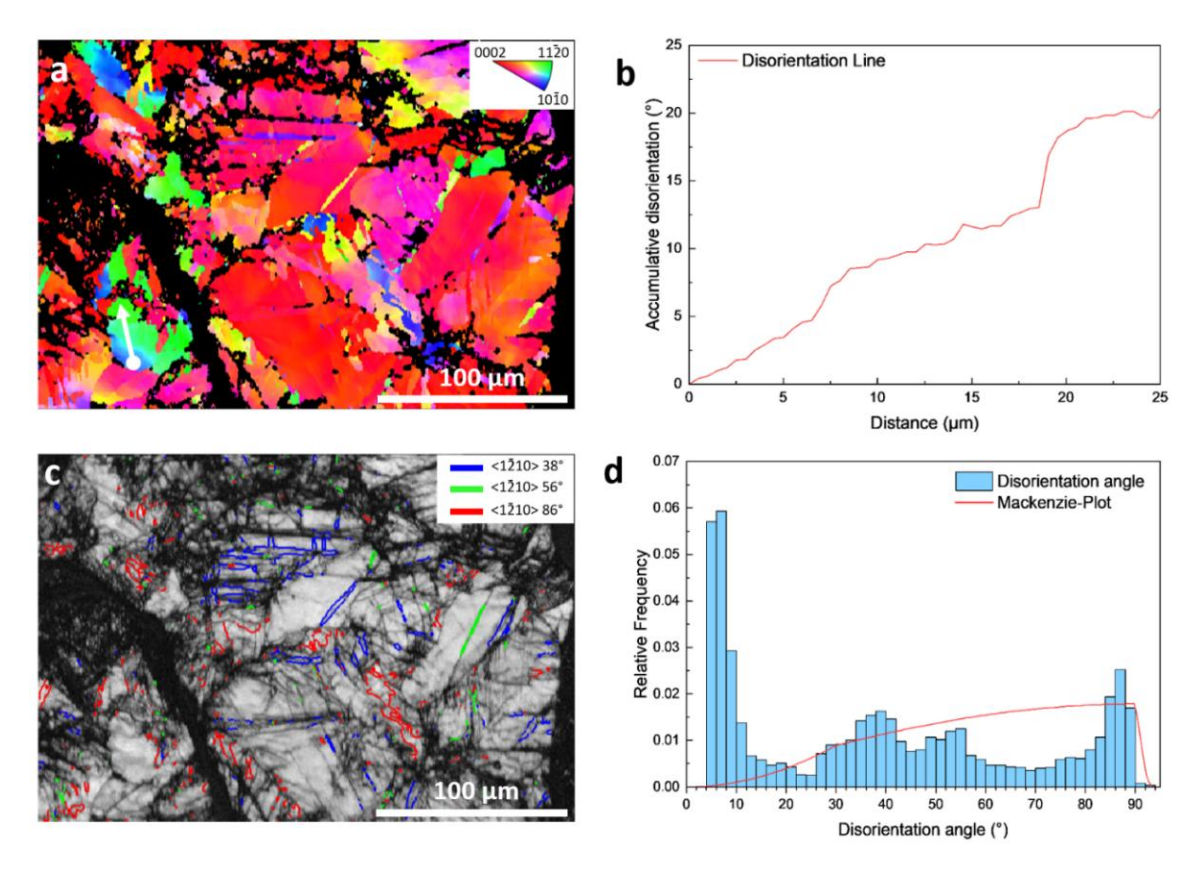


Figure 5.3 (a) EBSD IPF of the scrap, (b) The accumulative disorientation plot within in a grain, corresponding to the white arrow in the IPF map. (c). Band contrast map with an over layer of special grain boundaries, (d) relative frequency of grain boundary disorientation map.

5.2.1.2 SPSed WE43C disk

The SEM-BSE image, and the corresponding EDS maps of the SPSed material are shown in Figure 5.4. It is clear that the coarse eutectic phase rich in RE was maintained, though the size and fraction of these eutectic phase decreased after the SPS. The fine cuboidal phase rich in Y were also maintained, at the vicinity of the eutectic phase particles. Another type of second phase is the interconnected thin-layered structures rich in Y in the SPSed material, forming a network structure. These layered structures are likely to be the oxide layer, yet they are too thin to be resolved by SEM. Further S/TEM images and EDS line scan are shown in Figure 5.5. The STEM-HAADF image clearly shows the existence of the residual eutectic phase, cuboidal phase, and thin-layered phase. TEM bright field image reveals that the thin layer has a thickness around 200-300 nm and comprises many finer nanoparticles, instead of a continuous layer of a single crystal or semicontinuous second

phases along grain boundaries. An EDS line scan across the thin layer reveals the chemical composition of it. It is rich in Y, and O compared to the surrounding matrix. Furthermore, in the central part of the thin layer, there is also a sudden increase of Mg concentration and drop of Y concentration, indicating a finer structure of chemical composition difference along the thickness direction of the thin-layered structure.

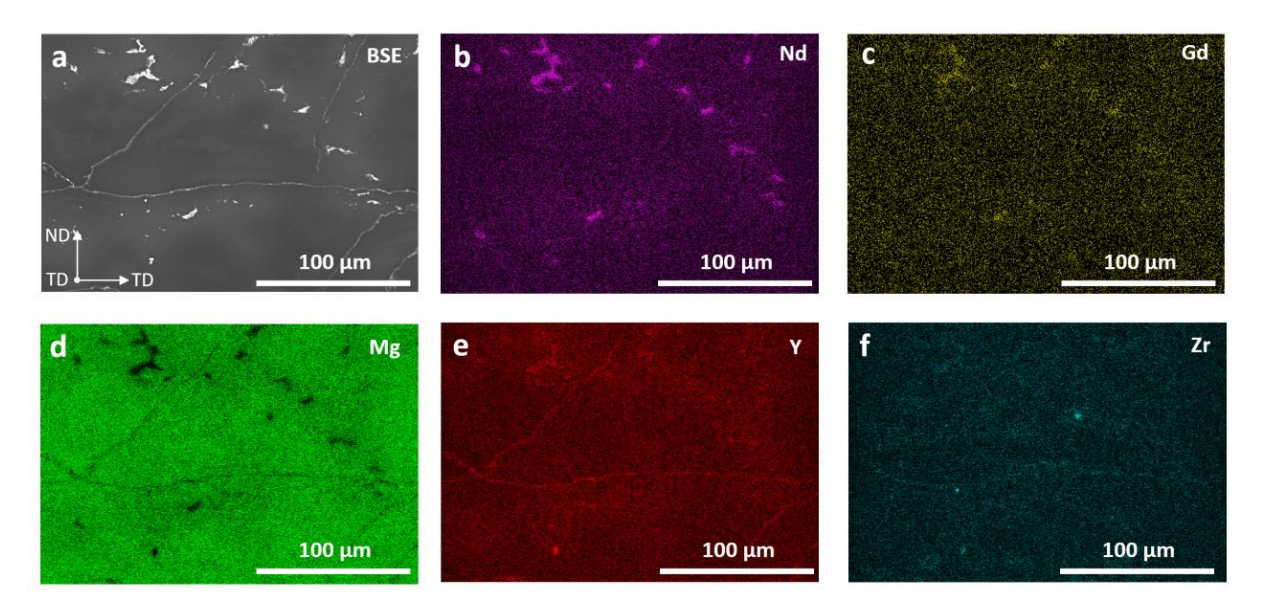


Figure 5.4 (a) SEM-BSE image of the SPSed disk, (b-f) ESD maps of the SPSed disk corresponding to the BSE image.

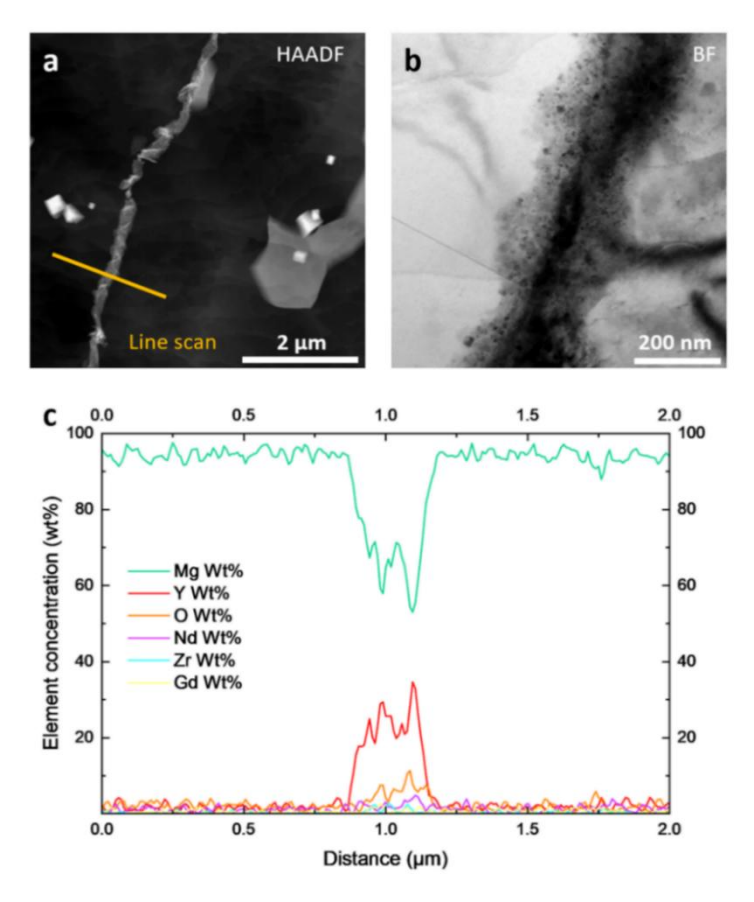


Figure 5.5 (a) STEM-HAADF image of the SPSed disk, (b) TEM-BF image of the thin-layered structure, (c) EDS line scan of the thin layered structure, at the site of the orange line in (a)

The 3D microstructural information of the SPSed sample is clearly revealed by the XCT scans, as shown in Figure 5.6. A cylindrical volume with a diameter of 5mm was extracted from the scan with a voxel size of 3.49 μ m (C1) and a cylindrical volume with a diameter of 1.2 mm was extracted from the scan with a voxel size of 1.35 μ m (C2) for further investigation. In addition to dense second phase particles, there are pores of significantly different sizes in the SPSed material. This was not clearly captured by the SEM images which is a 2D imaging method. The volume fraction of porosity $f_{pore-SPS}$ was calculated to be 1.8% based on C1. The average size of these pores was evaluated using the equivalent circle diameter EqD of the pore. $EqD_{pore-SPS}$ was calculated to be 154.0 μ m. The size of these pores is smaller along the z-axis, which is the loading axis during the SPS process, making the pores have a flake-like shape. The average length of these pores $L_{pore-SPS}$ was measured to be 490.9 μ m, whilst the average thickness $T_{pore-SPS}$ was measured to be 98.5 μ m. In addition, some of the pores

in the SPSed disk were extremely large. About 20% of the pores exhibited a length of over 1mm. The volume fraction of the second phases $f_{2nd\ phase-SPS}$ was calculated to be 3.1% and the average size $EqD_{2nd\ phase-SPS}$ was calculated to be 13.9 µm, based on C2. The average length of these second phases $L_{2nd\ phase-SPS}$ was measured to be 29.7 µm. It needs to be noted that as most of the thin layered second phases and the cuboidal phases had a thickness of less than 1 µm, and thus cannot be well resolved by the XCT scans. The fraction of second phases can be considered as the fraction of the eutectic phase. And the shape of the eutectic phase is far away from a sphere. This makes the value of the $L_{2nd\ phase-SPS}$ instead of the $EqD_{2nd\ phase-SPS}$ looks more consistent with the size of second phases in the SEM images.

The EBSD IPF map, corresponding pole figure and SEM-BSE image of the SPSed sample are shown in Figure 5.7. After the SPS, equiaxed grains with an average grain size of 12.9±9.7 µm were obtained. The fraction of grains with GOS<2° was measured to be 93.4%. These indicate that the SPSed microstructure is nearly fully recrystallised. A random texture was obtained after the SPS, with a maximum multiples of uniform density (MUD) value of 4.4. In addition, in some regions in the SPSed material, one side of grain boundaries of a string of grains looks continuous and smooth, as shown in Figure 5.7a. And such a distribution matches the distribution of the thin layered second phases, as shown in Figure 5.7d.

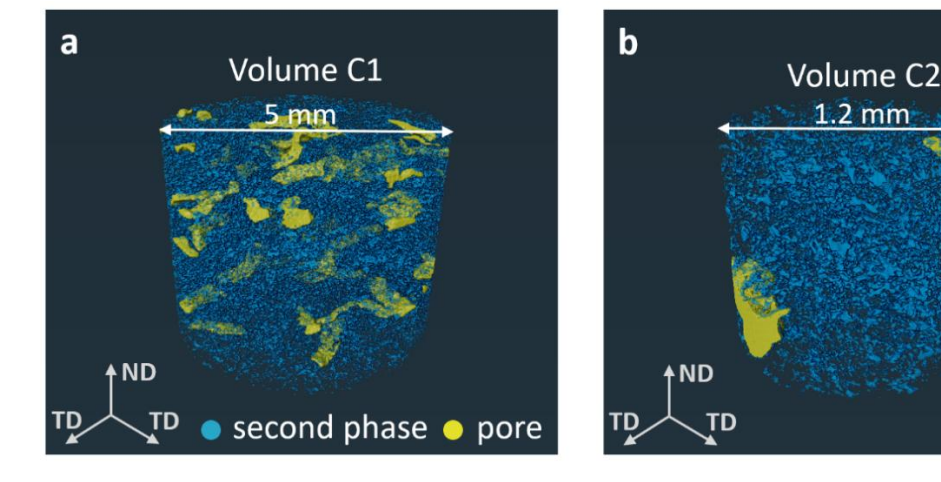


Figure 5.6 3D view of second phases and pores in the SPSed disk (a) 5mm-diameter cylindrical volume (C1), (b) 1.2mm-diameter cylindrical volume (C2)

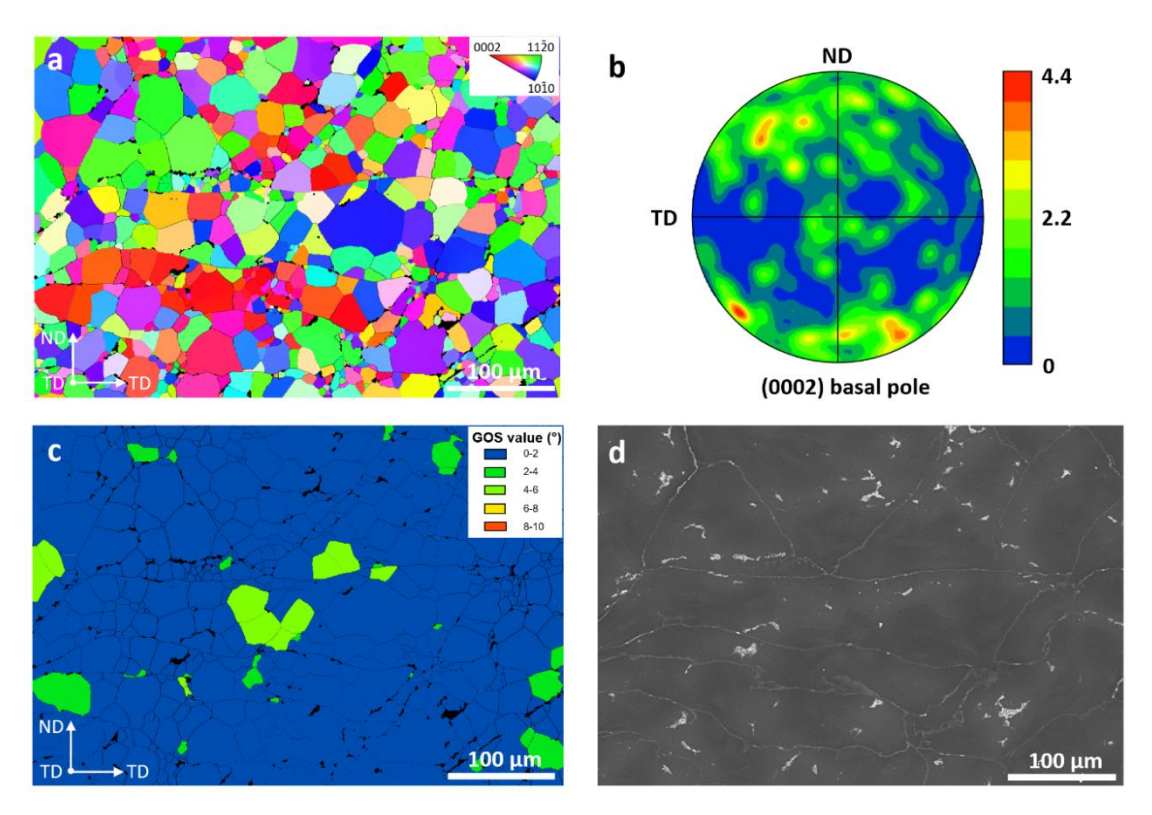


Figure 5.7 (a) IPF map of the SPSed disk, (b) Pole figure, (c) GOS map of the SPSed disk, (d) the BSE image of the EBSD region

5.2.1.3 SS-FSC extruded WE43C wire

The SEM-BSE images of SS-FSC extruded WE43 is shown in Figure 5.8. The overview of the SEM-BSE image of the ND-TD1 plane suggests a uniform distribution of second phase particles from the wire edge to the wire centre. It also reveals the difference between the material flow behaviour as there are distinctive oriented material flow from the wire edge to the wire centre. In other words, the material flow behaviour is dependent on the distance of the material from the wall of the exit hole or the central line of the wire. The flow lines at the edge of the wire tend to get aligned parallel to the ED, whilst when it is moving toward the centre of the wire, the flow lines tend to get aligned parallel to the TD1. And such orientation change of the flow line is not linear to the distance from the wire edge to the wire centre. There is a abrupt shift of flow line angles adjacent the edge part, whilst such change is less significant around the centre part of the wire. When comparing the SEM-BSE images of the wire edge and wire centre part, it is evident that the grains are slightly elongated along

the flow line direction and the second phase particles are also distributed in a same way. Except for a few larger particles around 1 μ m, there are dense nanoparticles distributed across the region, generally uniformly yet with a minor tendency at the grain boundaries.

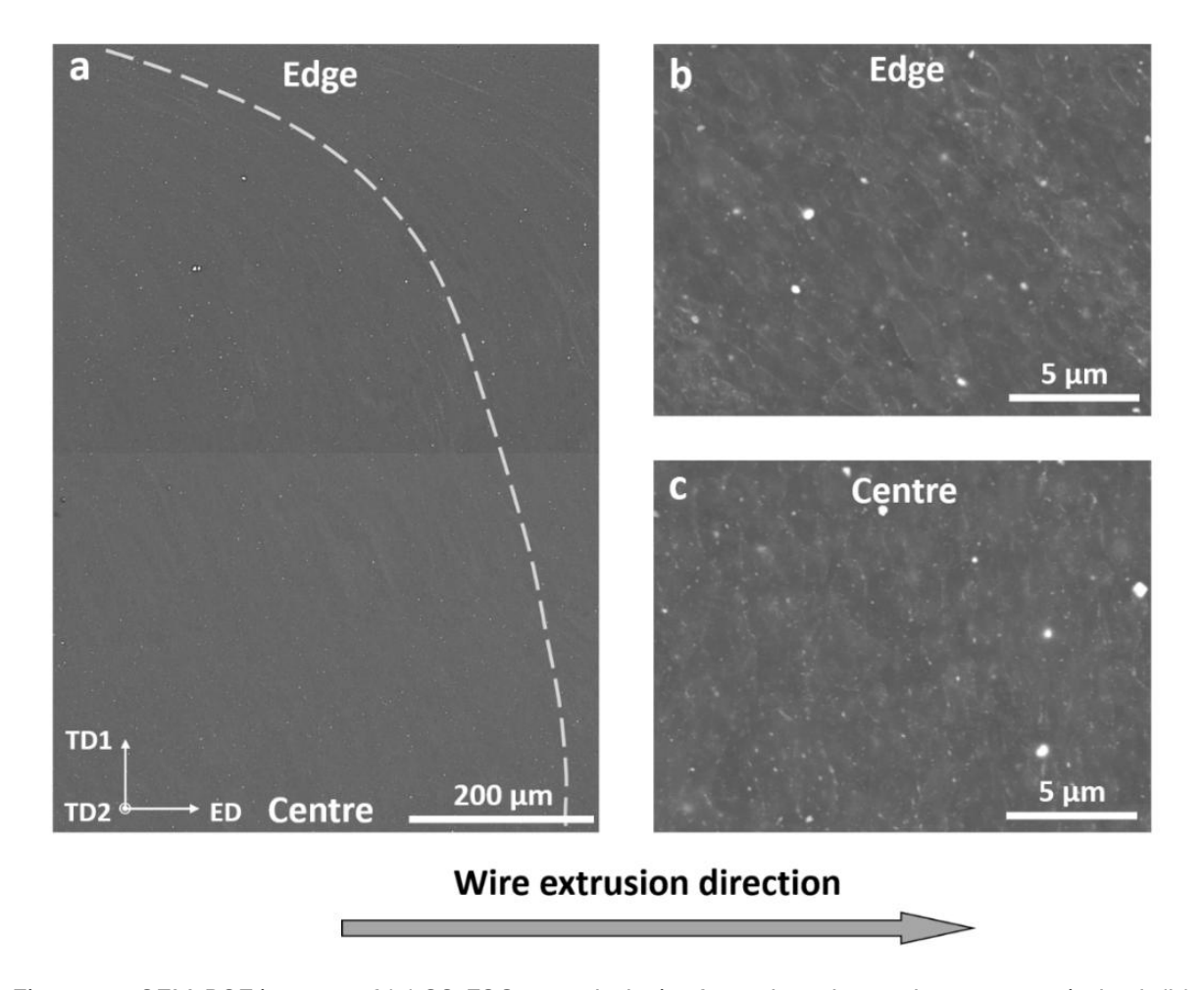


Figure 5.8 SEM-BSE images of (a) SS-FSC extruded wire from the edge to the centre, stitched, (b) wire edge, (c) wire centre.

The XCT scan result of SS-FSC extruded WE43C is shown in Figure 5.9. An 2D slice of TD1-TD2 plane indicates that the SS-FSC extruded wire exhibited an ideal circular cross-section. No large second phase particles can be identified from the 2D slice, which matches the result of SEM-BSE image. Since the size of the second phase particles is mainly below 1 μ m and the voxel size of the XCT scan was 1.35 μ m, most of the second phase particles cannot be well resolved. Only a few coarse second phase particles were clearly captured by the XCT scan. Around the edge of the wire, a low density region of dark colour can be

observed and this matches the feature of pores. Further 3D view of the SS-FSC extruded wire is shown in Figure 5.9b. Several flake-like pores were identified to be distributed around the edge part of the wire. The volume fraction of the pores in the SS-FSC extruded wire $f_{pore-wire}$ was calculated to be less than 0.1%, which is nearly one order of magnitude smaller than that in the SPSed disk. The average size evaluated by equivalent diameter $EqD_{pore-SSFSC}$ was calculated to be 10.1 μ m, which is also about one order of magnitude smaller than the $EqD_{pore-SPS}$ of 154.0 μ m in the SPSed disk. The size of these pores is smaller along the radius direction (TD) but larger along the ED, making the pores have a flake-like shape. The average length of these pores $L_{pore-SSFSC}$ was measured to be 24.6 μ m, whilst the average thickness $T_{pore-SSFSC}$ was measured to be 8.8 μ m. The summary of the pore measurement is shown in Figure 5.10.

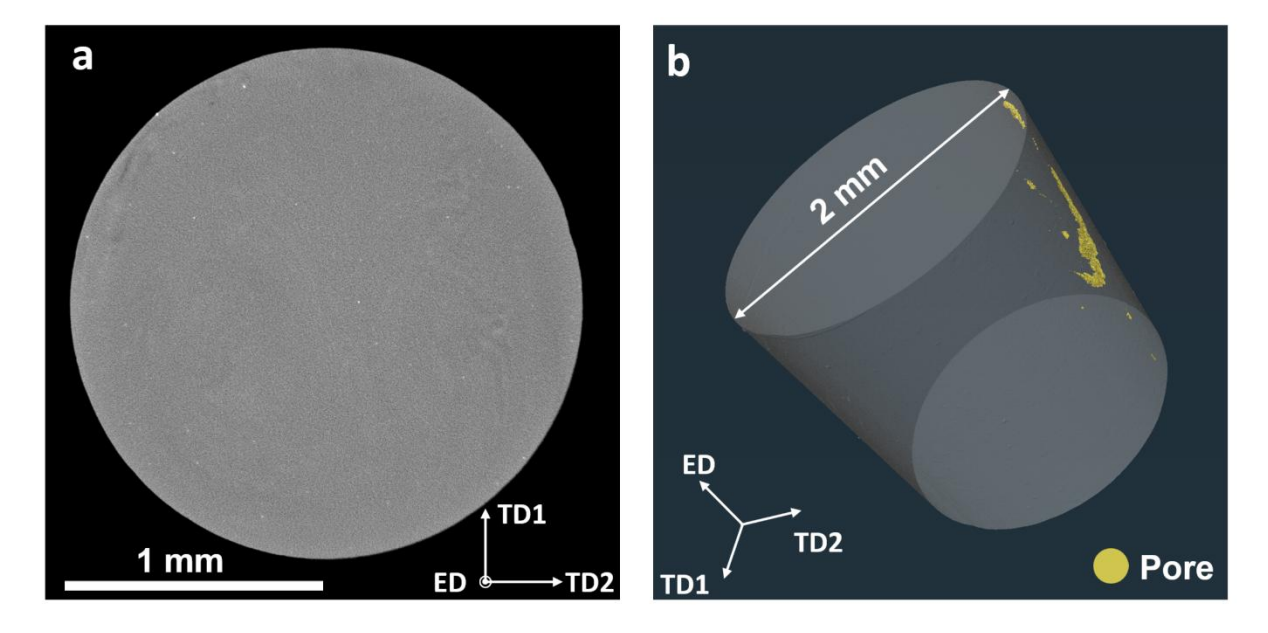


Figure 5.9 (a) A representative XCT 2d slice of the TD1-TD2 plane, (b) 3D view of the pore in the SS-FSC extruded wire.

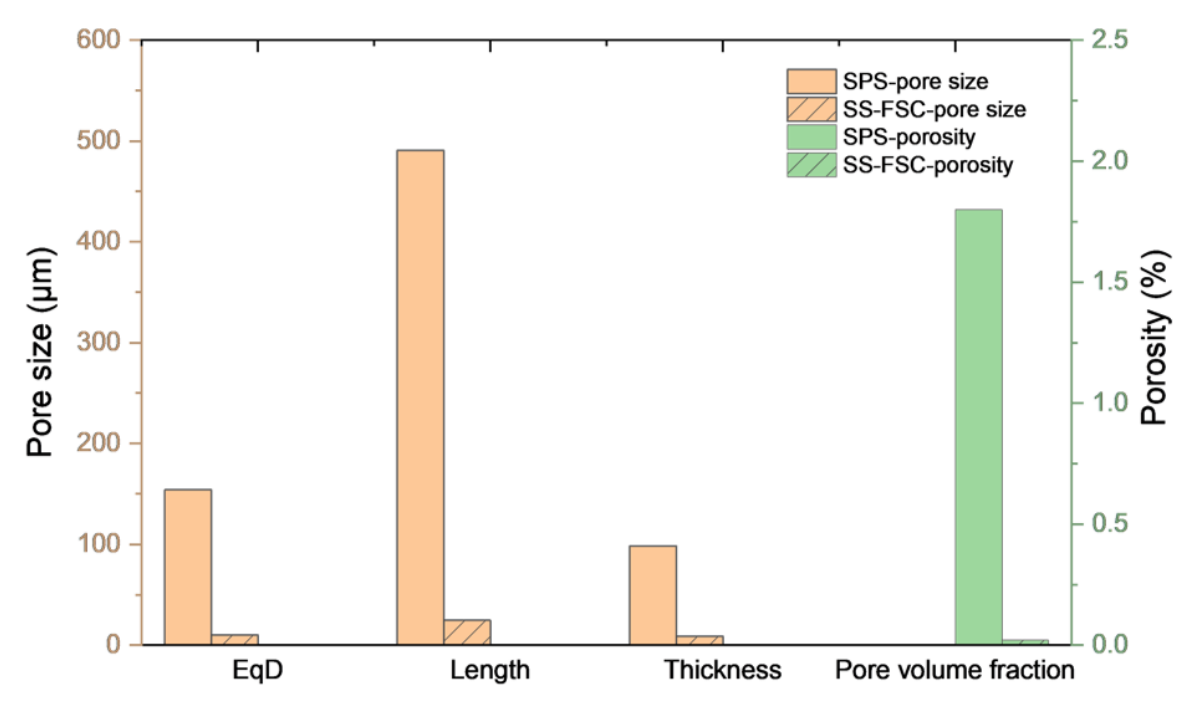


Figure 5.10 The comparison regarding pores in the SPSed and SS-FSC extruded material

The EBSD-IPF map and GOS map covering the wire edge to the wire centre and the corresponding pole figure are shown in Figure 5.11. There was an obvious gradient structure along the TD1 in the SS-FSC extruded WE43C. At the edge of the wire, grains with blue and green colours are dominant, which means the $<10\overline{1}0>$ and $<11\overline{2}0>$ direction of the grains tend to align with the ED. In other words, the (0001) basal planes are mainly aligned parallel to the ED. When it comes to the centre of the wire, grains with red colour are dominant, which means the <0001> direction of the grains tends to align with the ED. This also produced a widespread and weakened basal texture, as shown in the pole figure. The overall (0001) basal pole is relatively scattered and exhibits about 45° against the ED. The GOS map of the same site also reveals that there was a GOS value difference in grains from the wire edge the wire centre.

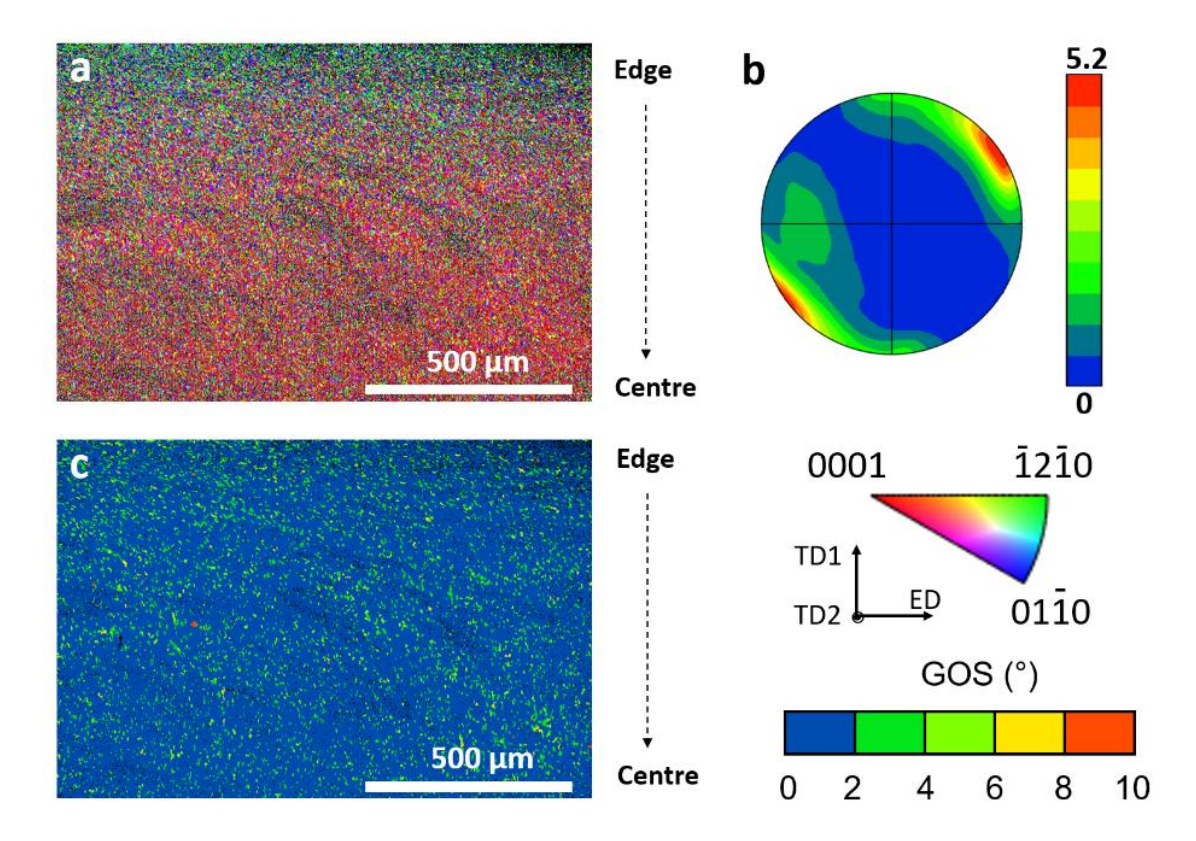


Figure 5.11 (a) EBSD IPF map, IPF//ED (b) pole figure (c) GOS map of the SS-FSC extruded WE43C wire.

To systematically investigate the grain structure and texture across the TD from the edge to the centre, 5 regions from the wire edge to the centre was further scanned for detailed analysis, as shown in Figure 5.11. The regions from the wire edge to the centre are divided into R1-R5. The measured average grain size of R1-R5 from the EBSD-IPF map are 2.6±1.2 μm, 2.5±1.1 μm, 2.4±1.1 μm, 2.3±1.0 μm, and 2.0±0.8 μm. The average grain size in the SS-FSC extruded WE43C wire is much finer than that in the SPSed disk, and there is a minor grain size decrease from R1-R5 which is from the wire edge to the centre. The fraction of grains with GOS values below 2° in R1-R5 was calculated. The values from R1-R5 are 81%, 88%, 90%, 91%, and 93%. Except R1 which shows a slightly lower value, there is little difference between R2-R5 regarding the fraction of grains with GOS values below 2°. Further pole figures reveal the texture orientation and intensity of R1-R5. Regarding the orientation, there is a gradual shift of (0001) basal pole from TD1 to ED. The maximum MUD values of the basal texture in R1-R5 are 7.5, 7.2, 8.1, 8.0, and 5.3.

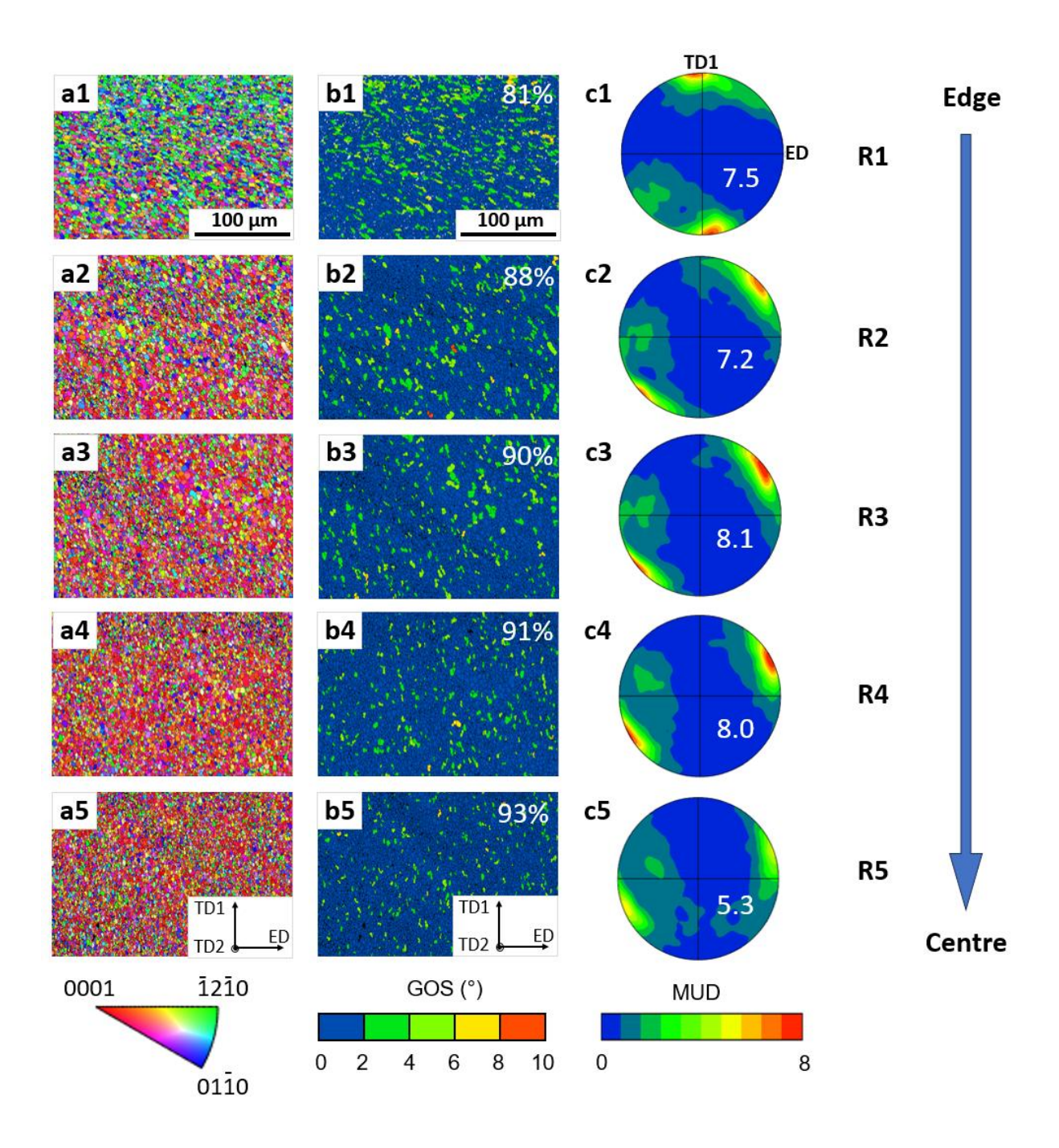


Figure 5.12 (a1-a5) EBSD-IPF maps of R1-R5, IPF//ED, (b1-b5) GOS maps of R1-R5, (c1-c5) Pole figures of R1-R5

5.2.2 Mechanical properties

5.2.2.1 Microhardness tests

Considering the possible variation of hardness values due to the gradient microstructure and texture, Vickers micro hardness tests of the SS-FSC extruded wire were

done at three different parts. The Vickers microhardness values HV0.2 from the wire centre to the wire edge are 83.8±1.2, 81.9±2.9, 85.8±2.3, as shown in Figure 5.13. Although there was a gradient structure regarding the recrystallisation level and texture orientation along the TD1, the hardness test results did not show any statistically meaningful difference. The following T5 heat treatment further increased the hardness of the material. At the ageing time at 200°C for around 30 h, the hardness of the wire reached the highest value of 94.7±1.9 HV, as shown in Figure 5.14. The Vickers hardness value of the SPSed material, SS-FSC extruded wire and peak-aged SS-FSC extruded wire at 200°C are shown in Figure 5.15. Compared to the SPSed disk, the hardness of SS-FSC extruded wire increased by 10.7 HV, and further ageing increased the hardness by 11.4 HV. T6 treatment was not carried out and there are two main reasons. First, in the non-treated SS-FSC extruded WE43C wire, few second phases were observed. The microstructure is close to the super saturated solid solution condition, and thus the solid solution treatment is believed to have limited effects. Second, a fine grain structure around 2.0 – 2.6 μm and further solid solution treatment (SST) may cause significant grain growth, weakening the grain boundary strengthening.

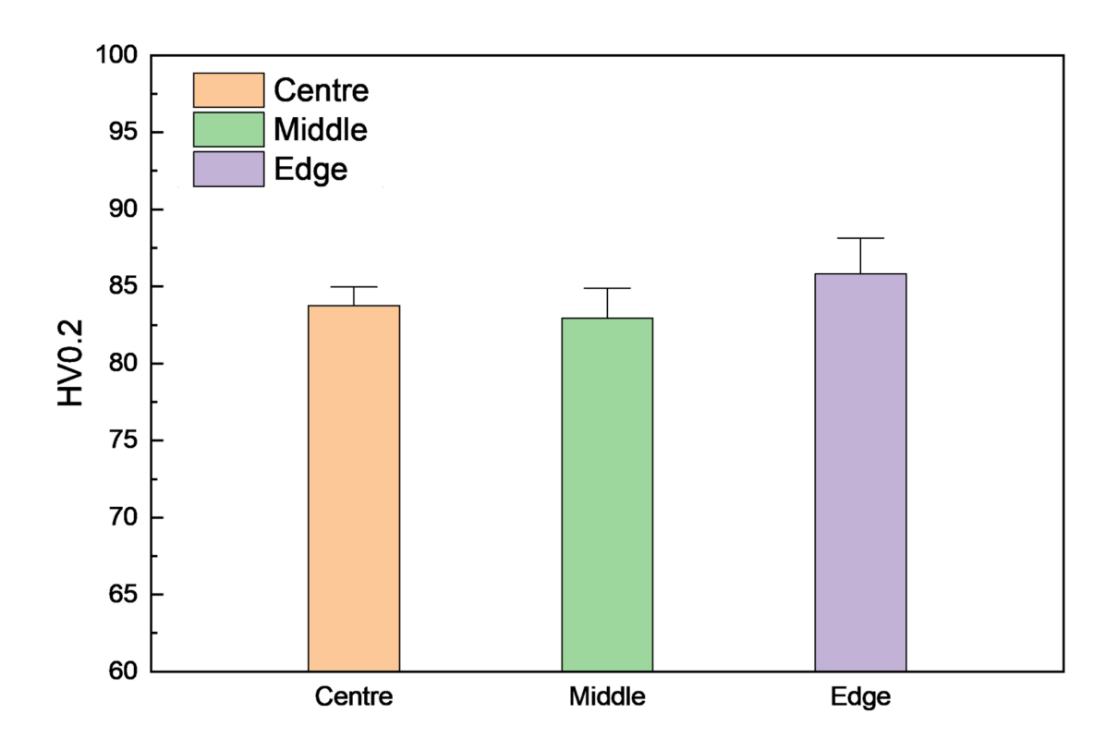


Figure 5.13 Vickers microhardness values of the SS-FSC extruded wire at 3 different sites

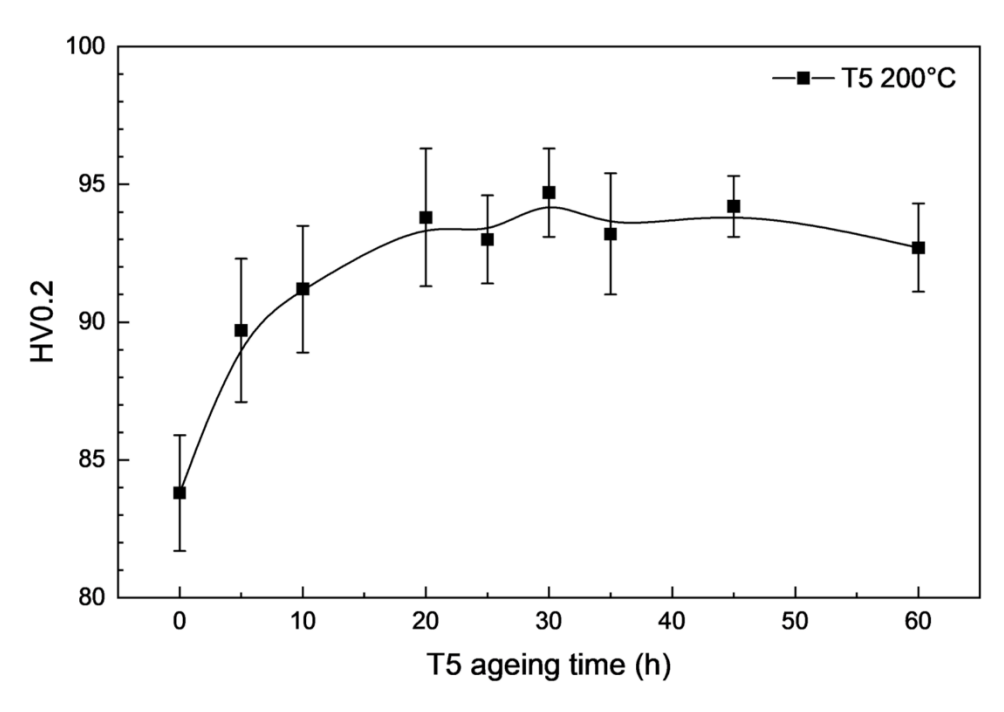


Figure 5.14 Vickers microhardness evolution during the T5 heat treatment at 200 °C

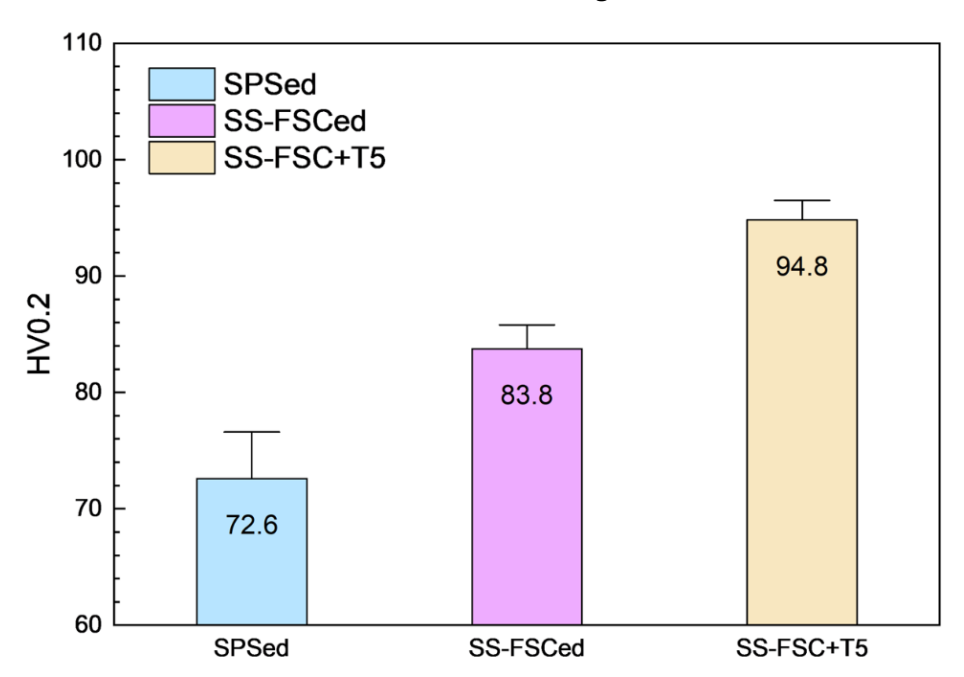


Figure 5.15 Hardness values of SPSed, SS-FSCed, and SS-FSC+T5 treated sample

5.2.2.2 Tensile tests and fractography

The summary of the tensile test results is listed below in Table 5.2. The YS and UTS were increased by ~39 MPa and ~28 MPa by carrying out further T5 heat treatment at 200°C for around 30 h, respectively. Meanwhile, the EI of the material only slightly decreased from

~13.4% to ~11.7%. Stress-strain curves of two types of samples are shown in Figure 5.16. Fractured surfaces of the specimens were scanned using SEM and the images are shown in Figure 5.17. Combining the stress-strain curves and the fractured surface SEM images, necking occurred in the SS-FSC extruded sample, whilst in the sample subjected to further T5, necking was insignificant. Despite the difference in the necking behaviour, both samples exhibited similar fractured surface structure dominated by dimples with tear ridges. SEM-BSE images show that there were denser precipitates on the fractured surface in the T5 treated sample.

Table 5.2 YS, UTS, and El of SS-FSC and SS-FSC + T5 treated WE43C

Specimen	Yield strength (MPa)	Ultimate tensile strength (MPa)	Elongation (%)
SS-FSC	211.5±8.8	289.7±6.5	13.4±2.9
SS-FSC + T5	250.6±23.6	317.5±6.8	11.7±0.4

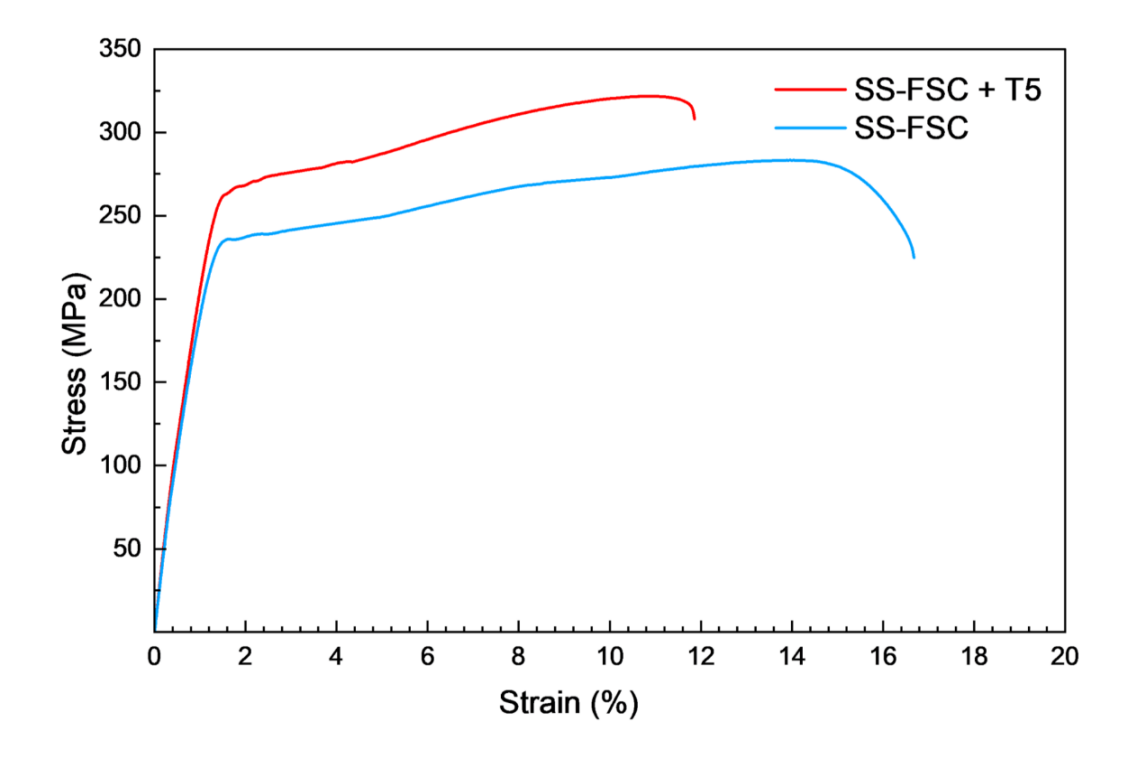


Figure 5.16 Stress strain curves of SS-FSC recycled WE43C sample and SS-FSC +T5 sample

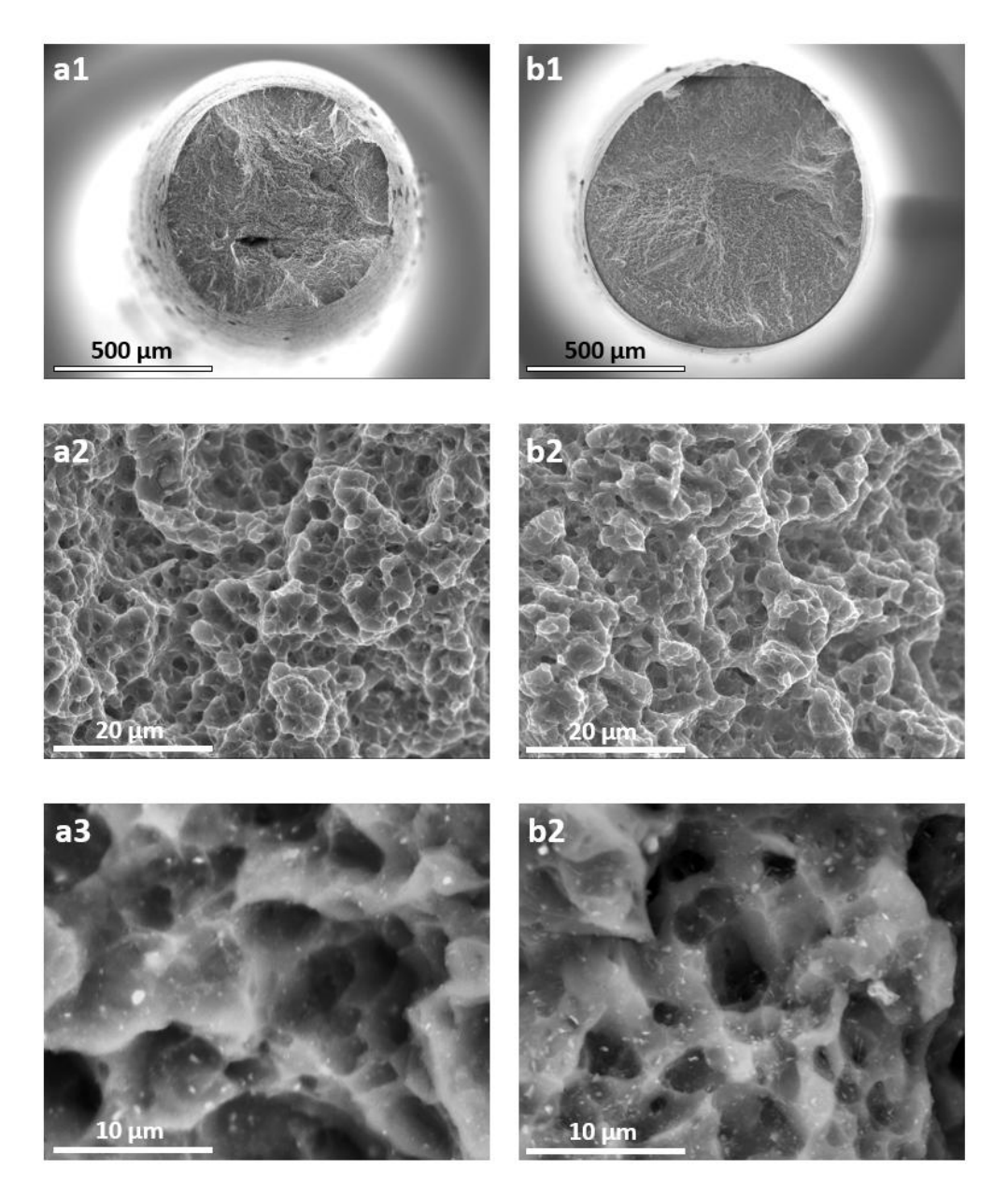


Figure 5.17 (a1-a3) SEM-SE image of the entire fractured surface, magnified fractured surface, and BSE image in the SS-FSCed sample, (b1-b3) SEM-SE image of the entire fractured surface, magnified fractured surface, and BSE image in the SS-FSC+T5 treatment sample.

5.3 Discussion

5.3.1 Evolution of microstructure and texture

5.3.1.1 WE43C scrap and SPSed disk

The significant change of the microstructure during the recycling process is attributed to the combination of deformation and high temperature during the recycling process. In the

waste scraps, large second phase particles were found rich in rare earth elements Nd and Gd, as well as a minor increase of Y. This matches the reported chemical composition of the eutectic phase β-Mg₁₄Nd₂Y in the Mg-Y-RE alloy system, partly substituted by Gd [23, 45, 177, 178], indicating these are eutectic phase from the original cast material. Adjacent to or between the lamellas of these eutectic phases, there were sub-micron scale cuboidal particles rich in Y. There are two major possibilities of the cuboidal Y-rich particles. The first one is YH₂. YH₂ has been reported to be one of the common inclusions in Mg-Y and Mg-Y-RE alloys [48]. It has been reported that it can form during the casting stage at elevated temperatures [179]. The other possibility is Mg₂₄Y₅, which is a stable phase in Mg-Y system and can form in the Mg-Y-RE via the decomposition of β-Mg₁₄Nd₂Y phase [45, 178]. Considering these cuboidal phases are mainly around the eutectic phases, they are more likely to be Mg₂₄Y₅. Broken eutectic phase particles, shear bands, twins and inner grain disorientation indicate the scraps were subjected to large deformation during the machining. Alloying elements such as Y and Nd tend to segregate at grain boundaries and heavily deformed zones, when comparing the EDS maps in Figure 5.2 and EBSD maps in Figure 5.3, to reduce the system energy [47, 180, 181].

After SPS, the eutectic phase was maintained, verified by the EDS scans and the shape from the SEM-BSE image. Yet the fraction and size both decreased, which can be easily found by comparing the SEM-BSE images of scraps in Figure 5.2, and the SPSed sample in Figure 5.4. This is because the high temperature during the sintering process promotes the dissolution of eutectic phases. It was reported by Milkereit et al. [162] that 510 °C is enough to dissolve almost all the second phases in the equilibrium state. And 525 °C has been widely used for the solid-solution treatment for Mg-4Y-3RE alloys [41, 49, 182, 183]. Since the material was held at 500 °C for 10 min, the dissolution of eutectic phases occurred but only partly dissolved. Whilst the Mg₂₄Y₅ phase was reported to be stable at this temperature, and thus maintained after the SPS. The oxide film formation can be attributed to two parts. First, the oxide film formed on the original WE43C scrap surface. Second, although

a vacuum condition was applied during the SPS, there was still adsorbed oxygen on the scrap surface and trapped air between scraps as sources of oxygen. The oxide formation in SPSed Mg-Y-RE has been widely reported [69, 73, 115]. The oxidation of Mg alloys is a complex process and significantly affected by the temperature and alloying elements. It is reported that at lower temperatures and under ambient conditions, the major products of oxidation of the pure Mg may contain MgO, Mg(OH)₂, and MgCO₃ [114, 184, 185]. The addition of reactive elements such as RE will lead to a preferred reaction between oxygen and reactive elements, from the perspective of thermodynamics [184]. However, considering the kinetics, it was reported that the initial oxidation stage of Mg-Y-RE alloying firstly involves the formation of MgO, and then with the further diffusion, reactive element oxides such as Y₂O₃ and Nd₂O₃ form together with MgO beneath the outer layer [185, 186]. This explains the higher concentration of Mg in the central part of the oxide layer in Figure 5.5. The central layer of the structure is where the outer layer of two scraps meet, and the MgO is expected to be the dominant oxidation product. Whilst the two sides of the layer structure are at deeper positions during oxidation process, and the reactive element oxide Y₂O₃ which has the lowest formation enthalpy becomes more [187]. Via the combination of high temperature and applied pressure, metallurgical bonding can be achieved. The oxide film formation in the powder based product of Mg-Y-RE material has also been reported by other researchers [46, 72, 115]. Although a vacuum condition was applied, the irregular shapes of the scraps led to looser compaction compared to powder materials, leaving disk-like pores in the SPSed disk. The XCT data indicates that the minimum length of the pores was basically aligned along the ND, which was the loading axis during the SPS. This matches the condition in SPS as a thickness reduction along the ND was observed, whilst the size long the radial direction was confined by the mould. The high temperature during the SPS also triggered a rapid recrystallisation in the deformed state. Interestingly, the formed oxide film on the scrap surface effectively impeded the migration of grain boundaries, leading to grain boundaries aligned with the oxide layer. In other words, any recrystallised grains could not grow beyond the original scrap regime. The random

texture in the SPSed disk is attributed to the random orientation of scraps when the waste scraps were loaded into the mould, instead of real randomised nucleation or grain growth during the SPS.

5.3.1.2 SS-FSC extruded WE43C wire

Compared to the microstructure in the SPSed WE43C disk, the second phases in the SS-FSC extruded wire are much finer. The coarse eutectic β -Mg₁₄Nd₂Y phase and oxide films can no longer be seen in the SS-FSC extruded wire. The refinement can be attributed to the effects of both mechanical stirring and elevated temperature during the SS-FSC process. The significant large total strain caused by the mechanical stirring can break large second phase particles into smaller pieces, which fragmented the eutectic phase particles and oxide films. In addition, the friction stir heat can raise up the temperature, leading to the dissolution of the eutectic phase β -Mg₁₄Nd₂Y into α -Mg matrix. As for the oxide film in the SPSed disk, no dissolution of oxide particles is expected to occur considering the high stability of oxides [188-190]. The fragmentation and redistribution by carrying out the SS-FSC lead to an emerging homogeneous distribution of refined particles.

Significant grain refinement was also achieved by the SS-FSC process. Compared to the average grain size in the SS-FSC extruded AZ31B which exhibited a final average grain size of around 6-7 µm, the grain refinement in the SS-FSC extruded WE43C was more significant. Such efficient grain refinement can be attributed to several factors. Compared to the SS-FSC parameters of AZ31B, the rotational speed of the tool was same but the traverse speed for SPSed WE43C was only 50% of that for the AZ31B plate. This is because the resistance of WE43C against the tool higher is than that of AZ31B, and thus the decrease of traverse speed is essential to avoid the failure of the probe. By reducing the traverse speed, there is expected to be an equivalent strain rate but an increase in the processing temperature for the SS-FSC of WE43C. The increased temperature can further allow the completeness of CDRX. The grains with GOS values below 2° reached 87%, which is much higher than that in

the SS-FSC extruded AZ31B of around 35%. This indicates the level of recrystallisation in the SS-FSC extruded WE43 is higher. The higher temperature during the processing of WE43C ensures the continuous movement of dislocations to the site of LAGBs and increases the disorientation between neighbouring LAGBs, transforming from LAGBs to HAGBs. This process turns grains composed of several subgrains into several grains, and thus produces finer DRXed grains. However, once the DRX finishes, the elevated temperature can also lead to further grain growth of the recrystallised grains. The SEM-BSE images show that the SS-FSC process produced uniformly distributed fine second-phase particles and oxide particles, which can act as obstacles for grain boundary migration. The strong pinning effects against grain boundaries was observed in the SPSed material. This is also referred to as Zener pinning [191].

There was also a gradient structure in the SS-FSC extruded WE43C wire from the centre to the edge, especially the recrystallisation and texture variation. Although there is a descending trend of the average grain size from R1-R5 (i.e. from the wire edge to the wire centre), the difference is negligible considering the total difference is only about 0.6 µm. Despite the gradient texture from R1-R5, the texture orientations are different from those in the SS-FSC extruded AZ31B wire. R1 exhibited a basal texture with the basal poles aligned around the north pole toward the TD1. This means the R1, which is the edge of the wire, has a texture resembling those in traditional extruded bars [5, 14, 55, 121]. In extruded Mg alloys, due to the intense interaction between the surface material and the mould wall, basal planes tend to align parallel to the mould inner surface [5, 14]. Whilst R2-R5 exhibited basal poles spread on the great circle from TD1 to ED. There is a sharp change of basal poles orientations from R1-R2, which is measured to be around 45°. From R2-R5, the basal poles only gently rotated further toward the ED for about 30°. The basal pole orientation rotation is a result of the synergy of rotational effects around the ED axis by the rotational probe and the pressure by extrusion along the ED. Such shift of the material deformation behaviour is also reflected by the GOS maps. The recrystallisation fraction of the material increased from the wire edge

to the wire centre, especially from R1-R2. From R2-R5, there was only an increase of 5%, whilst from R1-R2, there was an increase of 7%. The more significant change in the recrystallisation fraction is believed to be closely related to the strong interaction between the outer layer material of the wire and the surface of the mould of the exit hole[192]. A larger resistance was created at the edge part of the wire due to the interaction between the extruded material and the wall of the exit hole, whilst the small size of the cross section and the solid state process potentially led to a relatively homogeneous temperature distribution along the radial direction. Besides, after being extruded out, the contact of the outer layer with the air also can supress the following static recrystallisation process. These factors lead to the lower recrystallisation level of the R1, compared to other inner regions. Although a gradient texture in the SS-FSC extruded WE43C wire was observed, the orientation is different from that in the SS-FSC extruded AZ31B. This is believed to be the result of the difference in the traverse speed of the processing. The tool traverse speed of the WE43C was only half of that used for AZ31B. This leads to a difference in the material flow due to the variation in the combination of helical movement and linear movement along the ED. The interaction between the material and the channel mould was stronger in the extrusion of WE43C and thus the normal direction of (0001) planes in the SS-FSCed WE43C was nearly perpendicular to the ED.

It is apparent that the relative density of the material was significantly increased by carrying out the SS-FSC. The volume fraction of pores was successfully decreased from about 1.8 % to below 0.1%. Besides, the average size of the pores was also significantly reduced from 154.0 µm to 10.1 µm. This means the shearing and compression during the SS-FSC contribute to the pore closure. Despite the effective densification of the SS-FSC process, there were still some pores mainly distributed adjacent to the surface of the probe. This is believed to be a result of the different modes of material flow along the radial direction discussed previously. The outer layer R1 was strongly affected by the exit hole and the material flow is predominantly along the ED, whilst the material at R2 is less affected by the wall of the exhibit hole but more affected by the rotation during the SS-FSC, exhibiting a helical material flow

mode. The abrupt shift of material flow behaviour at the vicinity of the wire edge, with the presence of pre-existing large pores, leads to the formation of residual flake-like pores at the junction region between R1 and R2. In other words, the pore closure effects by SS-FSC are weakened in the region between R1 and R2 due to the change of material flow behaviour.

5.3.2 Effects of post heat treatment and mechanical properties

Compared to the SPSed material, the hardness was apparently improved after the SS-FSC extrusion, which mainly benefits from the grain refinement during the processing. The solid solution strengthening by dissolving eutectic phases and densification by pore closure are two other factors for the hardness increment. The following ageing treatment further increased the hardness by producing fine metastable precipitates. In addition, the closure of pores can also contribute to the hardness increase. The tensile test results indicate the T5 treatment increased both the yield strength (YS) and the ultimate tensile strength (UTS). It has been reported that the major precipitation at the peak ageing contributing to the strengthening in the Mg-Y-RE alloys is the plate-like β_1 phase [43, 44, 162, 193]. These plate like β_1 phase formed on $\{10\overline{1}0\}$ planes can act as strong obstacles against the basal $\langle a \rangle$ slip and thus increase the strength. It can be especially essential in the SS-FSC extruded wire here, considering the texture effect during the tensile tests. As mentioned in the precious section, except the outer layer (i.e. R1) of the wire, the inner parts, especially R2-R4 regions, had their basal pole aligned around 45° against the ED. The ED is the loading direction during the tensile tests and also a softer direction for basal <a> slip to be activated due to the high Schmid factor [9]. The presence of precipitates increase the stresses needed for basal $\langle a \rangle$ slip to be activated and thus increases the strength of the material. In addition, the fragmented and redistributed oxide particles are also believed to contribute to the strength improvement. Although there is lack of the direct observation of the interaction between oxides and dislocations, the effectiveness of oxide particles has been observed in other alloy systems

such as steel [194, 195], Al alloy [196], etc. Meanwhile, the weakened gradient basal texture with the soft orientation under tension ensures the ductility during the tests.

The strengths and elongations plot of the SS-FSC recycled material and other prime products is shown in Figure 5.18. It is apparent that the wrought Mg-4Y-3RE alloys represented by yellow labels, including rolling and extrusion, have the best strength-ductility combination. Alloys produced by additively manufacturing (AM) and casting exhibit slightly lower strengths and ductility compared to wrought alloys. For the SS-FSC recycled secondary material, the strength-ductility combination is apparently better than the cast and AMed counterparts. It is within in top right part of the regime of wrought products, indicating WE43C wire recycled by incorporating SPS and SS-FSC has equivalent mechanical properties as the wrought products. These mechanical property variations are attributed to the microstructure features, especially the grain size and precipitation. The cast alloys exhibited the coarsest grains among these products due to the solidification process, and compared to AMed materials using LPBF, LDED and WAAM, the cooling rate is also lower [136]. Materials prepared by AM methods exhibited a heterogeneous or bimodal grain structure [131, 197]. Within the regime of the melting pool during the deposition, there is cooling rate difference from the edge to the centre of the melting pool. This often produces columnar grains at the inner part of the melting pool and fine equiaxed grains around the melting pool edge, which is often referred to as columnar to equiaxed transition (CET) [131, 132]. In wrought alloys, fine equiaxed grains were commonly observed due to the refinement of grains by DRX. Coarse grains mean little contribution by the grain boundary strengthening and weaker synergy between grains during the plastic deformation, leading to a lower strength and ductility in the cast material. Due to the combination effects of the grain refinement, gradient texture with specific orientation, precipitates by ageing, and fragmented oxide particles, the SS-FSC extruded WE43C exhibited a good combination of strength and ductility. This is a promising result for the solid-state recycling method incorporating SPS and SS-FSC. It indicates the

potential of using waste scraps generated during the production to fabricate secondary products with equivalent performance.

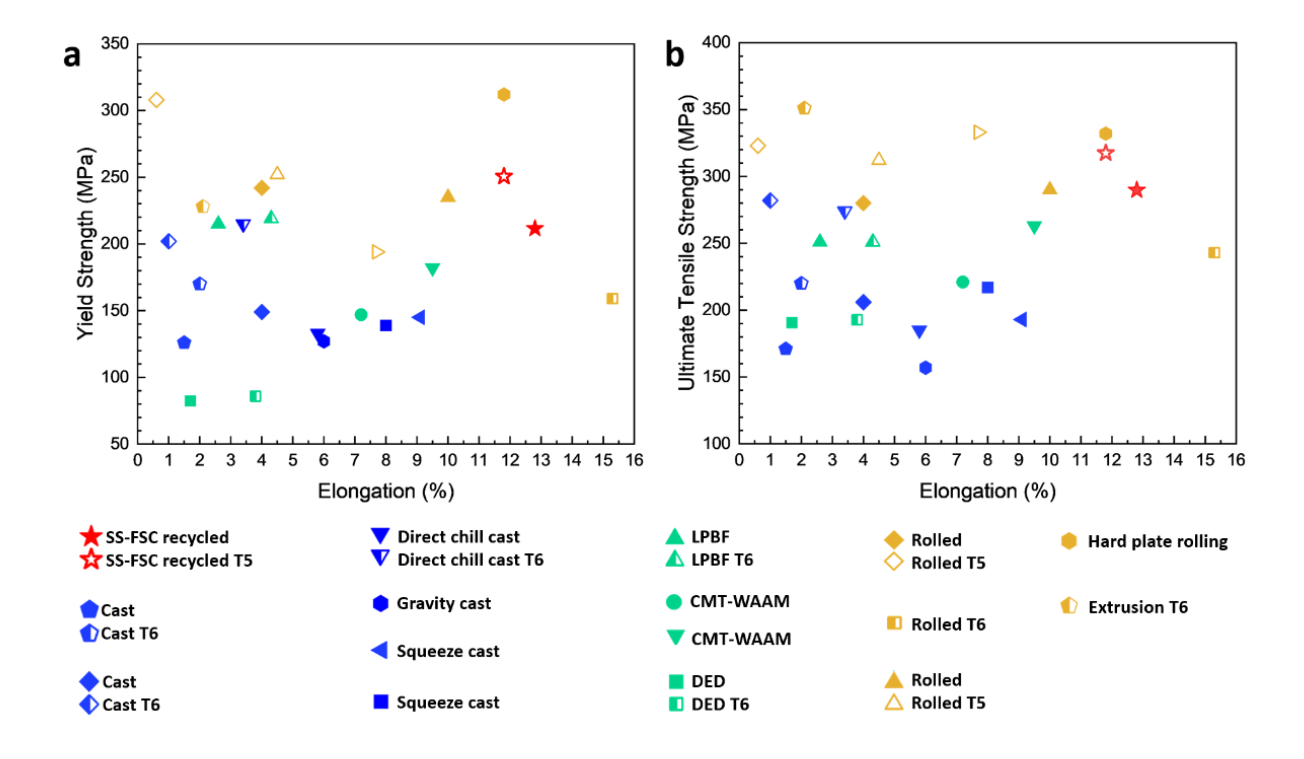


Figure 5.18 Scattered point plot of mechanical properties of WE43C alloys prepared by various methods and the SS-FSC recycled material (a) yield strength-elongation plot and (b) ultimate tensile strength-elongation plot. [39, 43, 45, 86, 129, 135, 178, 198-203]

5.4 Conclusions

In this part of work, spark plasma sintering (SPS) and stationary friction stir channelling (SS-FSC)/CoreFlow were used to achieve the solid-state recycling of WE43C Mg alloys, turning waste scraps into consolidated wires. The main findings are shown below:

(1) In the waste scraps, coarse fragmented eutectic phase composed of Mg, Y, and Nd was the dominant second phase. Scraps had a heavily deformed microstructure featuring large inner grain disorientation, prominent twins, and shear bands.

- (2) After SPS, scraps were consolidated to a disk. Eutectic phases partially dissolved into the matrix under the elevated temperature during SPS. Oxide films with a thickness around 200-300 μm formed between scraps. These oxide layers were mainly composed of MgO and Y₂O₃ nanoparticles. Although a relative density of 98.2% was achieved, the average size of the pore reached 154.0 μm. A recrystallised structure of coarse equiaxed grains with an average grain size of 12.9±9.7 μm formed.
- (3) The following SS-FSC produced densified wires from the SPSed disk. The porosity decreased to below 0.1% and the average size of pore was reduced to 10.1 μm. Grains were refined to about 2.0-2.6 μm. A gradient basal texture with the <0001> rotated from TD toward ED from the wire edge to the wire centre was produced. Pre-existing eutectic phases nearly fully dissolved into the matrix, and oxide films were fragmented to small pieces and homogeneously re-distributed.
- (4) The YS, UTS and El of the SS-FSC extruded wire were 211.5±8.8 MPa, 289.7±6.5 MPa, and 13.4±2.9%, respectively. Further ageing treatment at 200° for 30 h led to increases in YS and UTS to 250.6±23.6 MPa, 317.5±6.8 MPa. The El was slightly reduced to 11.8±0.4%. The recycled samples showed a good combination of strength and ductility equivalent to wrought products. This is the results of several factors including the grain refinement, gradient texture with specific orientation, precipitates by ageing, and fragmented oxide particles.

Chapter 6 Recycled WE43C disk preparation incorporating SPS and FSP

6.1 Introduction

In the previous chapter, the microstructure and texture evolution from the waste WE43C scraps to the SPSed disk and the SS-FSC extruded (SS-FSC extruded) wire were systematically investigated. The effectiveness of grain refinement, second phase particle refinement, oxide film fragmentation and dispersion has been proven to be achieved by the SS-FSC. And these enabled recycled products to have nearly equivalent mechanical properties as the commercial extrudate. Despite the success of the application of SPS and SS-FSC in Mg scrap recycling, the SS-FSC technique can only produce wires with limited diameters and cannot fulfil the need for the production of disks or plates. To achieve the production of larger samples such as disks and plates, the work of FSP on SPSed disks was done. An overlap strategy of FSP was used to process the SPSed disk. The entire process is shown in Figure 6.1. The microstructure evolution and corresponding mechanical properties were thoroughly investigated to understand the effects of FSP.

Part of this work has been published on:

X. Zhao, Y. Xie, J. Gandra, M. Murphy, W. M. Rainforth, and D. Guan, "A Succinct Method to Recycle WE43 Mg Alloys—From Wasted Chips to Consolidated Billets," in *TMS Annual Meeting & Exhibition*, 2024: Springer, pp. 151-153.

TEM data was collected by staff from the Sorby Centre at the University of Sheffield and Kaiple Electron Microscope Centre. XCT data was collected by staff from μ -VIS at University of Southampton.

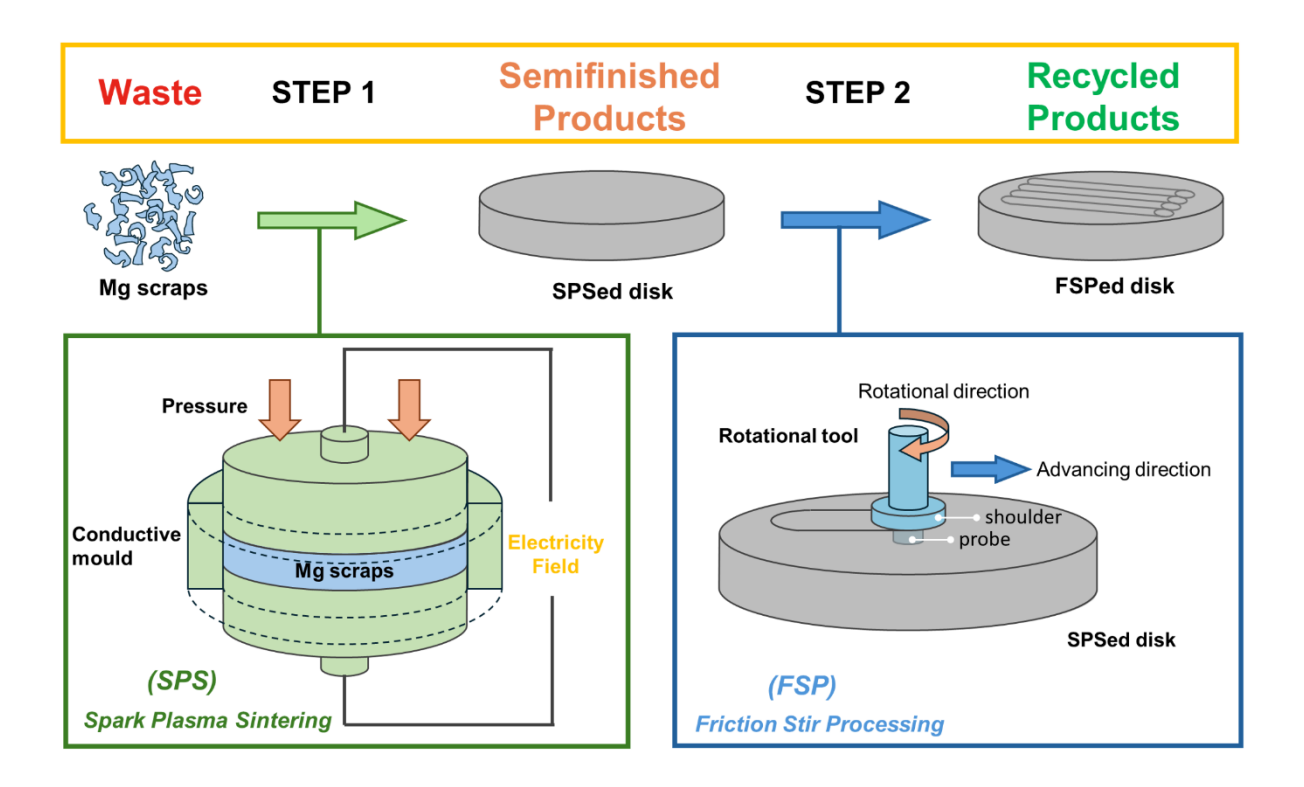


Figure 6.1 Schematic of the solid-state recycling method combining SPS and FSP

6.2 Results

6.2.1 Microstructure and texture evolution from scraps to FSPed disk

6.2.1.1 WE43C scrap and SPSed disk

The microstructure and texture of the scrap and SPSed disk can be found in Chapter 5.

6.2.1.2 FSPed WE43C disk

The microstructure of the material after FSP was significantly different from the SPSed sample, as shown in Figure 6.2. There are two typical regions in the FSPed WE43. The first one is the homogeneous region, where the grains have similar sizes and fine second phase particles are evenly distributed both at grain boundaries and within grains. The second one is the heterogeneous region, where narrow band regions with finer grains and much denser second phases are observed, making these regions look like 'fuzzy'. Adjacent to the 'fuzzy' regions, there are also some darker regions identified as residual pores. The oxide film can

no longer be seen in the FSPed material. Instead, they were broken, agglomerated and redistributed during the FSP, as shown in Figure 6.3. The second phase particles with irregular shape around 1 μ m was identified to a have higher concentration of Y, O compared to the surrounding matrix.

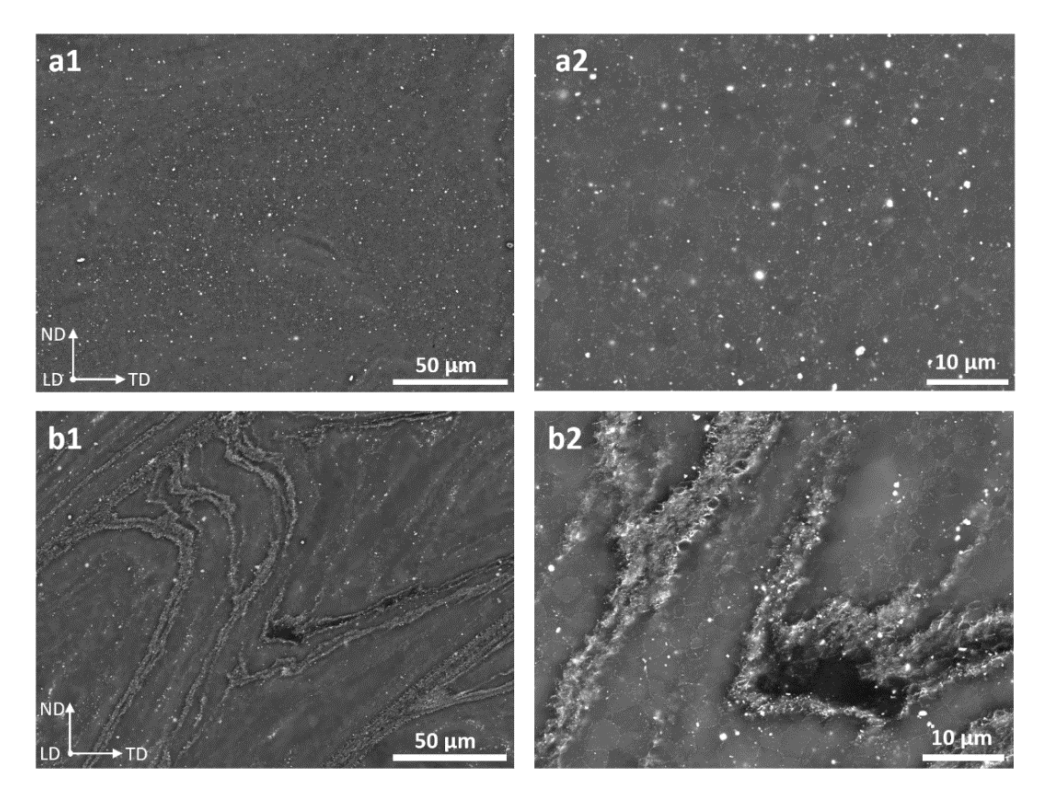


Figure 6.2 (a1-a2) regions with homogeneous microstructure, (b1-b2) regions with heterogeneous microstructure, 'fuzzy' regions with finer grains and denser second phases, together with a pore.

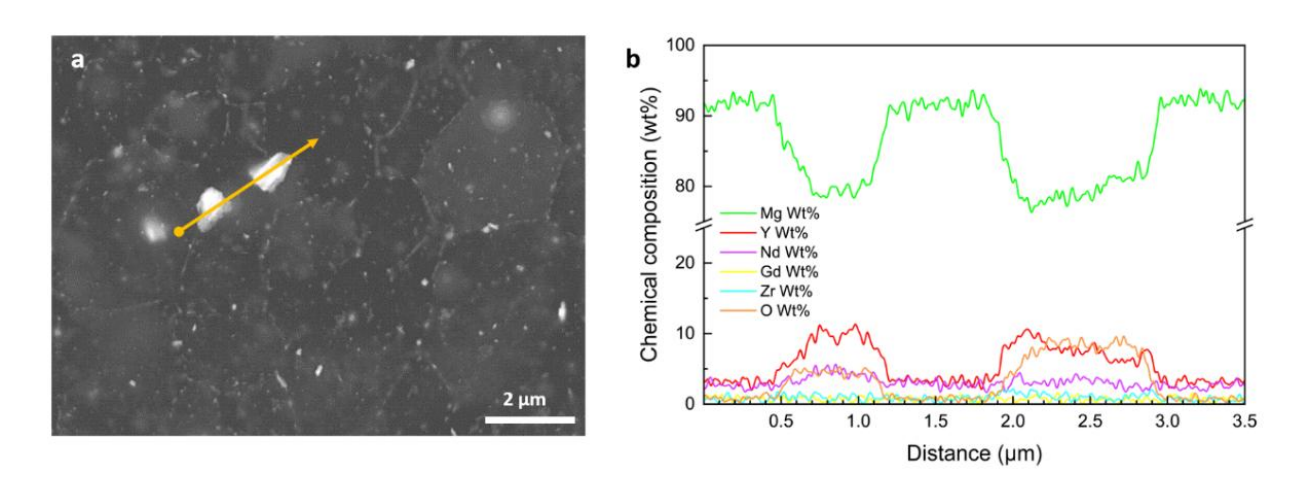


Figure 6.3 (a) SEM-BSE image of oxide particles in the FSPed disk, (b) EDS line scan data

Further XCT scans reveal the distribution and morphology of second phases and pores, as shown in Figure 6.4. A cylindrical volume with a diameter of 5mm was extracted from the scan with a voxel size of 3.49 µm (C3) and a cylindrical volume with a diameter of 1.2 mm was extracted from the scan with a voxel size of 1.35 µm (C4) for further investigation. It needs to be noted that based on the SEM images of the FSPed sample, most of the second phases in the FSPed disk were too small to be well resolved by the XCT scan, and they also tend to aligned together, which lead the XCT scan to identify these as a large elongated particle. And thus the fraction and size of second phases in C3 and C4 are not calculated. However, it is still helpful to use the 3D view of C3 and C4 to understand the distribution of the second phase particles. The comparison regarding the pores between the SPSed sample and FSPed sample is shown in Figure 6.5. The volume fraction of porosity after FSP $f_{pore'}$ was measured to be about 0.8%, decreased by about 56% compared to that of the SPSed material. The average size of these pores in after FSP $EqD_{pore'}$ was measured to be 35.7 μ m, decreased by 77% compared to that of the SPSed material. Elongated and curved pores are well aligned along the PD of the FSP. The pores also have a flake shape but the thickness direction is not along the z-axis which is the loading axis for the previous SPS stage. The average length and thickness of pores were calculated to be 143.7 µm and 25.4 µm, respectively. Although there were still a few pores with a length over 1mm, they only accounted for 2.3% of all the pores. It is apparent that both the volume fraction and size of the pores decreased after the FSP process. Besides, there was a completed porosity-free zone around the boundary of two tracks, as shown in Figure 6.4a. Regions of intense second phase particles are also distributed in the same way, adjacent to the curved pores.

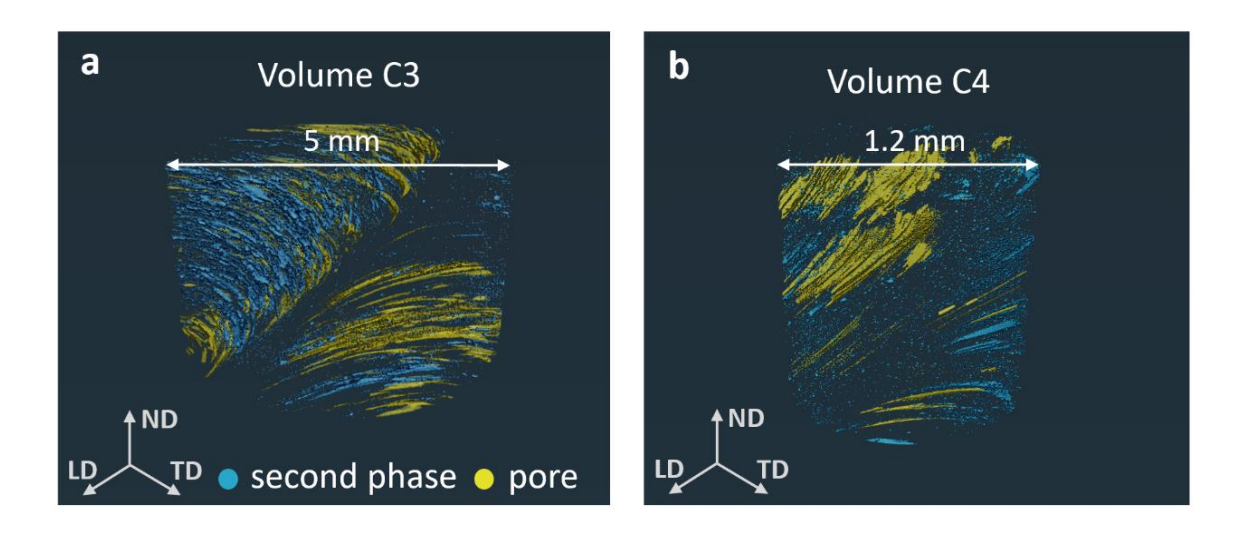


Figure 6.4 3D view of second phases and pores in the FSPed disk (a) 5mm-diameter cylindrical volume (C3), (b) 1.2mm-diameter cylindrical volume (C4)

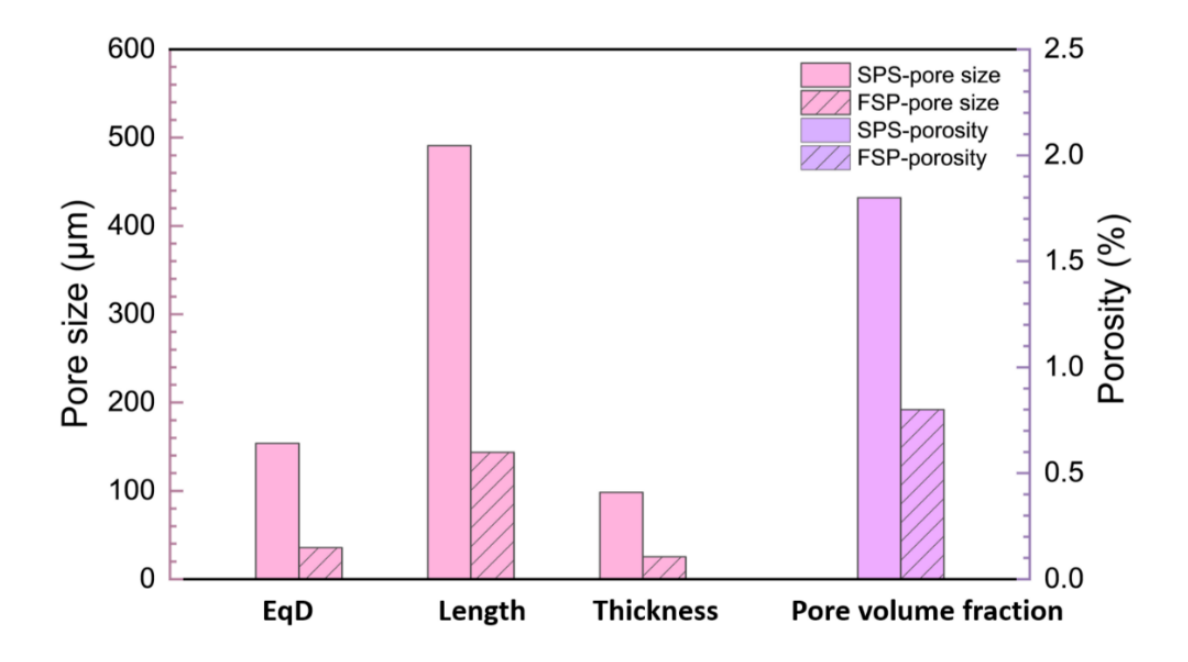


Figure 6.5 The comparison regarding pores in the SPSed and FSPed material

The multi-track FSP operated on the SPSed disk is expected to generate a periodic texture and thus regions within one periodicity were investigated by EBSD. The EBSD IPF maps with the average grain size and their position in the cross-section of the track are shown in Figure 6.6, a photo of the observed region is shown in Figure 6.7 and their corresponding GOS maps are shown in Figure 6.8. The distance between each column is 1.5 mm and the distance between each row is 1.2 mm. The microstructures of the material subjected to FSP

are usually divided into four groups, including stir zone (SZ), thermal mechanically affected zone (TMAZ), heat affected zone (HAZ), and unaffected base material (BM), based on the effect of deformation and heat input [85]. The grains were successfully refined from around 13 µm to about 1-3 µm after FSP. R1-1, R1-4, and R2-3 clearly have the largest grain size of 3.0 µm. These regions also have the lowest fraction of grains with GOS<2°, from 55-65%, indicating a lower level of recrystallisation. These three regions are at the outer layer of the stir zone and identified as TMAZ. The rest regions all exhibit more equiaxed recrystallised grains. The average grain size of the top layer ranges from 2.0-2.8µm, and decreases to 1.2 µm, from the top to the bottom. These regions are identified as SZ. In addition, there are ribbon-like unindexed regions, a higher magnification IPF map of the R2-4 is shown in Figure 6.9. These unindexed regions in the lower magnification map are ultra-fine equiaxed grains, which match the much smaller grain size in the aforementioned 'fuzzy' regions shown in Figure 6.2b2.

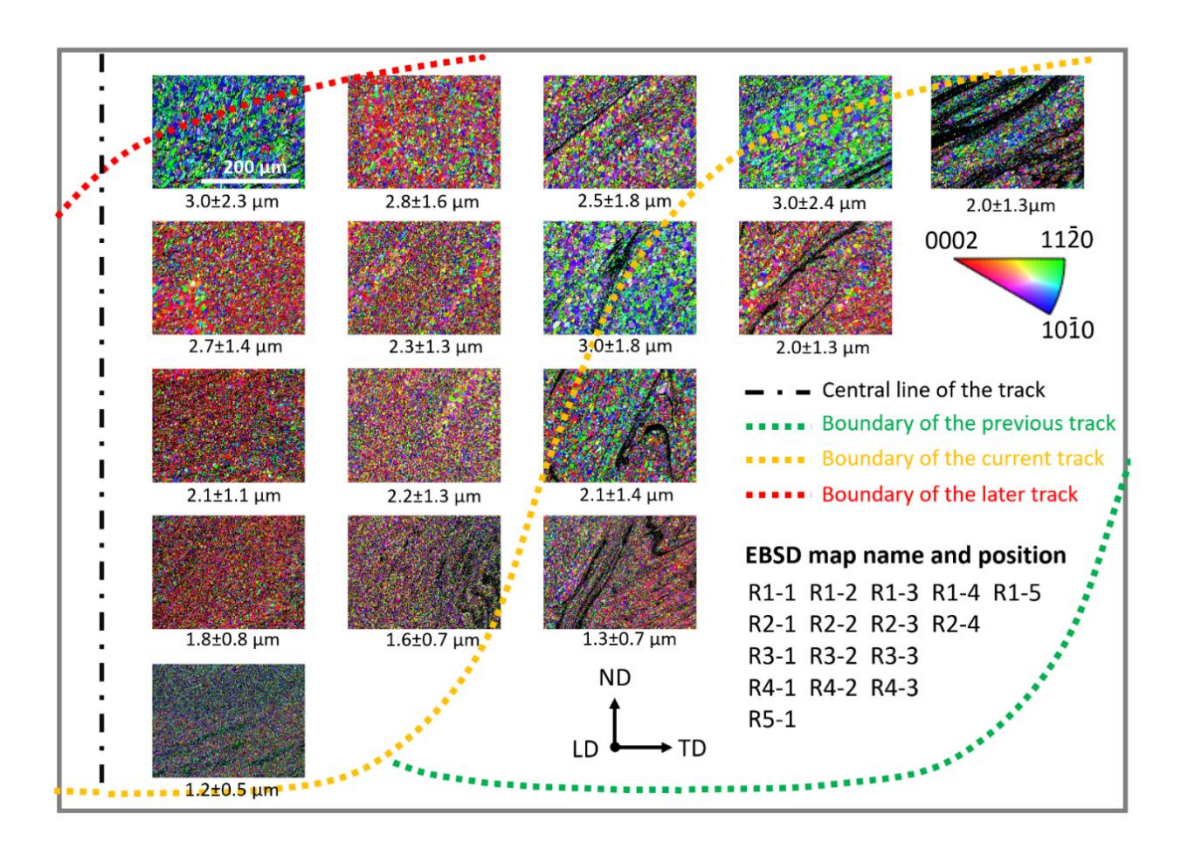


Figure 6.6 EBSD IPF maps of the FSPed material at different sites in the processed zone.

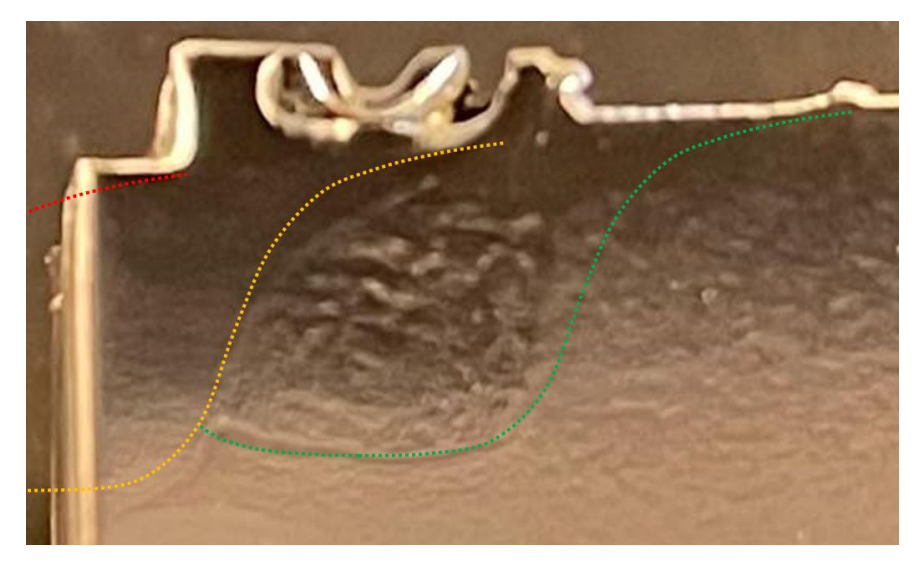


Figure 6.7 The corresponding region of the observed zone in Figure 6.6

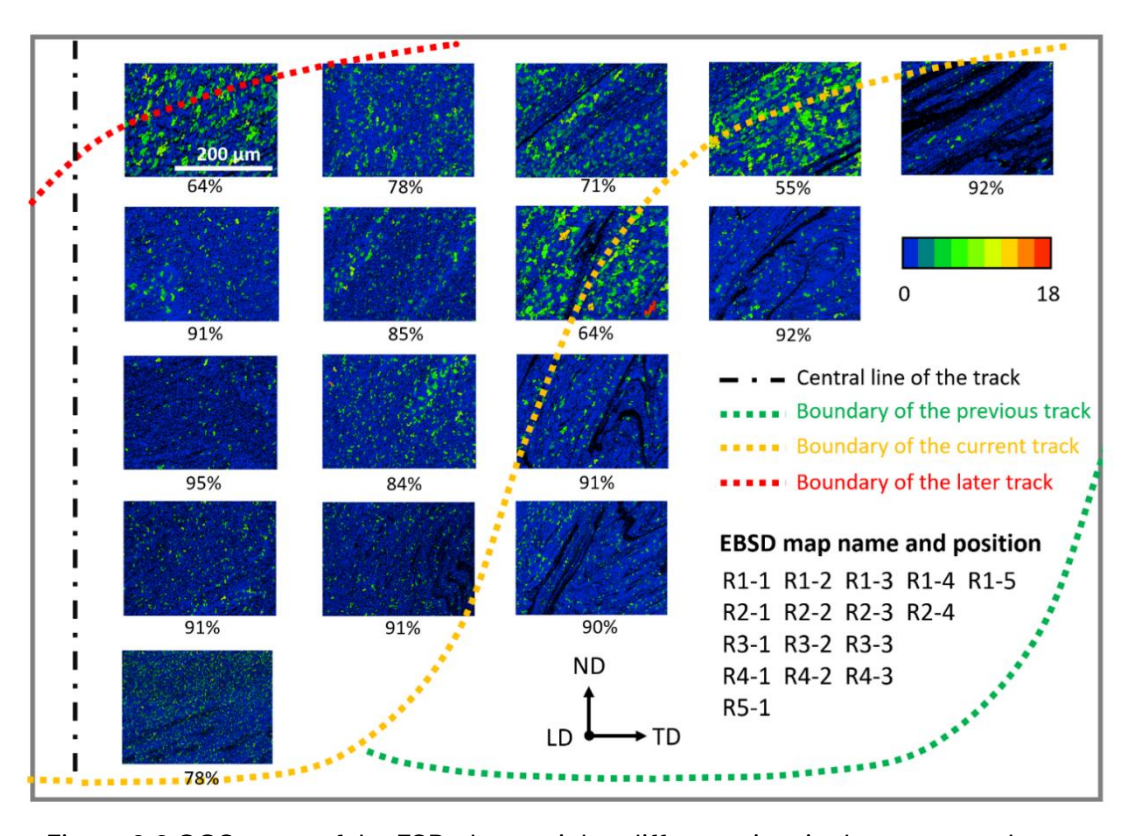


Figure 6.8 GOS maps of the FSPed material at different sites in the processed zone.

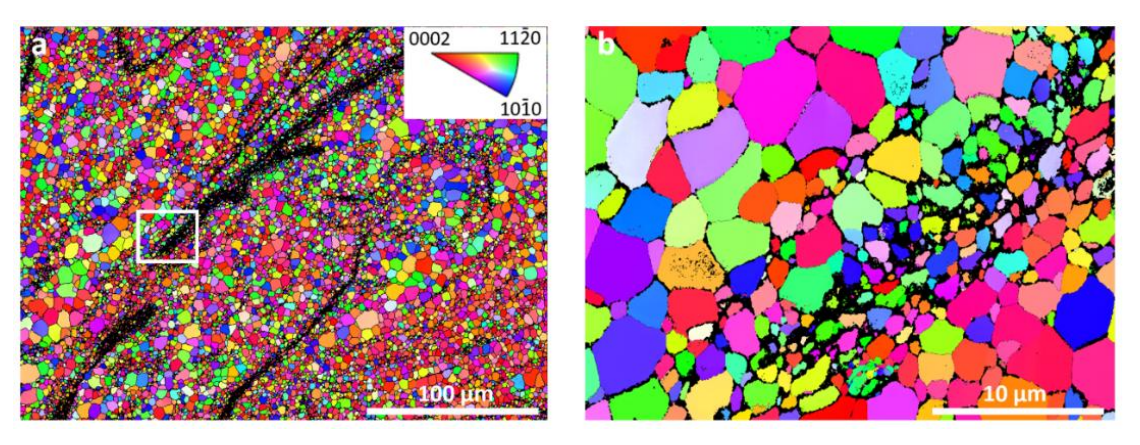


Figure 6.9 (a) EBSD IPF map of R2-4, (b) higher magnification map of the unindexed region

There are also significant differences regarding the texture components and intensity across the processed zone. To investigate the texture, pole figures of these regions are plotted in Figure 6.10. Based on the orientation and intensity of the basal poles, they can be roughly divided into three groups. Texture A, including R1-1, R1-3, R1-4 and R5-1, exhibits a strong basal texture with the basal poles perpendicular to the LD-TD plane. The texture intensity reached a very high level. Texture B, including R2-2, R2-3, R3-1, R3-2, R4-1 and R4-2, also had a strong basal texture, yet the basal poles were perpendicular to the ND axis. The texture intensity was higher than 8 MUD. The remaining regions belong to Texture C, including R1-2, R1-5, R2-1, R2-4, R3-3, and R4-3. Although a basal texture developed in these regions, the intensity is much lower than the other regions, around 8 MUD, and some of the regions even showed a split basal texture. Besides, regions identified as TMAZ, including R1-1, R1-4, and R2-3, have much stronger basal textures compared to other regions.

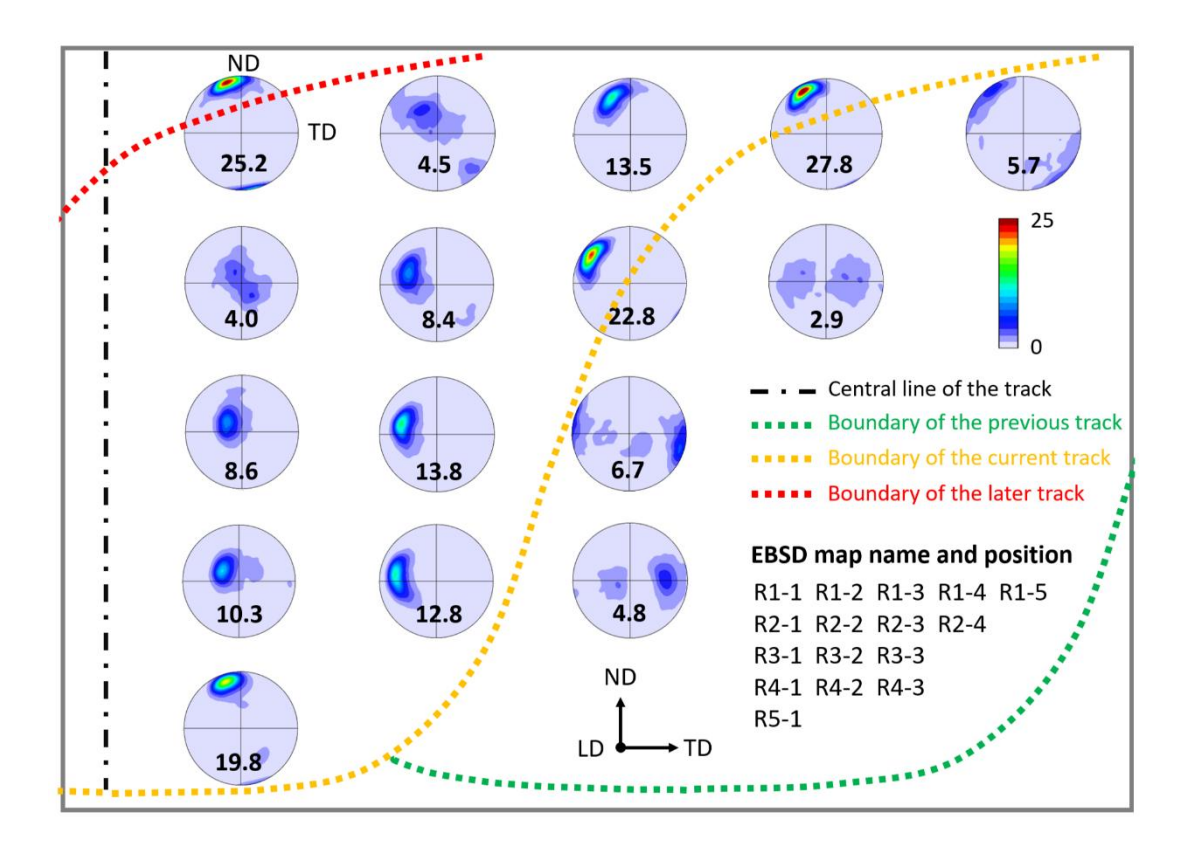


Figure 6.10 (0002) pole figures of the FSPed material at different sites in the processed zone.

6.2.2 Ageing treatment and the resulting hardness and precipitation evolution

The evolution of hardness with the ageing time is shown in shown in Figure 6.11. The hardness of the FSPed sample was measured to be 83.5±4.7 HV. After being kept at 200 °C for 40 hours, the hardness reached the maximum value of 94.6±4.3 HV. After that, there was a slow drop in the hardness as the ageing time further increased. A conclusive comparison of the hardness between the SPSed, FSPed, FSP+aged samples is shown in the bar chart in Figure 6.11b. It is clear that the hardness of the SPSed sample was the lowest, around 72.6±2.7 HV. After the FSP, the hardness increased by 10.9 HV and the following T5 heat treatment further increased the hardness by 11.1 HV. T6 treatment was not carried out and there are two main reasons. First, in the non-treated SS-FSC extruded WE43C wire, few second phases were observed. The microstructure is close to the super saturated solid solution condition, and thus the solid solution treatment is believed to have limited effects.

Second, a fine grain structure around 1-3 µm and further solid solution treatment (SST) may cause significant grain growth, weakening the grain boundary strengthening.

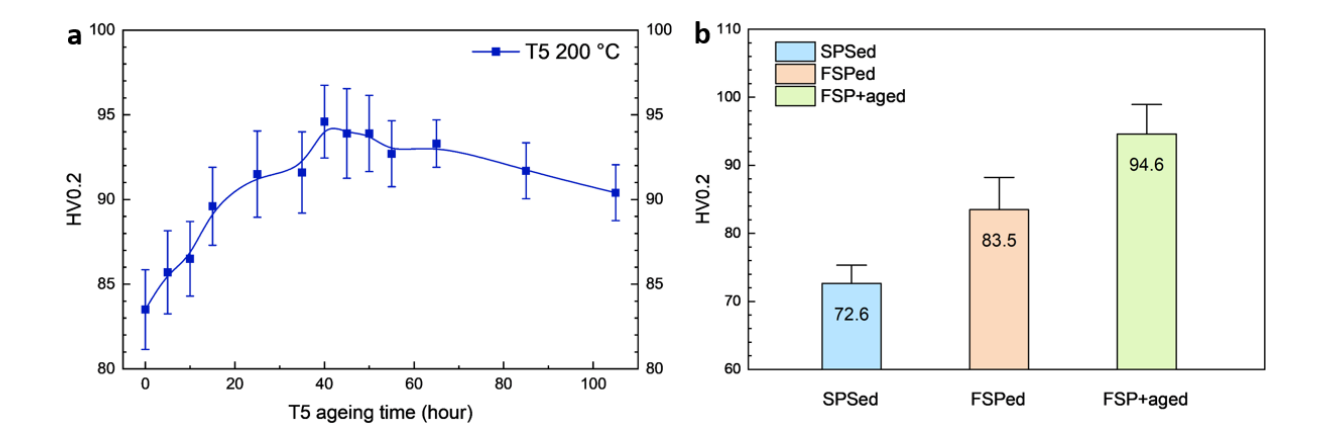


Figure 6.11 (a) Hardness evolution during the T5 treatment at 200 °C, (b) comparison of the hardness of SPSed, FSPed, and FSP+aged WE43C

The grain size and texture evolution are not expected to occur during the following T5 heat treatment and thus only precipitation process was investigated. After being kept at 200 °C for 40 hours, the peak ageing state was achieved. The ageing process is expected to produce new precipitates, and thus the comparison of the XRD spectrum of the FSPed and FSP+aged sample is shown in Figure 6.12. There are some emerging peaks in the T5 treated material, suggesting the formation of β₁ phase. By comparing the SEM-BSE image of the as-FSPed and FSP+aged sample, it is apparent that there were dense emerging precipitates within grains after T5 treatment. The STEM-HAADF image of the FSP+aged smaple is shown in Figure 6.13. There are plate-like second phase particles in the aged sample. The SAED pattern of the [0001] zone axis shows the extra diffraction spots of the plate-like precipitates. These extra spots matches the pattern of the β₁ in the Mg-Y-RE alloy [177]. The HRTEM image of the second phase in Figure 6.13c further validates these are β₁. The zone axis of the image is $[11\bar{2}0]$ of the matrix. The d-spacing of the $(1\bar{1}00)$ plane and (0001) plane of the matrix were measured to be 0.279 nm and 0.518 nm, respectively. These match the theoretical d-spacings of Mg, which are 0.278 nm and 0.521 nm, for $(1\bar{1}00)$ plane and (0001) plane, respectively [23, 199]. The d-spacings of the plate along the same direction were measured

to be 0.301 nm and 0.525 nm, respectively. These match the d-spacings of (110) and ($\bar{1}12$) of β_1 phase, which are 0.302 nm and 0.523 nm, respectively. The orientation relationship is also consistent with $[110]_{\beta_1} \| (0001)_{\alpha-Mg}$ and $(\bar{1}12)_{\beta_1} \| (1\bar{1}00)_{\alpha-Mg}$, which has been reported in the Mg-Y-RE system [23, 199].

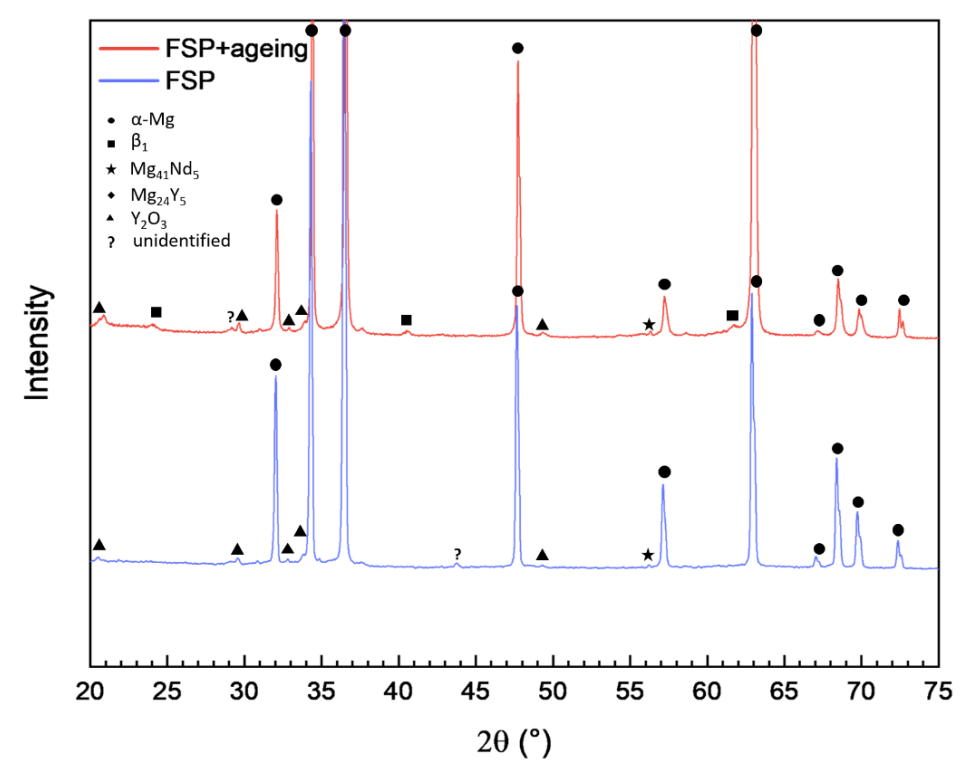


Figure 6.12 XRD spectrum of FSPed and FSP+aged WE43C

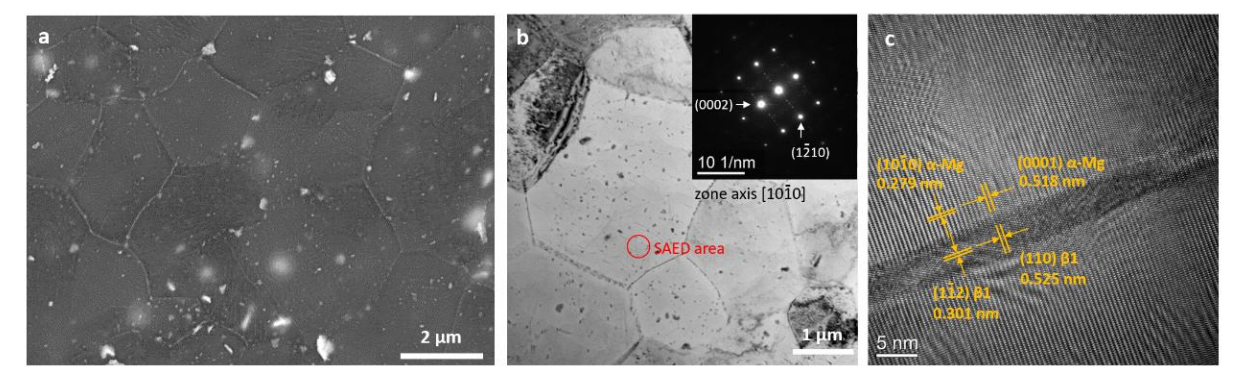


Figure 6.13 (a) SEM-BSE image of the FSP+aged sample, (b) STEM-HAADF image and SAED pattern of the precipitates. (c) HRTEM image of the β_1 precipitate.

6.2.3 Tensile tests and fractography

The tensile test were operated along the LD and the results of FSPed and FSP+aged specimens, including the yield strength (YS), ultimate tensile strength (UTS), and elongation (EI) are listed in Table 6.1. Due to limited number of tensile specimens, the tensile tests were not done along the TD, although an anisotropy is possible. It is clear that after ageing, the YS and UTS both further increased by ~19% by carrying out T5 treatment, although it also led to a decrease in elongation. Photos of FSPed and FSP+aged samples after tensile tests are shown in Figure 6.14. The shape of the fractured site is different from typical modes, which usually have a fractured surface perpendicular or 45° against the loading axis. Instead, the shape of the fractured surface is along the shape of the patterns of the FSPed track. For the stress-strain curves of the FSPed specimens, there are two samples showing a sudden drop of stress but after that the elongation continues. This is because during the tensile tests, part of the specimen fractured and the remaining part continued to bear the load until the complete failure of the specimen. Based on the SEM images of the fractured surface of FSPed specimen, there are mainly shallow and large dimples across the fractured surface. Whilst for the FSP+aged specimen, the dimples are even much shallower and the tear ridges are not clear, compared to the FSPed specimen. There are also well-defined cleavages, as shown in Figure 6.15.

Table 6.1 Tensile tests results of FSPed and FSP+aged specimen

Specimen	Yield strength (MPa)	Ultimate tensile strength (MPa)	Elongation (%)
FSPed	190.3	210.8	3.8
FSP+aged	226.5	251.2	2.2

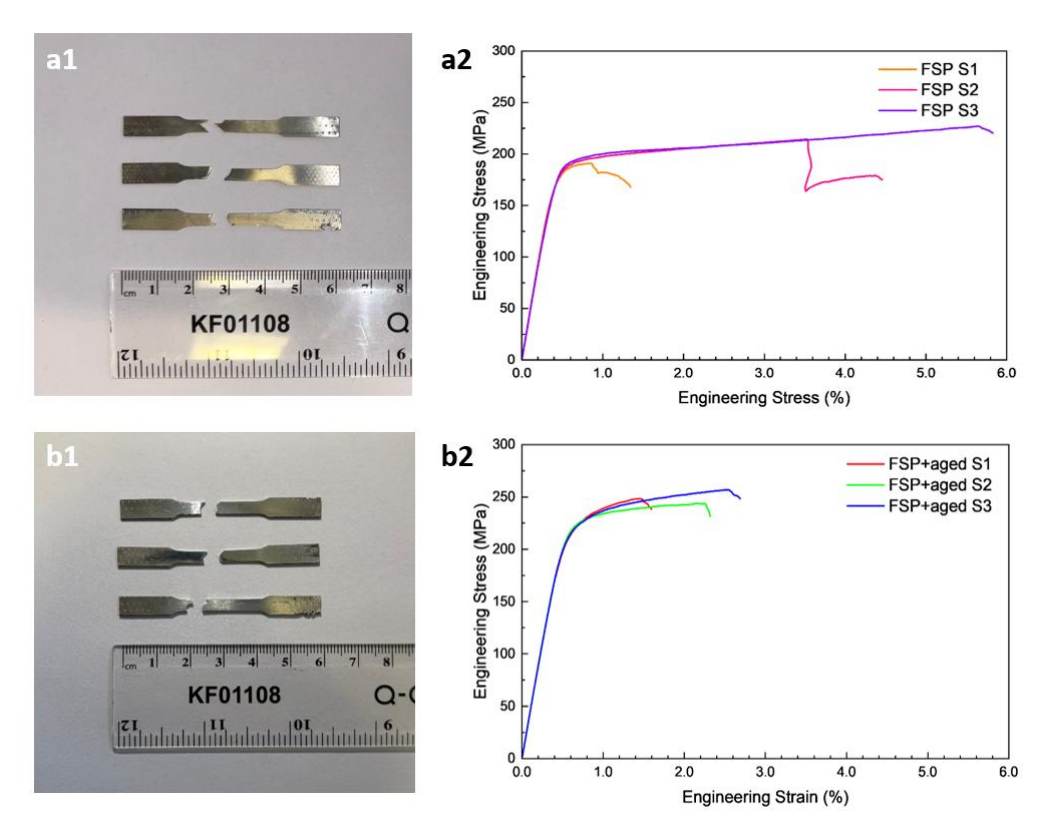


Figure 6.14 (a1) Photo of the FSPed specimens after fracture, (a2) engineering stress-strain curves of the FSPed specimens, (b) Photo of the FSP+aged specimens after fracture, (b2) engineering stress-strain curves of the FSP+aged specimens

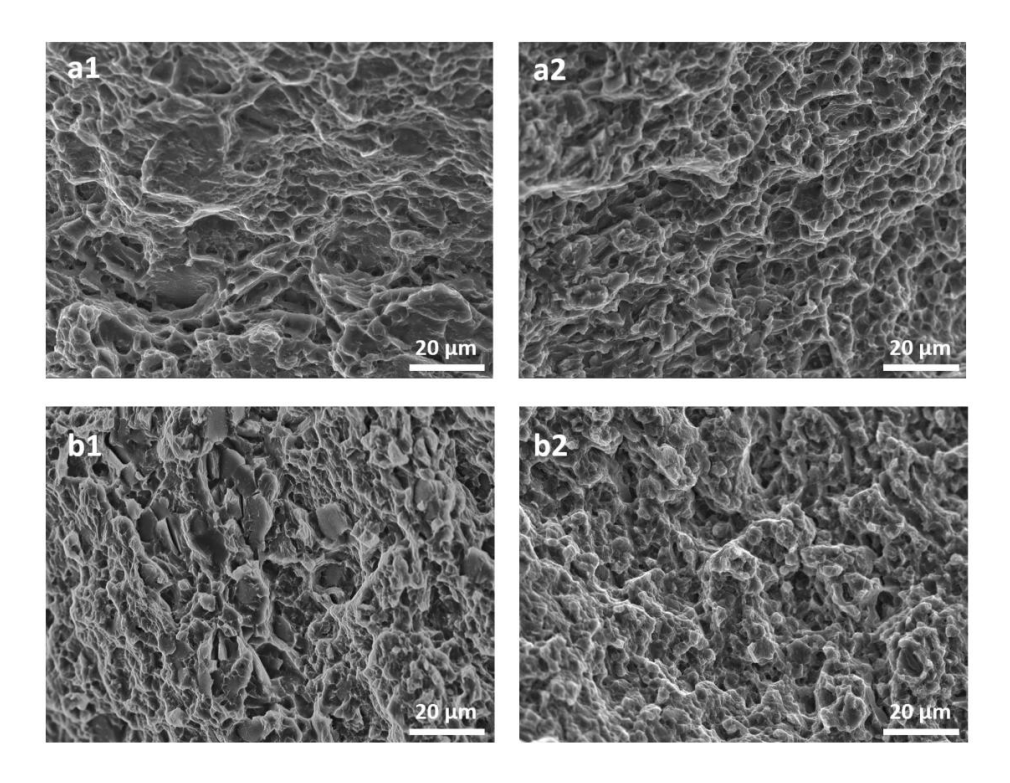


Figure 6.15 (a1-a2) SEM image of the fractured surface of the FSPed specimens, (b1-b2) SEM image of the fractured surface of the FSP+aged specimens

6.3 Discussion

6.3.1 Evolution of grain size, second phases, texture and porosity

The microstructural evolution of WE43C scraps and SPSed disk was discussed in the previous chapter and thus will not be discussed here.

In the FSP, the eutectic phase and oxide layer network can no longer be seen, which is attributed to the result of both mechanical stirring and friction heat. The stirring by the probe generated an extremely high strain, fragmenting the large particles into small pieces. The friction heat also led to the dissolution of some of the second phases into the matrix, such as the β-Mg₁₄Nd₂Y. These dissolved alloying elements from the previous eutectic phase partly reprecipitated during the following cooling stage, both in the grain interior and along grain boundaries, yet a grain boundary is considered a more favourable site, based on the SEM images. Combining the XRD spectrum, these second phase formed during the FSP can be indexed as Mg₄₁Nd₅ phase. Whilst some thermal stable phases only underwent fragmentation or redistribution, such as Mg₂₄Y₅ and oxides like Y₂O₃. The oxide layer also agglomerated to form micro-scale particles to reduce the surface energy, which is common in Mg alloys and other alloy systems [187, 196]. The oxide-oxide interface has much lower energy compared to the oxide-metal matrix interface. For oxide particles, there was no preferential sites between the grain interior and grain boundary.

The material flow across the processed zone was very different from site to site and thus produced an extremely complex heterogeneous microstructure and texture. From the top to the bottom of the processed zone, there was a decreasing tendency in the average grain size, from about 3.0 µm to 1.2 µm. Such grain refinement is attributed to the dynamic recrystallisation (DRX) during the FSP [85, 176, 192, 204]. The microstructures of the material subjected to FSP usually can be divided into four groups, SZ, TMAZ, HAZ, and BM, based on the effect of deformation and heat input [85]. R1-1, R1-4, and R2-3 clearly have the largest

grain size of 3.0 µm. These regions also have the lowest fraction of grains with GOS<2°, from 55-65%, indicating a lower level of recrystallisation. These three regions are at the outer layer of the stir zone when checking the position of the EBSD maps and the photo of the sample cross section, and thus are identified as TMAZ. Due to the lack of heat input compared to SZ, the DRX did not thoroughly occur and thus left grains with higher level of inner grain disorientation and subgrain boundaries, exhibiting larger grains and higher GOS values. The rest regions all exhibit more equiaxed and highly recrystallised grains and are identified as SZ. There is a decrease of the average grain size from the top to the bottom. Such gradient structure is related to the friction heat generation and heat transfer. Several researches have reported the temperature gradient in the FSWed Mg alloys [78, 205]. There is usually a temperature decrease from the top to the bottom due to the extra friction between the shoulder and the material surface, and from the central line to the edge because of the heat transfer [78, 205]. No regions with coarse grains were identified next to the TMAZ, which usually belong to HAZ. Several factors contributed to diminish of the HAZ. First, the relatively low rotational speed and high traverse speed lead to a lower maximum temperature and heat input in the nearby material. Second, the oxide particles and precipitates formed in the previous track hindered the grain boundary migration when subjected to the thermal cycles of friction heat from the following track by Zener pinning. In addition to the macro-scale grain size variation, even at the same site, there could be apparent grain size differences, as shown in Figure 6.98. There are ribbon-like regions of ultra-fine equiaxed grains, which match the much smaller grain size in the aforementioned 'fuzzy' regions shown in Figure 6.2. The formation of regions with much finer grains was reported in research of Mg-Y-RE alloy system subjected to hot deformation [48] or other friction stir based technologies [206]. The local material flow variation is believed as a reason for such microstructure [9, 207, 208]. In this study, it is also related to the pore evolution during the FSP. As mentioned in the previous section, these regions are the boundaries of pores. During the FSP, large pores in the SPSed disk are broken into smaller ones and travel with the tool. Although a deliberate increase in the plunge depth

for each track was applied, there were still some large pores which were not completely removed. This can be attributed to two factors. First, the high porosity and large pores in the SPSed disk exceeds the capability of pore closure by FSP. Second, the tool design can potentially increase the chance of pore formation. Patterns on the tool surface can increase the chance of pore formation during the FSP, which was in-situ observed by Agiwal et al. [209]. These pores promote further oxidation of the material around them. The dense newly formed nano-oxide particles at the vicinity of pores lower the growth of recrystallised grains and leave these ribbon-like 'fuzzy' regions with ultra fine grains in the recycled disk.

Although the texture in the stir zone varies from site to site, they are closely related to the material flow during the processing. In thermal mechanically prepared Mg alloys, the basal planes tend to arrange parallel to the material flow plane [27, 169, 210, 211]. Texture A, including R1-1, R1-3, R1-4 and R5-1, has a strong basal texture with the basal pole around the ND, slighted toward the negative direction of TD. These sites were strongly affected by the shoulder or the bottom of the probe, the material flow mainly occurred within the LD-TD plane. Texture B, including R2-2, R2-3, R3-1, R3-2, R4-1 and R4-2, also has a strong basal texture. These sites were strongly affected by the side surface of the probe, and thus the basal poles were distributed within a latitude line within the LD-TD plane, with minor shifting away due to the cone shape of the probe. Whilst for Texture C, which is a special group, does not have a common orientation but show weak basal or split basal poles. They are at the right side of the stir zone, adjacent to the TMAZ, and thus formed during the first processing track but also affected by the heat generated in the second track. The extra heat input allows further texture evolution by static recrystallisation (SRX), which leads to the weakening of previously formed strong basal texture. Such basal texture weakening phenomenon in the Mg-Y-RE alloy system during SRX has been widely reported [32, 33, 108].

6.3.2 Effects of post heat treatment and mechanical properties

Compared to the SPSed material, the FSPed material showed a higher hardness value, and this is attributed to the changes in the contribution from different strengthening mechanisms. After FSP, the grain size was decreased by nearly one order of magnitude, and thus the grain boundary strengthening is more significant in the FSPed material. The significant dissolution of second phases leads to the enhancement of solid solution strengthening. Regarding the dislocation strengthening, although there were some not fully recrystallised grains in the FSPed material, the recrystallised structure was dominant, and thus there should be little difference between the SPSed and FSPed material. Both the SPSed samples and as-FSPed were not aged, though there were second phase particles, the strengthening effects are expected to be weak. After further T5 treatment, the formation of fine precipitates and densification of material lead to a remarkable hardness increase. The ageing peak appears at around 40 h, reaching a value of 94.6 HV, increased by 11.1 HV. However, the hardness increase is lower than the commonly reported Mg-4Y-3RE alloy with T5 heat treatment [41, 212]. Several factors are believed to contribute to this phenomenon. First, different to the conventional processing methods, SPS-FSP recycled disk exhibited more oxide, which were identified as dominantly composed of Y₂O₃. And the precipitation sequence of the Mg-Y-Nd alloys was widely reported in Figure 6.16.

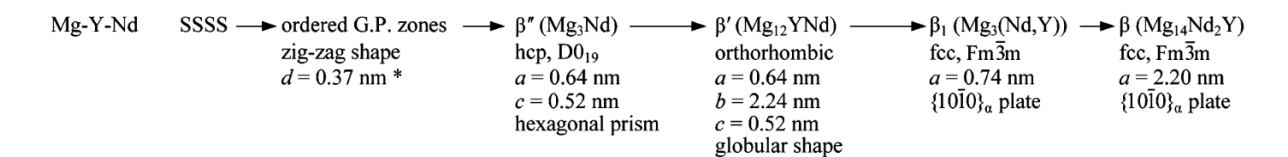


Figure 6.16 precipitation sequence in the Mg-Y-Nd alloy system [23]

The major phase responsible for the strengthening effect is the fine plate-like β_1 [23], These β_1 precipitates in the grain interior lie on $\{11\overline{2}0\}$ and are expected to act as obstacles for basal slip activation [23], strengthening the material. Such a phase was identified by the TEM result. The formation of Y_2O_3 consumed part of the Y in the matrix and thus fewer Y-containing phase

 β' could nucleate, and thus the fraction of the major strengthening phase β_1 is decreased. Besides, the FSPed disk exhibited smaller grain size compared to the alloys produced by casting, rolling or extrusion. The smaller grain size plays an important role in this phenomenon. Sun et al. [213] reported the special ageing response in a nanograined Mg alloy where most of the alloying elements diffuse to the grain boundary instead of forming grain interior precipitates following the aforementioned precipitation sequence. This is because the segregation of alloying elements along grain boundaries is more energetically favourable and the nano sized grains provide the condition for the alloying element to diffuse to the grain boundaries instead of forming inner grain precipitates. Although in this work, the grain was not small enough to allow most of the alloying elements diffuse to the grain boundary forming segregation, smaller grains means the increased grain boundary region, and thus more alloying elements adjacent to the grain boundary precipitate out along grain boundaries, instead of forming β_1 within grains. These precipitates along grain boundaries are not able to generate strong strengthening effects as β_1 . Regions adjacent to the grain boundaries, due to the formation of second phases along grain boundaries, are depleted in alloying elements and form precipitation free zone (PFZ). The lack of precipitation in these regions also lead to an insufficient ageing response in the micro scale

The tensile test results match the hardness test results. After the ageing treatment, the YS and the UTS both increased whilst the elongation decreased. The drop of elongation can be clearly revealed by the change in the fractured surface after the test. Based on the SEM images of the fractured surface of FSPed specimen, there were mainly shallow dimples across the fractured surface. Whilst for the FSP+aged specimen, the dimples were even much shallower, compared to the FSPed specimen. There were also well-defined cleavage steps. For the FSPed specimens, there was a ductile fracture mode, whilst for the FSP+aged specimens, there was a combination of ductile fracture and brittle fracture.

Compared to the SS-FSC recycled material, the strengths of the FSP recycled samples are lower, and the elongations at failure are significantly lower. Considering the similarity regarding the average grain size, and the post heat treatment, the obvious difference of the mechanical properties between these two recycled materials can be attributed to the larger residual pores and higher fraction of pores in the FSP recycled material. The photos in Figure 6.14 indicate that the crack propagation is along the FSP track pattern and this is also related to the sudden stress drop before the complete failure of the specimen. Interestingly, two of the FSPed tensile specimens exhibited a sudden drop in stress during the tensile process due to premature partial fracture of the cross section. The remaining part underwent further elongation and then completely failed. These only occurred in the FSPed specimens which cover two tracks (FSP S1 and FSP S2 in Figure 6.16a2). This can be explained by the following process. During the tensile test, the crack nucleates at the pore tip and propagates, leading to the fracture of part of the specimen. However, due to the curved shape of the pores, the direction of the crack gets deflected and stops at the boundary position between the two tracks. The tension continues until the failure of the second part. For those tensile specimens that fell in one track, since there was no abrupt change in texture orientation and pore distribution, the stress-strain curve went smoothly.

The strengths and elongations plot of the SPS-FSP recycled material and other prime products is shown in Figure 6.17. It is apparent that the wrought WE43C alloys (marked by yellow labels), including rolling and extrusion have the best strength-ductility combination. Additively manufactured (AMed) alloys generally have higher strengths with slightly lower ductility, compared to the cast alloys. For the SPS-FSP recycled secondary material, the strength-ductility combination is lower than the deformed material but equivalent to the AMed and cast materials. This is a promising result for the recycled material, though the performance is not as good as the SS-FSC recycled counterparts. With further efforts of the pore closure optimisation, the combination use of SPS and FSP can potentially produce recycled plates

with competitive mechanical properties as commercial extruded or rolled products. This would be beneficial to the eco-friendly production of Mg alloys, yet further improvement is still needed.

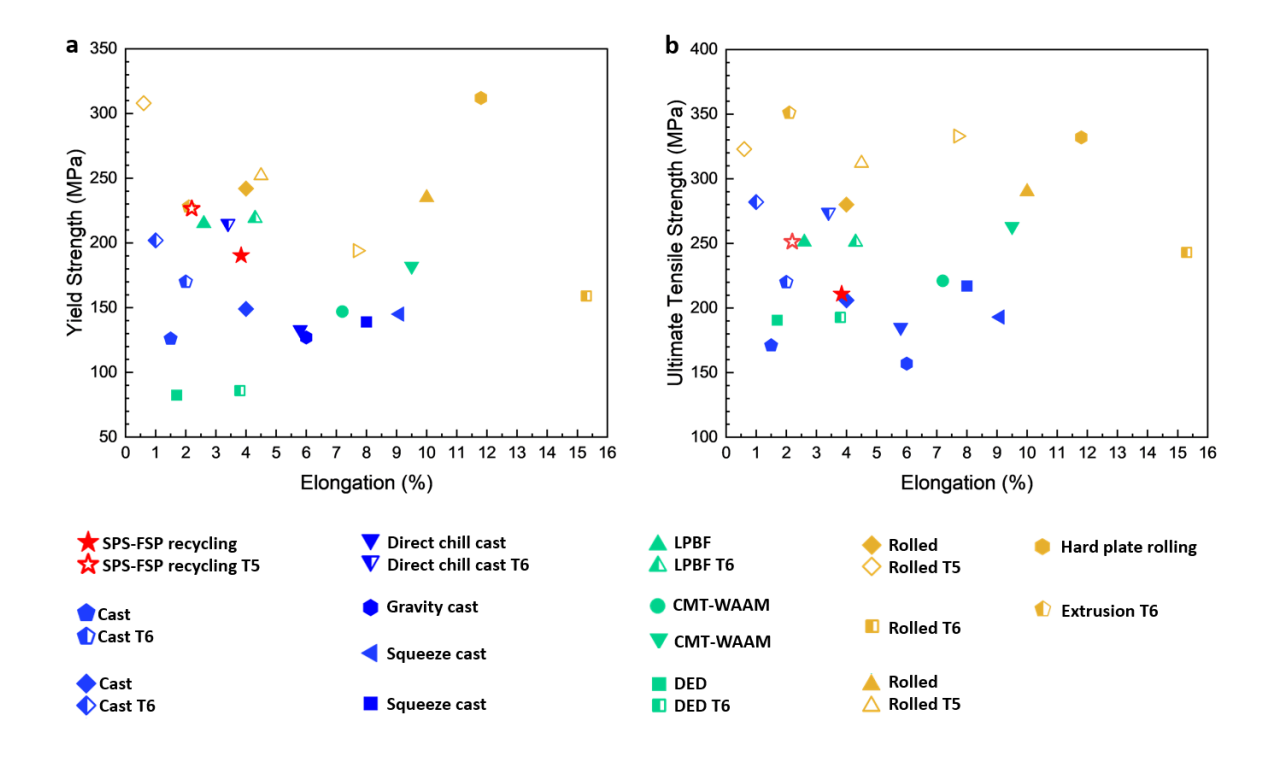


Figure 6.17 Scattered point plot of mechanical properties of Mg-4Y-3RE alloys prepared by various methods and the SPS-FSP recycled material (a) yield strength-elongation plot and (b) ultimate tensile strength-elongation plot. [39, 43, 45, 86, 129, 135, 178, 198-203]

6.4 Conclusions

A solid-state recycling method integrated spark plasma sintering (SPS) and friction stir processing (FSP) was used to recycle waste WE43C alloy, turning scraps into a consolidated disk. The major findings are shown below:

(1) After FSP, eutectic phases were broken, re-dissolved and partially precipitated out as Mg₄₁Nd₅ mainly along grain boundaries. Oxide layers were also broken, agglomerated, and redistributed. The microstructure can be categorised into two regions, homogeneous regions and heterogeneous regions. In the heterogeneous regions, there were ribbon-like

- 'fuzzy' regions with much finer grains, denser oxide nanoparticles and residual pores. Nevertheless, the porosity decreased by \sim 56%, reaching a relative density of 99.2% and the average size of the pore was decreased to 35.7 μ m.
- (2) In the FSPed disk, a gradient fine-grained structure from the bottom to the top of the processed zone, with the average size ranging from 1.2-3.0 μm. The largest grain size appeared in the regions exhibiting TMAZ features, whilst no obvious HZ with coarse grains was observed due particle pinning effects. The textures were complex but can be roughly divided into 3 types, based on the material flow direction and thermal history. They include regions with strong basal textures affected by the bottom of the shoulder and probe, regions with strong basal textures affected by the side of the probe, and regions with weak or split basal textures induced by the heat from the adjacent track.
- (3) The FSPed material exhibited a yield strength (YS) of 190.3 MPa, an ultimate tensile strength (UTS) of 210.8 MPa, and an elongation (EI) of 3.8%. Further T5 heat treatment produced fine plate-like β_1 . This led to the YS and UTS increase to 226.5 MPa and 251.2 MPa, whilst the EI decreased to 2.2%. Such strength-ductility combination is comparable to some of the cast and additively manufactured products, yet still lower than that of the wrought products and SS-FSC recycled wire. The relative low elongation in the recycled material compared to wrought products and SS-FSC recycled wire is attributed to the elongated residual pores.

Chapter 7 Solid-state additive manufacturing of WE43C by additive friction stir deposition (AFSD)

7.1 Introduction

AFSD is a novel AM technology which is different from traditional melting-solidification process. Instead, the process relies on the plastic deformation to form a thin layer of printed material. By repeating this process, components with designated size and geometry can be produced. AFSD has been successfully used for the production of various kinds of alloys, including Cu alloys, Ti alloys, Al alloy, Mg alloys, etc. Although a few research regarding Mg-Y-RE alloys have been carried out, the understanding of the material flow, texture evolution, second phase evolution, pore evolution remains at the very early stage. Besides, one of the advantage of the AFSD is free of gas protection which is impossible for laser-based printing of Mg alloys, yet oxides can still form during the printing. The effects of these oxides on the properties have not been reported yet.

In this chapter, a systematic investigation of the microstructure evolution and the resulting mechanical properties of an AFSDed component is illustrated, including the texture evolution, grain size evolution, second phase particle evolution, oxide formation, and pore formation. Further post heat treatment was carried out to characterise the exceptional thermal stability and the uncommon ageing response in the AFSDed WE43C. Tensile tests were used to evaluate the performance of the AMed product.

Part of this work has been published on:

X. Zhao, D. Olden, B. Williams, A. Pariyar, D. Zhang, M. Murphy, P. Reed, P. Allison, B. Jordon, J. Qi, W.M. Rainforth, D. Guan, Grain growth stagnation at 525° C by nanoparticles in a solid-state additively manufactured Mg-4Y-3RE alloy, *Journal of Magnesium and Alloys* (2024).

7.2 Results

7.2.1 Microstructure of the feedstock

The feedstocks for the AFSD were hot extruded bars with square cross-section. The length of the cross-section was 9.5 mm. The EBSD IPF map in Figure 7.1a shows that the WE43C feedstock has fine equiaxed grains. The average size was measured to be 2.64 ± 1.27 μ m. The pole figure indicates that the basal pole distribution of the feedstock spreads widely from the ND to the TD. The inverse pole figure reveals that the $<10\bar{1}0>$ direction of grains are aligned parallel with the extrusion direction (ED). The SEM-BSE image shows that there are two different kinds of second phase particle distribution. The first kind is fine particles distributed along grain boundaries and triple junctions, and the second kind is coarse particles linearly distributed along the ED.

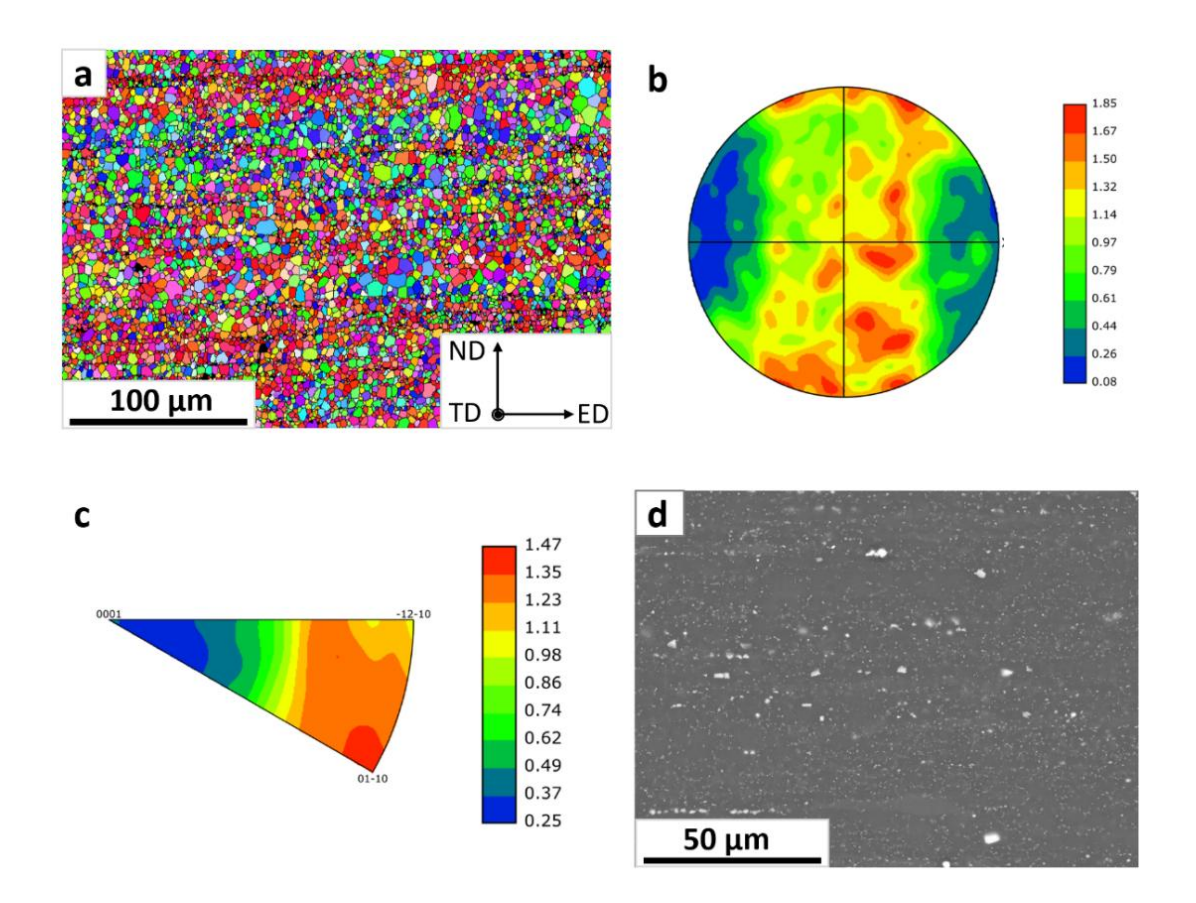


Figure 7.1 (a) EBSD IPF map of the feedstock, IPF//ED, (b) (0002) pole figure, (c) inverse pole figure along the ED, (d) SEM-BSE image of the feedstock.

7.2.2 Microstructure of the as-printed WE43C

7.2.2.1 Grain structure and texture

The microstructure and texture in the AFSDed material exhibited a gradient structure with heterogeneity. An EBSD IPF maps of a large region from the base material to the AFSDded material indicates that there was a heterogeneous bimodal grain structure composed of alternating coarse grained regions and fine grained regions along the BD. Further EBSD IPF maps of three regions were chosen from the same deposited layer from the AFSDed component and are shown in Figure 7.2c1-c3. In the central sample and the middle sample, there are distinct fine equiaxed grain regions and coarse equiaxed grain regions with different grain sizes. For the edge sample, although nearly homogeneous fine equiaxed grain region were detected, there were still small ribbon-like regions with a slightly larger grain size. From the centre to the edge of the AFSDed material, there is a tendency of decrease in the average grain size. The grain size variation is summarised in Table 7.1. In the centre part, the average grain size was measured to be 6.1±4.9 µm. For the regions with finer grains, the average grain size is 4.3±2.1 µm. For the regions with coarser grains, the average size is 15.2±4.1 µm. In the middle part, the average grain size was measured to be 2.9±2.1 μm. For the regions with coarser grains, the average grain size is 11.6±6.4 μm. For the regions with finer grains, the average size is 2.6±0.7 µm. In the edge part, the average grain size was measured to be 2.7±0.9 µm. For the regions with coarser grains, the average grain size is 6.4±1.6 µm. For the regions with finer grains, the average size is 2.6±0.7 µm, which is the same as the grain size in the middle part. It is apparent that the decrease in the average grain size from the centre of the printed component to the edge happened in both the coarse grain region and the fine grain region. The overall grain orientation spread (GOS) value from the centre to the edge exhibits in the coarse grained region and the fine grained region also exhibits differences, as shown in Figure 7.3. The fraction of grains with a mean GOS value no larger than 2°, which are regarded as fully recrystallised grains, in the centre part, the middle part and the edge part, are 86%, 85%, and 85%, respectively. However, there was a significant difference of the mean GOS value between the coarse grained regions and fine grained regions in all three sites. All the coarse grain regions from three sites exhibit lower recrystallisation fraction compared to the fine grain regions, and from the centre to the edge there is a significant drop of the recrystallise fraction, as shown in Figure 7.3. The fractions of grains with a mean GOS value below 2° for the coarse grain region in centre part, the middle part and the edge part are 83%, 72%, and 44%, respectively. The fractions for the fine grain regions in these three parts are 92%, 95%, and 90%, respectively. There is little difference between the fine grain regions from three different parts of the AFSDed material. Considering the relatively small grain size in the fine grain regions compared to the step size of 0.5 µm may potentially affect the accuracy of GOS values due to the limited pixels, a further scan of higher magnification with a step size of 0.1 µm is provided in the later part in Figure 7.11. The fraction of grains with a mean GOS value below 2° is 87%, which is consistent with the previous scans, and thus proves the reliability of the low magnification scans. Despite the grain size variation from the centre to the edge, the texture components exhibited similar distribution along the TD. All three regions were found to have basal textures with the basal poles around the North Pole, which is the BD, as shown in Figure 7.4. The texture intensities of the centre part, middle part and edge part are 10.6, 11.2 and 9.2, respectively. From the centre to the edge, there was only a minor rotation of basal poles toward the TD.

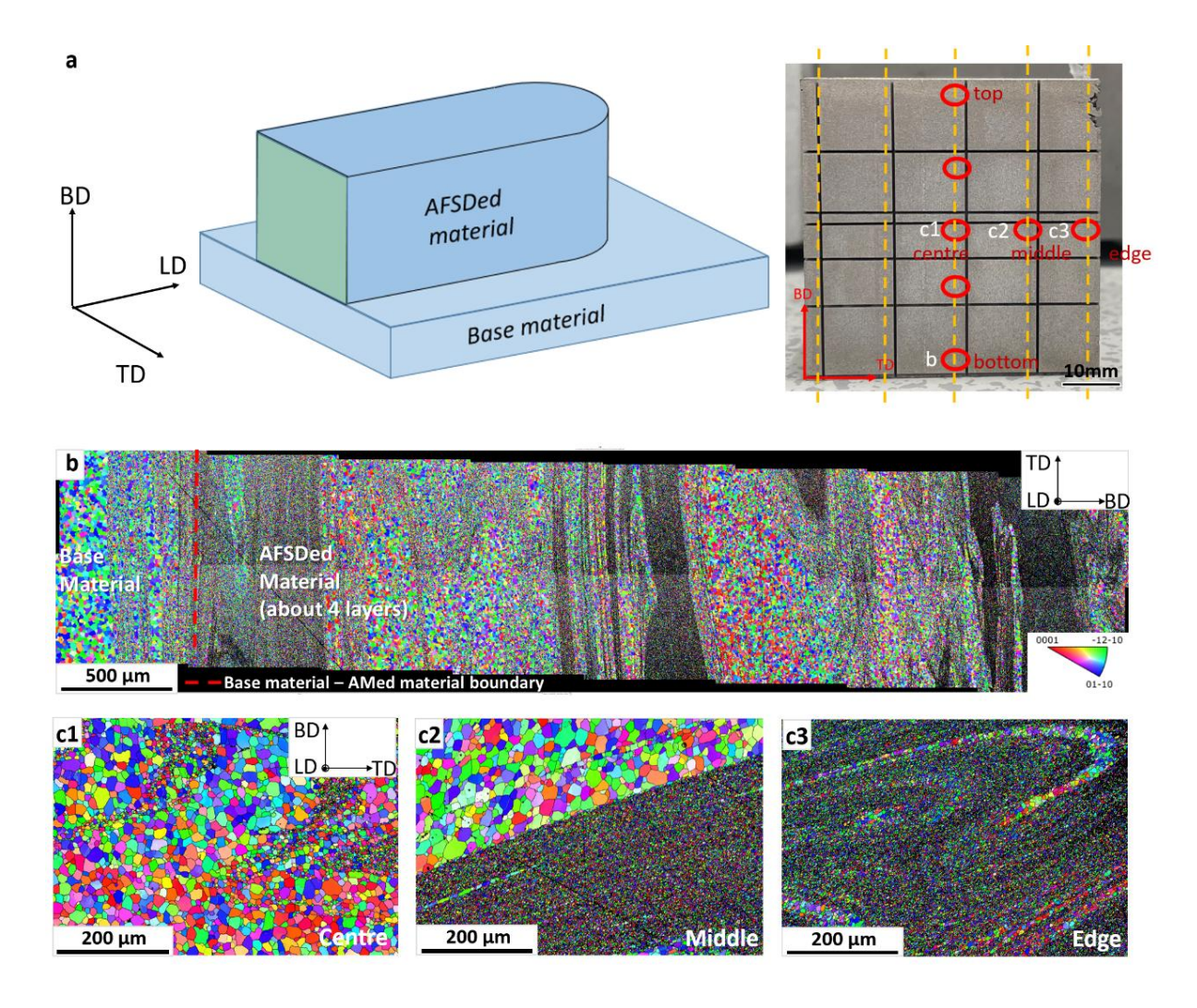


Figure 7.2 (a) position of samples taken from the printed WE43C component, (b) a large-area EBSD IPF maps of the base material-printed material interface, (c1-3) EBSD IPF maps of the centre part, middle part, edge part in the centre layer of the printed wall.

Table 7.1 Summary of grain size for three different sites taken from the centre layer

Site	Grain size in coarse grained	Grain size in fine grained	Overall grain size	
	region (μm)	region (µm)	(µm)	
Centre	15.2±4.1	4.3±2.1	6.1±4.9	
Middle	11.6±6.4	2.6±0.7	2.9±2.1	
Edge	6.4±1.6	2.6±0.7	2.7±0.9	

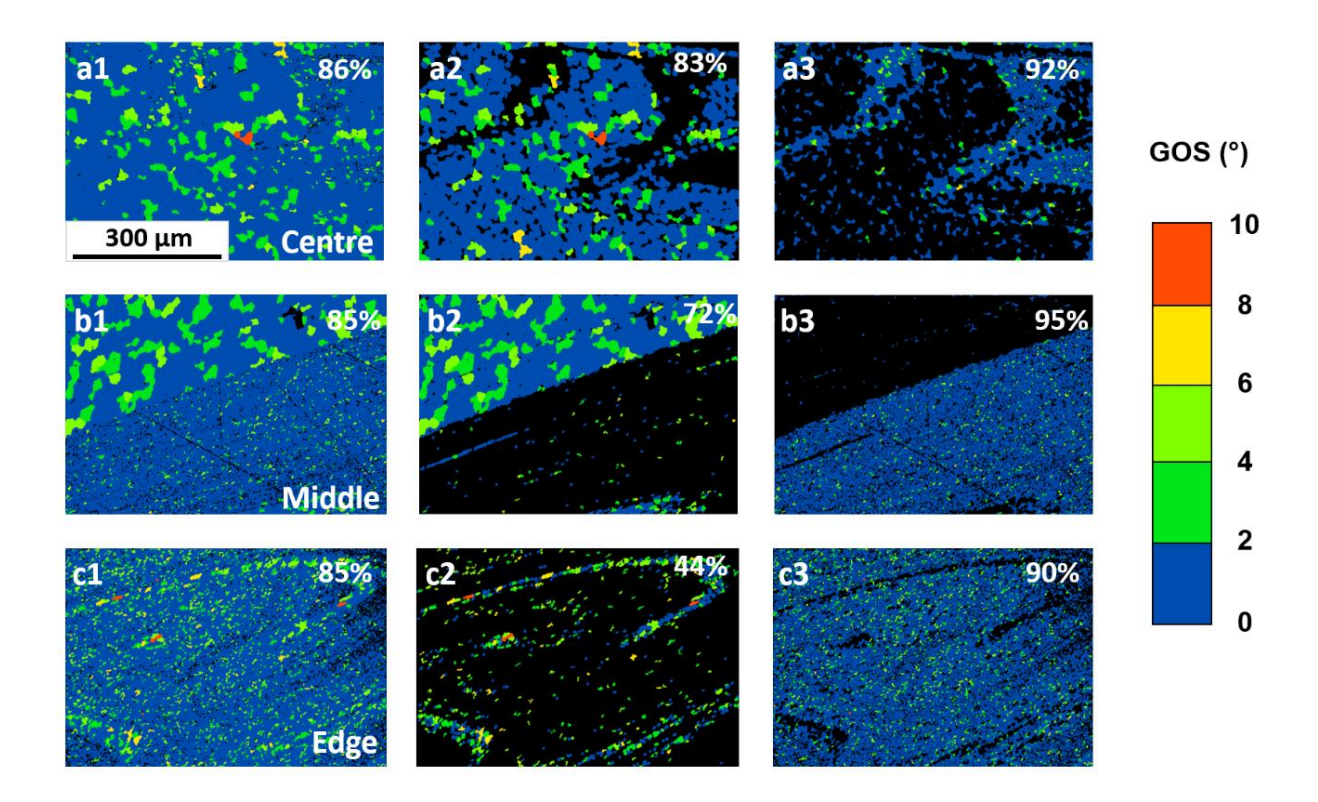


Figure 7.3 (a1-a3) GOS map of the centre part, including overall map, carse grain regions and fine grain regions, (b1-b3) GOS map of the middle part, including overall map, carse grain regions and fine grain regions, (c1-c3) GOS map of the edge part, including overall map, carse grain regions and fine grain regions

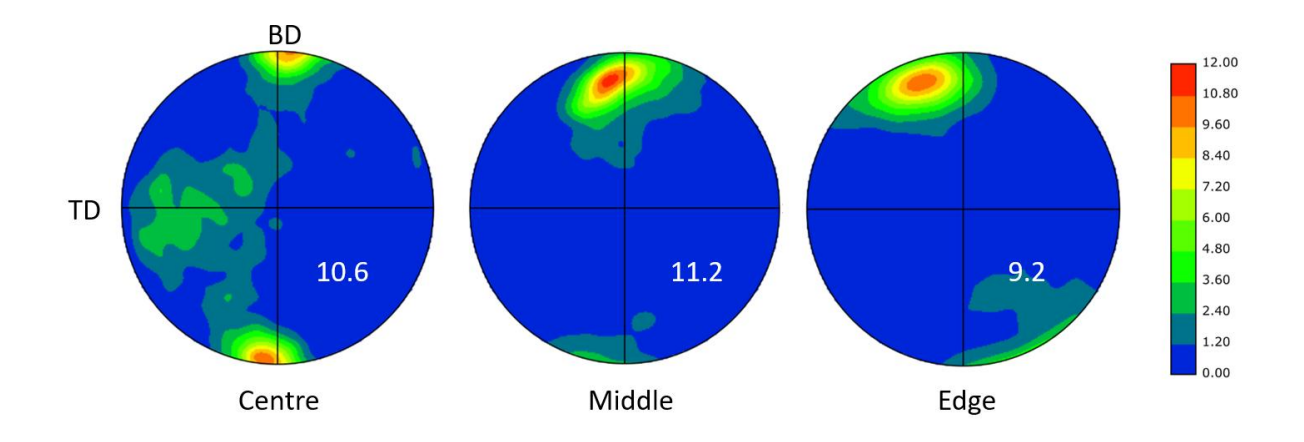


Figure 7.4 Pole figures of (0002) basal planes in the regions at centre, middle, and edge part

7.2.2.2 Second phases and oxides

The SEM-BSE images in Figure 7.5 reveal the second phase particles in the AFSDed component. These images indicate there are significant differences of the second phase

particle distribution, size and geometry in the coarser grain regions and finer grain regions. In the coarse grained regions, polygonal second phases below 1 µm are distributed mainly along the grain boundaries, exhibiting a necklace-like structure. The grain interior is relatively depleted in second phases compared to the grain boundary area. Only a few submicron phases can be occasionally observed. Further EDS scans indicate that these second phases along grain boundaries are rich in RE element of Nd, as shown in Figure 7.6. In the fine grained regions, there were also polygonal second phases. These polygonal phases are much larger than those in the coarse grain regions, mainly around 1 µm. These larger second phases are mainly distributed at the triple junctions and grain boundaries. The EDS scan result suggests that these particles are also rich in Nd. Across the fine grained region, there are also dense nanoparticles. These nanoparticles are not only distributed at grain boundaries but also in the grain interior. Due to the small size of these particles, the detailed shape or chemical composition cannot be clearly illustrated by SEM images.

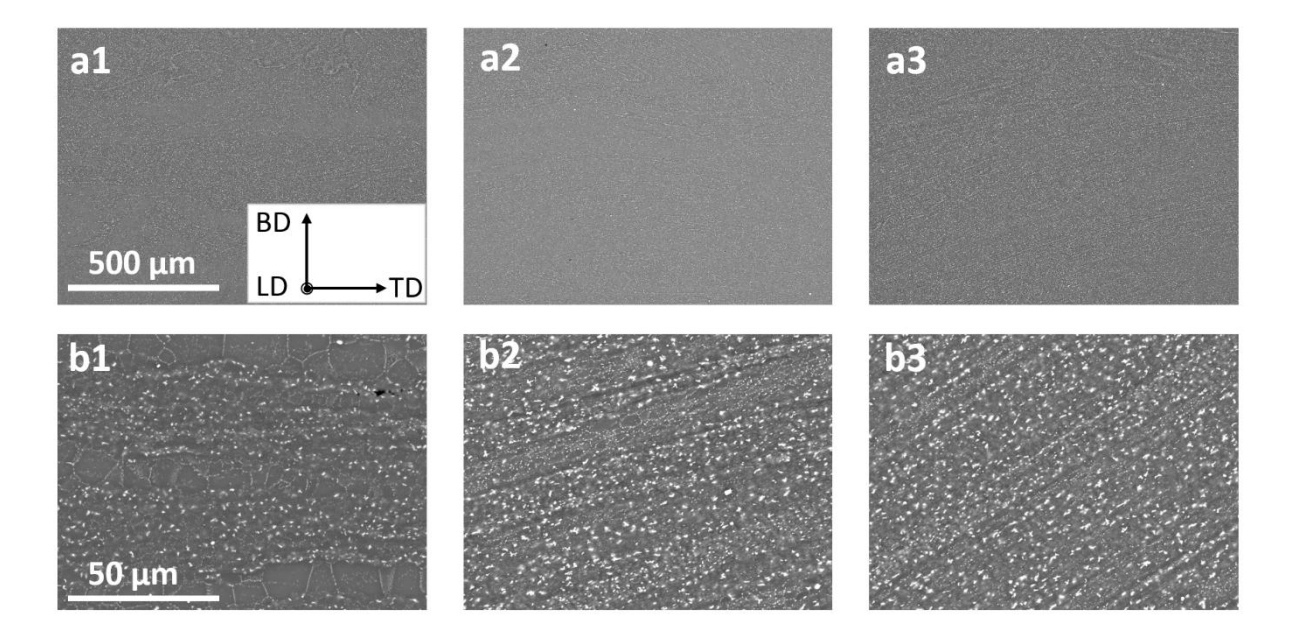


Figure 7.5 (a1-a3) SEM images of the centre, middle and edge part, 100 times magnification, (b1-b3) SEM images of the centre, middle and edge part, 1000 times magnification.

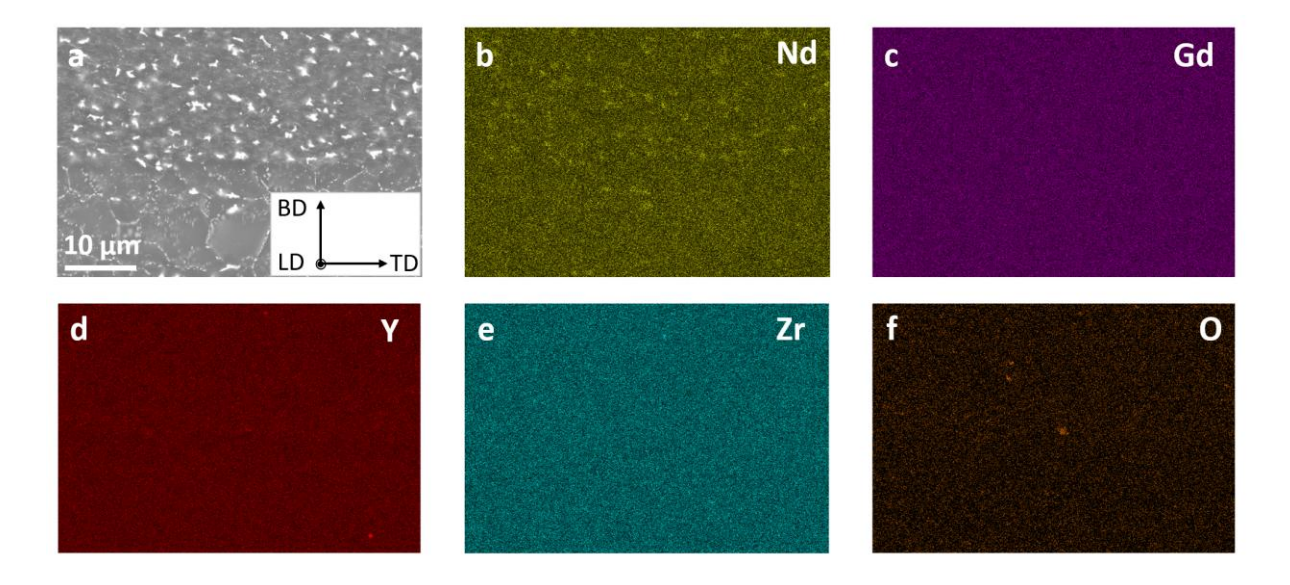


Figure 7.6 SEM-BSE image containing coarse grain regions and fine grain regions, and the corresponding EDS maps.

Further TEM results revealed more details of the second phases in the AFSDed material in the fine grained region, as shown in Figure 7.7. TEM-HAADF images match the result of the BSE images. There are polygonal particles around 1 µm along grain boundaries and nanoparticles across the whole region. What is more, a particle density difference in the coarse grain regions and fine grain regions is distinguished. In the coarse grain regions, there are nanoparticles distributed both along the grain boundaries and in the grain interior, yet the density is apparently lower than that in the fine grained regions. The TEM-EDS results of the AFSDed in Figure 7.8 reveal the chemical composition of the second phases at the grain boundaries. EDS maps show that the large polygonal second phase are rich in RE elements of Nd and Gd. Further selective area electron diffraction (SAED) pattern of the second phase particle was obtained. The measurement of interplanar spacing and angles confirms it has the $Mg_{41}RE_5$ structure (tetragonal crystal structure, a = b = 14.74 Å and c = 10.40 Å [131]). EDS maps in Figure 7.8b suggest that nanoparticles which were not clearly resolved by the SEM images are mainly rich in Y and O, though Nd, Gd, Zr, were also detected. It needs to be noted that the EDS maps here do not reveal the quantitative concentration of the elements. The element concentration of nanoparticles and matrix were collected from selected points (Points A-B marked by red arrows in Fig. 7.8b) and shown in Table 7.2. In the Mg matrix region, all the alloying elements show a concentration below 1 at%. O was also detected, which is believed to come from the sample surface oxidation. In the nanoparticle regions, the concentration of Nd, Gd, Zr is slightly higher than that in the matrix. The concentration of Y is one order of magnitude higher than that in the matrix, reaching nearly 10 at%. The concentration of O is also higher in the nanoparticles, reaching over 10 at%. The atomic fraction between Y to O is close to 2:3, indicating these nanoparticles are highly likely to be Y2O3, yet further characterisation also needs to be done for validation. The Mg signal in the EDS spectra from these nanoparticles is attributed to the interaction volume of the electron beam being larger than the nanoparticles and therefore including signals from adjacent matrix regions. In some of the grain boundaries, alloying element segregation of Nd was also detected, whilst the segregation of other alloying elements were not observed.

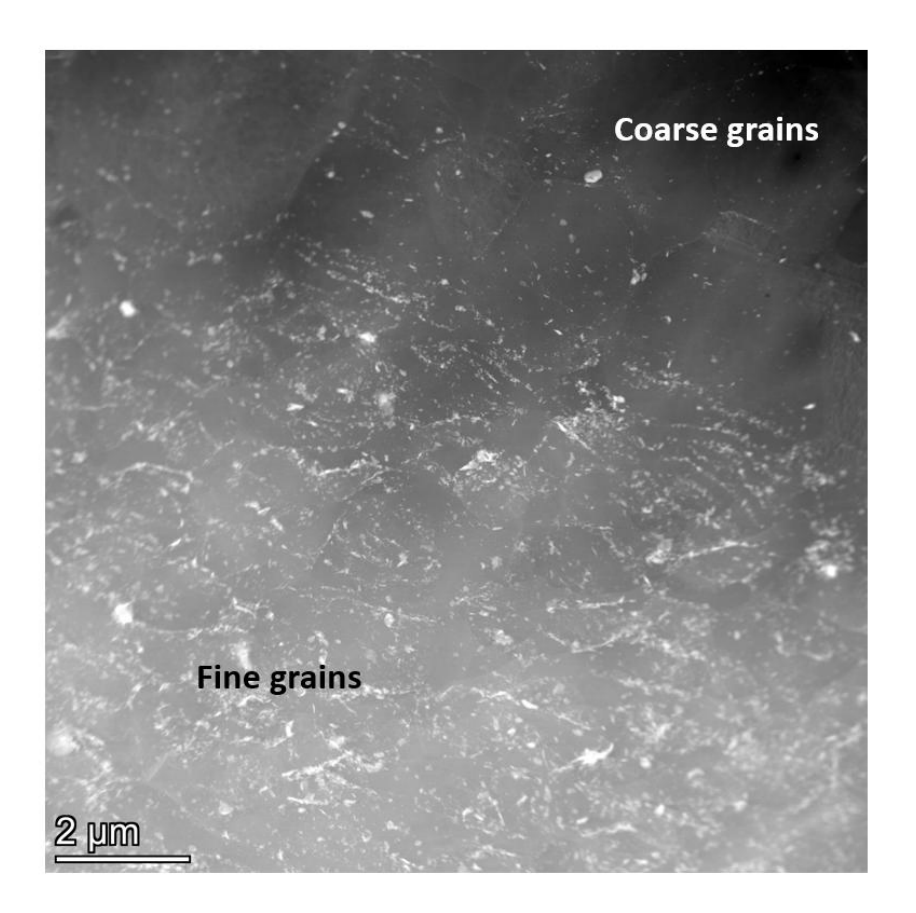


Figure 7.7 TEM-HAADF image showing the second phase difference between coarse grained and fine grained regions

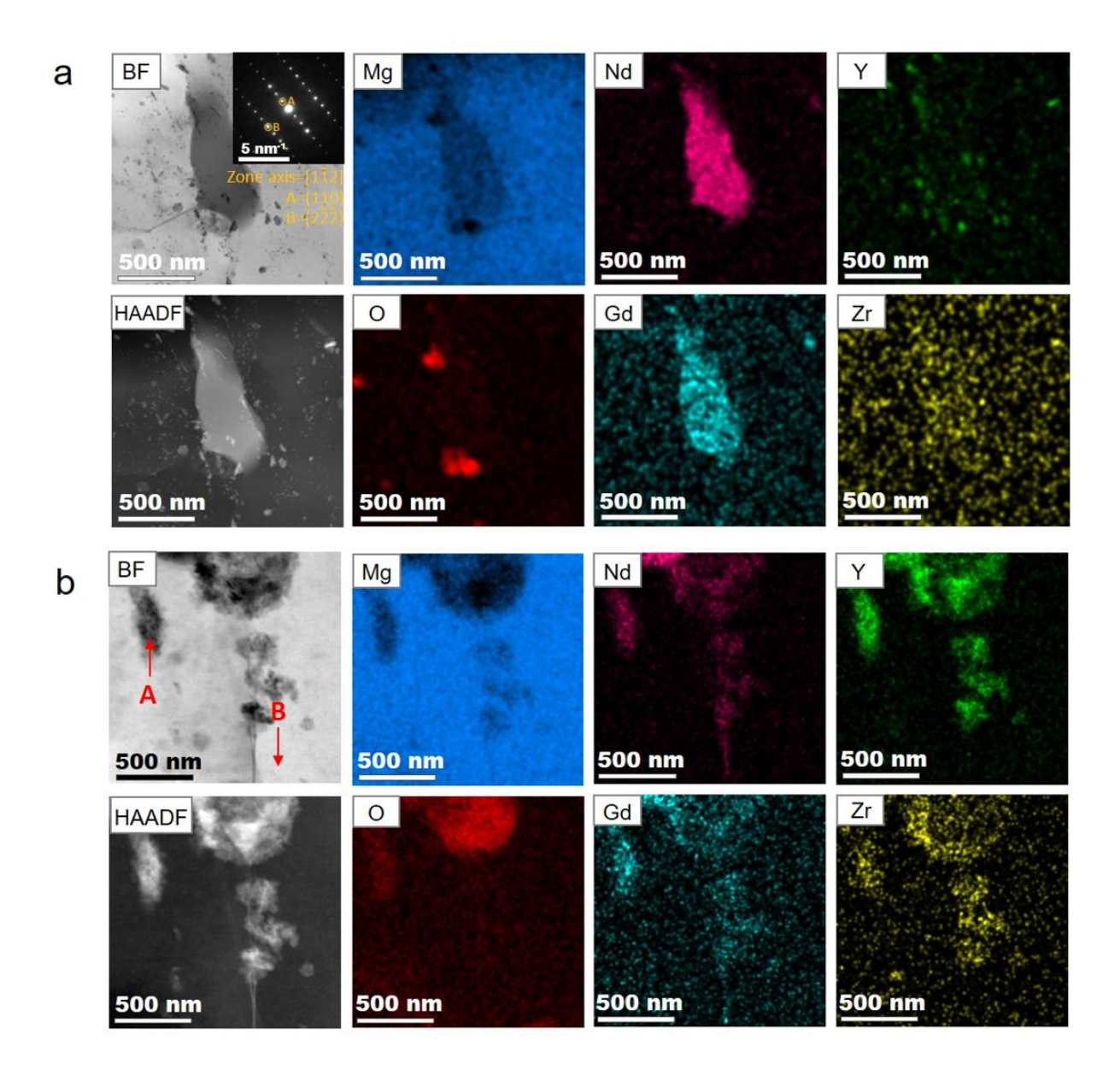
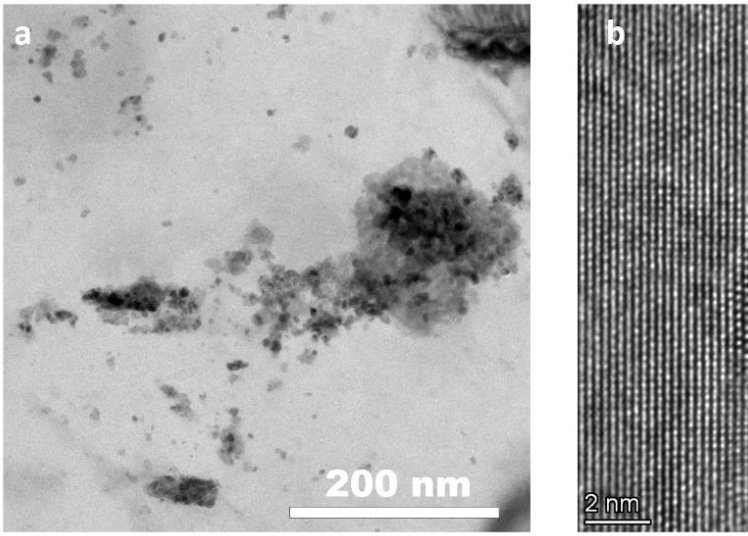


Figure 7.8 TEM images and EDS maps of (a) coarse second phases around 1 μ m (b) nanoparticles in the AFSDed WE43C

Table 7.2 EDS scan results of the nanoparticles in the AFSDed WE43C

	Mg	Y	Nd	Gd	Zr	0
Site A (particle)	76.4%	8.1%	1.3%	0.5%	1.4%	14.1%
Site B (matrix)	90.1%	0.6%	0.2%	0.1%	0.3%	8.7%

TEM-BF images and high resolution TEM (HRTEM) images reveal more detailed structure of the nanoparticles, as shown in Figure 7.9. Some of the nanoparticles are agglomerations of many finer particles instead of a single crystal. The single particles usually have a circular or elliptical shape, and the size mostly ranges from 5-20 nm. They are distributed both in the grain interior and along grain boundaries. Some of the single nanoparticles exhibit orientation relationship with the α-Mg matrix, as shown in Figure 7.9b. The agglomerated particles have irregular shapes, and the size ranges from tens to hundreds of nanometres. This explains why there was a slight increase of Nd, Gd, and Zr concentration in the nanoparticle region, as alloying elements would segregate at boundaries in the agglomerated particles. These agglomerated particles are also distributed both in the grain interior and along grain boundaries.



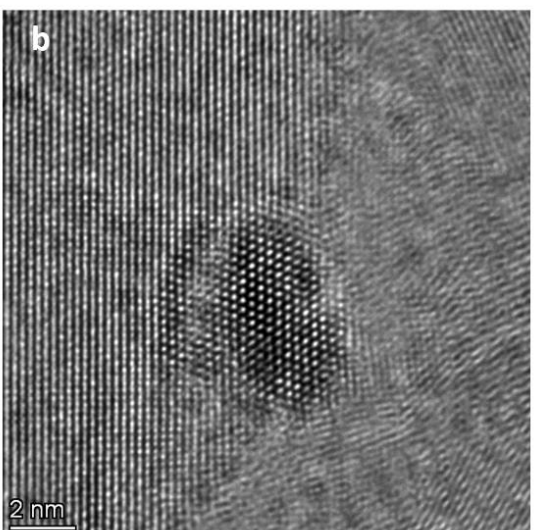


Figure 7.9 TEM images of nanoparticles (a) different structures and sizes, (b) orientation relationship between the single particle and the matrix.

7.2.2.3 Pore structure

Three 3D view images of the pore in the AFSDed material taken from the centre part, middle part, and the edge part are shown in Figure 7.10. The volumes of ROI are represented in the grey cuboids. The surfaces of the internal pores are marked by red colour. The pore size is really small compared to the ROI cuboid and thus cannot be clearly visualised from the

overview image. A magnified picture of a representative pore in Figure 7.10b is presented. The quantitative analysis results suggest that all three sites have a very low fraction of pores. The porosities for all three sites are below 0.01%, in other words, the relative density of the printed material from the centre to the edge are all above 99.99%. The average pore sizes characterised by the equivalent diameter for the centre, middle, and edge part are 19.2 μm, 16.0 μm and 15.5 μm, respectively. Although the average size of the pore in the centre part is slightly larger than the other two parts, considering a voxel size of 3.49 μm was used, it is safe to say that there is no statistically meaningful differences in the pore size along the TD. The Length/Thickness values of three regions are around 3-4, suggesting that the pores are far from the spherical shape. Combining the images, it is clear that the longest measurement of pores is mainly within the LD-TD plane and the shortest measurement of pores is mainly along the BD, which means the pores have flake-like shapes with the thickness direction parallel to the BD.

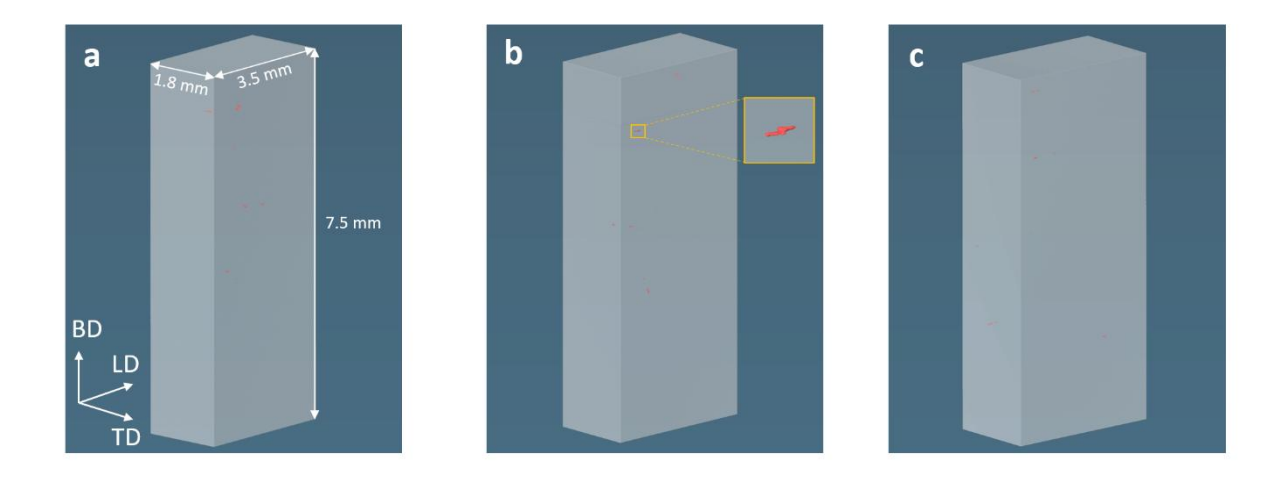


Figure 7.10 3D view of XCT results of of the (a) centre part, (b) middle part, (c) edge part.

7.2.3 Hardness tests of the as-printed WE43C

The hardness test results of the AFSDed component along the TD and the BD are shown in Figure 7.11. Along the TD direction from the centre to the edge, there is an increase of the hardness. The measured hardness values HV0.2 are 75.3±3.9, 78.1±4.4, and 80.0±2.1.

Along the BD direction from the bottom to the top, there are also variations in the hardness. The top part of the AFSDed material exhibited the highest hardness value of 88.1±5.4 HV. When it moves further down to the bottom, the measured hardness HV0.2 are 79.4±1.8, 75.3±3.9, 78.4±2.3, 75.3±3.0, respectively. It is apparent that the hardness values of these four regions are similar but lower than that of the top part.

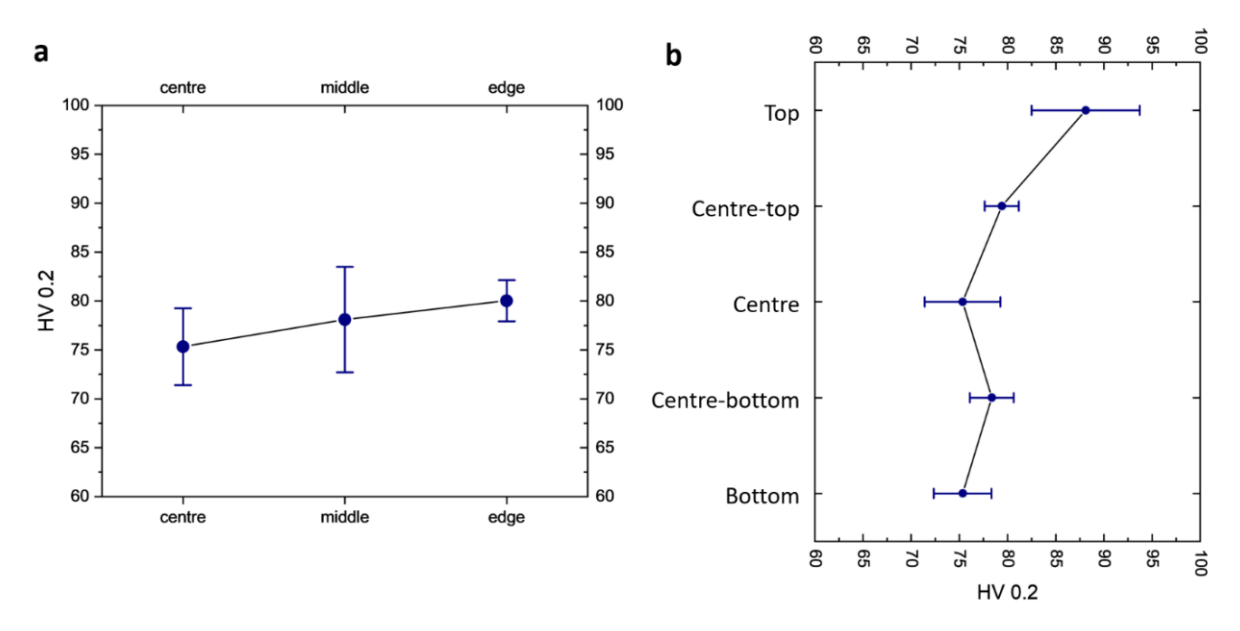


Figure 7.11 (a) Vickers microhardness test results along the TD, (b) Vickers microhardness test results along the BD. Both corresponding to the locations shown in Figure 7.2a

7.2.4 Solid solution treatment (SST) and thermal stability

Since there were dense second phases of Mg41Nd5 in the as-AFSDed material, solid solution treatment (SST) was employed to dissolve them into the matrix and prepare for the following ageing treatment. An extraordinary thermal stability of AFSDed material was discovered in this stage. Grain size evolution of the AFSD and the feedstock samples are provided in Figure 7.12a-d and Figure 7.12e-h, respectively. The average grain size of the AFSDed sample was measured to be 1.05±0.49 μm based on the EBSD IPF map in Figure 7.11a. The UFG structure remained unchanged after 4h-SST at 525 °C, measured 1.03±0.47 μm, as shown in Figure 7.12b. The grain size even remained unchanged after 24h-SST and 72h-SST at 525 °C as shown in Figure 7.12c-d, measured 1.05±0.47 μm and 1.06±0.48 μm,

respectively. In contrast, the average grain size in the non- heat treated feedstock material was measured to be $2.64\pm1.27~\mu m$, but quickly grew to $32.0\pm17.3~\mu m$, $42.0\pm22.1~\mu m$, and $56.5\pm30.3~\mu m$ after being kept at the same temperature for 0.5h, 1h, and 2h, respectively, as shown in Figure 7.12e-h.

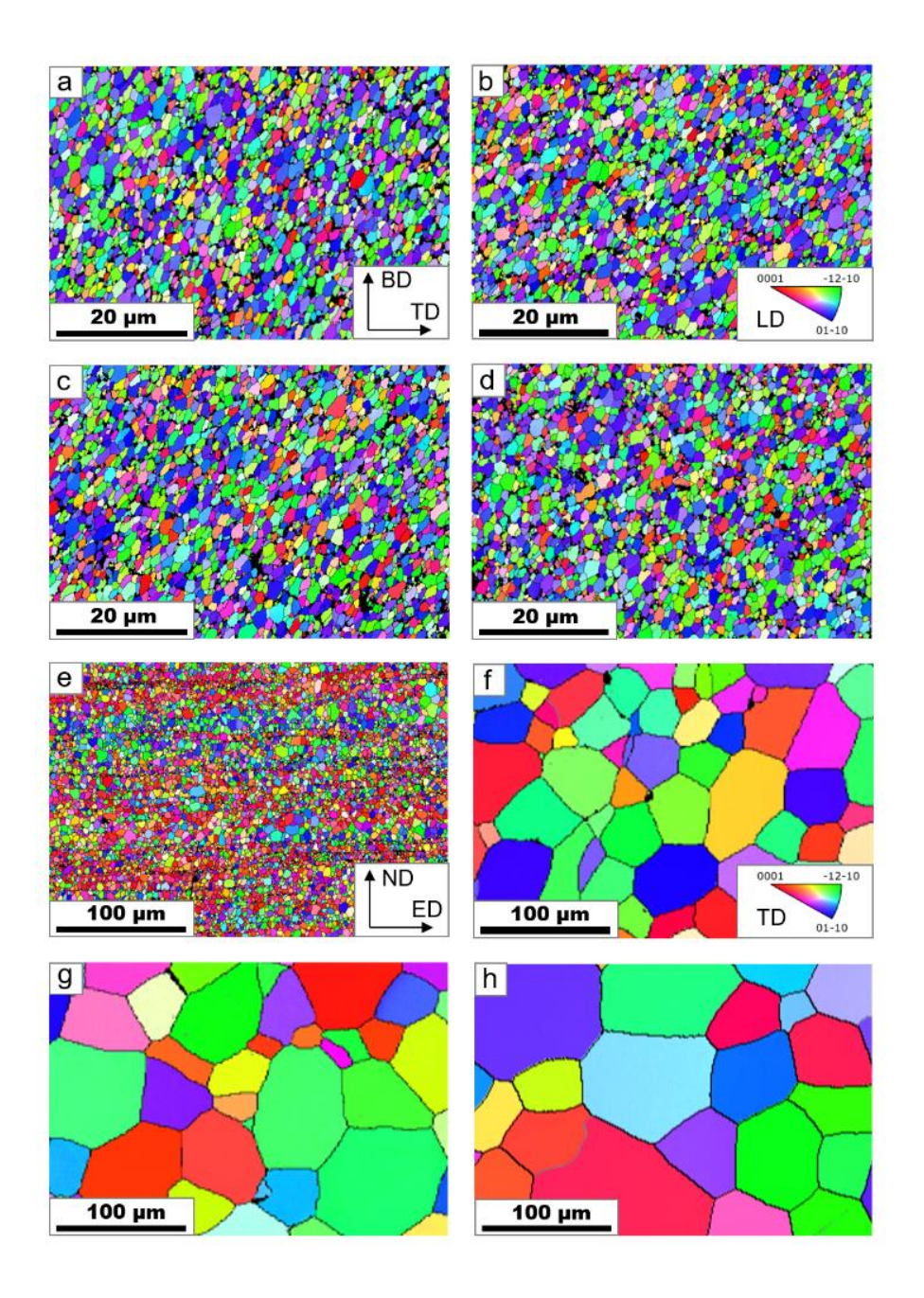


Figure 7.12 EBSD IPF maps of AFSDed samples after SST for (a) 0h, (b) 4h, (c) 24h, (d) 72h, under ×500 magnification. BD is the building direction, TD is the transverse direction, LDis the processing direction (longitudinal direction); and extruded feedstock samples after SST for (e) 0h, (f) 0.5h, (g) 1h, (h) 2h, under ×400, ×150, ×150, and ×100 magnification.

Figure 7.13 shows the second phase evolution in the AFSDed and feedstock sample before and after SST. For the AFSDed sample, the fraction of second phases significantly decreased, as shown in the typical SEM-BSE images (Figure 7.13a, d). As shown in the high angle annular dark field (HAADF) images and corresponding bright field (BF) images (Figure 7.13b, 2c, 2e, 2f), the AFSDed sample contains polygonal second phase particles with a size ranging from hundreds of nanometres to a few micrometres distributed along the grain boundaries. There are also dense fine particles distributed across the entire sample surface. After 4h-SST, those large polygonal second phase particles could no longer be observed, whilst for those nanoparticles, the fraction, size, and distribution remained approximately unchanged (Figure 7.13e). In addition, a few particles with round or tetragonal shape were also observed. For the feedstock sample, there were fine second phases along grain boundaries and large second phases linearly distributed along the extrusion direction (Figure 7.13g). After 2h-SST, second phases along grain boundaries were fully dissolved into the matrix, whilst linearly distributed round and tetragonal shape particles (Figure 7.13h). These residual second phases in both samples are believed to be common inclusions such as cuboidal rare earth compounds (e.g. REH₂, Mg₂₄Y₅) and oxides [48, 155, 160]. Further XRD spectrum in Figure 7.14 show that in the as-AFSDed material, there were Mg₄₁RE₅, Y₂O₃, $Mg_{24}Y_5$, in addition to the matrix α -Mg. It validates that some of the cuboidal phases are $Mg_{24}Y_5$. After 4h-SST, the peaks corresponding to Mg₄₁RE₅ can no longer be seen in the SSTed material. Thermally stable phases, including Y₂O₃ and cuboidal Mg₂₄Y5, maintained after the SST. This is consistent with the disappearance of large second phases in the SEM and TEM images. Further EDS maps in Figure 7.15 and point scan results in Table 7.3 suggest that the nanoparticles in the 4h-SST sample have a similar composition to the as-AFSDed material.

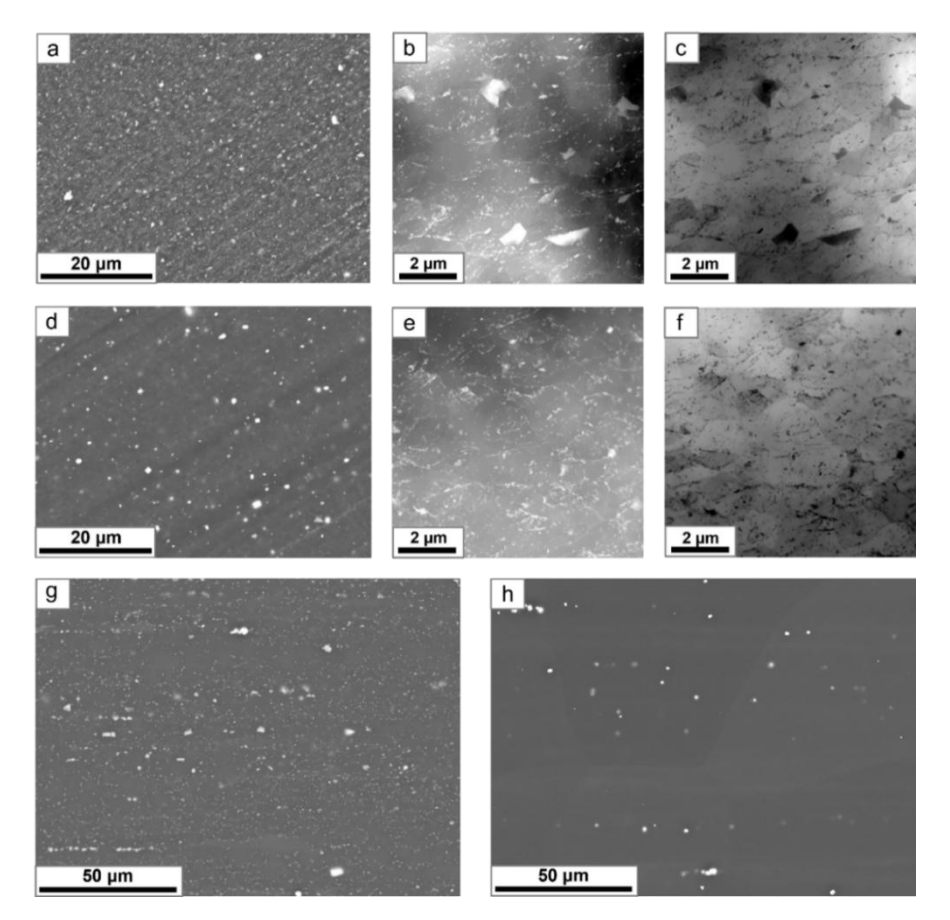


Figure 7.13 AFSDed sample (a) SEM-BSE image, (b) HAADF image, (c) BF image; AFSDed-4h-SST sample (d) SEM-BSE image, (e) HAADF image, (f) BF image; SEM-BSE images of feedstock sample (g) 0h-SST, (h) 2h-SST

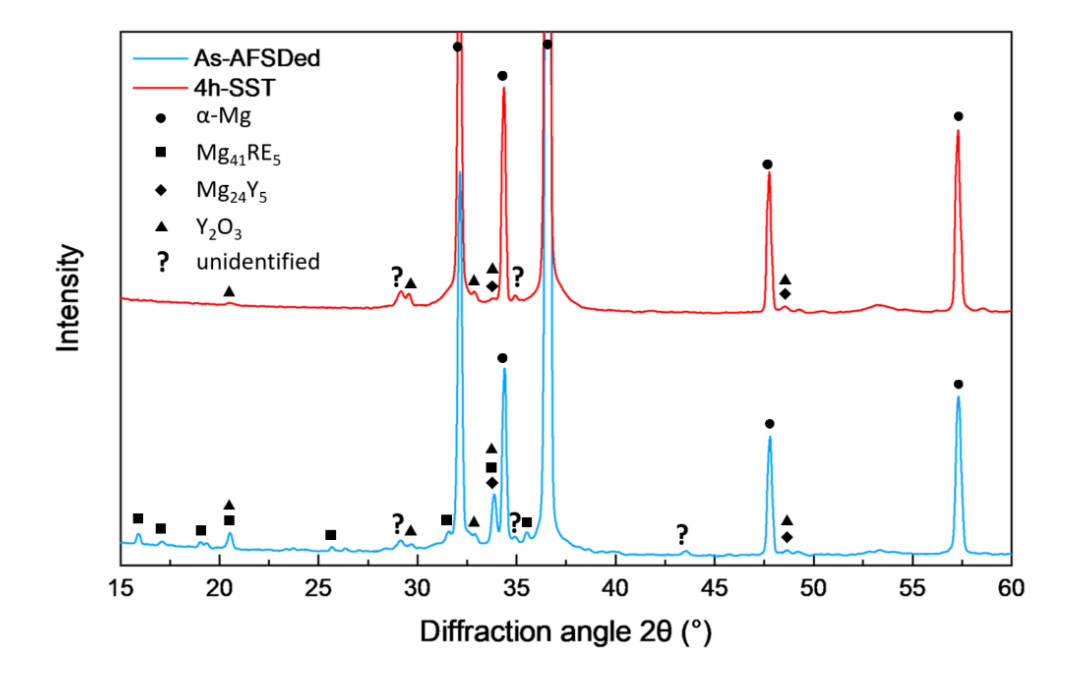


Figure 7.14 XRD spectrum of as-AFSDed material and 4h-SST

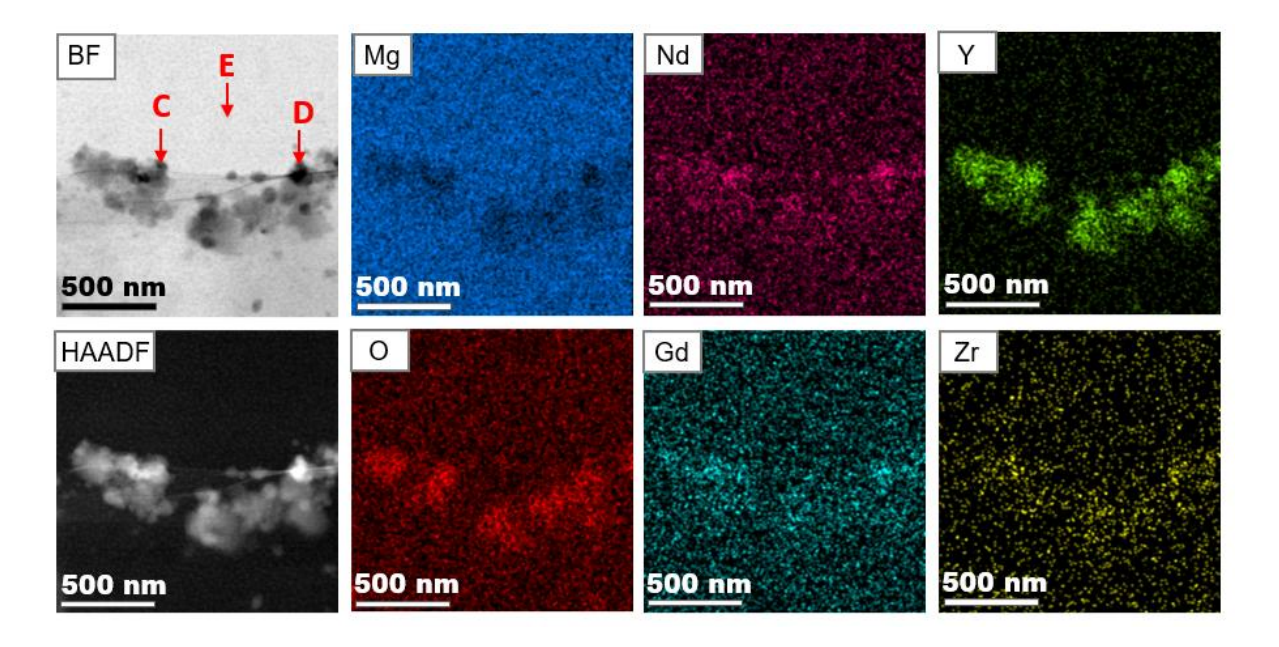


Figure 7.15 BF images, HAADF images, and EDS maps of nanoparticles in the 4h-SST sample

Table 7.3 EDS Chemical composition (atomic %) for regions detailed in Figure 7.14.

	Mg	Y	Nd	Gd	Zr	0
Site C (particle)	79.2%	7.9%	0.8%	0.3%	0.7%	11.1%
Site D (particle)	77.9%	9.1%	1.2%	0.4%	1.5%	10.0%
Site E (matrix)	93.5%	0.7%	0.3%	0.1%	0.2%	5.2%

The nanoparticles interacted strongly with grain boundaries and triple junctions, and key information is marked for illustration, as shown in Figure 7.16. Interestingly, the grain boundary between G3 and G4, which is free of nanoparticles, is relatively straight. Whilst there is significant change of grain boundary curvature (i.e. grain boundary bowing) around the nanoparticles, such as the grain boundaries between G1-G2, and G1-G3. At the triple junction TJ1 where is free of nanoparticles, the angles are around 120°, whilst at TJ2 where

nanoparticles present, the angles are not close to 120°. Such interaction was commonly observed in other regions in the sample, as shown in Figure 7.16d-f, indicated by red arrows.

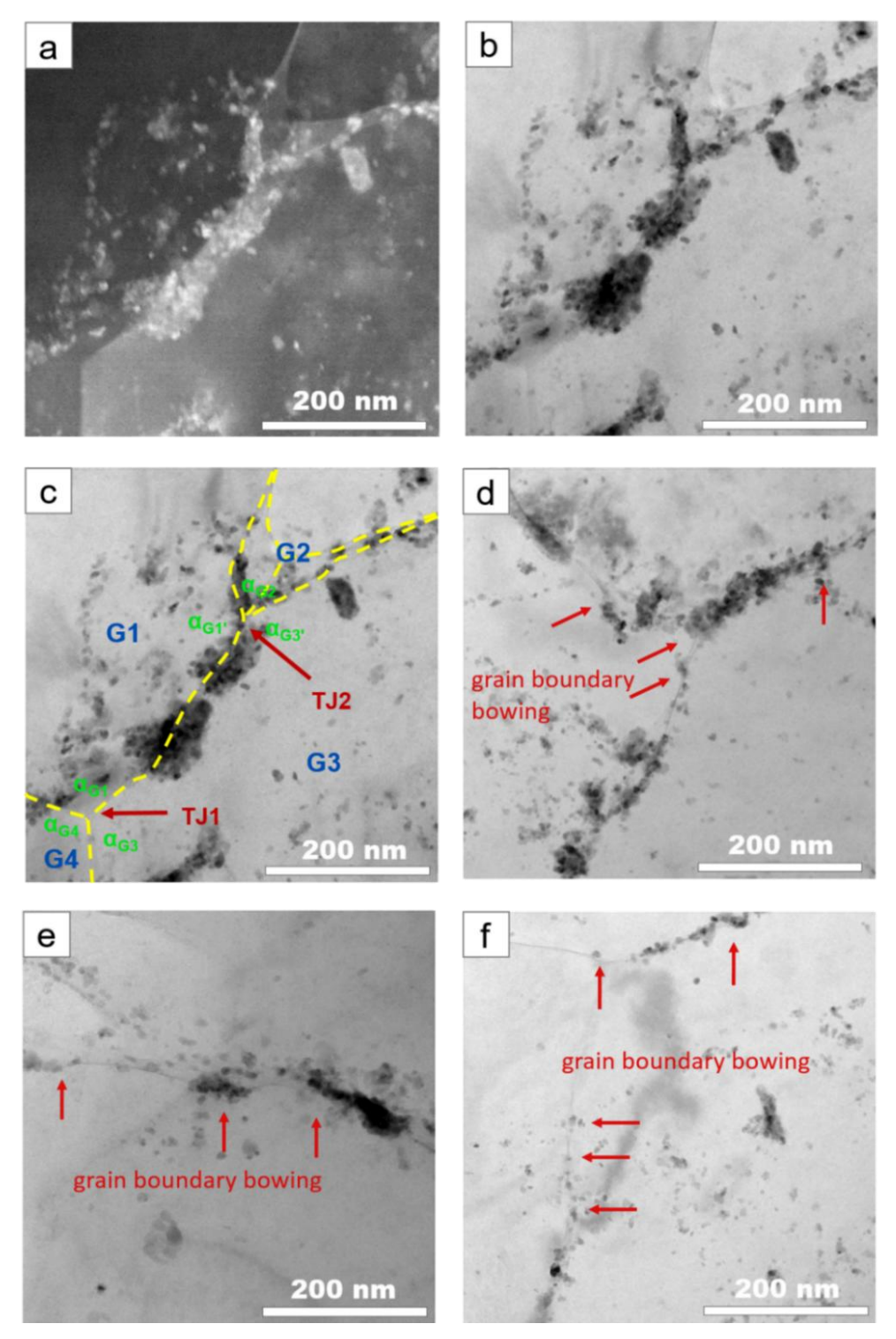


Figure 7.16 S/TEM images of a region in AFSDed-4h-SST (a) HAADF image, (b) BF image, (c) BF image with a sketch of grain boundaries. (d)-(f) BF images of other regions with grain boundary bowing, indicated by red arrows.

7.2.5 Ageing treatment and mechanical properties

In the previous SST experiments, samples were subjected to 525 °C for different periods. Since nearly all the second phase particles except thermal stable Y-rich particles such as possible $Mg_{24}Y_5$ particles and oxides dominated by Y_2O_3 were dissolved into the matrix, and no significant grain growth occurred after SST at 525 °C for 4h, the SST time was determined to be 4h and the following ageing treatment was based on 4h-SST samples. The Vickers microhardness evolution of the 4h-SSTed sample during the ageing is shown in Figure 7.17 below. The hardness decreased from 88.6 ± 2.3 HV to 83.6 ± 3.5 HV after the SST. During the following ageing treatment, the hardness reached the maximum value of 91.7 ± 2.2 HV after holding at 200 °C for about 30-35 h. After reaching the ageing peak, the hardness quickly dropped. The comparison of the hardness of WE43C at different state is shown in Figure 7.18. Compared to the feedstock, the T6 treated AFSD sample exhibited a maximum increase of ~14 HV in hardness.

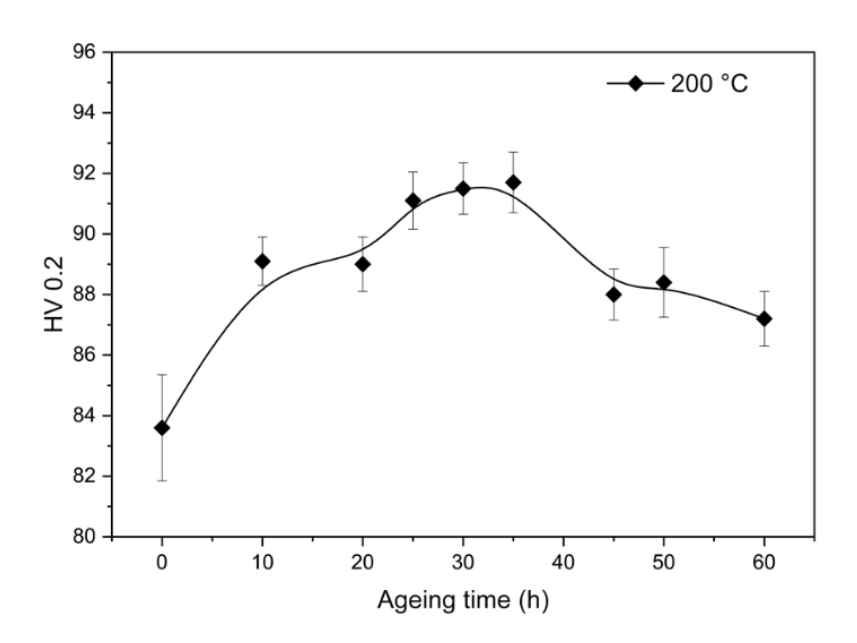


Figure 7.17 Microhardness value evolution during the T6 post heat treatment

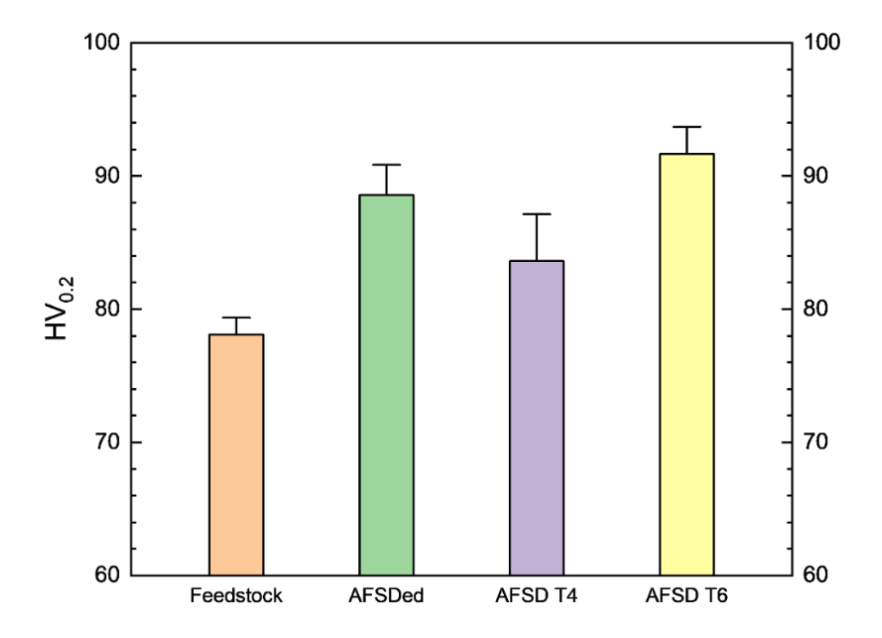


Figure 7.18 Vickers hardness test results of WE43C in different conditions

TEM images reveal the microstructure after the peak ageing treatment, as shown in Figure 7.19. There are two major emerging phases compared to the 4h-SSTed material. In the grain interior, there are dense plate-like nano precipitates. The EDS scan of these particles indicates chemical composition are slightly different. For precipitates along the grain boundaries, enrichment of Nd and Gd was detected, whilst Y did not participate in the formation of those particles. For the precipitates in the grain interior, enrichment of Nd, Gd, and Y were all identified. Further HRTEM images indicate that these precipitates have an orientation relationship with the matrix as shown in Figure 7.20. By measuring the interplanar spacing of the precipitate and the matrix, these precipitates are determined to be β_1 , as the orientation relationship is consistent with $[110]_{\beta 1} \parallel (0001)_{\alpha-Mg}$ and $(\bar{1}12)_{\beta 1} \parallel (1\bar{1}00)_{\alpha-Mg}$, which has been reported in the Mg-Y-RE system [23, 199]. Unlike the plate-like β_1 precipitates, second phases along grain boundaries did not show any orientation relationship with the matrix.

Tensile tests of as-AFSDed along the LD were done by Luxfer MEL. The YS, UTS, and El of the as-AFSDed WE43C along the LD were measured to be 197.0±7.9 MPa, 269.0±4.2 MPa, and 17.6±1.8%, respectively. The collective stress strain curves are shown in

Figure 7.21. The raw data was not provided Luxfer MEL Technologies and thus only a screenshot is shown here. Besides, the T6 treatment was not applied to the tensile specimen as they had other plans on the specimen.

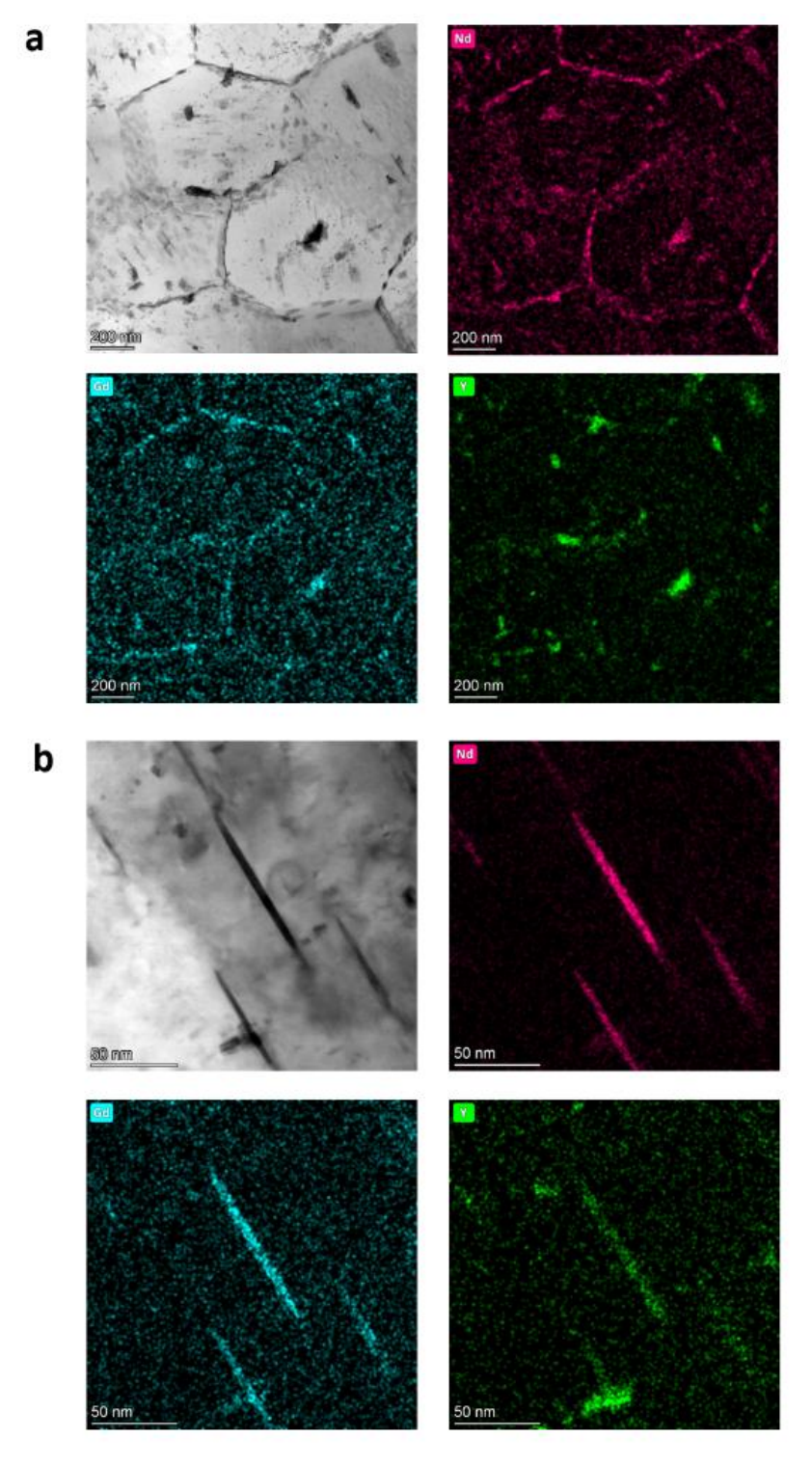


Figure 7.19 TEM-BF images and EDS scans of (a) precipitates at grain boundaries (b) plate-like precipitates in the grain interior.

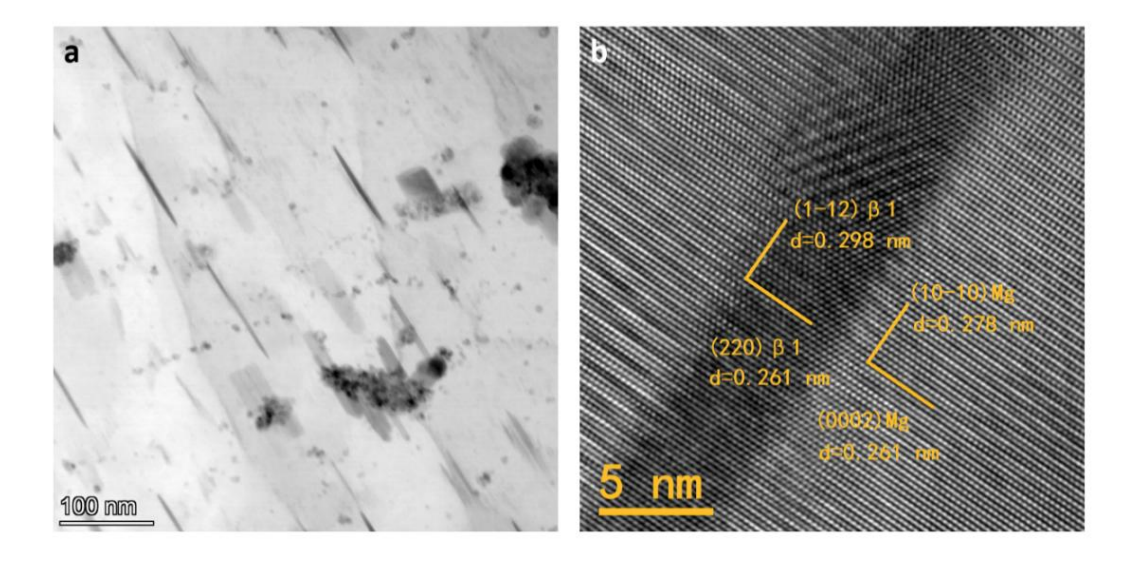


Figure 7.20 (a) STEM-BF images of precipitates (b) HRTEM images of the plate-like precipitate

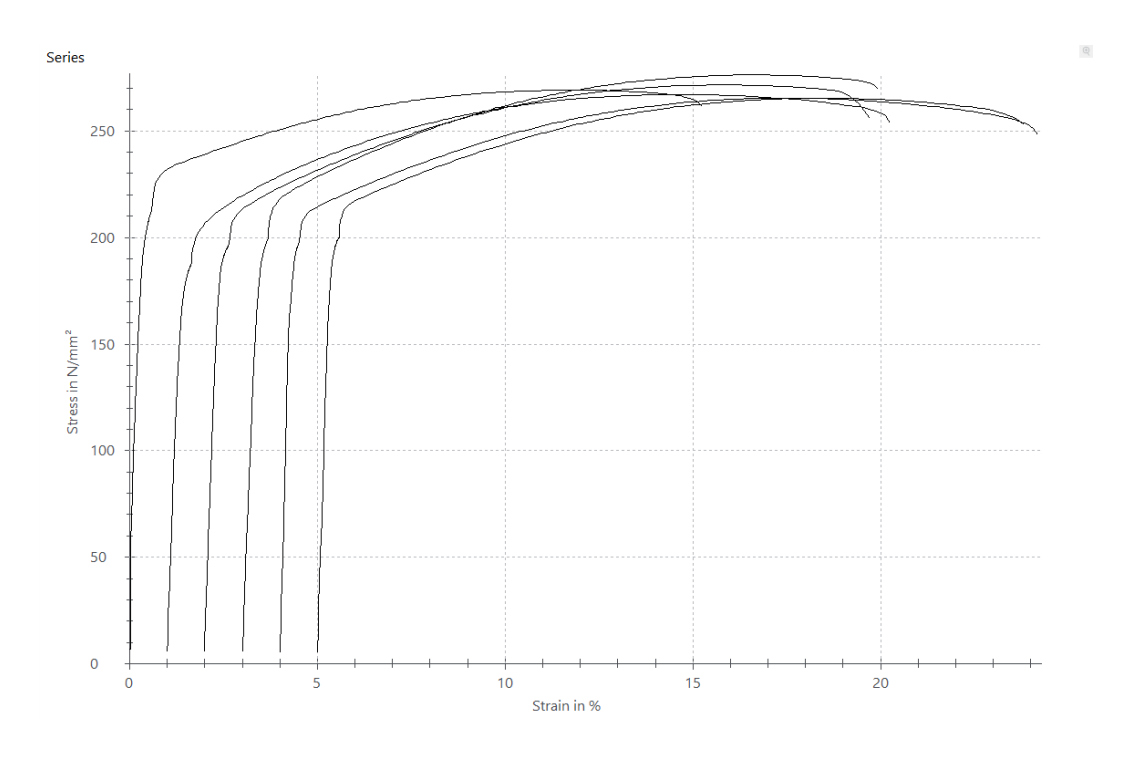


Figure 7.21 stress strain curves of as-AFSDed WE43C, tension along the LD

7.3 Discussion

7.3.1 Microstructure and texture evolution during AFSD

The extruded feedstock exhibited a typical basal fibre texture, with the normal direction of $\{0002\}$ planes perpendicular to the ED and $<10\overline{1}0>$ direction parallel to the ED. During the AFSD, the feedstock was compressed and deformed to fill the gap between the tool and the base material. According to the deformation mechanism of AZ31B Mg alloy during the AFSD proposed by Wang et al. [214], since the initial {0002} planes in the feedstock were parallel to the feeding direction (i.e. BD), the compression of the feedstock can produce extension twins with the orientation of {0002} shifting around 86° in the early stage. Among the 6 possible twin variants, those with basal poles near the north or south poles are favourable due to the high Schmid factor. This may promote the formation of texture with {0002} planes parallel to the LD-TD plane in the early stage of the deformation. Nevertheless, this mechanism may not be suitable to explain the early stage of texture evolution in this work, as the average grain size of the feedstock was only about 2.6 µm. The small grain size can suppress the formation of twins. The following stage, when the feedstock material was extruded out and squeezed to fill the gap between the tool and the base material, is believed to play a key role in the final texture formation. The material flow is confined within the LD-TD plane, which is revealed by the SEM images of flow lines in the AFSDed material. The intense material flow within the LD-TD plane with elevated temperature and high strain is favourable for the alignment of <0002> with the BD. The basal pole of the material slightly shifted away from the BD, and this is believed to be the result of the different constrains from the top and bottom surface of the material during the deposition process. The bottom surface of the deposited material achieves metallurgical bonding with the base material, whilst the top surface of the deposited material only have friction interaction with the bottom surface of the tool. This imbalance between the interaction form the top and bottom surface of the deposited material leads to the slight shift of the material flow behaviour away from the LD-TD plane and causes the basal pole shift. This is consistent with the finite element modelling (FEM) based pseudo-mechanical thermal model proposed by Sharma et al. [215]. Their model pointed out that the upper and lower part within the deposited layer undergoes different strain and strain rate, especially around the edge part of the deposited layer. The lower part is closer to a stationary state.

There were significant coarse grained regions and fine grained regions in the AFSDed material, and with the increase of the distance away from the central line, there was an increase of the fraction of fine grains and a drop in the average grain size. In the coarse grained regions and fine grained regions, the second phase particles also exhibited differences regarding the size and distribution. The formation of this special heterogeneous microstructure with gradient can be attributed to the characteristics of the AFSD processing. Sharma et al. proposed an equation to predict the DRX grain size in the AFSDed material [215], which is expressed as:

$$D = CZ^{(\frac{4}{n}-1)}$$
 (7.1)

where D is the average grain size after DRX, C is a fitting constant, Z is the Zener-Hollomon parameter, n is the stress exponent. The Zener-Hollomon parameter Z is defined as

$$Z = \dot{\varepsilon} \exp\left(Q/RT\right) \tag{7.2}$$

Where $\dot{\varepsilon}$ is the strain rate, Q is the activation energy of lattice diffusion of the material, R is the gas constant, and T is the temperature during the processing. This empirical equation successfully predicted the average grain size in an AFSDed AZ31B material, which exhibited a larger grain size in the centre part but smaller grain size at the edge part. In this work, the stress exponent could not be evaluated as it is a material-dependent parameter and there is lack of data about WE43C. Thus, another empirical equation which was proved to be consistent with their equation is used here. Chang et al. proposed empirical equation aiming at evaluating the grain size in the FSPed material [92-94], which is

$$lnD = c - klnZ \tag{7.3}$$

where D is the average grain size, C is a constant depending on the material, E is a parameter depending on the material, and E is the Zener-Hollomon parameter. Although quantitative analysis cannot be applied due to the lack of corresponding data, qualitative analysis is still possible. It is apparent that the most fundamental factors influencing the final grain size are the strain rate E and the processing temperature E. The final grain size increase with the increase in E and the decrease in E. For the AFSD process, the overall strain rates E for different site from the centre to the edge are expected to be similar. The processing temperature E is higher at the centre and lower at the edge. This is mainly due to the temperature gradient along the TD caused by faster heat transfer at the edge and the heat accumulation in the centre of the deposited material, which has been revealed by the simulation and experiments [128, 215]. In addition, the number density of nano-oxide particles is higher in the edge region compared to the centre region. This also contributes to the grain refinement at the edge region by Zener pining. Details of the effects of these nanoparticle will be discussed in the later section. These factors lead to the decrease of the grain size from the component centre to the edge.

In addition to the grain size variation along the TD in macro-scale, there was a significant size difference in a small region, as shown in the SEM images and EBSD map. The formation of such structure will be divided in three stages, as shown in Figure 7.22. The first stage is the deposition of the material, which will be referred to as Layer A. During this stage, the local strain and strain rate variation in the Layer A leads to the grain size difference. Although the work of FEM did not show the abrupt change of strain or strain rate at local region [216], experiments [101, 130] and smoothed particle hydrodynamic (SPH) modelling [128] which is a mesh free method, showed that there could be significant history of the adjacent material during the AFSD process. Meanwhile, it is not possible to have micro-scale regions with significantly higher or lower temperature during the AFSD processing. As a result, the formation of coarse grained and fine grained regions in Layer A is mainly attributed to the local strain rate difference. The second stage is when the deposition of the next layer of the material

which will be referred to as Layer B on the deposited layer (i.e. Layer A). During this stage, the condition of the Layer A is similar to the aforementioned TMAZ. The deposited material Layer A is heated again due to the friction. At the same time, the deposition of the Layer B inevitably generates some minor deformation by shearing and torsion. The deformation is not significant enough to produce further DRX, but dynamic recovery (DRV) can still occur, whilst due to the strengthening by grain boundaries, no noticeable change in microstructure happen in the fine grained regions. During the deposition of the next layer which is Layer C, Layer A is no longer affected by the deformation but only affected by the transferred heat. Only limited static recovery can occur. Because of the presence of nano oxide particles and relatively low driving force of both DRV and SRV, the recovery process is significantly suppressed and thus a higher level of GOS values is maintained in the coarse grained regions. This high GOS value is becoming more significant when it is going toward the edge part, as the temperature is lower compared to the centre part and thus the recovery is much less active.

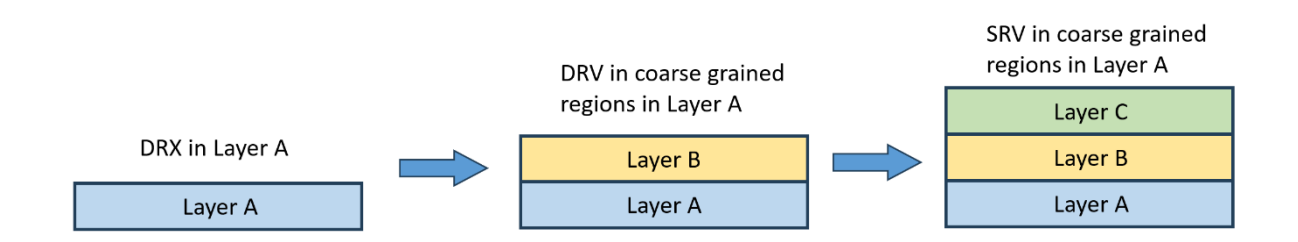


Figure 7.22 A schematic of the grain evolution history during the AFSD

In the AFSDed material, there were two major second phase particles. The first one is the Mg₄₁RE₅ at grain boundaries and triple junctions, which is a common second phase in Mg-Y-RE alloys. The second one is the nanoparticles in the grain interior and along grain boundaries. These nanoparticles were not observed in the feedstock and therefore formed insitu during the AFSD process. The high temperature generated by friction and surface exposure to air enables the rapid formation of oxides. Considering the relatively low temperature (i.e. solid state processing) and short exposure time during the AFSD process,

the formed oxide particles remained the nano-size. In addition, the mechanical stirring generates material flow, re-distributing particles in the material [192]. The protrusions on the tool (i.e. 'teardrop' structures, see Figure 3.8) assisted material flow along the building direction. This allows oxides to be redistributed throughout the deposited material instead of staying on the surface layer. Regarding the chemical composition of oxide particles, Zhao et al. [186] pointed out that the very initial oxidation stage involves the formation of zirconium oxides, magnesium oxides, and yttrium oxides, and later only yttrium oxides remain. Soderlind et al. also [73] suggested that magnesium oxide would transform to yttrium oxide at elevated temperatures. Such evolution is consistent with the Gibbs free energy of the formation of the alloying element oxides [217]. Y has the lowest Gibbs free energy when forming oxides and thus yttrium oxide is more thermodynamically stable, compared to other alloying elements and Mg. Although there is lack of direct observation of the oxide evolution in the AFSD process, based on EDS results in this work, oxidation process by other researchers, and thermodynamic data, the oxide formation process during AFSD and the following SST can be summarised. At the early stage of oxide formation, there is mainly Y₂O₃, yet small amount of other phases will also form, including ZrO₂, MgO, possibly Nd₂O₃, and Gd₂O₃. There is also possibly ternary oxide, such as Y₂Zr₂O₇. In the following heat treatment process, alloying elements in the less stable oxides (e.g. Mg and Zr) will be substituted by other elements which can form more stable oxides (e.g. Y). In other words, the process that less stable oxides transform to more stable oxides will be activated during the following SST. Considering the negligible solubility of O in metallic materials, further formation of new oxide nuclei or change in oxide fraction is not possible during the following heat treatment.

The pore formation in the AFSDed component is closely related to the material flow and tool design. Due to the protrusions on the tool bottom surface, when the material is extruded from the feedstock and fill the gap between the tool and the base material, the deposited material will interact with the protrusions. This can leave some minor pores between the deposited material and the protrusions under the high rotation condition, suggested by

Agiwal et al. [209]. Because of the strong material flow within the LD-TD plane, the pores tend to become thinner along the BD. This is one of the negative effects of the tool surface protrusion design. This design aims at achieving a better bonding between each layer by weakening the material flow within LD-TD planes to some extend and increase the material flow ability by generating more friction heat from the protrusions. It also leads to the formation of some micro voids in the deposited layer. Nevertheless, the porosity remained at a relatively low level, which is far smaller than 0.1%. This indicates the relative density of the AFSD is evidently higher than those traditional AM technologies, including LPBF, DED, etc [39, 131, 134, 218, 219].

7.3.2 SST and Thermal stability

7.3.2.1 Grain growth behaviour

The change of grain size with temperature is plotted in Figure 7.22. The rapid grain growth behaviour was observed in the WE43C feedstock sample. The grain size increased by over 21 times after keeping at 525 °C for 2h. Such quick grain coarsening at elevated temperatures in Mg-4Y-3RE has also been widely reported by other researchers [33, 48, 108]. However, there was no statistically meaningful grain growth in the AFSDed material. To quantitatively evaluate the difference in grain growth behaviour between the feedstock and the AFSDed material, the following equation [191] is applied:

$$D^n - D_0^n = ct \qquad (7.4)$$

where D_0 is the initial grain size, D is the final grain size, n is the grain growth exponent, t is the dwelling time, and c is the grain growth constant that describes the rate of grain growth. For the grain growth in this work, the initial grain size D_0 and the final grain size D were measured from the EBSD maps, and the time t was recorded. The grain growth exponent t0 depends on the material and sometimes also the temperature. The grain growth exponent t1 of the feedstock can be extracted from Figure 7.23a by analysing the relationship between t3 ln(dD/dt) and lnD [220, 221], which is determined to be ~2.5. It should also work for the

AFSDed material which were heat treated at the same temperature. Thus the relationship between $D^n - D_0^n$ and t can be plotted. The slope from Figure 7.23b is the grain growth rate c, according to Equation (7.4). The grain growth rate c of the feedstock is calculated to be 200 μ m^{2.5}/min. For the AFSDed sample, as $D \approx D_0$, the value of the grain growth constant c is nearly 0, indicating complete grain growth stagnation. This result statistically shows the extraordinary thermal stability of the grain structure in the AFSDed material.

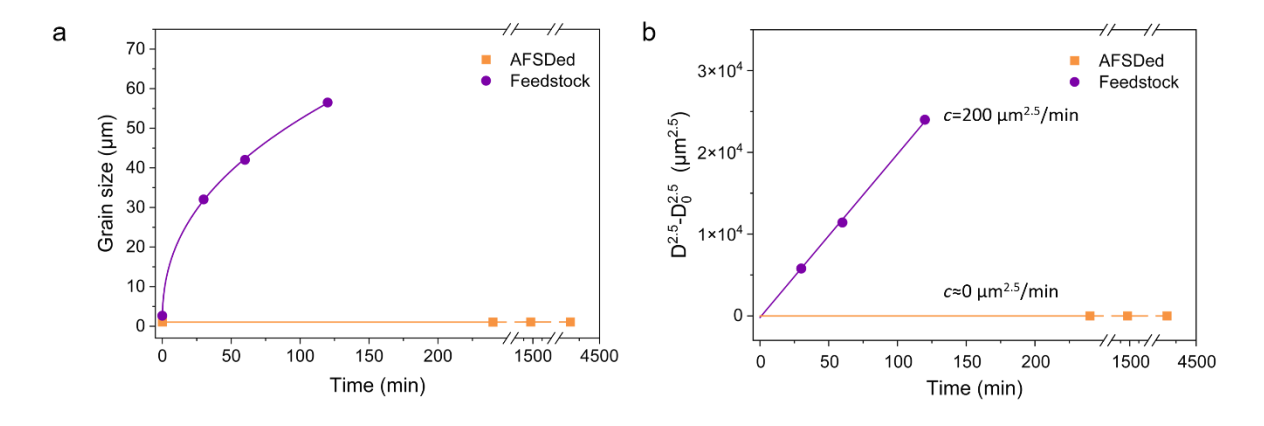


Figure 7.23 (a) Grain size change with time, (b) Plot of $D^{2.5}-D_0^{2.5}$ against time

7.3.2.2 Driving force and retarding force of the grain growth

To understand the significant difference in the grain growth rate for the material with the same chemical composition, it is worth carrying out a detailed analysis from the perspective of the driving force and the retarding force. Two major sources of the driving force for grain boundaries to migrate are the stored deformation energy and the stored surface energy in the grain boundaries. The stored deformation energy promotes the grain boundary migration by recrystallisation. Grain orientation spread (GOS) maps of the AFSDed sample and the feedstock are shown in Figure 7.24. Grains with a GOS value smaller than 2° are regarded as recrystallised grains. The recrystallisation fraction measured from the map was 87% for the AFSDed sample and 93% for the feedstock. Both samples showed a highly recrystallised structure and the contribution of stored deformation energy should be similar and negligible. The surface energy stored in the grain boundaries promotes a system to reduce the grain boundary area by grain growth, which is driven by the boundary curvature

and thus closely related to the grain size. The driving force originates from the curvature is described as [33]:

$$P_c = \frac{4\gamma}{D} \tag{7.5}$$

where P_c is the driving force by grain boundary curvature, γ is the grain boundary energy, D is the grain size. Both samples have the same grain boundary energy $\gamma \sim 0.4$ J/m² [33]. Then the driving force provided by the grain boundary curvature in the AFSDed sample should be nearly twice that in the feedstock, since the average grain size in the AFSDed sample is only about half of that in the feedstock. In addition to the boundary curvature, texture components sometimes play an important role in boundary mobility [191, 222]. In Mg alloys, it has been reported that grains with (0001) <11 $\bar{2}$ 0> texture components tend to grow quicker than other grains [223], which is the case for the AFSDed sample, as shown in the Figure 7.25 Nevertheless, at elevated temperatures (e.g. 525 °C in this work), such preferential grain growth is believed to be significantly extenuated [223]. In summary, the overall driving force for grain growth in the AFSDed material is expected to be higher than that in the feedstock.

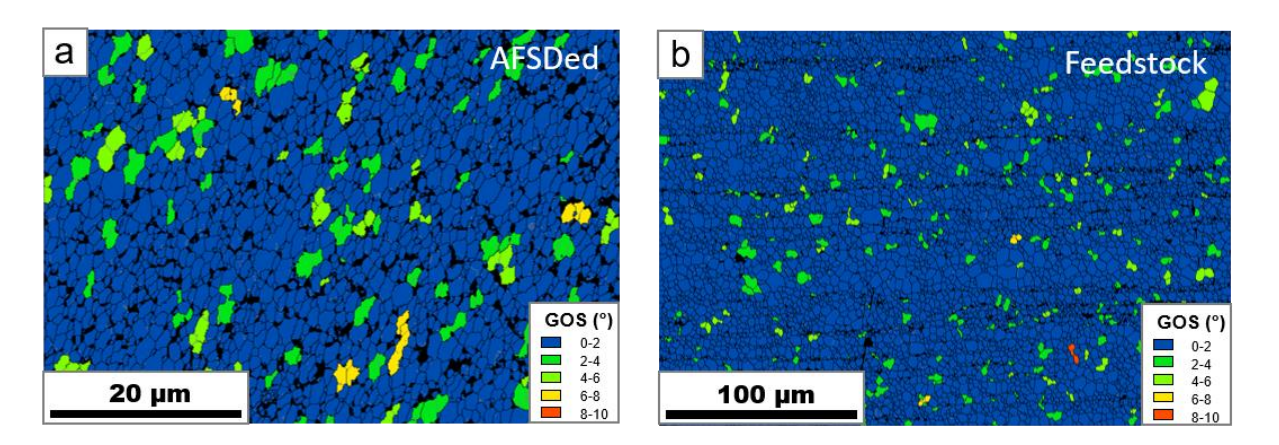


Figure 7.24 GOS maps of (a) AFSDed sample; (b) feedstock material

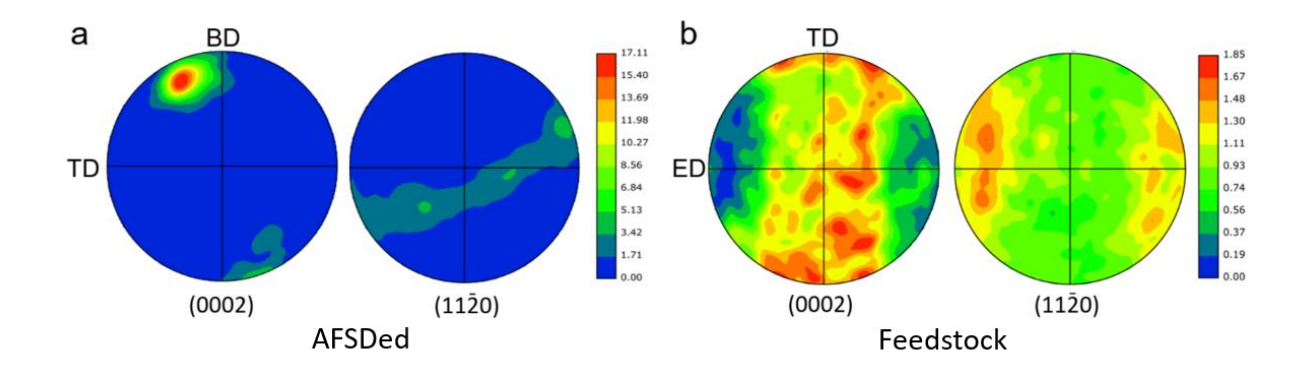


Figure 7.25 Pole figures of (a) AFSDed sample, (b) feedstock material

However, the experiment results suggested that there was rapid grain growth in the feedstock but grain growth stagnation in the AFSDed material. This indicates that there must be strong retarding force in the AFSDed material. There are two major microstructural factors retarding the grain boundary migration, grain boundary solute segregation [22, 224] and particles [20, 191, 196, 224]. The solute atoms segregating at grain boundaries apply retarding force by solute drag [191]. However, the solute drag effect has been reported to become negligible at elevated temperatures [32, 33, 108]. Particles can also effectively retard grain growth by pinning the grain boundary and triple junction movement [181, 225]. Despite the effectiveness of particle pinning, the SST temperature is expected to promote the dissolution of Mg-Y, Mg-RE, or Mg-Y-RE phase (e.g. the Mg₄₁RE₅ phase), into the matrix and thus rendering most of the particles ineffective in the restriction of grain growth [33], which is the case for the feedstock material. There were small amount of residual large particles which are believed to be large oxides and rare earth hydrides, but they did not exhibit effective pinning effects. In contrast, in the AFSDed-4h-SST sample, nanoparticles did not show any statistically meaningful change in size, distribution, and density after a long period of holding at 525 °C, exhibiting exceptional thermal stability. There is no doubt that these nanoparticles play a fundamental role in grain growth stagnation.

7.3.2.3 Effects of nanoparticles

The interaction between nanoparticles-grain boundaries and nanoparticles-triple junctions was observed in AFSD-4h-SSTed sample as shown in Figure 7.16. The significant grain boundary bowing indicates that the nanoparticles contribute to the pinning of grain boundary movement during the SST, which is usually referred to as Zener pinning [191]. The driving force of grain growth and Zener pinning force is usually expressed as [33, 191]:

$$P_z = \frac{3f\gamma}{2r} \tag{7.6}$$

$$P_{z\prime} = \frac{Df\gamma}{4r^2} \tag{7.7}$$

where f is the volume fraction of particles, r is the radius of particles, P_z is the Zener pressure when particles are distributed randomly, $P_{z'}$ is the Zener pressure when particles are fully distributed at grain boundaries. It is obvious that for Zener pining, in addition to the grain boundary energy γ , the pinning force is also influenced by the volume fraction and size of the particles. A larger volume fraction of particles and smaller particle size can generate stronger Zener pinning force. The particle distribution also affects the effectiveness of Zener pining, and the grain size needs to be considered for the situation when particles accumulate at grain boundaries. There is a limiting grain size for Zener pining when the driving force is equal to the Zener pinning force, and it can be calculated as [191]:

$$D_z = \frac{8r}{3f} \tag{7.8}$$

$$D_{z'} = \frac{4r}{\sqrt{f}} \tag{7.9}$$

where D_z is the Zener limiting grain size when $P_z = P_c$, D_z , is the Zener limiting grain size when $P_z = P_c$, corresponding to the two different particle distribution situations in the AFSDed sample, D was measured to be around 1.05 μ m, f and r was calculated by using ImageJ to be about 0.07 and 32 nm, respectively. It is clear that P_z , is larger than P_z in this situation. This means in the AFSDed sample, the preferential distribution of nanoparticles at grain boundaries provides stronger pinning effects, compared to the random distribution, and the equilibrium grain size should fall between D_z and D_z . D_z was calculated to be about 1.37

 μ m and $D_{Z^{\prime}}$ was calculated to be about 0.48 μ m. This is consistent with the measured grain size of 1.05 μ m, verifying the role of Zener pining and the effectiveness of grain boundary accumulation.

For triple junction sites, there should be an angle of 120° when three grains meet at the vertex, to achieve the balanced state. This is often expressed as the following equation [191]:

$$\frac{\gamma_{12}}{\sin \alpha_3} = \frac{\gamma_{13}}{\sin \alpha_2} = \frac{\gamma_{23}}{\sin \alpha_1}$$
 (7.10)

where α_1 , α_2 , α_3 are the corresponding angles opposite to the boundaries. This is the case for the TJ1 in Figure 7.16, where no nanoparticles are present. The boundary tension forces are similar and the three angles α_{G1} , α_{G3} , α_{G4} are around 120°. For TJ2 where G1, G2, and G3 meet, the angles $\alpha_{G1'}$, α_{G2} , $\alpha_{G3'}$ are away from 120°. This is because the nanoparticles provide an extra restraining effect, bringing it to a balanced state without achieving angles equal to 120°.

7.3.3 Mechanical property evolution during the ageing heat treatment

In the AFSDed material, there was a gradient in the hardness along the TD. This is believed to be mainly attributed to the refinement of grains when it is approaching the edge of the printed component, which is the major difference along the TD. In addition, the slightly higher number density of nanoparticles is another factor contributing to the strengthening at the edge part. The top layer of the AFSDed material also exhibited higher hardness values compared to other regions, which is also the result of grain refinement. The top layer of the material did not go through rounds of thermal cycles and thus a finer grain structure was maintained in the top layer, whilst the lower part of the AFSDed material which were subjected to several thermal cycles, experienced grain growth and thus the effectiveness of grain boundary strengthening decreased.

In addition to the strong pinning effects on grain boundary movement, the nanoparticles also contribute to the hardness increase, which is straightforward when making comparisons between the feedstock and the AFSDed material. The hardness of the AFSDed sample is ~10 HV higher than that of the feedstock. The hardness contribution from grain boundary strengthening can be calculated by the following equation:

$$\Delta H V_{GB} = Ckd^{-1/2} \tag{7.11}$$

where C is the yield strength-micro hardness proportional constant ~0.3 HV/MPa, and k is Hall-Petch constant for Mg-Y-RE alloys ~40.7MPa· μ m^{1/2} [33]. Considering the minor grain size difference between 1.05 μ m and 2.64 μ m in two samples, ΔHV_{GB} difference can be calculated ~4 HV, smaller than the overall difference ~10 HV. Oxide nanoparticles are believed to provide extra strengthening effects in addition to the grain boundary strengthening [88, 194-196]. While systematic investigations of the effects of thermally stable nanoparticles on grain boundaries in magnesium alloys remain in the initial stages, it is well known that in ODS alloys, dispersed oxides improve mechanical properties at elevated temperatures, inhibiting the dissolution of strengthening precipitates, grain growth, grain boundary sliding, and grain rotation [88, 194, 195]. The influence of oxide nanoparticles on grain growth has been discussed in this work and other aforementioned potential effects will be investigated in the future.

In the following SST, there was a drop in the hardness due to the dissolution of second phase particles. The strengthening effects from hard second phase particles were removed, though the solid solution strengthening was enhanced. Further ageing treatment produced fine β_1 and acts as effective obstacles for dislocation movement, which was discussed in detail in the previous chapter. The peak ageing time was similar that for the SS-FSC extruded and FSPed material. However, the T6 treatment is expected to drastically increase the hardness of the material, yet the peak aged material only exhibited an increase of \sim 8 HV, which is even lower than the hardness improvement in the T5 treated SS-FSC extruded and FSPed WE43C

counterparts. One reason was discussed in the previous chapter, which is the reduced precipitation of β_1 phase in the grain interior due to the refined grains. The other one is the formation of intense oxides reduces the solute alloying elements. This means the potential maximum precipitates which can form during the ageing treatment, even if a SST is operated, are significantly reduced. In other words, the AFSDed material, when subjected to ageing treatment, does not respond as Mg-4Y-3RE but as Mg-(4-x)Y-(3-y)RE. The fewer alloying elements lead to a drop in the ageing peak.

Results of the as-AFSDed samples showed a good combination of strength of ductility, as shown in Figure 7.25. Compared to WE43C fabricated by all other methods, AFSDed material exhibited intermediate strengths but significantly higher ductility. The reason for the strength-ductility combination is believed to be the bimodal grain structure in the AFSDed WE43C. Zhang et al. [167] suggested that the individual role and synergy effects from fine grains and coarse grains contribute to an enhanced ductility in Mg alloys. At the early stage, the deformation is mainly accommodated by the fine grains. With the ongoing of tension, when the stress level exceeds the CRSS value of the pyramidal slip, coarse grains can play a major role in dislocation storage.

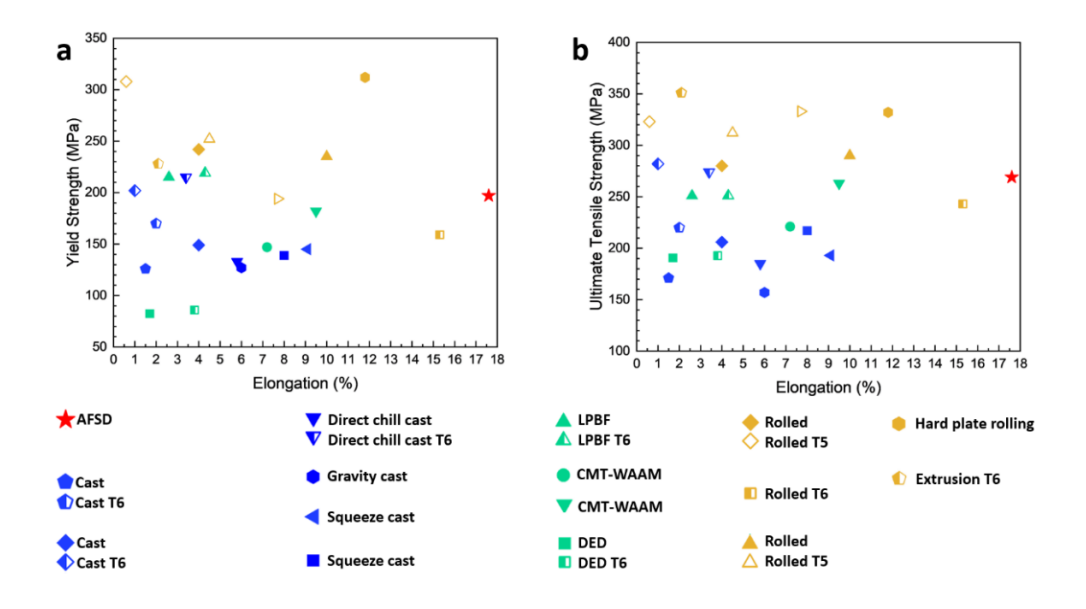


Figure 7.26 Scattered point plot of mechanical properties of Mg-4Y-3RE alloys prepared by various methods and the SPS-FSP recycled material (a) yield strength-elongation plot and (b) ultimate tensile strength-elongation plot. [39, 43, 45, 86, 129, 135, 178, 198-203]

7.4 Conclusions

A component of WE43C was successfully fabricated by AFSD. By using this solid-state AM technology, a quicker deposition of material was achieved compared to traditional AM technologies represented by PBF or DED. The main findings of the AFSDed WE43C is shown below.

- (1) A bimodal grain structure of well-defined coarse grains and fine grains was observed in the AFSDed material. There was a gradient in grain size in the printed material along the TD, with the average grain size decreasing from 6.1±4.9 µm to 2.9±2.1 µm from the centre to the edge part in the middle layer. The bimodal structure stems from the difference of local strain rate and second phase particle heterogeneous, and the gradient structure is mainly attributed to the temperature gradient from the centre to the edge.
- (2) All three sites from the centre to the edge exhibited a basal texture with their {0001} planes nearly parallel to the LD-TD plane, which is consistent with the material flow behaviour. The texture intensities for three sites from the centre to the edge were 10.6, 11.2 and 9.2, respectively.
- (3) The porosity of the AFSDed material was below 0.01%. The average pore size from the centre to the edge was 19.2 μ m, 16.0 μ m, and 15.5 μ m, respectively. Pores exhibited flak-like shapes with the thickness direction along the BD, which is believed to be a result of material flow within the LD-TD plane.
- (4) Two major second phases were identified in the AFSDed material, including large Mg₄₁RE₅ particles around 1 μm, and dense nanoparticles mainly composed of Y and O, either in the form of single crystals around or agglomerations. The nanoparticles were not in the feedstock but in-situ formed during the AFSD process due to the elevated temperature. They were redistributed throughout the deposited layer by the friction stirring, instead of

- staying on the surface.
- (5) The grain growth stagnation at 525 °C for 72h was observed which is attributed to the long-lasting and strong Zener pinning effects by oxide nanoparticles. It benefits from several features of nanoparticles including high thermal stability, high volume fraction, small size, and preferential distribution along grain boundaries.
- (6) With the extraordinary thermal stability, T6 treatment was carried out without causing drastic grain growth. β_1 phase produced during the T6 generates precipitation hardening and the hardness reached 91.7 HV at the peak ageing condition.
- (7) Tensile tests indicate the AFSDed WE43C exhibited a good combination of strength and ductility, the YS, UTS, and El were measured to be 197.0±7.9 MPa, 269.0±4.2 MPa, and 17.6±1.8%, respectively. The ductility of the AFSDed WE43C is higher than most of the counterparts fabricated by casting, AM, rolling and extrusion.

Chapter 8 Conclusive discussion and summary

All three techniques are variants of friction stir welding (FSW), and share the same characteristics of material deformation including high strain, high strain rate, and elevated temperatures. The mechanical stirring and generated friction heat during the processing, and thus dynamic recrystallisation (DRX), especially the continuous dynamic recrsytallisation (CDRX) actively participated in the grain evolution. DRX occurred during the fabrication produced refined grains with an average grain size ~1-10 µm in the final products. Besides, the presence of fine thermal stable oxide particles either originated from the oxide film grown during the spark plasma sintering (SPS) or in-situ formed during the processing can further assist control the grain size. Due to the mechanical stirring and elevated temperature during the processing, pre-existing second phase particles can be fragmented and re-dissolve into the matrix. Pre-existing oxide films, if there were some in the material, can also be fragmented but not re-dissolved. These particles were further redistributed throughout the material. In the as-prepared WE43C, the major second phases include Mg₄₁RE₅ mainly distributed along grain boundaries and triple junctions, and oxide particles of rare earth elements. There were also some cuboidal Mg₂₄Y₅ particles but not playing an essential role in the following heat treatment and mechanical properties. Basal texture developed during the deformation. The orientation of the {0001} planes was strongly dependent on the material flow behaviour, which is mainly parallel to the material flow plane. Pores were detected in the material. Pore shape is closely related to the material flow behaviour as they all exhibited flake-like shapes and the thickness were parallel to the normal direction of the material flow plane.

According to the Hall-Petch relationship, refined grain size provided strengthening effects by the increase in grain boundaries, contributing to the strength improvement of the material. When subjected to further ageing treatment at 200 °C, β_1 plates precipitated on $\{10\overline{1}0\}$ planes of α -Mg matrix. These precipitates acted as obstacles to the movement of dislocations and thus increased the strength of the fabricated material. In addition, a quicker

ageing response was observed. The peak ageing time of Mg-4Y-3RE at 200 °C has been reported to be around 64-128 h [183, 226, 227]. In this research, the peak ageing for the material prepared by friction stir based technologies ranged between 30-40h. However, the ageing response in this research was generally lower than the reported data. In this research, the hardness increase after T5 was about 10 HV, whilst the hardness increase after T5 treatment at the same temperature was mainly around 20 HV [41, 49, 138]. The quicker ageing response with reduced hardness increase by T5 can be attributed to several factors. The small grain size led to more alloy elements segregated and precipitated at grain boundaries. Besides the formation of oxide also led to a decrease of alloy element dissolved in the matrix. These led to a decrease of β_1 formation in the grain interior and weakened the precipitation strengthening by ageing treatment, compared to alloys prepared by traditional methods which is oxide free. Apart from these factors, pores also played an essential role in the mechanical properties, especially the elongation of the material. FSPed material, where the pore size and fraction were higher than the other two samples, exhibited much lower elongation and even partly failure of the material during tensile tests. This can be attributed to the severe stress concentration around the tip of the large pores. Although SS-FSCed and AFSDed material both exhibited high elongation, the reason are slightly different. For the SS-FSCed material, the grain are mainly around the soft orientation, whilst for the AFSDed material, a bimodal structure provided the enhanced ductility.

In addition, grain growth stagnation at 525 °C for 72h was observed in the AFSDed WE43C component. The extraordinary thermal stability is attributed to the long-lasting and strong Zener pinning effects by oxide nanoparticles. It benefits from several features of nanoparticles including high thermal stability, high volume fraction, small size, and preferential distribution along grain boundaries.

Despite the absence of systematic comparison of the energy consumption and environmental impact of Mg alloy production in this work, evaluation of the friction stir based

technologies can still be made based on other researches. It has been pointed out that for the recycling work of brass, the energy consumption, carbon dioxide emission and material wastage were 0.173 kWh, 0.104 kg and 1 kg per to [2]. Whilst for the melting-based technologies, even if the most environmentally friendly method channel cored induction furnace is used, it would cost 0.482 kWh, 0.289 kg and 7 kg per ton [2]. Nevertheless, compared to the melting based technologies, friction stir based technologies still show some limits, including low production capacity, high labour cost, etc [2].

In conclusions, although the pores cannot be completely removed in the final product, when proper control of the pore size and alignment is achieved, stir based technologies can produce WE43 Mg alloys with a good combination of strength and ductility. The combination of strength and ductility is attributed to the refined grain structure, tailored texture, and further β_1 precipitates by ageing treatment.

Chapter 9 Future work

9.1 Future exploration of SS-FSC for WE43C recycling

The initial trials of wire extrusion from SPSed WE43C disk have been proved to be possible and the mechanical properties were comparable to commercial rolled or extruded counterparts. Further investigation of the deformation mode difference due to the gradient texture is expected to be carried out for understanding the detailed contribution of grains with different orientations during the tensile tests. This part of work aims at using EBSD to analyse the deformation details including shear bands, twins, in the fractured material. Preliminary tests of thermal stability tests were carried out and results showed that in the initial stage there was no grain growth at the temperature of 525 °C. However, with the increase of the dwelling time, abnormal grain growth (AGG) occurred from the edge part of the wire, as shown in Figure 9.1, which is different from the behaviour in the feedstock and the AFSDed WE43C. The reason for it is assume to be the oxide particles, yet no evidence was identified. Further comparisons by EBSD and TEM for different heat treatment time and between grains maintained stable and underwent abnormal grain growth are planned to be made to understand the mechanism of the AGG. This part of work can help understand the role of thermal stable particles in pinning the grain boundary migration.

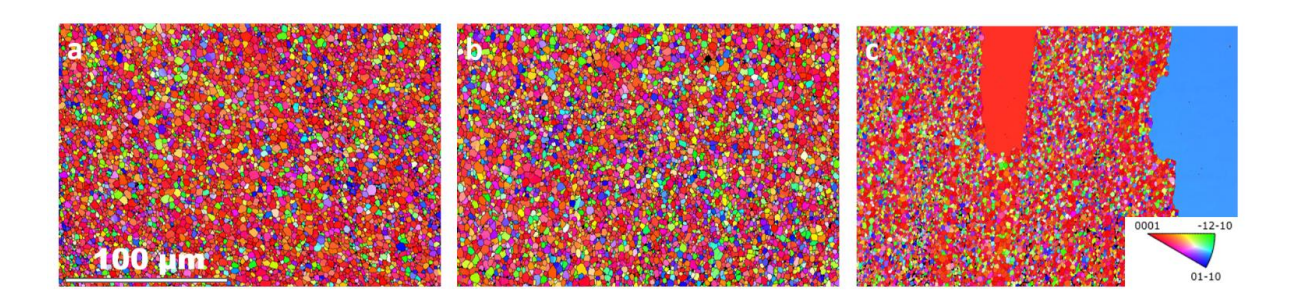


Figure 9.1 EBSD IPF maps of SS-FSC recycled wire (a) as-received state (b) 30min SST (c) 4h SST

9.2 Optimisation of processing parameters for WE43C recycling by FSP

Despite the equivalent hardness of FSP recycled WE43C to the commercial extruded products, the FSP recycled material exhibited a relative low ductility during the tensile tests, which was similar to cast products. The main reason for this is the large flake-like pores. This means the processing parameters need to be further improved to reduce the pore fraction and size. Action can be taken from the two aspects. First, the SPS processing parameters, including the temperature, stress, and the combination of them with time. Second the FSP setup, including the tool design, plunge depth, rotational speed and traverse speed. The recycled material can be investigated using XCT to evaluate the residual pores in the recycled material.

9.3 High temperature mechanical tests of AFSDed WE43C

In this work, the AFSDed WE43C material exhibited an extraordinarily high thermal stability at 525 °C for 72h. Such a high thermal stability was not observed in the WE series alloys previously. This is attributed to the dense nano-oxide particles in the AFSDed WE43C, and these particles may also lead to an improvement in the mechanical properties. These oxides can potentially strengthen the grain boundaries at elevated temperatures and act as obstacles to the dislocation movement. Whilst these hypotheses need to be investigated by mechanical tests at elevated temperatures, such as high temperature hardness tests, high temperature tensile tests, and creep tests. After that, the microstructure and texture can be characterised using SEM and TEM.

Appendix A [List of publications and attended conferences]

List of publications

- [1] **X. Zhao**, X. Zeng, L. Yuan, J. Gandra, Q. Hayat, M. Bai, W.M. Rainforth, D. Guan, A novel approach for producing Mg-3Al-1Zn-0.2 Mn alloy wire with a promising combination of strength and ductility using CoreFlowTM, Scripta Materialia 227 (2023) 115301.
- [2] **X. Zhao**, Y. Xie, J. Gandra, M. Murphy, W.M. Rainforth, D. Guan, A Succinct Method to Recycle WE43 Mg Alloys—From Wasted Chips to Consolidated Billets, TMS Annual Meeting & Exhibition, Springer, (2024), 151-153.
- [3] **X. Zhao**, D. Olden, B. Williams, A. Pariyar, D. Zhang, M. Murphy, P. Reed, P. Allison, B. Jordon, J. Qi, W.M. Rainforth, D. Guan, Grain growth stagnation at 525° C by nanoparticles in a solid-state additively manufactured Mg-4Y-3RE alloy, Journal of Magnesium and Alloys (2024), 4976-4987.
- [4] **X. Zhao**, J. Gandra, M. Murphy, R. Mitchell, F. A. Borges, S. Holdsworth, L. Ma, B. Guan, W. M. Rainforth, D. Guan, A solid-state recycling method for Mg-4Y-3RE alloy scraps incorporating spark plasma sintering and friction stir processing, in preparation

List of attended conferences

- The UK Solidification Workshop 2022, Uxbridge, United Kingdom, 2022
 Attended
- 2. Joint International Symposium of Friction Stir Welding and Processing, Lüneburg, Germany, 2022

Oral presentation

3. The 8th International Conference on Magnesium & the 13th International Conference on Magnesium Alloys and their Applications, Chongqing, China, 2024

Oral presentation

- [1] P. Dudek, J. Piwowońska, T. Polczyk, Microstructure of castings made of magnesium alloys based on recycling of the circulating scrap, Journal of Materials Research and Technology 14 (2021) 2357-2364.
- [2] P. Asadi, M. Akbari, A. Armani, M.R.M. Aliha, M. Peyghami, T. Sadowski, Recycling of brass chips by sustainable friction stir extrusion, Journal of Cleaner Production 418 (2023).
- [3] Z. Abbasi, R. Ebrahimi, J.M. Cabrera, Investigation on Texture Evolution and Recrystallization Aspects of Novel Mg–Zn–Gd–Y–Nd Alloys, Metals and Materials International (2020).
- [4] K.U. Kainer, Magnesium Alloys and Technology, 2003.
- [5] Z. Zeng, N. Stanford, C.H.J. Davies, J.-F. Nie, N. Birbilis, Magnesium extrusion alloys: a review of developments and prospects, International Materials Reviews 64(1) (2018) 27-62.
- [6] H.E. Friedrich, B. L.Mordi, Magnesium Technology: Metallurgy, Design Data, Applications, Springe2006.
- [7] B. Jiang, X. Zeng, J. Song, Q. Le, C. Liu, D. Tie, R. Guan, F. Li, Development Strategies for China's Advanced Magnesium Alloy Industry Toward 2035, Chinese Journal of Engineering Science 22(5) (2020).
- [8] I. Polmear, D. StJohn, J.-F. Nie, M. Qian, Light Alloys: Metallurgy of the Light Metals, 2017.
- [9] J.F. Nie, K.S. Shin, Z.R. Zeng, Microstructure, Deformation, and Property of Wrought Magnesium Alloys, Metallurgical and Materials Transactions A 51(12) (2020) 6045-6109.
- [10] H. Yu, C. Li, Y. Xin, A. Chapuis, X. Huang, Q. Liu, The mechanism for the high dependence of the Hall-Petch slope for twinning/slip on texture in Mg alloys, Acta Materialia 128 (2017) 313-326.
- [11] B. Song, Q. Yang, T. Zhou, L. Chai, N. Guo, T. Liu, S. Guo, R. Xin, Texture control by {10-12} twinning to improve the formability of Mg alloys: A review, Journal of Materials Science & Technology 35(10) (2019) 2269-2282.
- [12] A. Jäger, S. Habr, K. Tesař, Twinning-detwinning assisted reversible plasticity in thin magnesium wires prepared by one-step direct extrusion, Materials & Design 110 (2016) 895-902.
- [13] M.G. Jiang, C. Xu, H. Yan, G.H. Fan, T. Nakata, C.S. Lao, R.S. Chen, S. Kamado, E.H. Han, B.H. Lu, Unveiling the formation of basal texture variations based on twinning and dynamic recrystallization in AZ31 magnesium alloy during extrusion, Acta Materialia 157 (2018) 53-71.
- [14] Z.R. Zeng, Y.M. Zhu, R.L. Liu, S.W. Xu, C.H.J. Davies, J.F. Nie, N. Birbilis, Achieving exceptionally high strength in Mg 3Al 1Zn-0.3Mn extrusions via suppressing intergranular deformation, Acta Materialia 160 (2018) 97-108.
- [15] J. Xu, B. Guan, Y. Xin, X. Wei, G. Huang, C. Liu, Q. Liu, A weak texture dependence of Hall–Petch relation in a rare-earth containing magnesium alloy, Journal of Materials Science & Technology 99 (2022) 251-259.

- [16] M. Ghazisaeidi, W.A. Curtin, Analysis of dissociation of (c) and (c+a) dislocations to nucleate \$(1\,0\,\bar{1}\,2)\$ twins in Mg, Modelling and Simulation in Materials Science and Engineering 21(5) (2013).
- [17] F. Wang, Y. Gu, R.J. McCabe, L. Capolungo, J.A. El-Awady, S.R. Agnew, 〈c+a〉 dislocations in {101²} twins in Mg: A kinematic and energetic requirement, Acta Materialia 195 (2020) 13-24.
- [18] M. Yuasa, K. Masunaga, T. Yoshida, M. Mabuchi, Y. Chino, Interactions of a screw dislocation with a {101}–{102} double twin in Mg, Acta Materialia 61(13) (2013) 4714-4725.
- [19] J.J. Bhattacharyya, F. Wang, N. Stanford, S.R. Agnew, Slip mode dependency of dislocation shearing and looping of precipitates in Mg alloy WE43, Acta Materialia 146 (2018) 55-62.
- [20] J. Gao, S. Jiang, H. Zhang, Y. Huang, D. Guan, Y. Xu, S. Guan, L.A. Bendersky, A.V. Davydov, Y. Wu, H. Zhu, Y. Wang, Z. Lu, W.M. Rainforth, Facile route to bulk ultrafine-grain steels for high strength and ductility, Nature 590(7845) (2021) 262-267.
- [21] D. Guan, X. Liu, J. Gao, L. Ma, B.P. Wynne, W.M. Rainforth, Exploring the mechanism of "Rare Earth" texture evolution in a lean Mg-Zn-Ca alloy, Sci Rep 9(1) (2019) 7152.
- [22] R. Pei, Y. Zhao, M. Zubair, S. Yi, T. Al-Samman, Solute drag-controlled grain growth in magnesium investigated by quasi in-situ orientation mapping and level-set simulations, Journal of Magnesium and Alloys 11(7) (2023) 2312-2325.
- [23] J.-F. Nie, Precipitation and Hardening in Magnesium Alloys, Metallurgical and Materials Transactions A 43(11) (2012) 3891-3939.
- [24] S. Duwe, Pyrometallurgical Magnesium Recycling by Precipitation of Intermetallic Phases, Chemie Ingenieur Technik 87(11) (2015) 1609-1612.
- [25] Q. Wu, H. Yan, J. Chen, W. Xia, M. Song, B. Su, T. Ding, Dynamic Precipitation, Dynamic Recrystallization, and Texture Evolution of Mg-5Zn Alloy Sheets with Trace Ca and Sr Additions, Microsc Microanal 26(5) (2020) 886-894.
- [26] J. Peng, Z. Zhang, Z. Liu, Y. Li, P. Guo, W. Zhou, Y. Wu, The effect of texture and grain size on improving the mechanical properties of Mg-Al-Zn alloys by friction stir processing, Sci Rep 8(1) (2018) 4196.
- [27] V. Patel, W. Li, X. Liu, Q. Wen, Y. Su, J. Shen, B. Fu, Tailoring grain refinement through thickness in magnesium alloy via stationary shoulder friction stir processing and copper backing plate, Materials Science and Engineering: A 784 (2020).
- [28] C. Wang, M. Sun, F. Zheng, L. Peng, W. Ding, Improvement in grain refinement efficiency of Mg–Zr master alloy for magnesium alloy by friction stir processing, Journal of Magnesium and Alloys 2(3) (2014) 239-244.
- [29] N. Ansari, R. Sarvesha, S.Y. Lee, S.S. Singh, J. Jain, Influence of yttrium addition on recrystallization, texture and mechanical properties of binary Mg–Y alloys, Materials Science and Engineering: A 793 (2020).
- [30] Y.I. Bourezg, H. Azzeddine, T. Baudin, A.-L. Helbert, Y. Huang, D. Bradai, T.G. Langdon, Texture and microhardness of Mg-Rare Earth (Nd and Ce) alloys processed by high-pressure torsion, Materials Science and Engineering: A 724 (2018) 477-485.

- [31] A.E. Davis, J.D. Robson, M. Turski, The effect of multiple precipitate types and texture on yield asymmetry in Mg-Sn-Zn(-Al-Na-Ca) alloys, Acta Materialia 158 (2018) 1-12.
- [32] D. Guan, W.M. Rainforth, J. Gao, J. Sharp, B. Wynne, L. Ma, Individual effect of recrystallisation nucleation sites on texture weakening in a magnesium alloy: Part 1- double twins, Acta Materialia 135 (2017) 14-24.
- [33] D. Guan, W.M. Rainforth, J. Gao, L. Ma, B. Wynne, Individual effect of recrystallisation nucleation sites on texture weakening in a magnesium alloy: Part 2- shear bands, Acta Materialia 145 (2018) 399-412.
- [34] X. Li, W. Qi, Effect of initial texture on texture and microstructure evolution of ME20 Mg alloy subjected to hot rolling, Materials Science and Engineering: A 560 (2013) 321-331.
- [35] G. Zhang, Z. Zhang, X. Li, Z. Yan, X. Che, J. Yu, Y. Meng, Effects of repetitive upsetting-extrusion parameters on microstructure and texture evolution of Mg–Gd–Y–Zn–Zr alloy, Journal of Alloys and Compounds 790 (2019) 48-57.
- [36] X. Zhou, W. Xiong, G. Zeng, H. Xiao, J. Zhang, X. Lu, X. Chen, Combined effects of LPSO orientation and α-Mg texture on tensile anisotropy of an extruded Mg-Gd-Y-Zn-Zr alloy, Materials Science and Engineering: A 805 (2021).
- [37] A. Jain, O. Duygulu, D.W. Brown, C.N. Tomé, S.R. Agnew, Grain size effects on the tensile properties and deformation mechanisms of a magnesium alloy, AZ31B, sheet, Materials Science and Engineering: A 486(1-2) (2008) 545-555.
- [38] S. Wu, Z. Ji, T. Zhang, Microstructure and mechanical properties of AZ31B magnesium alloy recycled by solid-state process from different size chips, Journal of Materials Processing Technology 209(12-13) (2009) 5319-5324.
- [39] C. Hartmann, K. Venkatesan, G. de Looze, K. Takashima, S. Shen, R. Wilson, Additive manufacturing of WE43 and modified AZ91D magnesium alloys using the laser engineered net shaping process, Materials Today Communications 39 (2024).
- [40] D. Dvorský, J. Kubásek, D. Vojtěch, M. Čavojský, Advanced Mechanical and Corrosion Properties of WE43 Alloy Prepared by Powder Metallurgy, Acta Physica Polonica A 134(3) (2018) 748-752.
- [41] J.J. Bhattacharyya, F. Wang, P.J. McQuade, S.R. Agnew, Deformation and fracture behavior of Mg alloy, WE43, after various aging heat treatments, Materials Science and Engineering: A 705 (2017) 79-88.
- [42] M. Esmaily, Z. Zeng, A.N. Mortazavi, A. Gullino, S. Choudhary, T. Derra, F. Benn, F. D'Elia, M. Müther, S. Thomas, A. Huang, A. Allanore, A. Kopp, N. Birbilis, A detailed microstructural and corrosion analysis of magnesium alloy WE43 manufactured by selective laser melting, Additive Manufacturing 35 (2020).
- [43] M. Zha, X. Ma, H.-L. Jia, Z.-M. Hua, Z.-X. Fan, Z.-Z. Yang, Y.-P. Gao, H.-Y. Wang, Dynamic precipitation and deformation behaviors of a bimodal-grained WE43 alloy with enhanced mechanical properties, International Journal of Plasticity 167 (2023).
- [44] S.M. Fatemi, S. Aliyari, S.M. Miresmaeili, Dynamic precipitation and dynamic recrystallization during hot deformation of a solutionized WE43 magnesium alloy, Materials Science and Engineering: A 762 (2019).

- [45] C. Xiang, N. Gupta, P. Coelho, K. Cho, Effect of microstructure on tensile and compressive behavior of WE43 alloy in as cast and heat treated conditions, Materials Science and Engineering: A 710 (2018) 74-85.
- [46] D. Dvorský, J. Kubásek, M. Roudnická, F. Průša, D. Nečas, P. Minárik, J. Stráská, D. Vojtěch, The effect of powder size on the mechanical and corrosion properties and the ignition temperature of WE43 alloy prepared by spark plasma sintering, Journal of Magnesium and Alloys 9(4) (2021) 1349-1362.
- [47] P. Minárik, J. Veselý, J. Čížek, M. Zemková, T. Vlasák, T. Krajňák, J. Kubásek, R. Král, D. Hofman, J. Stráská, Effect of secondary phase particles on thermal stability of ultra-fine grained Mg-4Y-3RE alloy prepared by equal channel angular pressing, Materials Characterization 140 (2018) 207-216.
- [48] A. Salandari-Rabori, A. Zarei-Hanzaki, S. Asqardoust, H.R. Abedi, T. Krajňák, P. Minárik, J. Veselý, Novel RE-texture component and bimodal microstructure formation during post-annealing of an accumulative back extruded WE43 alloy, Materials Letters 337 (2023).
- [49] E.A. Lukyanova, N.S. Martynenko, I. Shakhova, A.N. Belyakov, L.L. Rokhlin, S.V. Dobatkin, Y.Z. Estrin, Strengthening of age-hardenable WE43 magnesium alloy processed by high pressure torsion, Materials Letters 170 (2016) 5-9.
- [50] S. Rahimpour Golroudbary, I. Makarava, A. Kraslawski, Environmental Assessment of Global Magnesium Production, Mineral Processing and Extractive Metallurgy Review (2022) 1-18.
- [51] H.Y. Wang, E.B. Zhang, X.L. Nan, L. Zhang, Z.P. Guan, Q.C. Jiang, A comparison of microstructure and mechanical properties of Mg–9Al–1Zn sheets rolled from as-cast, cast-rolling and as-extruded alloys, Materials & Design 89 (2016) 167-172.
- [52] S. Tzamtzis, H. Zhang, M. Xia, N.H. Babu, Z. Fan, Recycling of high grade die casting AM series magnesium scrap with the melt conditioned high pressure die casting (MC-HPDC) process, Materials Science and Engineering: A 528(6) (2011) 2664-2669.
- [53] F. Pan, M. Yang, X. Chen, A Review on Casting Magnesium Alloys: Modification of Commercial Alloys and Development of New Alloys, Journal of Materials Science & Technology 32(12) (2016) 1211-1221.
- [54] L.Y. Zhao, H. Yan, R.S. Chen, E.-H. Han, Oriented nucleation causing unusual texture transition during static recrystallization annealing in cold-rolled Mg–Zn–Gd alloys, Scripta Materialia 188 (2020) 200-205.
- [55] H.-G. Brokmeier, Hot Rectangular Extrusion Textures of Six Mg-Alloys Via Neutron Diffraction, Advanced Engineering Materials 20(4) (2018).
- [56] S. Gall, S. Mueller, W. Reimers, Magnesium sheet production by using the extrusion process, International Journal of Material Forming 3(S1) (2010) 371-374.
- [57] W. Zhang, H. Zhang, L. Wang, J. Fan, X. Li, L. Zhu, S. Chen, H.J. Roven, S. Zhang, Microstructure Evolution and Mechanical Properties of AZ31 Magnesium Alloy Sheets Prepared by Low-Speed Extrusion with Different Temperature, Crystals 10(8) (2020).

- [58] A. Milenin, M. Gzyl, T. Rec, B. Plonka, Computer Aided Design of Wires Extrusion from Biocompatible Mg-Ca Magnesium Alloy, Archives of Metallurgy and Materials 59(2) (2014) 551-556.
- [59] M. Sabbaghian, N. Fakhar, P. Nagy, K. Fekete, J. Gubicza, Investigation of shear and tensile mechanical properties of ZK60 Mg alloy sheet processed by rolling and sheet extrusion, Materials Science and Engineering: A 828 (2021).
- [60] M. Nienaber, S. Yi, K.U. Kainer, D. Letzig, J. Bohlen, On the Direct Extrusion of Magnesium Wires from Mg-Al-Zn Series Alloys, Metals 10(9) (2020).
- [61] H. Pan, F. Pan, J. Peng, J. Gou, A. Tang, L. Wu, H. Dong, High-conductivity binary Mg–Zn sheet processed by cold rolling and subsequent aging, Journal of Alloys and Compounds 578 (2013) 493-500.
- [62] T. Wu, L. Jin, W.X. Wu, L. Gao, J. Wang, Z.Y. Zhang, J. Dong, Improved ductility of Mg–Zn–Ce alloy by hot pack-rolling, Materials Science and Engineering: A 584 (2013) 97-102.
- [63] Z.S. Ji, L.H. Wen, X.L. Li, Mechanical properties and fracture behavior of Mg–2.4Nd–0.6Zn–0.6Zr alloys fabricated by solid recycling process, Journal of Materials Processing Technology 209(4) (2009) 2128-2134.
- [64] C.-j. Wang, J.-w. Kang, K.-k. Deng, K.-b. Nie, W. Liang, W.-g. Li, Microstructure and mechanical properties of Mg-4Zn-xGd (x=0, 0.5, 1, 2) alloys, Journal of Magnesium and Alloys 8(2) (2020) 441-451.
- [65] S.S. Joshi, S.M. Patil, S. Mazumder, S. Sharma, D.A. Riley, S. Dowden, R. Banerjee, N.B. Dahotre, Additive friction stir deposition of AZ31B magnesium alloy, Journal of Magnesium and Alloys 10(9) (2022) 2404-2420.
- [66] H.-f. Sun, H.-y. Chao, E.-d. Wang, Microstructure stability of cold drawn AZ31 magnesium alloy during annealing process, Transactions of Nonferrous Metals Society of China 21 (2011) s215-s221.
- [67] T. Bajor, Structure Analysis of Magnesium Alloy (AZ31) Wires at Different Stages of a Multistage Cold Drawing Process, Key Engineering Materials 682 (2016) 125-131.
- [68] H.-W. Lee, T.-S. Lui, L.-H. Chen, Studies on the improvement of tensile ductility of hot-extrusion AZ31 alloy by subsequent friction stir process, Journal of Alloys and Compounds 475(1-2) (2009) 139-144.
- [69] M. Mondet, E. Barraud, S. Lemonnier, N. Allain, T. Grosdidier, Optimisation of the mechanical properties of a Spark Plasma Sintered (SPS) magnesium alloy through a post-sintering in-situ precipitation treatment, Journal of Alloys and Compounds 698 (2017) 259-266.
- [70] B. Li, B. Teng, Z. Zhu, Solid state recycling of Mg–Gd–Y–Zn–Zr alloy chips by spark plasma sintering, Journal of Magnesium and Alloys 8(4) (2020) 1154-1165.
- [71] D. Paraskevas, S. Dadbakhsh, J. Vleugels, K. Vanmeensel, W. Dewulf, J.R. Duflou, Solid state recycling of pure Mg and AZ31 Mg machining chips via spark plasma sintering, Materials & Design 109 (2016) 520-529.

- [72] M. Knapek, P. Minárik, A. Greš, M. Zemková, F. Lukáč, J. Bohlen, F. Chmelík, R. Král, Spark plasma sintered Mg-4Y-3Nd with exceptional tensile performance, Materials Science and Engineering: A 849 (2022).
- [73] J. Soderlind, M. Cihova, R. Schaublin, S. Risbud, J.F. Loffler, Towards refining microstructures of biodegradable magnesium alloy WE43 by spark plasma sintering, Acta Biomater 98 (2019) 67-80.
- [74] Q.-h. Zang, H.-m. Chen, F.-y. Lan, J. Zhang, Y.-x. Jin, Effect of friction stir processing on microstructure and damping capacity of AZ31 alloy, Journal of Central South University 24(5) (2017) 1034-1039.
- [75] F. Kiani, C. Wen, Y. Li, Prospects and strategies for magnesium alloys as biodegradable implants from crystalline to bulk metallic glasses and composites-A review, Acta Biomater 103 (2020) 1-23.
- [76] K. Kumar, R.S. Gill, U. Batra, Challenges and opportunities for biodegradable magnesium alloy implants, Materials Technology 33(2) (2017) 153-172.
- [77] Z. Liu, Y. Cai, J. Chen, J. Han, Z. Mao, M. Chen, Fabrication and characterization of friction stir–processed Mg-Zn-Ca biomaterials strengthened with MgO particles, The International Journal of Advanced Manufacturing Technology 117(3-4) (2021) 919-932.
- [78] W. Liu, Y. Yan, T. Sun, S. Wu, Y. Shen, Influence of cooling water temperature on ME20M magnesium alloy submerged friction stir welding: a numerical and experimental study, The International Journal of Advanced Manufacturing Technology 105(12) (2019) 5203-5215.
- [79] M.M.Z. Ahmed, B.P. Wynne, M.M. El-Sayed Seleman, W.M. Rainforth, A comparison of crystallographic texture and grain structure development in aluminum generated by friction stir welding and high strain torsion, Materials & Design 103 (2016) 259-267.
- [80] P.S. Davies, B.P. Wynne, W.M. Rainforth, M.J. Thomas, P.L. Threadgill, Development of Microstructure and Crystallographic Texture during Stationary Shoulder Friction Stir Welding of Ti-6Al-4V, Metallurgical and Materials Transactions A 42(8) (2011) 2278-2289.
- [81] L. Commin, M. Dumont, J.E. Masse, L. Barrallier, Friction stir welding of AZ31 magnesium alloy rolled sheets: Influence of processing parameters, Acta Materialia 57(2) (2009) 326-334.
- [82] A.M. Desai, B.C. Khatri, V. Patel, H. Rana, Friction stir welding of AZ31 magnesium alloy: A review, Materials Today: Proceedings 47 (2021) 6576-6584.
- [83] S. Ugender, Influence of tool pin profile and rotational speed on the formation of friction stir welding zone in AZ31 magnesium alloy, Journal of Magnesium and Alloys 6(2) (2018) 205-213.
- [84] Y. Huang, Y. Wang, L. Wan, H. Liu, J. Shen, J.F. dos Santos, L. Zhou, J. Feng, Material-flow behavior during friction-stir welding of 6082-T6 aluminum alloy, The International Journal of Advanced Manufacturing Technology 87(1-4) (2016) 1115-1123.
- [85] A. Heidarzadeh, S. Mironov, R. Kaibyshev, G. Çam, A. Simar, A. Gerlich, F. Khodabakhshi, A. Mostafaei, D.P. Field, J.D. Robson, A. Deschamps, P.J. Withers, Friction stir welding/processing of metals and alloys: A comprehensive review on microstructural evolution, Progress in Materials Science 117 (2021).

- [86] D.X. Liu, X. Pang, D.L. Li, C.G. Guo, J. Wongsa-Ngam, T.G. Langdon, M.A. Meyers, Microstructural Evolution and Properties of a Hot Extruded and HPT-Processed Resorbable Magnesium WE43 Alloy Advanced Engineering Materials 19(3) (2017).
- [87] P. Seenuvasaperumal, K. Doi, D.A. Basha, A. Singh, A. Elayaperumal, K. Tsuchiya, Wear behavior of HPT processed UFG AZ31B magnesium alloy, Materials Letters 227 (2018) 194-198.
- [88] A.P. Zykova, S.Y. Tarasov, A.V. Chumaevskiy, E.A. Kolubaev, A Review of Friction Stir Processing of Structural Metallic Materials: Process, Properties, and Methods, Metals 10(6) (2020).
- [89] Z. Zheng, Q. Li, X. Chen, A. Gao, N. Zhang, Application Status and Prospects of Friction Stir Processing in Wrought Magnesium Alloys: A Review, Transactions of the Indian Institute of Metals 77(8) (2024) 1891-1906.
- [90] A. Alavi Nia, H. Omidvar, S.H. Nourbakhsh, Effects of an overlapping multi-pass friction stir process and rapid cooling on the mechanical properties and microstructure of AZ31 magnesium alloy, Materials & Design 58 (2014) 298-304.
- [91] R. Taghiabadi, H. Jalali, Quality Index Assessment of Multi-Pass Friction Stir Processed Al–Si–Mg Alloys Fully Produced by Recycling of Machining Chips, Transactions of the Indian Institute of Metals 74(2) (2021) 273-284.
- [92] C.I. Chang, X.H. Du, J.C. Huang, Achieving ultrafine grain size in Mg–Al–Zn alloy by friction stir processing, Scripta Materialia 57(3) (2007) 209-212.
- [93] C. Chang, X. Du, J. Huang, Producing nanograined microstructure in Mg–Al–Zn alloy by two-step friction stir processing, Scripta Materialia 59(3) (2008) 356-359.
- [94] C.I. Chang, C.J. Lee, J.C. Huang, Relationship between grain size and Zener–Holloman parameter during friction stir processing in AZ31 Mg alloys, Scripta Materialia 51(6) (2004) 509-514.
- [95] B. Darras, E. Kishta, Submerged friction stir processing of AZ31 Magnesium alloy, Materials & Design 47 (2013) 133-137.
- [96] F. Liu, Y. Ji, Z. Sun, J. Liu, Y. Bai, Z. Shen, Enhancing corrosion resistance and mechanical properties of AZ31 magnesium alloy by friction stir processing with the same speed ratio, Journal of Alloys and Compounds 829 (2020).
- [97] S. Pandya, R.S. Mishra, A. Arora, Channel formation during friction stir channeling process A material flow study using X-Ray micro-computed tomography and optical microscopy, Journal of Manufacturing Processes 41 (2019) 48-55.
- [98] A. Rashidi, A. Mostafapour, Influence of machine parameters on material flow behavior during channeling in modified friction stir channeling, International Journal of Material Forming 9(1) (2014) 1-8.
- [99] A. Rashidi, A. Mostafapour, S. Salahi, V. Rezazadeh, Modified Friction Stir Channeling: A Novel Technique for Fabrication of Friction Stir Channel, Applied Mechanics and Materials 302 (2013) 365-370.
- [100] K.P. Mehta, P. Vilaça, A review on friction stir-based channeling, Critical Reviews in Solid State and Materials Sciences 47(1) (2021) 1-45.

- [101] M.E.J. Perry, H.A. Rauch, R.J. Griffiths, D. Garcia, J.M. Sietins, Y. Zhu, Y. Zhu, H.Z. Yu, Tracing plastic deformation path and concurrent grain refinement during additive friction stir deposition, Materialia 18 (2021).
- [102] T. Luo, W. Tang, R. Wang, S. Wang, L. Xiao, X. Yang, Microstructure heterogeneity and mechanical properties of Mg-Gd-Y-Zr alloy fabricated by force-controlled additive friction stir deposition, Materials Letters 340 (2023).
- [103] J. Zhang, J. Miao, N. Balasubramani, D.H. Cho, T. Avey, C.-Y. Chang, A.A. Luo, Magnesium research and applications: Past, present and future, Journal of Magnesium and Alloys 11(11) (2023) 3867-3895.
- [104] S. Shamsudin, M.A. Lajis, Z.W. Zhong, Solid-state recycling of light metals: A review, Advances in Mechanical Engineering 8(8) (2016).
- [105] X. Hao, Z. Xu, C.M. Gourlay, Q. Li, Grain refinement of magnesium castings using recycled machining chips, Materials & Design 244 (2024).
- [106] C. Wang, S. Huo, S. Liu, Q. Hu, Q. Zhang, Z. Liu, Recycle of magnesium alloy scrap for improving fire resistance, thermal stability, and water tolerance of intumescent fire-retardant coatings, Journal of Coatings Technology and Research 18(2) (2020) 447-458.
- [107] J. Su, M. Sanjari, A.S.H. Kabir, I.-H. Jung, S. Yue, Dynamic recrystallization mechanisms during high speed rolling of Mg–3Al–1Zn alloy sheets, Scripta Materialia 113 (2016) 198-201.
- [108] Q. Wang, H. Zhai, H. Xia, L. Liu, J. He, D. Xia, H. Yang, B. Jiang, Relating Initial Texture to Deformation Behavior During Cold Rolling and Static Recrystallization Upon Subsequent Annealing of an Extruded WE43 Alloy, Acta Metallurgica Sinica (English Letters) 35(11) (2022) 1793-1811.
- [109] S. Ehrenberger, H.E. Friedrich, Life-Cycle Assessment of the Recycling of Magnesium Vehicle Components, Jom 65(10) (2013) 1303-1309.
- [110] M. Akbari, P. Asadi, R.A. Behnagh, F. Bedir, N. Choupani, T. Sadowski, Process Parameters and Tool Design in Friction Stir Extrusion: A Sustainable Recycling Technique, Engineering Reports 7(1) (2024).
- [111] E. Taherkhani, M.R. Sabour, G. Faraji, Sustainable magnesium recycling: Insights into grain refinement through plastic deformation-assisted solid-state recycling (SSR), Journal of Magnesium and Alloys 12(10) (2024) 3947-3966.
- [112] T. Guo, Y. Geng, X. Song, X. Rui, Z. Ge, Tracing magnesium flows in China: A dynamic material flow analysis, Resources Policy 83 (2023).
- [113] G. Liu, Y. Wang, Z. Fan, A physical approach to the direct recycling of Mg-alloy scrap by the rheo-diecasting process, Materials Science and Engineering: A 472(1-2) (2008) 251-257.
- [114] Q. Tan, A. Atrens, N. Mo, M.-X. Zhang, Oxidation of magnesium alloys at elevated temperatures in air: A review, Corrosion Science 112 (2016) 734-759.
- [115] P. Minárik, M. Zemková, F. Lukáč, J. Bohlen, M. Knapek, R. Král, Microstructure of the novel biomedical Mg–4Y–3Nd alloy prepared by spark plasma sintering, Journal of Alloys and Compounds 819 (2020).

- [116] T. Peng, Q.D. Wang, Y.K. Han, J. Zheng, W. Guo, Consolidation behavior of Mg–10Gd–2Y–0.5Zr chips during solid-state recycling, Journal of Alloys and Compounds 503(1) (2010) 253-259.
- [117] L. Wen, Z. Ji, X. Li, Effect of extrusion ratio on microstructure and mechanical properties of Mg–Nd–Zn–Zr alloys prepared by a solid recycling process, Materials Characterization 59(11) (2008) 1655-1660.
- [118] J. Miao, B. Ye, Q. Wang, T. Peng, Mechanical properties and corrosion resistance of Mg–10Gd–2Y–0.5Zr alloy by hot extrusion solid-state recycling, Journal of Alloys and Compounds 561 (2013) 184-192.
- [119] YING Tao, ZHENG Ming-yi, HU Xiao-shi, W. Kun, Recycling of AZ91 Mg alloy through consolidation of machined chips by extrusion and ECAP, Trans. Nonferrous Met. Soc. China 20 (2010) s604–s607.
- [120] Y. Pei, H. Ma, M. Yuan, B. Teng, Solid state recycling of Mg–Gd–Y–Zn–Zr alloy chips by isothermal sintering and equal channel angular pressing, Journal of Magnesium and Alloys 12(7) (2024) 2725-2740.
- [121] L. Hendriok, M. Nienaber, G. Kurz, N. Ben Khalifa, Die geometry influence on the texture and microstructure development during extrusion of AZ31 and ZK60 magnesium alloy chips, Materials & Design 249 (2025).
- [122] G. Buffa, D. Campanella, L. Fratini, F. Micari, AZ31 magnesium alloy recycling through friction stir extrusion process, International Journal of Material Forming 9(5) (2015) 613-618.
- [123] D. Baffari, G. Buffa, L. Fratini, Influence of Process Parameters on the Product Integrity in Friction Stir Extrusion of Magnesium Alloys, Key Engineering Materials 716 (2016) 39-48.
- [124] D. Baffari, G. Buffa, L. Fratini, A numerical model for Wire integrity prediction in Friction Stir Extrusion of magnesium alloys, Journal of Materials Processing Technology 247 (2017) 1-10.
- [125] T. Peng, Q.D. Wang, M.P. Liu, J. Zheng, J.B. Lin, An optimization approach for hot compaction technology of Mg–10Gd–2Y–0.5Zr alloy during solid-state recycling, Powder Technology 194(1-2) (2009) 142-148.
- [126] M. Gor, M. Barnett, D. Fabijanic, P.P. Bhattacharjee, Additive friction stir deposition of super duplex stainless steel: Microstructure and mechanical properties, Additive Manufacturing Letters 9 (2024).
- [127] M.B. Wilms, S.-K. Rittinghaus, M. Goßling, B. Gökce, Additive manufacturing of oxide-dispersion strengthened alloys: Materials, synthesis and manufacturing, Progress in Materials Science 133 (2023).
- [128] G.G. Stubblefield, K.A. Fraser, T.W. Robinson, N. Zhu, R.P. Kinser, J.Z. Tew, B.T. Cordle, J.B. Jordon, P.G. Allison, A computational and experimental approach to understanding material flow behavior during additive friction stir deposition (AFSD), Computational Particle Mechanics 10(6) (2023) 1629-1643.
- [129] F. Chen, X. Cai, B. Dong, S. Lin, Microstructure and mechanical properties of WE43 magnesium alloy fabricated by wire-arc additive manufacturing, Thin-Walled Structures 206 (2025).

- [130] A. Pariyar, E. Yasa, A. Sharman, C.S. Perugu, L. Yuan, J. Hughes, D. Guan, Understanding process parameter-induced variability for tailoring precipitation behavior, grain structure, and mechanical properties of Al-Mg-Si-Mn alloy during solid-state additive manufacturing, Materials & Design 245 (2024).
- [131] F. Bar, L. Berger, L. Jauer, G. Kurtuldu, R. Schaublin, J.H. Schleifenbaum, J.F. Loffler, Laser additive manufacturing of biodegradable magnesium alloy WE43: A detailed microstructure analysis, Acta Biomater 98 (2019) 36-49.
- [132] N.D. Dejene, H.G. Lemu, Current Status and Challenges of Powder Bed Fusion-Based Metal Additive Manufacturing: Literature Review, Metals 13(2) (2023).
- [133] M. Tebianian, S. Aghaie, N.S. Razavi Jafari, S.R. Elmi Hosseini, A.B. Pereira, F.A.O. Fernandes, M. Farbakhti, C. Chen, Y. Huo, A Review of the Metal Additive Manufacturing Processes, Materials (Basel) 16(24) (2023).
- [134] X. Tong, G. Wu, M.A. Easton, M. Sun, Q. Wang, L. Zhang, Microstructural evolution and strengthening mechanism of Mg-Y-RE-Zr alloy fabricated by quasi-directed energy deposition, Additive Manufacturing 67 (2023).
- [135] K. Li, B. Li, L. Zhu, X. Hou, Z. Li, L.E. Murr, B. Jiang, F. Pan, Optimizing microstructure and strength of CMT-wire arc additive manufactured WE43 Mg alloy through a novel active cooling technique, Thin-Walled Structures 205 (2024).
- [136] F. Badkoobeh, H. Mostaan, M. Rafiei, H.R. Bakhsheshi-Rad, S. RamaKrishna, X. Chen, Additive manufacturing of biodegradable magnesium-based materials: Design strategies, properties, and biomedical applications, Journal of Magnesium and Alloys 11(3) (2023) 801-839.
- [137] Z. Li, S. Sui, X. Ma, H. Tan, C. Zhong, G. Bi, A.T. Clare, A. Gasser, J. Chen, High deposition rate powder- and wire-based laser directed energy deposition of metallic materials: A review, International Journal of Machine Tools and Manufacture 181 (2022).
- [138] R. Karunakaran, S. Ortgies, A. Tamayol, F. Bobaru, M.P. Sealy, Additive manufacturing of magnesium alloys, Bioact Mater 5(1) (2020) 44-54.
- [139] H. Hyer, L. Zhou, G. Benson, B. McWilliams, K. Cho, Y. Sohn, Additive manufacturing of dense WE43 Mg alloy by laser powder bed fusion, Additive Manufacturing 33 (2020).
- [140] M. Korgancı, Y. Bozkurt, Recent developments in additive friction stir deposition (AFSD), Journal of Materials Research and Technology 30 (2024) 4572-4583.
- [141] R.S. Mishra, R.S. Haridas, P. Agrawal, Friction stir-based additive manufacturing, Science and Technology of Welding and Joining 27(3) (2022) 141-165.
- [142] H. Dong, X. Li, K. Xu, Z. Zang, X. Liu, Z. Zhang, W. Xiao, Y. Li, A Review on Solid-State-Based Additive Friction Stir Deposition, Aerospace 9(10) (2022).
- [143] H. Daiy, Y. Najafi, Z.D. Ragheb, H.R. Abedi, A review study on thermal stability of powder-based additively manufactured alloys, Journal of Alloys and Compounds 965 (2023).
- [144] A. Imandoust, C.D. Barrett, T. Al-Samman, K.A. Inal, H. El Kadiri, A review on the effect of rare-earth elements on texture evolution during processing of magnesium alloys, Journal of Materials Science 52(1) (2016) 1-29.

- [145] M. Mosayebi, A. Zarei-Hanzaki, H.R. Abedi, A.M. Jamili, A. Ghaderi, M. Barnett, Development of a novel RE-texture component in a Mg-Y-RE/SiCp magnesium composite through friction stir processing, Materials Letters 260 (2020).
- [146] A. Salandari-Rabori, A. Zarei-Hanzaki, H.R. Abedi, J.S. Lecomte, H. Khatami-Hamedani, Micro and macro texture evolution during multiaxial forging of a WE43 magnesium alloy, Journal of Alloys and Compounds 739 (2018) 249-259.
- [147] J. Wu, L. Jin, J. Dong, F. Wang, S. Dong, The texture and its optimization in magnesium alloy, Journal of Materials Science & Technology 42 (2020) 175-189.
- [148] F.R. Cao, G.Q. Xue, B.J. Zhou, S.C. Wang, High-Temperature Deformation Behavior of Duplex Mg–8.41Li–1.80Al–1.77Zn Alloy Processed by Friction Stir Processing, Metals and Materials International 25(3) (2018) 570-583.
- [149] V. Segal, Review: Modes and Processes of Severe Plastic Deformation (SPD), Materials (Basel) 11(7) (2018).
- [150] A. Azushima, R. Kopp, A. Korhonen, D.Y. Yang, F. Micari, G.D. Lahoti, P. Groche, J. Yanagimoto, N. Tsuji, A. Rosochowski, A. Yanagida, Severe plastic deformation (SPD) processes for metals, CIRP Annals 57(2) (2008) 716-735.
- [151] A. Ojdanic, J. Horky, B. Mingler, M. Fanetti, S. Gardonio, M. Valant, B. Sulkowski, E. Schafler, D. Orlov, M. J. Zehetbauer, The Effects of Severe Plastic Deformation and/or Thermal Treatment on the Mechanical Properties of Biodegradable Mg-Alloys, Metals 10(8) (2020).
- [152] P. Mansoor, S.M. Dasharath, Microstructural and mechanical properties of magnesium alloy processed by severe plastic deformation (SPD) A review, Materials Today: Proceedings 20 (2020) 145-154.
- [153] L. Cizek, S. Rusz, O. Hilser, R. Śliwa, D. Kuc, T. Tański, M. Tkocz, Microstructure and Properties of Selected Magnesium-Aluminum Alloys Prepared for SPD Processing Technology, Archives of Metallurgy and Materials 62(4) (2017) 2365-2370.
- [154] T. Krajňák, P. Minárik, J. Gubicza, K. Máthis, R. Kužel, M. Janeček, Influence of equal channel angular pressing routes on texture, microstructure and mechanical properties of extruded AX41 magnesium alloy, Materials Characterization 123 (2017) 282-293.
- [155] P. Minárik, J. Veselý, R. Král, J. Bohlen, J. Kubásek, M. Janeček, J. Stráská, Exceptional mechanical properties of ultra-fine grain Mg-4Y-3RE alloy processed by ECAP, Materials Science and Engineering: A 708 (2017) 193-198.
- [156] M.-y. Zhan, W.-w. Zhang, D.-t. Zhang, Production of Mg-Al-Zn magnesium alloy sheets with ultrafine-grain microstructure by accumulative roll-bonding, Transactions of Nonferrous Metals Society of China 21(5) (2011) 991-997.
- [157] H. Utsunomiya, K.-i. Izumi, T. Sakai, T. Mukai, Grain refinement of magnesium alloy sheets by ARB using high-speed rolling mill, Journal of Physics: Conference Series 165 (2009).
- [158] X. Li, T. Al-Samman, G. Gottstein, Microstructure development and texture evolution of ME20 sheets processed by accumulative roll bonding, Materials Letters 65(12) (2011) 1907-1910.

- [159] S.M. Ghalehbandi, M. Malaki, M. Gupta, <applsci-09-03627.pdf>, Applied Sciences 9(17) (2019) 3627.
- [160] M.B. Williams, T.W. Robinson, C.J. Williamson, R.P. Kinser, N.A. Ashmore, P.G. Allison, J.B. Jordon, Elucidating the Effect of Additive Friction Stir Deposition on the Resulting Microstructure and Mechanical Properties of Magnesium Alloy WE43, Metals 11(11) (2021).
- [161] Y.H. Kang, D. Wu, R.S. Chen, E.H. Han, Effects of Quenching Rate on the Microstructures and Mechanical Properties of the Heat Treatable Mg-4.2Y-2.3Nd-1.0Gd-0.6Zr Magnesium Alloy, Materials Science Forum 816 (2015) 356-361.
- [162] B. Milkereit, L. Burgschat, R.H. Kemsies, A. Springer, C. Schick, O. Kessler, In situ differential scanning calorimetry analysis of dissolution and precipitation kinetics in Mg–Y–RE alloy WE43, Journal of Magnesium and Alloys 7(1) (2019) 1-14.
- [163] X.-y. Yang, Z.-s. Ji, H. Miura, T. Sakai, Dynamic recrystallization and texture development during hot deformation of magnesium alloy AZ31, Transactions of Nonferrous Metals Society of China 19(1) (2009) 55-60.
- [164] Z. Zhang, X. Yang, Z. Xiao, J. Wang, D. Zhang, C. Liu, T. Sakai, Dynamic recrystallization behaviors of a Mg-4Y-2Nd-0.2Zn-0.5Zr alloy and the resultant mechanical properties after hot compression, Materials & Design 97 (2016) 25-32.
- [165] T. Al-Samman, G. Gottstein, Dynamic recrystallization during high temperature deformation of magnesium, Materials Science and Engineering: A 490(1-2) (2008) 411-420.
- [166] Q. Ma, B. Li, W.R. Whittington, A.L. Oppedal, P.T. Wang, M.F. Horstemeyer, Texture evolution during dynamic recrystallization in a magnesium alloy at 450°C, Acta Materialia 67 (2014) 102-115.
- [167] H. Zhang, H.y. Wang, J.g. Wang, J. Rong, M. Zha, C. Wang, P.k. Ma, Q.c. Jiang, The synergy effect of fine and coarse grains on enhanced ductility of bimodal-structured Mg alloys, Journal of Alloys and Compounds 780 (2019) 312-317.
- [168] S. Berbenni, V. Favier, M. Berveiller, Impact of the grain size distribution on the yield stress of heterogeneous materials, International Journal of Plasticity 23(1) (2007) 114-142.
- [169] W.Z. Chen, X. Wang, M.N. Kyalo, E.D. Wang, Z.Y. Liu, Yield strength behavior for rolled magnesium alloy sheets with texture variation, Materials Science and Engineering: A 580 (2013) 77-82.
- [170] W. Yuan, S.K. Panigrahi, J.Q. Su, R.S. Mishra, Influence of grain size and texture on Hall–Petch relationship for a magnesium alloy, Scripta Materialia 65(11) (2011) 994-997.
- [171] Z. Zhang, J. Zhang, W. Wang, S. Liu, B. Sun, J. Xie, T. xiao, Unveiling the deformation mechanism of highly deformable magnesium alloy with heterogeneous grains, Scripta Materialia 221 (2022).
- [172] A. Maqbool, N.F. Lone, N.Z. Khan, A.N. Siddiquee, D. Chen, Exceptional tensile strength-ductility synergy in friction stir processed Mg-Y-Nd-Zr alloy achieved through bimodal grain size distribution, Materials Science and Engineering: A 919 (2025).
- [173] M.K. Gupta, Friction stir process: a green fabrication technique for surface composites—a review paper, SN Applied Sciences 2(4) (2020).

- [174] Z. Zulkfli, N. Fatchurrohman, Advancement in friction stir processing on magnesium alloys, 2020.
- [175] G.K. Padhy, C.S. Wu, S. Gao, Friction stir based welding and processing technologies processes, parameters, microstructures and applications: A review, Journal of Materials Science & Technology 34(1) (2018) 1-38.
- [176] W. Wang, P. Han, P. Peng, T. Zhang, Q. Liu, S.-N. Yuan, L.-Y. Huang, H.-L. Yu, K. Qiao, K.-S. Wang, Friction Stir Processing of Magnesium Alloys: A Review, Acta Metallurgica Sinica (English Letters) 33(1) (2019) 43-57.
- [177] S. Kandalam, P. Agrawal, G.S. Avadhani, S. Kumar, S. Suwas, Precipitation response of the magnesium alloy WE43 in strained and unstrained conditions, Journal of Alloys and Compounds 623 (2015) 317-323.
- [178] H.S. Jiang, M.Y. Zheng, X.G. Qiao, K. Wu, Q.Y. Peng, S.H. Yang, Y.H. Yuan, J.H. Luo, Microstructure and mechanical properties of WE43 magnesium alloy fabricated by direct-chill casting, Materials Science and Engineering: A 684 (2017) 158-164.
- [179] S.M. Zhu, J.F. Nie, M.A. Gibson, M.A. Easton, On the unexpected formation of rare earth hydrides in magnesium–rare earth casting alloys, Scripta Materialia 77 (2014) 21-24.
- [180] Y. Li, C. Qu, J. Wang, R. Xu, Exceptional aging hardening behaviour of nanocrystalline Mg–Y-Nd-Gd-Zr alloy prepared by high pressure torsion, Journal of Alloys and Compounds 813 (2020).
- [181] W. Sun, Y. He, X. Qiao, X. Zhao, H. Chen, N. Gao, M.J. Starink, M. Zheng, Exceptional thermal stability and enhanced hardness in a nanostructured Mg-Gd-Y-Zn-Zr alloy processed by high pressure torsion, Journal of Magnesium and Alloys 11(12) (2023) 4589-4602.
- [182] N. Babacan, E. Yurtkuran, A. Balci, M. Bieda-Niemiec, A. Jarzębska, Effects of Non-isothermal Aging on Microstructure and Mechanical Properties of WE43 Alloy, Journal of Materials Engineering and Performance 30(11) (2021) 7909-7916.
- [183] P. Mengucci, G. Barucca, G. Riontino, D. Lussana, M. Massazza, R. Ferragut, E.H. Aly, Structure evolution of a WE43 Mg alloy submitted to different thermal treatments, Materials Science and Engineering: A 479(1-2) (2008) 37-44.
- [184] R. Ding, H. Yan, F. Ning, Y. Song, J. Xu, R. Chen, Formation mechanism of high-temperature oxidation film on WE43 magnesium alloy and its effect on corrosion performance, Journal of Rare Earths 42(12) (2024) 2316-2324.
- [185] F. Czerwinski, The reactive element effect on high-temperature oxidation of magnesium, International Materials Reviews 60(5) (2015) 264-296.
- [186] X. Zhao, Z. Ning, Z. Li, W. Zou, B. Li, K. He, F. Cao, J. Sun, A.A. Luo, In-mold oxidation behavior of Mg–4.32Y–2.83Nd–0.41Zr alloy, Journal of Materials Science 53(15) (2018) 11091-11103.
- [187] X. Zhao, D. Olden, B. Williams, A. Pariyar, D. Zhang, M. Murphy, P. Reed, P. Allison, B. Jordon, J. Qi, Grain growth stagnation at 525° C by nanoparticles in a solid-state additively manufactured Mg-4Y-3RE alloy, Journal of Magnesium and Alloys (2024).

- [188] S. Fida Hassan, S. Zabiullah, N. Al-Aqeeli, M. Gupta, Magnesium nanocomposite: Effect of melt dispersion of different oxides nano particles, Journal of Materials Research 31(1) (2016) 100-108.
- [189] K.-L. Ou, C.-C. Chen, C. Chiu, Production of Oxide Dispersion Strengthened Mg-Zn-Y Alloy by Equal Channel Angular Pressing of Mechanically Alloyed Powder, Metals 10(5) (2020).
- [190] S. Tekumalla, Y. Nandigam, N. Bibhanshu, S. Rajashekara, C. Yang, S. Suwas, M. Gupta, A strong and deformable in-situ magnesium nanocomposite igniting above 1000 degrees C, Sci Rep 8(1) (2018) 7038.
- [191] J. Humphreys, G.S. Rohrer, A. Rollett, Recrystallization and Related Annealing Phenomena, 2017.
- [192] X. Zhao, X. Zeng, L. Yuan, J. Gandra, Q. Hayat, M. Bai, W.M. Rainforth, D. Guan, A novel approach for producing Mg-3Al-1Zn-0.2Mn alloy wire with a promising combination of strength and ductility using CoreFlowTM, Scripta Materialia 227 (2023).
- [193] P. Maier, R. Peters, C.L. Mendis, S. Müller, N. Hort, Influence of Precipitation Hardening in Mg-Y-Nd on Mechanical and Corrosion Properties, Jom 68(4) (2015) 1183-1190.
- [194] R. Gao, T. Zhang, X.P. Wang, Q.F. Fang, C.S. Liu, Effect of zirconium addition on the microstructure and mechanical properties of ODS ferritic steels containing aluminum, Journal of Nuclear Materials 444(1-3) (2014) 462-468.
- [195] P. Dou, S. Jiang, L. Qiu, A. Kimura, Effects of contents of Al, Zr and Ti on oxide particles in Fe–15Cr–2W–0.35Y2O3 ODS steels, Journal of Nuclear Materials 531 (2020).
- [196] X. Bai, H. Xie, X. Zhang, D. Zhao, X. Rong, S. Jin, E. Liu, N. Zhao, C. He, Heat-resistant super-dispersed oxide strengthened aluminium alloys, Nat Mater 23(6) (2024) 747-754.
- [197] H. Wang, X. Wang, J. Zou, H. Zhou, Q. Zheng, J. Bi, M.D. Starostenkov, G. Dong, C. Tan, Recent progress on the control strategies of microstructure and mechanical properties of LPBF-printed aluminum alloys, The International Journal of Advanced Manufacturing Technology 134(9-10) (2024) 4015-4039.
- [198] G.-L. Jia, L.-P. Wang, Y.-C. Feng, E.-J. Guo, Y.-H. Chen, C.-L. Wang, Microstructure, mechanical properties and fracture behavior of a new WE43 alloy, Rare Metals 40(8) (2020) 2197-2205.
- [199] Y.-H. Kang, H. Yan, R.-S. Chen, Effects of heat treatment on the precipitates and mechanical properties of sand-cast Mg–4Y–2.3Nd–1Gd–0.6Zr magnesium alloy, Materials Science and Engineering: A 645 (2015) 361-368.
- [200] J.-c. Bian, B.-y. Yu, J.-f. Hao, H.-w. Zhu, H.-s. Wu, B. Chen, W.-r. Li, Y.-f. Li, L. Zheng, R.-x. Li, Improvement of microstructure, mechanical properties, and corrosion resistance of WE43 alloy by squeeze casting, China Foundry 19(5) (2022) 419-426.
- [201] N. Kumar, N. Dendge, R. Banerjee, R.S. Mishra, Effect of microstructure on the uniaxial tensile deformation behavior of Mg–4Y–3RE alloy, Materials Science and Engineering: A 590 (2014) 116-131.

- [202] S. Ganesan, M. Yaghoobi, A. Githens, Z. Chen, S. Daly, J.E. Allison, V. Sundararaghavan, The effects of heat treatment on the response of WE43 Mg alloy: crystal plasticity finite element simulation and SEM-DIC experiment, International Journal of Plasticity 137 (2021).
- [203] X. Wang, C. Liu, L. Xu, H. Xiao, L. Zheng, Microstructure and mechanical properties of the hot-rolled Mg–Y–Nd–Zr alloy, Journal of Materials Research 28(10) (2013) 1386-1393.
- [204] S. Chen, Y. Han, X. Jiang, X. Li, T. Yuan, W. Jiang, X. Wang, Study on in-situ material flow behaviour during friction stir welding via a novel material tracing technology, Journal of Materials Processing Technology 297 (2021).
- [205] W. Liu, Y. Yan, R. Ni, T. Sun, S. Wu, Y. Shen, Numerical simulation and experimental investigation of subzero liquid SFSW of ME20M magnesium alloy, Journal of Adhesion Science and Technology (2021) 1-16.
- [206] J. Li, D. Zhang, F. Chai, Influence of processing speed on microstructures and mechanical properties of friction stir processed Mg–Y–Nd–Zr casting alloy, Materials Research Innovations 18(sup4) (2014) S4-142-S4-147.
- [207] M.M. Hoseini-Athar, R. Mahmudi, R. Prasath Babu, P. Hedström, Tailoring the texture of an extruded Mg sheet through constrained groove pressing for achieving low mechanical anisotropy and high yield strength, Scripta Materialia 186 (2020) 253-258.
- [208] S. Sanyal, S. Kanodia, R. Saha, T.K. Bandyopadhyay, S. Mandal, Influence of hard plate hot forging temperature on the microstructure, texture and mechanical properties in a lean Mg–Zn–Al alloy, Journal of Alloys and Compounds 800 (2019) 343-354.
- [209] H. Agiwal, M. Ali Ansari, D. Franke, P. Faue, S.J. Clark, K. Fezzaa, S. Rudraraju, M. Zinn, F.E. Pfefferkorn, Material flow visualization during friction stir welding using high-speed X-ray imaging, Manufacturing Letters 34 (2022) 62-66.
- [210] S.-i. Inoue, M. Yamasaki, M. Ohata, S. Kakiuchi, Y. Kawamura, H. Terasaki, Texture evolution and fracture behavior of friction-stir-welded non-flammable Mg–Al–Ca alloy extrusions, Materials Science and Engineering: A 799 (2021).
- [211] A.M. Jamili, A. Zarei-Hanzaki, H.R. Abedi, P. Minárik, R. Soltani, The microstructure, texture, and room temperature mechanical properties of friction stir processed Mg-Y-Nd alloy, Materials Science and Engineering: A 690 (2017) 244-253.
- [212] J. Zhang, S. Han, Y. Sun, X. Chen, P. Chen, Z. Li, G. Huang, F. Pan, Enhanced strength of WE43 magnesium-rare earth alloy via combining extrusion and aging, Materials Science and Engineering: A 880 (2023).
- [213] W.T. Sun, X.G. Qiao, M.Y. Zheng, X.J. Zhao, H.W. Chen, N. Gao, M.J. Starink, Achieving ultra-high hardness of nanostructured Mg-8.2Gd-3.2Y-1.0Zn-0.4Zr alloy produced by a combination of high pressure torsion and ageing treatment, Scripta Materialia 155 (2018) 21-25.
- [214] H. Wang, Y. Li, B. Yang, J. Wang, Z. Wang, Y. Li, Unveiling the mechanism of texture evolution in AZ31B Mg alloy during additive friction stir deposition, Journal of Alloys and Compounds 1011 (2025).
- [215] S. Sharma, K.V. Mani Krishna, M. Radhakrishnan, M.V. Pantawane, S.M. Patil, S.S. Joshi, R. Banerjee, N.B. Dahotre, A pseudo thermo-mechanical model linking process parameters to

- microstructural evolution in multilayer additive friction stir deposition of magnesium alloy, Materials & Design 224 (2022).
- [216] K.C. Kincaid, D.W. MacPhee, G.G. Stubblefield, J.B. Jordon, T.W. Rushing, P.G. Allison, A Finite Volume Framework for the Simulation of Additive Friction Stir Deposition, Journal of Engineering Materials and Technology 145(3) (2023).
- [217] I. Barin, Thermochemical Data of Pure Substances, 1995.
- [218] P. Krištofová, M. Roudnicka, J. Kubásek, A. Michalcová, D. Vojtech, J. Suchý, D. Paloušek, E. Alzubi, Magnesium Alloy WE43 Produced by 3D Printing (SLM), Defect and Diffusion Forum 405 (2020) 345-350.
- [219] O.G. Rivera, P.G. Allison, J.B. Jordon, O.L. Rodriguez, L.N. Brewer, Z. McClelland, W.R. Whittington, D. Francis, J. Su, R.L. Martens, N. Hardwick, Microstructures and mechanical behavior of Inconel 625 fabricated by solid-state additive manufacturing, Materials Science and Engineering: A 694 (2017) 1-9.
- [220] X. Wang, L. Hu, K. Liu, Y. Zhang, Grain growth kinetics of bulk AZ31 magnesium alloy by hot pressing, Journal of Alloys and Compounds 527 (2012) 193-196.
- [221] Q. Miao, L. Hu, X. Wang, E. Wang, Grain growth kinetics of a fine-grained AZ31 magnesium alloy produced by hot rolling, Journal of Alloys and Compounds 493(1-2) (2010) 87-90.
- [222] X. Zeng, H. Yi, Z. Zeng, L. Yuan, S. Yi, J. Gao, M. Rainforth, D. Guan, Track-Rex: A universal toolbox for tracking recrystallization nucleation and grain growth behaviors in polycrystalline materials, Journal of Materials Science & Technology 197 (2024) 149-159.
- [223] R. Pei, S. Korte-Kerzel, T. Al-Samman, Normal and abnormal grain growth in magnesium: Experimental observations and simulations, Journal of Materials Science & Technology 50 (2020) 257-270.
- [224] Z.-Y. Meng, C. Wang, Z.-M. Hua, M. Zha, H.-Y. Wang, Achieving extraordinary thermal stability of fine-grained structure in a dilute magnesium alloy, Materials Research Letters 10(12) (2022) 797-804.
- [225] Q. Zhang, W. Wang, Q. Yuan, Z. Wang, Z. Zhang, G. Xu, Effect of Niobium on the Thermal Stability and Mechanical Properties of a Low-Carbon Ultrafine Grain Steel, Metals and Materials International 29(7) (2022) 2018-2027.
- [226] G. Riontino, M. Massazza, D. Lussana, P. Mengucci, G. Barucca, R. Ferragut, A novel thermal treatment on a Mg–4.2Y–2.3Nd–0.6Zr (WE43) alloy, Materials Science and Engineering: A 494(1-2) (2008) 445-448.
- [227] N. Kumar, R.S. Mishra, N.B. Dahotre, R.E. Brennan, K.J. Doherty, K.C. Cho, Effect of friction stir processing on microstructure and mechanical properties of laser-processed Mg 4Y 3Nd alloy, Materials & Design 110 (2016) 663-675.